Experimental Investigation of Natural Gas Kinetics Using a Fuel Substitution Method

By

Daniel Janecek

A document submitted in partial fulfillment of
the requirements for the degree of

Doctor of Philosophy
(Mechanical Engineering)

at the
UNIVERSITY OF WISCONSIN - MADISON
2018

Date of final oral examination: 6/29/18

The dissertation is approved by the following members of the Final Oral Committee:

Jaal Ghandhi, Professor, Mechanical Engineering
David Rothamer, Professor, Mechanical Engineering
Sage Kokjohn, Professor, Mechanical Engineering
Scott Sanders, Professor, Mechanical Engineering
George Huber, Professor, Chemical and Biological Engineering

Abstract

The objective of this work was to develop reference data for validation of kinetics mechanisms at engine-relevant conditions where limited data exist. Fuel substitution sweeps were run for six homogeneous-charge compression-ignition conditions. The sweeps were performed with constant combustion phasing and boundary conditions. Baseline mixtures of both methane/hydrogen and methane/propane were used and the required ratio change of the two baseline fuels to meet the operation constraint as a test fuel was added was used to define the test fuel's reactivity.

Three in-cylinder temperature measurement methods were performed: a trapped-mass state equation calculation, water absorption spectroscopy, and fast-response thermocouples. At intake valve close (IVC), the 95% confidence intervals for the three methods overlapped for most test conditions. Uncertainty in the final IVC measured temperatures ranged from 5-10 K.

The required simulation IVC temperatures in a two-zone model for five mechanisms were compared to the experimental IVC temperatures. Four of the five mechanisms were accurate within experimental uncertainty for the methane/hydrogen cases, but only one of those four mechanisms was also accurate for the methane/propane cases.

Two simulation methods, using the three most accurate mechanisms from the previous simulation, were used to evaluate mechanism performance regarding the reactivities of nine test fuels relative to the two sets of baseline fuels: 1) fixed fueling, variable IVC temperature and 2) fixed IVC temperature, variable fueling. Consistent results were seen with the three mechanisms' ability to predict test fuel reactivities relative to methane/hydrogen; most test fuels' reactivities were under-predicted. Varying results were seen with the three mechanisms' ability to predict test fuel reactivities relative to

methane/propane. One mechanism showed consistent results to the methane/hydrogen cases, but the remaining two mechanisms tended to over-predict test fuel reactivities relative to methane/propane, which was different from the under-predictions seen for the methane/hydrogen cases.

A simplified method to characterize relative fuel reactivities using ignition delay calculations was developed to generate maps of the relative fuel reactivities over a wide range of thermodynamic conditions. At high temperatures, all hydrocarbon test fuels had similar reactivities to propane, but at low temperatures there was a large variation in relative reactivities.

Acknowledgements

I'd like to start off by thanking my advisors, Dr. Jaal Ghandhi and Dr. David Rothamer, for all of their help and guidance along this journey. Their advising style has been an excellent balance of guidance and a push in the right direction when necessary combined with giving me the independence to figure issues out on my own. They deserve much of the credit for my progress both on this research and more generally as an engineer over these last six years. I count myself incredibly lucky to have been able to work with both of them. I'd like to especially thank Jaal for his willingness to meet whenever I had questions or ideas I needed to bounce off of someone.

Other ERC staff who have been a major help are Josh Leach, Ralph Braun, and John Erb for their help with computer, mechanical, and electrical systems over the years.

Without funding supplied by Caterpillar, none of this work would have been possible. Specifically, thanks are owed to Chad Koci, Bobby John, Jon Anders, Russ Fitzgerald, and Chris Gehrke for their input and guidance throughout this work.

In terms of specific contributions to this dissertation work, there are several ERC students I would like to specifically thank: Scott Melin for his help with the water absorption spectroscopy testing, James Cherry for his help with the fast-response thermocouple testing, and Arun Ravindran for his help with the CFD simulations. Each of their contributions were crucial to the in-cylinder temperature measurements portion of this work.

I'd also like to specifically thank all of the DERC lab students who I have had the opportunity to work with over the years: Ryan Walker, Adam Dempsey, Eric Gingrich, Yizhou Zhang, Mike Groendyk, and Victor Zhang. Keeping the DERC lab functional has been a continuous battle, and would not have been possible without countless hours from each of them.

I would also like to specifically thank my fellow ERC students David Klos, Jordan Paz, Mike Tiry, Mike Groendyk, Grant Allen, and Tyler Strickland for their friendship

over the years. While it certainly did not help my research progress, the countless hours spent building racecars, playing foosball, or hanging out at the Library were some of the best memories I have of my time in Madison.

Outside of the ERC, I have had the opportunity to develop a great group of Madison soccer friends who have been the one constant throughout my time in Madison as school friends have graduated and moved away over the years. Having an outlet of the soccer field to reduce the stress that built up during the ups and downs of this dissertation work has been invaluable.

Last but certainly not least, I would like to thank all of my friends and family for supporting me through this endeavor. My mom deserves the biggest thanks for all the hard work and sacrifices she made to get me to this point.

Contents

List of Figures

List of Tables

Nomenclature

$AHRR$ Apparent heat release rate

$Aramco$ AramcoMech1.3 kinetics mechanism

BDC Bottom dead center

BN Butane number

$C5-49$ C5-49 kinetics mechanism

CA_{50} Location of 50% of the cumulative apparent heat release rate

CAD Crank angle degree

CFD Computational fluid dynamics

CI_{94} 95% confidence interval

DAQ Data acquisition

$degbTDC$ Degrees before top dead center

DOE Design of experiments

EVC Exhaust valve close

EVO Exhaust valve open

$FDML$ Fourier-domain mode-locked

$FWHM$ Full-width half-max

GRI GRI-Mech 3.0 kinetics mechanism

H/C Hydrogen-to-carbon

$HCCI$ Homogeneous-charge compression-ignition

HI Hydrogen index

HI Propane index

HRD Hydro-processed renewable diesel

Hz Hertz

$IMEP$ Indicated mean effective pressure

IVC Intake valve close

$KLSA$ Knock-limited spark advance

LAS Laser absorption spectroscopy

LHV Lower heating value

$LLNL$ n-Heptane Detailed Mechanism Version 3.1 kinetics mechanism

MFB Mass fraction burned

MN Methane number

MON Motored octane number

MSE Mean squared error

MW Molecular weight

NI National Instruments

NTC Negative temperature coefficient

NZT Normalized zone temperature

OI Octane index

PKI Propane knock index

PRF Primary reference fuel

RCM Rapid compression machine

RON Research octane number

RPM Revolutions per minute

SI Spark-ignition

SOC Start of combustion

T_{IVC} Temperature at intake valve close

TC Thermocouple

TDC Top dead center

TSA Thermal stratification analysis

UBC UBC 2.0 kinetics mechanism

Chapter 1

Introduction

1.1 Motivation and Objective

Natural gas has gained increasing popularity for transportation and stationary power generation over the past few decades due to its availability, low price, and high hydrogen-to-carbon (H/C) ratio resulting in lower CO_2 emissions relative to liquid hydrocarbon fuels such as gasoline and diesel. It is well known that pure methane has a high resistance to knock relative to gasoline, which makes it beneficial for use in spark-ignition (SI) engines; the composition of natural gas, however, varies significantly depending on its source [1], which can impact its performance in internal combustion engines.

Experimental engine testing or simulation must be done on the full range of possible natural gas mixtures to both meet emissions requirements and achieve the highest possible engine efficiency. It would be an extremely expensive and time-consuming process to experimentally test the full range of natural gas mixtures, which makes simulation an appealing option. In order to optimize engine design, computational tools are needed that can accurately simulate natural gas combustion and can accurately predict autoignition and knock in natural gas engines.

The chemical kinetics mechanisms used in engine simulations must accurately cap-

ture the change in fuel reactivity and propensity to knock as the natural gas composition is varied. While a wide variety of experimental data exist for validating kinetics mechanisms, there is a general lack of data at engine-relevant thermodynamic conditions. However, engine experiments typically are difficult to directly use for kinetics validation because the boundary conditions are not well known. The purpose of this research was to examine the effects of higher hydrocarbon fuels on natural gas mixture reactivity in well-controlled homogeneous-charge compression-ignition (HCCI) engine experiments. Experimental data were compared to simulated results to evaluate the accuracy of several chemical kinetics mechanisms.

1.2 Experimental Work

A homogeneous-charge compression-ignition (HCCI) combustion strategy was used to eliminate the complications involved with direct-injection or SI flame propagation, and a fuel substitution methodology was implemented to fix the experimental boundary conditions for the entirety of each set of testing. Fuel substitution (described more fully below) involving combinations of hydrogen, methane, ethane, ethylene, propane, butane, and *n*-heptane, and isooctane were performed at six different operating conditions that spanned a wide range of top dead center (TDC) temperatures and pressures. Two premixed combinations of the previously mentioned hydrocarbons were also tested at the same operating conditions.

The fuel substitution strategy works as follows. First, an HCCI baseline condition that uses two well-characterized fuels at the desired intake thermodynamic conditions was run on the engine. For this study, both methane/propane (CH_4/C_3H_8) and methane/hydrogen (CH_4/H_2) mixtures were chosen as the baseline fuels because their kinetics are reasonably well understood and form the basis of all mechanisms used to describe natural gas combustion, and because the latter pair of fuels are used in the methane

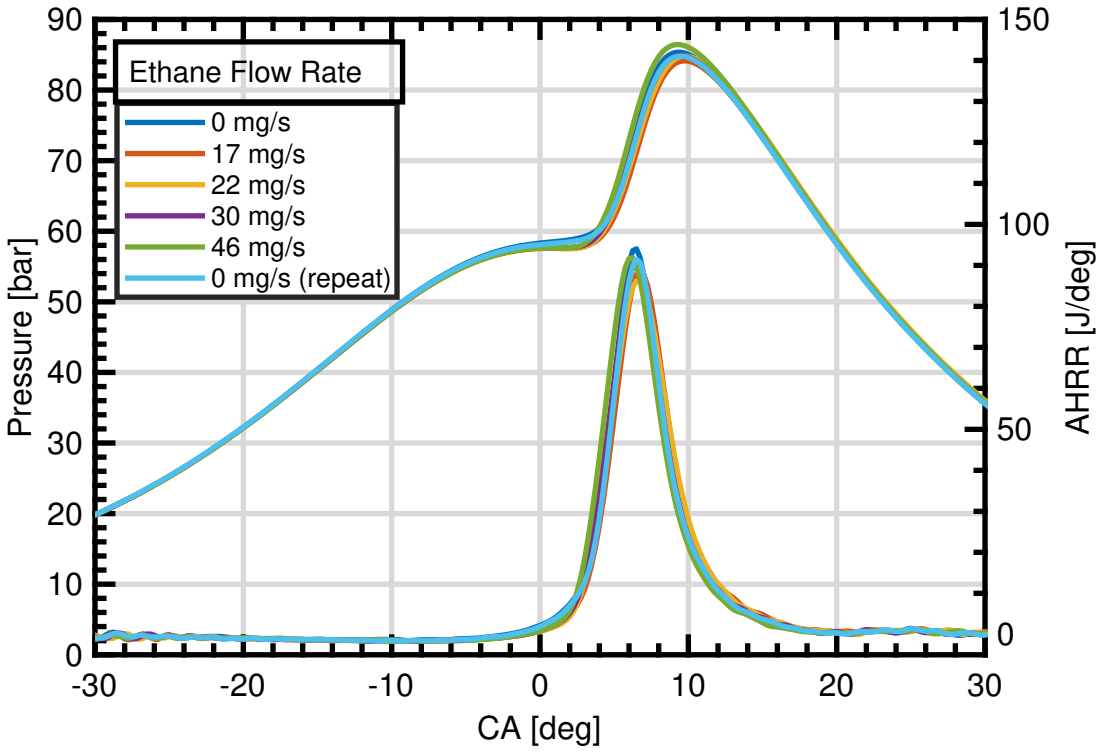

(a)

Figure 1.1: Pressure and apparent heat release rate with baseline fuels of methane and propane and test fuel of ethane for operating condition 1.

number (MN) characterization. Next, a test fuel was added in increasing amounts while the quantities of methane and hydrogen/propane were adjusted to keep engine load and combustion phasing constant. The in-cylinder pressure and apparent heat release rate (AHRR) for one sweep can be seen in Figure 1.1. Pressure and AHRR were held constant throughout the fuel substitution sweep. In a previous study, Janecek *et al.* [2] showed that the indicated mean effective pressure (IMEP) varied by less than 1.0%, the location of 50% of the cumulative AHRR, CA_{50}, varied from the mean by less than 0.5 deg, and the temperature at intake valve close, T_{IVC}, varied about the mean by less than 3.0 K.

The engine experiments' thermodynamic pressure and temperature histories must be quantified to ensure the simulations are accurately representing the experimental conditions. While in-cylinder pressure is relatively easily measured with a fast-response piezoelectric pressure transducer, in-cylinder temperature is much more difficult to measure.

Three main methods of temperature determination were investigated: (1) a state equation based on the estimated trapped mass, the measured pressure, and known volume, (2) water absorption spectroscopic thermometry, and (3) fast-response thermocouples. Each method has specific advantages and disadvantages that will be discussed along with a thorough uncertainty analysis.

1.3 Simulation Work

A simulation model was created in Cantera [3] and was used to evaluate the ability of the chemical kinetics mechanisms to match the experimental tests. The first objective of the simulation work was to evaluate the prediction of the absolute fuel reactivity for each kinetic mechanism for the fuel substitution baseline cases, which were run with reference fuel mixtures of CH_4/H_2 and CH_4/C_3H_8. The simulation modeled the closed-cycle portion – from intake valve close (IVC) to exhaust valve open (EVO) – of the engine cycle and used the experimentally measured pressure, fuel concentrations, and estimated IVC temperature as input conditions at IVC.

The second objective of the simulation work was to evaluate the accuracy of the relative fuel reactivity of each kinetic mechanism for all runs of each fuel substitution sweep. For these simulations, the baseline condition consisting of only reference fuels was 'tuned' by adjusting the T_{IVC} until combustion phasing in the simulation matched the experimental combustion phasing. Once this T_{IVC} value was found, all input conditions were held constant while the remaining cases for the fuel substitution sweep were simulated.

1.4 Dissertation Layout

The dissertation is structured as follows. Chapter 2 reviews literature relevant to the current work. The first topic reviewed is experimental methods used to test fuel kinetics; these test are divided into the categories: engine, shock tube, and rapid compression

machine (RCM) testing. Next, a review of several methods of estimating in-cylinder temperature in engines is discussed. The three methods investigated in this work were a trapped-mass state equation, water-absorption spectroscopy, and fast-response thermocouples. This is followed by a review of HCCI engine modeling strategies. Finally, the five chemical kinetics mechanisms investigated in the current work are discussed.

Chapters 3 and 4 describe the experimental setup and detail the results of the experimental fuel substitution testing. The results of all fuels tested with both CH_4/H_2 and CH_4/C_3H_8 reference fuels at six different operating conditions are presented.

Chapters 5-8 discuss the different methods used to estimate the in-cylinder temperatures of the engine experiments, with a focus on T_{IVC}. In addition to the measured values, a detailed uncertainty analysis is discussed for each method. Chapter 5 describes the trapped-mass state equation method for temperature estimation; this estimation is available for all operating conditions. Chapter 6 details the results of water-absorption spectroscopy testing performed on-engine for operating conditions 1-4 for both motored and fired conditions. Chapter 7 describes the results of two fast-response thermocouples used to measure in-cylinder temperature, with a focus on motored conditions. Chapter 8 discusses a set of computational fluid dynamics (CFD) simulations performed to gain insight on the biases associated with each temperature estimation method and provides a comparison of the calculated temperatures from each method.

Chapters 9-10 describe the model used to simulate the experimental fuel substitution tests, and compare the simulated and experimental results. Chapter 9 focuses on the engine model created in Cantera and compares the baseline cases run with only the CH_4/H_2 and CH_4/C_3H_8 reference fuels. Chapter 10 evaluates the ability of the kinetic mechanisms to match the test fuels' reactivities relative to the reference fuels.

Chapter 11 summarizes with the main contributions of the dissertation and provides suggestions for potential future work.

Chapter 2

Literature Review

2.1 Experimental Testing

A wide variety of experiments have been published to characterize the ignition quality of natural gas mixtures. These experiments can be divided into three main groups based on device: engine tests similar to those used for measuring the knock propensity of SI engine fuels, rapid compression machine (RCM) ignition delay measurements, and ignition delay measurements in shock tubes. Because RCM and shock tube tests aim to measure absolute ignition delay at fixed temperature and pressure conditions, fuel ignition delay times can be directly compared between those devices. Engine testing is generally comparative, *i.e.*, the ignition quality of a fuel is compared to that for a blend of reference fuels, due to the difficulty of quantifying time-varying in-cylinder conditions.

2.1.1 Engine Testing

Methane Number Testing

The research octane number (RON) and motored octane number (MON) of a fuel are defined by ASTM test standards D2699 and D2700, respectively, and compare the knock resistance of a fuel to a mixture of the primary reference fuels (PRFs) isooctane and

n-heptane [4]. Because the RON (solid) and MON (dashed) tests involve engine operating conditions that traverse different temperature-pressure states, specifically states encompassing the negative temperature coefficient (NTC) regime, real fuels typically have different RON and MON values [5]. A simple example of this is shown in Figure 2.1 by comparing the ignition delays of one of the PRF fuels, *n*-heptane, and methane; *n*-heptane shows NTC behavior while methane does not, which causes the relative ignition delays to change drastically as a function of temperature. The RON and MON curves were taken from the simulation work of Yates et al. [6]. At a pressure of 20 bar n-heptane has approximately the same ignition delay at 800 K and 950 K while the ignition delay of methane decreased by two to three orders of magnitude. At a pressure of 20 bar, RON conditions are represented by the 800 K temperature while MON conditions are represented by the 950 K temperature. This makes it difficult to describe a fuel's ignition quality over a range of operating conditions using only the RON or MON.

Due to the majority of natural gas components having a higher knock resistance than isooctane, an alternative method was developed to classify natural gas mixtures. Leiker et al. developed a procedure to compare the knock resistance of natural gas mixtures to a binary mixture of methane and hydrogen [7]. They called the result the Methane Number (MN). The test procedure was similar to the MON procedure, using an engine speed of 900 revolutions-per-minute (rpm) and a naturally aspirated engine run at a stoichiometric equivalence ratio (Φ=1) with a variable compression ratio ranging from 4-18. The main differences between the test procedures was that the MN test used an intake temperature of 21 °C, while the MON test used an intake temperature of 149 °C, and spark timing was fixed at 15 degrees before TDC (deg bTDC) for the MN test while spark timing varied from 19-26 deg bTDC as a function of compression ratio for the MON test. For a given test fuel, the compression ratio is adjusted until the onset of knock is detected. The test fuel's MN is defined as the mixture of methane and hydrogen that produces the same level of knock at the same compression ratio. A mixture of pure

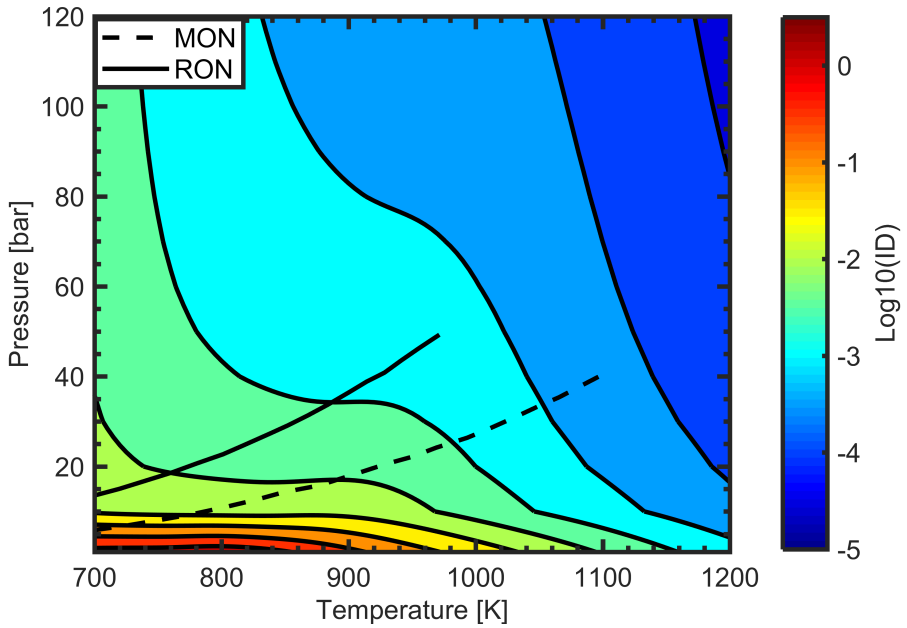

(a)

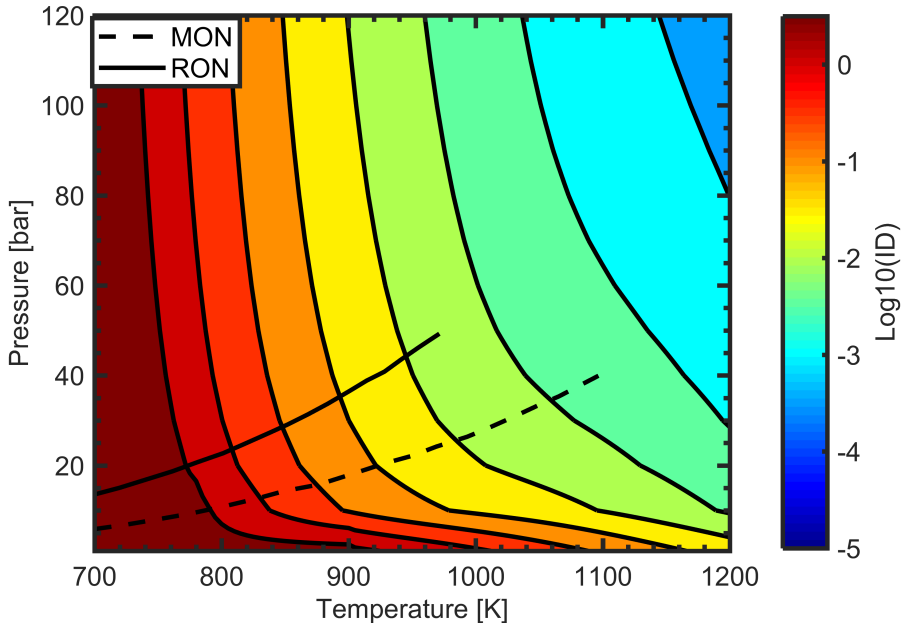

(b)

Figure 2.1: Log (base 10) of constant pressure ignition delay [s] for n-heptane (top) and methane (bottom) as a function of pressure and temperature using the Lawrence Livermore n-heptane mechanism with an equivalence ratio of 0.35. RON and MON curves reproduced from [6]

methane was defined as having a MN=100 and a mixture of pure hydrogen was defined as having MN=0. Methane-hydrogen mixtures were characterized on a gaseous volume basis. It was found that the MN of mixtures containing methane, ethane, propane, *n*-butane, ethylene, propylene, and hydrogen could be estimated with reasonable accuracy by assuming a linear mixing relation on a molar basis, *i.e.*,

$$MN = \sum x_i MN_i \tag{2.1}$$

Another advantage of MN testing is that the reference fuels used, methane and hydrogen, do not exhibit NTC behavior, as seen in the ignition delay contour plot of methane in Figure 2.1b. This makes them more suitable for describing the ignition quality of natural gas mixtures consisting of primarily methane and ethane. However, when natural gas mixtures contain heavier hydrocarbons such as propane or butane, they will show some NTC behavior and will therefore have a MN that varies with operating condition. The dependency of fuel relative reactivity based on operating condition, even for the MN reference fuels hydrogen and methane, can be seen in Figure 2.2. Typically, fuels with high MNs are expected to exhibit a high resistance to knock, but it can be seen that pure hydrogen, which has a MN of 0 (by definition), is actually less reactive than methane, which has a MN of 100 (by definition) at temperatures below 900 K.

Kubesh found a correlation between MON and the overall gas mixture hydrogen-to-carbon ratio (H/C), and between MON and MN by experimentally testing a variety of natural gas mixtures using the MON test procedure [8]. These correlations are

$$MN = -406 + 508(H/C) - 174(H/C)^2 + 20(H/C)^3, \tag{2.2}$$

$$MN = 1.62 \times MON - 119. \tag{2.3}$$

Figure 2.3 shows that these correlations can be used to predict the MON or MN of natural gas mixtures with compositions similar to the test mixtures. However, due to

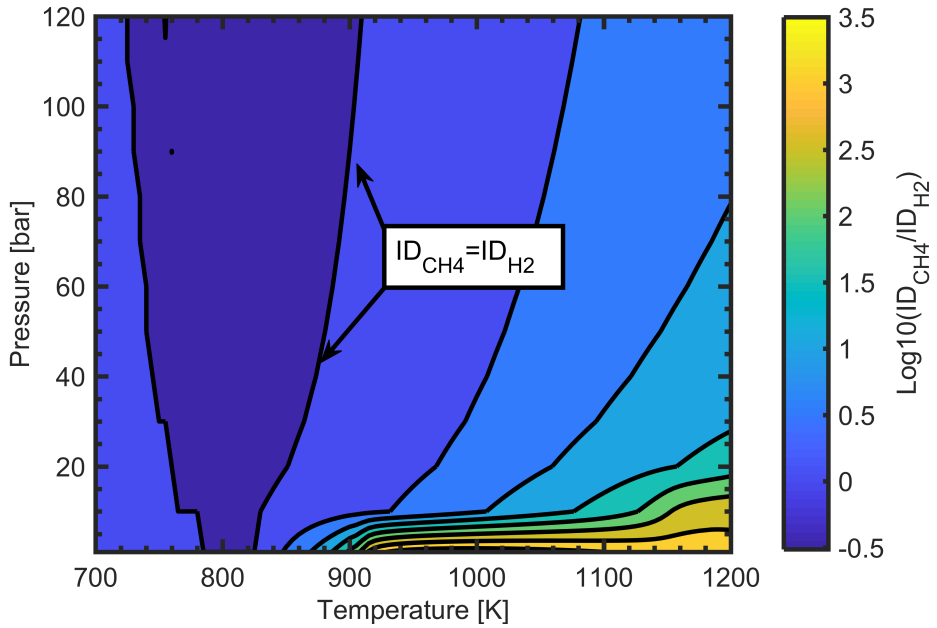

Figure 2.2: Log (base 10) of the ratio of constant pressure ignition delays (methane/hydrogen) using Lawrence Livermore n-heptane mechanism at an equivalence ratio of 0.35.

their empirical nature, these correlations only show relative knock behavior instead of an absolute ignition quality metric; additionally, there is no testing to indicate that these fuels would exhibit the same relative behavior at different thermodynamic engine operating conditions.

In a similar manner, Schaub and Hubbard devised a Butane Number (BN) scale ranging from 100 for pure n-butane to 0 for pure methane [9]. The BN scale suffers from the same issue as the RON and MON scales, it contains a reference fuel, butane, that exhibits NTC behavior. Due to the MN scale having a linear correlation with MON and higher resolution compared to the BN scale for typical natural gas mixtures, the MN has become the accepted method for natural gas mixture knock classification [10].

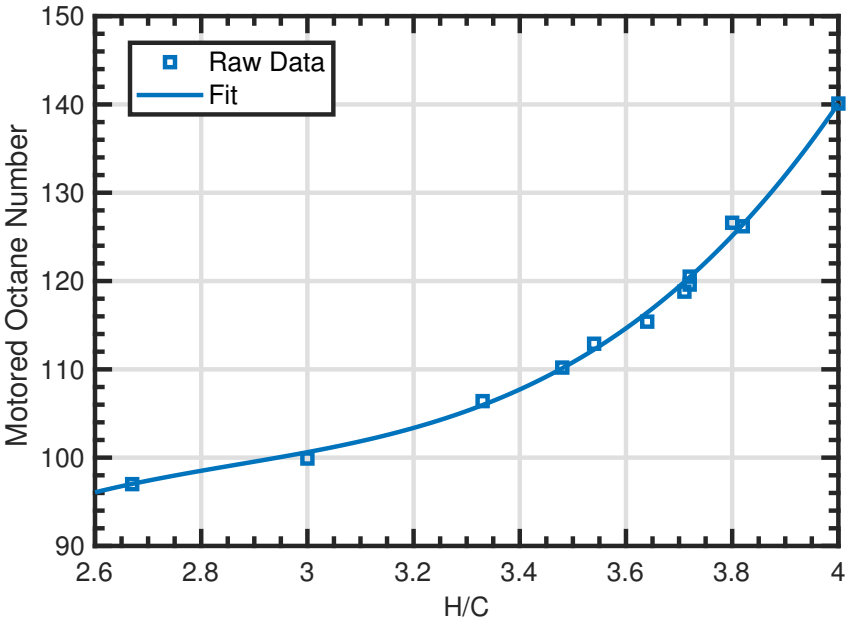

Figure 2.3: Comparison between calculated and measured MON as a function of mixture H/C for a variety of natural gas mixtures. Data points reproduced from [8].

Octane Index

Kalghatgi and Angstrom proposed an Octane Index (OI),

$$OI = (1 - K) \times RON + K \times MON, \tag{2.4}$$

to describe a fuel's ignition quality in HCCI engines [11], where K is an engine-specific constant that varies with operating condition. This equation seeks to describe the dependency of a fuel's ignition quality on thermodynamic conditions based on the difference of the RON and MON values and the engine operating condition. While adding the engine operating condition parameter is an improvement over only using the RON or MON value, because K is only dependent on engine operating condition and not dependent on fuel chemistry, this method implies that if two fuels exhibit similar RON and MON then they will exhibit similar ignition quality over the entire engine speed/load operating map.

From Equation 2.4, a K=1 indicates that the OI of a fuel is completely described by its MON, whereas a K=0 indicates that the OI of a fuel is equivalent to its RON. A negative K value indicates that the OI of a fuel will be directly related to its RON but inversely related to its MON. Pump octane ratings assume a K value of 0.5, making the OI an evenly weighted average of the RON and MON. Kalghatgi and Angstrom found a wide range of K values for different engine operating conditions, with K trending towards negative values for low intake temperature and high intake pressure conditions and towards positive values for high intake temperatures.

Propane Knock Index

Gersen et al. proposed a correlation of natural gas mixtures to a propane knock index (PKI) [12]. The PKI was defined as a fuel having an equivalent knock-limited spark advance (KLSA) as a mixture of propane and methane, with 100 referring to pure propane and 0 referring to pure methane. A lean SI operating condition was simulated using a two-zone thermodynamic combustion model combined with a chemical kinetics autoignition model. The PKI of a wide variety of natural gas mixtures was calculated by finding the ratio of propane and methane required in the simulation to match the test fuel's knock characteristics in the simulation. First, light knock for the test fuel was simulated by adjusting the starting end-gas temperature until autoignition occurred at the point at which 90% of the fuel was burned. With the starting end-gas temperature fixed, the ratio of propane and methane that resulted in autoignition occurring at the same 90% burn point was defined as the PKI for that test fuel. Experimental tests were then performed on a wide variety of natural gas mixtures containing methane, ethane, propane, butane, and hydrogen for a single lean SI operating condition to find the KLSA. Gersen found that the simulated PKI for each fuel had strong correlation with the experimentally measured KLSA of each fuel, seen in Figure 2.4. It is important to note that the initial comparison between simulated PKI and experimental KLSA showed much weaker

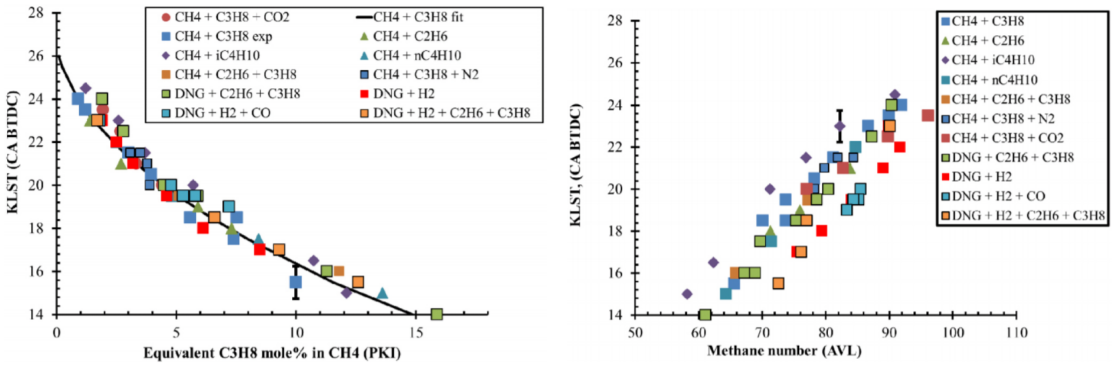

(a) (b)

Figure 2.4: Experimentally tested knock limited spark advance vs. simulated propane knock index using revised mechanism (a) and experimentally tested knock limited spark advance vs. calculated Methane Number (b). Reproduced from [12].

correlation until the chemical kinetics mechanism used in the simulation was revised by requiring it to match RCM data over the temperature and pressure ranges of interest. They also compared the MN of each fuel to the KLSA and found that there was much weaker correlation, seen in Figure 2.4. The relevant results of this study are two-fold: a simulated propane-methane index for natural gas mixtures was found to strongly correlate with experimental KLSA results while the MN showed a much weaker correlation with experimental KLSA results, and the reaction rates of the chemical kinetics mechanism utilized had to be updated to match RCM tests at engine-relevant conditions.

Engine Tests using HCCI Combustion

Natural gas has been involved in a number of experimental investigations using HCCI combustion. The majority of these studies focus on a single natural gas composition; however, there have been several studies performed on multi-component mixtures. El-Din et al. studied the effect of di-methyl ether and hydrogen addition to natural gas in order to extend the operating range [13]. Their method involved fixing intake conditions and sweeping equivalence ratio to find the misfire and knock limits. Jun et al. tested binary mixtures of n-butane and methane by fixing the intake conditions and investigating

how combustion phasing changed with different fuel blend percentages [14]. Yap et al. tested the reactivity of mixtures of hydrogen and natural gas by recording the intake temperature required to keep combustion phasing constant for different fuel blends [15]. Fiveland et al. investigated a number of binary fuel mixtures including methane, ethane, propane, and *n*-butane [16]. They investigated the fuel composition effect on misfire limit by first varying intake temperature in order to achieve a CA_{50} of 0 deg aTDC and then decreasing intake temperature until the misfire limit was reached.

The issue with using any of these HCCI experimental data to validate a kinetic model is that the boundary conditions are not fixed for any of the tests. There are two main classes of parameter variations in the previously listed experiments, either the combustion phasing is held constant while the intake conditions are varied, or the intake conditions are held constant while the combustion phasing varies. It is clear that when intake temperature or equivalence ratio change, the in-cylinder conditions leading up to the start of ignition will vary, but even when these inlet conditions are fixed the variation of combustion phasing will have an effect on wall boundary conditions, IVC temperature, and in-cylinder conditions at the start of combustion. These changing inlet and boundary conditions cause uncertainty in the inputs to the kinetic model, which makes it difficult to know whether observed differences are due to the kinetic mechanism or the physical model of the system, *i.e.*, the boundary conditions.

Janecek et al. measured piston temperatures and found that they were dependent on combustion phasing, even when intake temperature was held constant [2]. In order to minimize the effect of this boundary condition uncertainty, they devised a method that effectively froze boundary and initial conditions for the entirety of a fuel substitution sweep. The method was used to characterize the reactivity of F-76, a high-sulfur-content diesel fuel, and HRD, a hydro-processed renewable diesel fuel, relative to the PRFs isooctane and *n*-heptane. They found that F-76 had a reactivity equivalent to a mixture of 35/65 isooctane/*n*-heptane and that HRD was more reactive than *n*-heptane at the

four operating conditions tested. In their testing, the indicated mean effective pressure varied by less than 1.0%, the CA_{50} varied from the mean by less than 0.5 deg, and the IVC temperature varied about the mean by less than 3 K. First, an HCCI baseline condition that used the two PRF fuels at the desired intake thermodynamic conditions was run on the engine. Next, the test fuel, F-76 or HRD, was added in increasing amounts while the quantities of isooctane and *n*-heptane were adjusted to keep engine load and CA_{50} constant. Pressure and AHRR are held constant throughout the fuel substitution sweep. This method was used for the current experimental work and will be discussed in more detail.

2.1.2 Shock Tube Testing

Shock tubes operate on the principle of a reflected shock almost instantaneously creating high temperature and pressure thermodynamic conditions in which a fuel mixture's ignition delay can be measured. Typical thermodynamic ranges tested for kinetics experiments are temperatures between 600 and 2500 K and pressures up to 100 bar with ignition delays up to several milliseconds, although recent advances in methodologies can allow ignition delays of up to 50 milliseconds to be measured [17]. Due to the short ignition delay times, heat transfer is assumed to be negligible and thus the thermodynamic state is frozen. Simulations were traditionally performed assuming adiabatic, constant-volume conditions behind the reflected shock; alternatively, for longer ignition delay times where the constant-volume assumption is not valid, a pressure-temperature profile that assumes an isentropic compression process can be used [17]. Pang et al. found that the pressure rise occurred at a rate of 2%/ms due to facility-dependent effects [18]; significant differences were seen in simulated ignition delay times, especially for longer ignition delay times, compared to simulations using the constant volume assumption. The short ignition delay requirement defines a lower limit for the temperature range, especially when using lower reactivity fuels such as methane. Referring to Figure 2.2, shock tube testing

for methane at a pressure of 60 bar would have to be above a temperature of 1150 K to maintain an ignition delay below 2.0 ms. There have been numerous studies involving shock tube studies of natural gas mixtures, many of which are used as validation data for chemical kinetics optimization and validation due to their simple and well understood test conditions. Several of these studies will be discussed in more detail in Section 2.4.

2.1.3 Rapid Compression Machine Testing

Rapid compression machines rely on single or dual-opposed pistons to create an adiabatic compression process that occurs on a scale of approximately 20-50 milliseconds [19]. Once the compression occurs, the pistons are locked into place to maintain a constant thermodynamic state. Due to the compression process taking a substantial amount of time, the ignition delay of the fuel of interest must be long relative to the high temperature period of the compression process. Therefore, there is a limited amount of overlapping data between RCM and shock tube test methods. Another downside of testing longer ignition delay times is that heat transfer effects become relevant and the thermodynamic state after compression cannot be assumed to be frozen. The process is typically modeled as an adiabatic core that undergoes an isentropic expansion process as the pressure decreases due to heat transfer at the walls [20]. Since heat transfer will change based on thermodynamic conditions and mixture properties, tests are required with non-reacting mixtures in order to 'tune' a heat transfer model for each experiment. Mittal and Sung found that the RCM assumption of an adiabatic core was invalid for certain piston geometries due to increased mixing within the combustion chamber [21]. Experiments performed in different labs are, thus, difficult to simulate without access to the non-reacting pressure data due to each RCM having unique heat transfer characteristics. Studies used for the validation of the chemical kinetics mechanisms of interest will be discussed in more detail in 2.4.

2.2 Engine Temperature Estimation

In-cylinder thermodynamic conditions must be well known through the start of combustion (SOC) in order to accurately simulate engine experiments that are driven by chemical kinetic processes. While pressure can be directly measured with an in-cylinder pressure transducer, temperature can be difficult to quantify. The reasons for this difficulty are twofold; a non-invasive temperature sensor equivalent to a pressure transducer does not exist, and thermal stratification can cause a non-homogeneous temperature distribution; the highly nonlinear relationship of kinetics to temperature makes this critical. Dronniou and Dec used planar imaging thermometry to estimate the amount of thermal stratification in an HCCI engine [22]. Their testing showed that the bulk-gas temperature was fairly homogeneous, with the stratification occurring in the cold boundary layers near the cylinder walls. To address the issue of temperature determination and stratification, three main methods of temperature estimation were investigated in the current work: a trapped mass thermodynamic calculation, water-absorption spectroscopy, and fast-response thermocouples.

2.2.1 Trapped Mass Temperature Estimation

The simplest approach to estimating in-cylinder temperature is to assume the temperature at bottom dead center (BDC) is equal to the intake temperature. The benefit of this approach is that the only sensor requirement is a thermocouple located in the intake plenum. However, work by Sjoberg and Dec showed that there can be large difference between intake and BDC temperature due to heat transfer and mixing with hot exhaust residuals [23]. Alternatively, the ideal gas law state equation,

$$T = \frac{PV}{MR}, \tag{2.5}$$

can be used to directly calculate the in-cylinder mass-averaged temperature throughout the closed portion of the engine cycle, where T is the temperature, P is the pressure, M is the trapped mass, and R is the gas constant. The main assumptions involved with this procedure are that the cylinder contents are homogeneous and mass is constant. While most quantities can be directly measured with various sensors, the trapped mass calculation,

$$M = \frac{(m_{air} + m_{fuel})}{1 - y_{res}}, \tag{2.6}$$

where m_{air} and m_{fuel} are the air and fuel masses, requires knowledge of the internal exhaust residual mass fraction, y_{res}.

Residual Gas Estimation

A number of different estimations exist in the literature for calculating the internal exhaust residual concentration. Three methods considered for the current work were the Yun and Mirsky method [24], the Fox, Cheng and Heywood method [25], and an ideal gas model. The Yun and Mirsky method models the process from EVO to exhaust valve close (EVC) as a polytropic expansion,

$$y_{res} = \frac{V_{EVC}}{V_{EVO}} \left(\frac{P_{EVC}}{P_{EVO}} \right)^{\frac{1}{\gamma}}, \tag{2.7}$$

where V is the volume and γ is the specific heat ratio. The main uncertainty in this equation is the value of γ, which will vary based on temperature, exhaust contents, and heat transfer. Typically, heat transfer is assumed to be negligible which simplifies γ to the isentropic specific heat ratio of the exhaust gases.

Fox et al. created an empirical correlation that takes into account exhaust back-flow

during the valve overlap period; the resulting correlation is given by

$$y_{res} = 1.266 \frac{OF}{N} \frac{P_{int}}{P_{exh}}^{-0.87} \sqrt{|P_{exh} - P_{int}|} + 0.632 \frac{\Phi \left(\frac{P_{int}}{P_{exh}} \right)^{-0.74}}{r_c} \tag{2.8}$$

$$OF = \frac{D_{int} \int_{IVO}^{IV=EV} L_{int} d\theta + D_{exh} \int_{IV=EV}^{EVC} L_{exh} d\theta}{V_{dis}}, \tag{2.9}$$

where OF is the overlap factor, N is the engine speed, P_{exh} and P_{exh} are the exhaust and intake pressure, Φ is the equivalence ratio, r_c is the compression ratio, D_{int} and D_{exh} are the intake and exhaust inner valve seat diameters, L_{int} and L_{exh} are the intake and exhaust valve lift, and V_{dis} is the engine displacement volume. An important note with empirical equations is that they often produce inaccurate results when used outside of their correlated range; for their study equivalence ratios varied from 0.7 to 0.96 and intake pressure varied from 0.32 to 1 bar (absolute). Therefore, the applicability to the current work, which involved low equivalence ratios and boosted intake pressures, is unknown.

The ideal gas law can be used to estimate the residual mass with

$$m_{res} = \frac{P_{EVC} V_{EVC}}{R T_{EVC}}. \tag{2.10}$$

The main source of uncertainty in this equation is the temperature at EVC. Typically, mean exhaust temperature is used in place of T_{EVC} and either in-cylinder or mean exhaust pressure is used for P_{EVC}.

Albert and Ghandhi evaluated both the Yun and Mirsky and Fox, Cheng, and Heywood methods' accuracies by directly measuring the CO_2 concentrations in the exhaust and in-cylinder prior to combustion on a naturally aspirated, small engine [26]. They found that the Fox, Cheng, and Heywood method performed well only for low valve overlap conditions and greatly over-predicted y_{res} for high valve overlap conditions, while the Yun and Mirsky method consistently under-predicted y_{res}, most likely caused by

underestimating heat transfer during the exhaust stroke.

2.2.2 Spectroscopy Temperature Estimation

Laser absorption spectroscopy (LAS) is a technique that involves measuring the in-cylinder gas absorbance either over a spectral band or at several discrete wavelengths. It has the potential to be useful for engine diagnostics as a non-invasive technique to measure temperature [27]. The specific process used in the current work, called band shape thermometry, makes use of the temperature-dependent absorbance characteristics of water over the 7300-7500 cm^{-1} frequency range and is described in detail in [28]. Experimental absorbance data are processed and compared to simulation databases to find the best-fit temperature. The three spectral databases investigated in this study were BT2 [29] HITEMP2010 [30] and HITRAN [31].

Mattison et al. performed LAS measurements using a linepair spectroscopic process in an HCCI engine for both motored and fired operating conditions [32]. Comparison of temperature results from IVC through -30 crank angle degrees (CAD) to those calculated with a trapped mass state equation showed agreement within 3.0% for motored and 5.0% for fired conditions. Rieker et al. also performed LAS measurements in an engine using a modified spark plug [33]. Calibration testing in a static cell over a pressure range of 1-25 bar and a temperature range of 500-900 K gave a $\pm$3.0% accuracy, but validation of the accuracy of in-engine results was not reported. Das et al. performed similar LAS measurements in an RCM [34], [35]. The temperature results agreed with simulation results within 5.0 K through the compression process. Additionally, uncertainty propagation analysis was applied to the results, giving a temperature uncertainty of 0.6-1.6%. Kranendonk et al. used a Fourier-domain mode-locked laser (FDML) and a band-shape processing approach to perform LAS measurements on a motored optical engine [36], [37]. The temperature results had good precision, less than 1.0% deviation from a 10 CAD moving window average, but lacked validation of accuracy because excessive blow-

by in the engine caused errors in the trapped mass state equation calculations. Overall, good agreement was reported between various validation methods and LAS, although most authors note that the accuracy is very dependent on the spectroscopic database accuracy.

The main disadvantages of this method are: (1) uncertainty analysis is difficult due to the non-linear behavior of the processing, method, (2) temperature accuracy is dependent on the simulation database accuracy, and (3) baseline artifacts must be removed before comparing to the simulation database.

2.2.3 Thermocouple Temperature Estimation

Fast-response thermocouples have frequently been used to obtain piston, head, and wall temperature and heat flux measurements [38], [39], [40]. Thin-wire thermocouples have also been used for crank-angle resolved measurements of engine intake [41] and exhaust [42] temperatures. However, there is limited literature documenting the use of thin-wire thermocouples to measure in-cylinder gas temperature, most likely due to durability issues. A trade-off exists exists when choosing thermocouple size, where a larger diameter thermocouple will survive longer but will have a longer time constant due to its thermal inertia.

By assuming a lumped capacitance model for the thermocouple, the correction procedure is

$$T_{corr} = T_{raw} + \tau \frac{dT_{raw}}{dt}, \tag{2.11}$$

where T_{raw} is the raw thermocouple temperature, τ is the thermocouple time constant, and $\frac{dT_{raw}}{dt}$ is the derivative of the raw thermocouple temperature. If τ is known, the true gas temperature can be directly calculated. The time constant, however, is a function of both the thermocouple's thermal mass and the instantaneous convective heat transfer coefficient and will change substantially throughout the engine cycle as pressure and

temperature change.

$$\tau = \frac{\rho_w c_w d_w^2}{4 k_a Nu}, \tag{2.12}$$

$$Nu = 0.24 + 0.56 Re^{0.45}, and \tag{2.13}$$

$$Re = \frac{u d_w \rho_a}{\mu_a} \tag{2.14}$$

directly calculate the thermocouple time constant, assuming that the thermocouple can be described by a cylindrical wire [43], where ρ_w, c_w, and d_w are the thermocouple density, specific heat, and diameter (respectively), Nu is the Nusselt number, Re is the Reynolds number, and u, ρ_a, and μ_a are the velocity, density, and viscosity of the fluid surrounding the thermocouple. Scadron et al. also showed that conduction errors can be significant if the wire length is too short relative to the wire diameter [44], and radiation errors can be significant when the thermocouple temperature is much greater than cylinder wall temperatures [37]. The conduction error for a thin-wire thermocouple can be estimated by

$$\Delta T_{cond} = (T_b - T_{raw}) sech(\eta L) \tag{2.15}$$

$$\eta = \sqrt{\frac{1}{\kappa \tau}}, \tag{2.16}$$

where T_b is the support temperature, L is the length from the thermocouple junction to the support, and κ is the wire's thermal conductivity. The radiation error for a thin wire thermocouple can be estimated by

$$\Delta T_{rad} = 27 \frac{\epsilon_w \sqrt{d}}{\sqrt{Mp}} \left(\frac{T_w}{1000} \right)^{-0.18} [\left(\frac{T_{\text{raw}}}{1000} \right)^4 - \left(\frac{T_d}{1000} \right)^4], \tag{2.17}$$

where ϵ_w is the wall emissivity, d is the wire diameter in inches, M is the Mach number, p is the pressure in atmospheres, and T_d is the wall temperature in Rankine.

As an alternative to calculating the thermocouple time constant directly from physical parameters, there are methods that involve using two thermocouples having different time constants to calculate the gas temperature [45]. With the assumption that the thermocouples' time constants are fixed, $\overline{\tau}_1$ and $\overline{\tau}_2$ can be solved for by minimizing the mean squared error,

$$e = \frac{1}{N}\sum_{i=1}^{N}(T_{corr_1} - T_{corr_2})^2. \tag{2.18}$$

The direct solutions for τ_1 and τ_2 that minimize e are calculated by

$$\overline{\tau_1} = \frac{\sum G_2^2 * \sum G_1 \Delta T_{21} - \sum G_1 G_2 * \sum G_2 \Delta T_{21}}{\sum G_1^2 * \sum G_2^2 - \sum G_1 {G_2}^2} \tag{2.19}$$

$$\overline{\tau_2} = \frac{\sum G_1 G_2 * \sum G_1 \Delta T_{21} - \sum G_1^2 * \sum G_2 \Delta T_{21}}{\sum G_1^2 * \sum G_2^2 - \sum G_1 {G_2}^2} \tag{2.20}$$

$$\Delta T_{21} = T_2 - T_1, \tag{2.21}$$

where G_1 and G_2 are the time derivatives of $T_{raw,1}$ and $T_{raw,2}$. If the time constants are relatively constant over the selected data window, this allows the thermocouple time constants to be calculated with no knowledge of the physical properties. Additionally, $T_{corr,1}$ and $T_{corr,2}$ can be averaged to reduce the effects of individual signal noise.

2.3 Modeling HCCI Combustion

Methods of varying levels of accuracy and complexity have been used by researchers to simulate HCCI combustion. These methods can be classified as: zero-dimensional, quasi-dimensional, CFD-driven multi-zone, and CFD-coupled [46].

2.3.1 Zero-Dimensional, Single-Zone Model

A zero-dimensional, single-zone model assumes a completely homogeneous mixture. It, therefore, cannot account for colder gas temperatures in crevice volumes and boundary

layers near the cylinder walls, or any stratification in the air-fuel mixture. The benefits of a single-zone model are simplicity and the fact that heat transfer is the only unknown calibration parameter necessary to simulate engine experiments. The drawbacks are that predicted combustion duration is unrealistically short and peak pressure rise rates are uncharacteristically high due to the entire mixture having identical thermodynamic conditions [47]. The inaccuracy between the simulation and experiment will be dependent on the degree of thermal stratification in the combustion chamber. A zero-dimensional model can, however, accurately capture ignition timing behavior if its thermodynamic temperature and pressure time history match the mixture zone in the experiment that is the first to ignite.

2.3.2 Zero-Dimensional, Multi-Zone Model

In order to incorporate temperature stratification, a quasi-dimensional approach that involves multiple zones, each with its own unique homogeneous mixture and thermodynamic conditions can be used [48]. Multi-zone models assume each zone is a deformable control volume that may exchange mass and heat with the other zones. Typically, heat transfer to the cylinder walls is only allowed from the outer zones. Noda and Foster used this simulation method with the assumption that there was no mass or heat transfer interaction between zones in order to compare the effect of temperature stratification to fuel-air mixture stratification [49]. Their work showed that the ignition timing was much more sensitive to in-cylinder temperature inhomogeneity than equivalence ratio inhomogeneity, which indicated that it is reasonable to assume a homogeneous mixture of fuel and air for port-fuel injected conditions. Easley et al. used a six-zone model that included a crevice volume, boundary layer, outer core, and three adiabatic inner cores to perform a simulation study on the effect of crevice volume, engine speed, wall temperatures, and boundary layer thickness on engine performance and emissions [50]. Mass transfer was allowed between the crevice volume, boundary layer, and outer cores in order to maintain

a homogeneous pressure, and heat transfer was allowed from the boundary layer to the walls while the crevice volume was maintained at a constant temperature.

One of the difficulties with simulating engine experiments is the uncertainty involved with estimating boundary conditions such as piston and wall temperatures, exhaust residuals, and IVC temperature. Mehl et al. combined a 1-D model to simulate the gas exchange process and a multi-zone model consisting of a boundary layer and an adiabatic core to model HCCI combustion [51]. Kozarac et al. also used a 1-D model to simulate the full engine cycle and coupled this with a multi-zone model that included two inner cores, three boundary layers, and a crevice volume [52]. The model contained two main tuning parameters, a boundary layer thickness to influence heat transfer out of the cylinder and a heat transfer time constant to control the rate of heat transfer between different zones. Their model was validated by comparing to experimental HCCI data over a range of operating conditions, and they found that the simulation with constant values for both tuning parameters was able to reasonably match the experimental heat release and emissions. It is important to note that the intake system boundary temperatures were individually tuned in all cases in order to match start of combustion. From these studies, it was seen that a multi-zone model can more accurately simulate HCCI combustion performance and emissions compared to a single-zone model; however, the biggest issue with this method is that the degree of stratification must be known or tuned to be accurate.

2.3.3 CFD Modeling

The final two methods to improve the accuracy of HCCI simulations incorporate CFD models. The first method uses CFD of the gas exchange process up to a certain point in the compression stroke to obtain accurate estimates of in-cylinder conditions and then uses these conditions as inputs to a multi-zone model. Several of the studies listed previously utilized this strategy.

The alternative is to carry out the full combustion analysis with CFD software coupled with a chemical kinetics mechanism. While this method allows for the highest degree of accuracy, it is also by far the most computationally intensive. In addition, the accuracy of a CFD model will be dependent on its sub-models, such as turbulence and heat transfer estimation. Aceves et. al. performed an investigation comparing experimental tests and simulations with two different piston designs to study the effects of turbulence on HCCI combustion [53]. They used a non-reacting CFD model to simulate the air-gas mixture up to the point of ignition and used the results of this simulation as the temperature-pressure history for their multi-zone model. They found that experimental heat release and emissions were well described by the model for both piston designs; however, it is important to note their strategy for setting the simulation temperature at IVC was to use it as a tuning parameter to match the experimental start of ignition.

2.3.4 Lawler TSA Post-Processing Method

If the goal of a simulation is to accurately mimic experimental conditions, there is an additional method created by Lawler et al. known as Thermal Stratification Analysis (TSA) [54]. TSA first assumes an in-cylinder temperature distribution that varies from the wall temperature to a temperature resulting from an isentropic compression process beginning at IVC temperature and normalizes this distribution between 0 and 1, called the normalized zone temperature (NZT). Next, the autoignition integral is computed for each NZT using the experimental pressure trace and an ignition delay correlation in order to obtain the crank angle where combustion for each zone occurs. In parallel, the gross heat release rate is computed from the experimental data as a function of crank angle which can be related to mass fraction burned (MFB). The two distributions are then equated in order to obtain a relationship between normalized zone temperature and mass fraction burned which gives the mass-based temperature distribution. This relation can then be used as the temperature stratification input conditions for a multi-zone

model. Lawler et al. compared this method with both simulated data and experimental optical data and found very good agreement with TSA [55].

The main issue with using this technique is that the fuel kinetics, *i.e.*, the ignition delay correlation, must be well known to accurately predict the temperature distribution. While uncertainty in the kinetics can have an effect on the results, this method can be a powerful post-processing tool to assess the degree of thermal stratification that exists in the engine experiments. Using the TSA method on experimental pressure traces combined with a CFD simulation allows two different paths to assess the amount of temperature in-homogeneity for each test case.

2.3.5 Livengood Wu Integral Method for HCCI

HCCI engine experiments are difficult to compare to RCM and shock tube studies due to the rapidly changing thermodynamic conditions caused by the cylinder volume change. While shock tube ignition is assumed to occur at constant conditions, RCM conditions do vary with time due to heat transfer to the walls. Hoppe et al. utilized a method to correlate the RCM experimental data with an Arrhenius equation using the Livengood Wu integral method [56], [57]. The Arrhenius expression,

$$\tau_{ign} = A \times P^{-x} \times e^{(\frac{Ea}{R \times T})}, \tag{2.22}$$

contains three variables: A, x, and Ea.

The Livengood Wu integral method states that a fuel will ignite when the integral of the inverse ignition delay as a function of temperature and pressure following thermodynamic history of the mixture is equal to one,

$$\int_0^{\tau_{ign}} \frac{1}{\tau(P,T)} = 1. \tag{2.23}$$

By combining Equations 2.22 and 2.23, A, x, and Ea can be calculated for a set of

experimental data if the temperature-pressure history is known. While in the previously mentioned study this method was only applied to RCM machines, it can also be applied to HCCI and SI experiments. One of the main issues with this method is that an Arrhenius expression is not able to capture the NTC behavior seen in larger hydrocarbon fuels.

An alternative method devised by Douaud and Eyzat [58] equates the integral of the reciprocal ignition delay at a constant pressure and temperature over a specified time interval to the reciprocal integral of the ignition delay of the time-varying engine data,

$$\frac{t_{ref}}{\tau(p_{ref}, T_{ref})} = \int_0^{\tau_{ign}} \frac{dt}{\tau(p_{eng}(t), T_{eng}(t))}, \tag{2.24}$$

where t_{ref} is the specified time interval, p_{ref} and T_{ref} are the reference pressure and temperature, and p_{eng} and T_{eng} are the time-varying engine pressure and temperature values. This allows the time-varying thermodynamic history to be roughly equated to a single temperature-pressure value for comparison with shock tube and RCM tests.

2.4 Chemical Kinetics Mechanisms

There are two main groups of chemical kinetics mechanisms currently used to simulate natural gas constituents, one stemming from the work funded by the Gas Research Institute (GRI) and the other from work at Lawrence Livermore National Lab (LLNL). The GRI-Mech 3.0 and UBC 2.0 mechanisms both rely on initial work funded by the GRI, whereas the LLNL-n-heptane, AramcoMech1.3, and C5-49 mechanisms all build on work done by LLNL. These mechanisms are described in more detail in the following sections.

2.4.1 GRI 3.0 Mechanism

Smith et al. created a mechanism called GRI-Mech 3.0 [59] with the purpose of simulating natural gas kinetics. The baseline reaction rates were taken from a number of sources,

and these rates were then optimized to match a wide variety of natural gas experimental data, including shock tube, laminar flame speed, and flow- and stirred-reactor studies.

There were a variety of shock tube experiments used for this mechanism's development. Seery and Bowman performed shock tube testing in the temperature range of 1500-1850 K and pressure range of 1.6 to 3.8 atm with mixtures of methane, oxygen, and argon at an equivalence ratio of 0.5-5 [60]. Hidaka et al. performed shock tube testing at a temperature of 1600 K and pressure of 0.25 atm with mixtures of ethane at equivalence ratios of 0.275 to 0.764[61]. Frenklach and Bornside performed shock tube testing at a temperature of 1410 K and pressure of 2.5 atm with methane and propane mixtures at an equivalence ratio of 1.5 [62]. Spadaccini and Colket performed shock tube tests at temperatures of 1350-1690 K and pressures of 6-8 atm with mixtures of methane, propane, oxygen, and argon and methane and ethane at an equivalence ratio of 1.043 [63]. Petersen et al. performed shock tube tests at temperatures of 1400-1700 K and pressures of 35-84 atm with mixtures of methane at an equivalence ratio of 1.0 [64]. For all shock tube testing, the GRI 3.0 mechanism showed reasonable agreement with the experimental ignition delays.

While the ignition delay experimental data cover a wide range of thermodynamic conditions, the vast majority of the data were for pressures less than 10 atm and temperatures greater than 1500 K. In addition, most of the experimental data involved mixtures of pure methane with air and argon, although there were a small number of methane-ethane and methane-propane mixtures included. Due to the large number of optimization targets, there is a wide spread in the level of agreement between experimental and simulated tests. The mechanism consists of 53 species and 325 reactions.

2.4.2 UBC 2.0 Mechanism

Huang and Bushe created a mechanism named UBC 2.0 [65], which was based on the GRI 1.2 mechanism. The mechanism was optimized for a set of shock tube experiments

covering a range of pressures from 16-40 bar and temperatures from 900-1400 K with methane, ethane, and propane mixtures at an equivalence ratio of 1.0. The mechanism has 55 species and 278 reactions; and propane is the largest hydrocarbon included. The experiments involved pure methane and binary mixtures containing methane mixed with small amounts of ethane and propane, and thus is optimized for predicting the ignition quality of mixtures of mostly methane with relatively small amounts of larger hydrocarbons. The advantage of this mechanism relative to the GRI 3.0 mechanism is that the pressure and temperature ranges are more relevant to engine conditions; the disadvantage is that only one set of data was used to validate the mechanism. The shock tube simulations match reasonably well with the experimental data, although they appear to over-predict the ignition delay at the lower temperature range.

2.4.3 LLNL *n*-Heptane Detailed Mechanism

LLNL has spent decades working to provide accurate hydrocarbon chemical kinetics mechanisms. Lawrence Livermore National Laboratory created a detailed mechanism for simulating hydrocarbon fuels up to *n*-heptane [66]. It is named the *n*-Heptane Detailed Mechanism Version 3.1, but will be referred to as LLNL-*n*-Heptane herein. Mehl et al. validated the most recent version of the mechanism using experimental shock tube and RCM data ranging from pressures of 3-50 bar and temperatures of 650-1200 K. While most of the validation work for this mechanism was based on experimental data of larger hydrocarbon fuels such as toluene, isooctane, and *n*-heptane, it is also expected to be accurate for smaller hydrocarbon fuels based on the previous core model development.

The mechanism is quite large, with 634 species and 5258 reactions which makes it computationally intensive. However, the benefit to performing simulations with this mechanism is that accurate performance can be expected over a wide range of fuels, from small hydrocarbons such as methane and ethane up to larger hydrocarbons such as isooctane and *n*-heptane.

2.4.4 AramcoMech1.3 and C5-49 Mechanisms

Both the AramcoMech1.3 [67] and C5-49 [68], [69], [70], [71], [72], [73] mechanisms were based on previous work done by LLNL with the goals of more accurately modeling smaller hydrocarbon combustion with fewer species. The AramcoMech1.3 mechanism focused on C1 and C2 hydrocarbons, whereas the C5-49 mechanism focused on C1 to C5 hydrocarbons.

Metcalfe et al. created the AramcoMech1.3 [67] to simulate ignition delay and flame speed of small hydrocarbon mixtures. They used validation data from a number of sources, including flow- and jet-stirred reactors, shock tube, and flame studies. In the process of making the mechanism, the authors did an extensive literature review and attempted to minimize the amount of optimization or 'tuning' of rate constants. The final mechanism contained 124 species and 766 reactions and can simulate hydrocarbons including methane, methanol, ethane, ethanol, ethylene, and propane. An important note is that a new version of this mechanism, AramcoMech2.0 has been released since the start of this work. The updated mechanism builds on the previous version, and includes chemistry for *n*-butane and isobutane. The updated mechanism was not tested in the current work, but this would be a useful area for future work.

Similar to the LLNL-*n*-Heptane mechanism, there are too many experimental validation results to list; interested readers are invited to inspect the validation data listed in [67]. During the validation, the final AramcoMech1.3 shock tube simulation results were compared to simulations using the GRI3.0 mechanism for a variety of different fuels and conditions; the general trends were longer ignition delays for methane mixtures and shorter ignition delays for ethane mixtures relative to the GRI3.0 mechanism.

Unfortunately, no RCM validation data was shown and due to the limited range of conditions accessible in a shock tube, the lowest validation temperature shown was 1000 K in one low pressure test, with the majority of the testing having a minimum temperature of around 1200 K. As seen with other mechanisms, the simulations generally match quite

well with experimental data at higher temperatures but discrepancies are seen at lower temperatures.

Healy et al. created the C5-49 mechanism [67] and C5-49 [68], [69], [70], [71], [72], [73] to simulate natural gas mixtures over a wide range of temperatures and pressures. Mixtures of methane, ethane, propane, butane, and pentane at equivalence ratios from 0.3 to 3.0 were tested. Using both RCM and shock tube data allowed a wide range of temperatures (590-1570K) and pressures (1-45 bar) to be tested. The RCM experiments made up the lower temperature test data while the shock tube experiments made up the higher temperature test data with limited overlap between the two test methods. The final mechanism contains 293 species and 1588 reactions with n-pentane being the largest hydrocarbon included. There was good agreement between the model and experimental data over the included range of temperatures and pressures, although the authors note that the model appears to under-predict ignition quality at lower temperatures and higher pressures. These lower temperature points have longer ignition delay times and thus are more difficult to simulate as heat transfer in the RCM becomes substantial and must be accurately modeled. The previously mentioned PKI study done by Gersen et. al. found that the mechanism over-predicted ignition times of several natural gas mixtures by up to 50% when comparing to experimental RCM data.

2.4.5 Summary of Mechanisms

All of the mechanisms listed above follow one of two main paths to specify rate constants: a multi-objective optimization scheme, or a literature review of experimental rate coefficients with minimal optimization. The GRI 3.0 and UBC 2.0 mechanisms were created following the former method, while the C5-49, AramcoMech1.3, and LLNL-n-heptane were created utilizing the latter strategy. All of the mechanisms were validated using a wide array of experiments involving shock tubes, RCMs, flow- and stirred-reactors, and laminar flame speed measurement over a large range of thermodynamic conditions.

Table 2.1: Thermodynamic Conditions for Mechanism Optimization/Validation.

	RCM		Shock Tube	
Mechanism	Temperature [K]	Pressure [bar]	Temperature [K]	Pressure [bar]
GRI 3.0	-	-	1356-2400	0.25-83.9
UBC 2.0	-	-	900-1400	16-40
AramcoMech1.3	-	-	1000-2584	1.2-260
C5-49	630-1130	9-45	970-1550	9-45
LLNL-n-heptane	600-900	2.7-45	660-1350	3-60

Table 2.2: Summary of Mechanism Parameters.

Mechanism	Species	Reactions
GRI 3.0	53	325
UBC 2.0	55	278
AramcoMech1.3	124	766
C5-49	293	1588
LLNL-*n*-heptane	634	5258

Ignition quality is the most important parameter for predicting end-gas autoignition in a spark ignition engine, and thus validations related to shock tube and RCM experiments are the most important for this study. The thermodynamic ranges covered in these studies can be seen in Table 2.1. Due to most of the shock tube data having a lower temperature of around 1200 K, the RCM data are critical to predicting low- and mid-temperature ignition delays. As seen in Table 2.1, the C5-49 and LLNL-n-Heptane mechanisms both were validated with RCM data in the temperature ranges of interest. Table 2.2 shows a summary of the number of species and reactions of each mechanism; as expected, the mechanisms created to simulate larger hydrocarbons contain greater number of species and reactions, making them more computationally expensive to use.

Chapter 3

Experimental Setup

3.1 Hardware and Software

The experimental tests were carried out on a single-cylinder version of a General Motors/Fiat JTD 1.9L four-cylinder diesel engine. The stock engine was combined with a Ricardo Hydra single-cylinder block. Relevant engine parameters can be seen in Table 3.1.

Surge tanks were installed on both the intake and exhaust to dampen pressure fluctuations. National Instruments (NI) software was used for all controls and data acquisition. Intake air pressure and temperature were controlled through the use of an electronic regulator and several tape and band heaters. Airflow was measured with a set of choked flow orifices. The entirety of the intake system spanning from the choked flow orifices to

Table 3.1: Engine Parameters.

Compression Ratio	16.7
Displacement [L]	0.477
Stroke [mm]	90.4
Bore [mm]	82
Con. Rod Length [mm]	145.54
Intake Valve Closing [deg aTDC]	-132
Exhaust Valve Opening [deg aTDC]	112
Swirl Ratio	1.5
Piston Bowl Type	Stock (re-entrant)

Table 3.2: Instrumentation used to measure pressure, fuel flow, and temperatures.

Upstream orifice pressure	Omega PX209-100G5V	0-100 psig	0.25 [%FSO]
Downstream orifice pressure	Omega PX209-100G5V	0-100 psig	0.25 [%FSO]
Intake tank pressure	Omega PX209-100A5V	0-100 psia	0.25 [%FS]
Intake runner pressure	Kulite XTEL-190L-50A	0-50 psia	0.1 [%FSO]
Exhaust tank pressure	Omega PX209-100A5V	0-100 psia	0.25 [%FSO]
Fuel flow meter 1	Endress and Hauser Promass80A	0-1 [g/s]	0.28 [mg/s]/0.5 [%]
Fuel flow meter 2	Emerson CMFS010	0-2 [g/s]	0.56 [mg/s]/0.25 [%]
Various thermocouples	Omega Type K	-200-1350 [°C]	2.2 [°C]/0.75 [%]

the intake runner was heavily insulated to minimize heat losses. Relevant sensors along with their ranges and accuracies can be seen in Table 3.2. All pressure sensors had their calibrations verified in-house with a mechanical pressure gage (Wallace and Tiernan PN 61A-1A-0050) that had a range of 0-50 psia and an accuracy of 0.066% of full scale. The choked flow orifices were calibrated with an Endress and Hauser Promass 83M15 flow meter with a range of 0-6500 kg/hr and an accuracy of 0.325 kg/hr.

In-cylinder pressure was measured using both Kistler 6125B and AVL GU22CKA pressure transducers combined with a Kistler 5010 charge amplifier. Both transducers have identical physical dimensions; the reason for using two different versions will be discussed in more detail in Chapter 5. The pressure transducers were calibrated with a dead-weight tester (Chandler Engineering PN 61-1) with a range of 0-2000 psig and an accuracy of 0.05%. Pressure data were acquired for 300 engine cycles. An encoder with 0.25-degree resolution was fixed to the crankshaft and used as a timing clock for the high-speed data acquisition.

All fueling was injected using either gaseous (Quantum Technologies PN PQ2-3200 and Bosch NGI2 0280158829) or liquid (Trick Flow PN TFS-89055) injectors; injection timing and duration were controlled using NI Drivven software. Two fuel injectors were placed downstream of the intake surge tank in the intake runner, while the third injector was placed upstream of the surge tank. A diagram of the experimental setup can be seen in Figure 3.1. Gaseous fuels were purchased from Airgas and specified as having a minimum purity of 99.5%. Liquid fuels were purchased from Sigma-Aldrich and specified

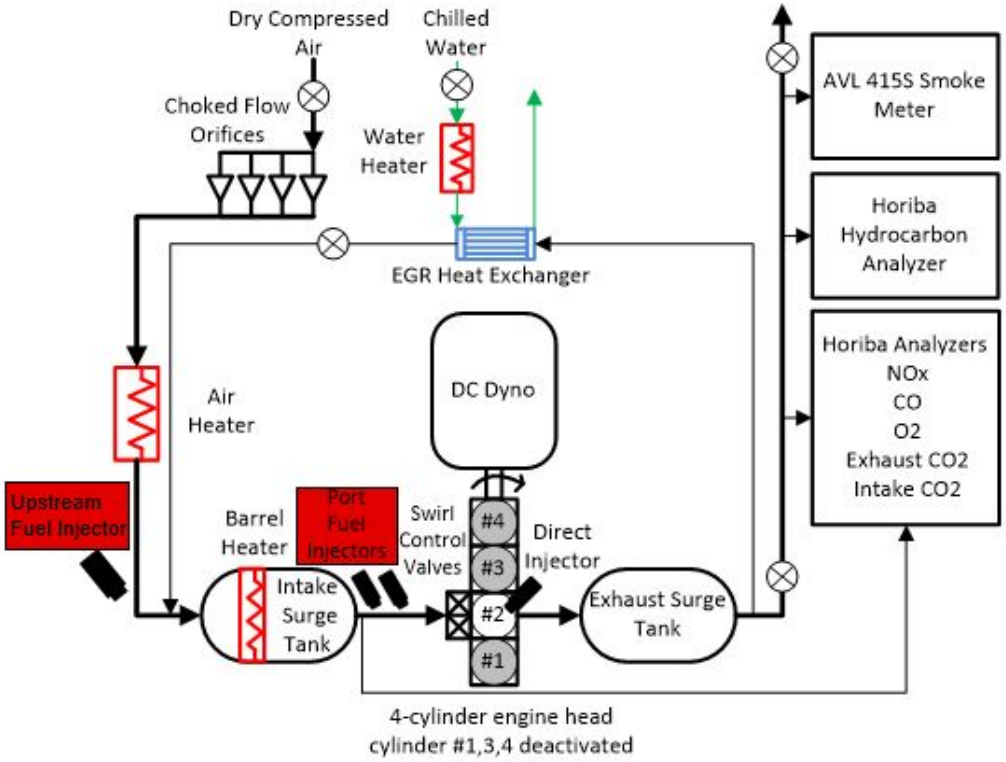

Figure 3.1: Diagram of lab setup.

as having a minimum purity of 99.5%. Fuel pressure was manually adjusted for each operating condition to values 10-30 psi above the intake pressure. The pressure difference between the fuel and intake was intentionally kept low in order to maximize the injector pulse-width vs. fuel flow-rate characteristics; this was necessary because of the low fuel flow rates used in these experiments. Gaseous fuels were stored at high pressure and regulated down to the injection pressure, while liquid fuels were pressurized with nitrogen gas. *N*-butane was especially challenging to work with because its vapor pressure at room temperature is very close to the highest intake pressures used in these experiments. It was injected as a liquid for the highest intake pressure conditions and a gas for the lower intake pressure conditions. A detailed description of the test procedure is found in Chapter 4.

3.2 Data Analysis

3.2.1 Low Speed Data Analysis

For each test point, low speed sensor readings were acquired at a rate of 1-2 Hertz (Hz) for a span of 2-3 minutes. The mean, $\overline{x}$, standard deviation, σ, and 95% confidence intervals, CI_{95}, were calculated by

$$\overline{x} = \frac{1}{N}\sum_{1}^{N} x_i \tag{3.1}$$

$$\sigma = \sqrt{\frac{1}{n-1}\sum_{1}^{N}(x_i - \overline{x})^2} \tag{3.2}$$

$$CI_{95} = \overline{x} \pm \frac{t(N,95)\sigma}{\sqrt{N}}, \tag{3.3}$$

where N is the number of samples and *t(N-1,95)* is the two-sided Student's t-distribution for a 95% confidence level. For N>40, *t(N-1,95)* is within 2% of 2.0 and approaches 1.96 for an infinite number of samples.

3.2.2 High Speed Pressure Analysis

Pressure data for 300 engine cycles were filtered and averaged to obtain a single set of pressure vs. crank angle values for each test point. The filter applied was a Fourier series band-pass filter with a Gaussian roll-off function having a transmission of 100% from 0 to 1600 Hz and dropping to 50% at 3600 Hz and 1% at 6720 Hz. Indicated work was calculated according to

$$W_n = \int_{-360}^{360} PdV \tag{3.4}$$

$$W_g = \int_{-180}^{180} PdV, \tag{3.5}$$

where net work, W_n, is the work over the full engine cycle and gross work, W_g, is the work over the compression and expansions strokes of the engine cycle. An alternative form of work, normalized by engine displacement, indicated mean effective pressure, ($IMEP$), is

$$IMEP = \frac{W}{V_d}, \tag{3.6}$$

where V_d is the displacement volume.

The apparent heat release rate ($AHRR$) was calculated using a first law analysis combined with an adiabatic assumption,

$$AHRR = \frac{\gamma}{\gamma - 1} P \frac{dV}{d\theta} + \frac{1}{\gamma - 1} V \frac{dP}{d\theta}, \tag{3.7}$$

where the polytropic coefficient, γ,was assumed to have a constant value of 1.34 for all cases. The cumulative heat release (CHR) was found by integrating the $AHRR$

$$CHR = \int_{-50}^{80} AHRR d\theta. \tag{3.8}$$

Values of CA_{10} and CA_{50} are the crank angle location where the CHR equals 10% and 50% (respectively) of the total CHR.

3.2.3 Operating Condition Uncertainty

Table 3.3 shows a summary of the normalized uncertainty of all engine operating conditions; nominal uncertainties were below 1% for all parameters. All parameters were calculated using Equation 3.3 for the precision uncertainty and Table 3.2 for the accuracy uncertainty. A more detailed description of uncertainty quantification is found in Chapter 5.

Table 3.3: Nominal uncertainty for engine operating conditions

Engine Speed [%]	<1
Intake Temp [%]	< 1
Intake Pressure [%]	< 1
Equivalence Ratio [%]	< 1

Chapter 4

Fuel Substitution Testing

The focus of this chapter is to describe the experimental fuel substitution testing and document the results. The results of all engine testing are described below; however, an in-depth analysis of the results will be covered in Chapters 9 and 10 along with comparison to simulations.

4.1 Test Procedure

The main goal of this project was to investigate the chemical kinetics of natural gas mixtures under engine-relevant conditions. Simulating engine experiments can be quite difficult due to the uncertainty of boundary conditions, and thus a large number of tuning factors may exist such as wall and piston temperatures, T_{IVC}, and heat transfer coefficients. As mentioned in Chapter 1, in order to minimize the effect of this uncertainty, a method was devised that effectively freezes boundary and initial conditions for the entirety of a fuel substitution sweep [2]. In a previous study, it was shown that the gross *IMEP* varied by less than 1.0%, the CA_{50} varied from the mean by less than 0.5 deg, and T_{IVC} varied about the mean by less than 3.0 K during a fuel substitution sweep. First, an HCCI baseline condition that used two well-characterized fuels at the desired intake thermodynamic conditions was run on the engine. For this study, both methane/propane

Table 4.1: Engine operating conditions for experimental sweeps for methane/propane (methane/hydrogen) reference fuels

	1	2	3	4	5	6
Engine Speed [rpm]	1000	2000	1000	2000	1000	2000
Intake Temp [K]	383	383	423	423	463	453
Intake Pressure [bar]	2.25	2.25	1.5	1.5	0.9	0.9
Φ [-]	0.33(0.38)	0.33(0.34)	0.41(0.44)	0.41(0.36)	0.54(0.5)	0.47(0.45)
Gross IMEP [bar]	7(8.3)	7.4(7.8)	5.5(5.8)	5.7(5)	4(3.7)	3.6(3.4)
TDC Temp [K]	1050	1120	1070	1150	1070	1110
TDC Pressure [bar]	89	95	57	61	34	35

and methane/hydrogen mixtures were chosen as the baseline fuels because their kinetics are reasonably well understood and form the basis of all mechanisms used to describe natural gas combustion, and because the latter pair of fuels are used in the methane number characterization. Next, a test fuel was introduced in increasing amounts while the quantities of methane/propane or methane/hydrogen were adjusted to keep engine load and CA_{50} constant. The in-cylinder pressure and $AHRR$ for one sweep can be seen in Figure 4.1; both pressure and $AHRR$ were held virtually constant throughout the fuel substitution sweep, with gross $IMEP$ and CA_{50} having average deviations from the mean of 1.1% and 0.5 degrees, respectively.

Sweeps were performed using hydrogen, ethane, ethylene, propane, n-butane, n-heptane, and isooctane as test fuels for six different operating conditions, listed in Table 4.1. Figure 4.2 shows the pre-ignition thermodynamic history for the six operating conditions. For each operating condition, combustion phasing was fixed at a CA_{50} of 7 deg aTDC. Engine speed and intake conditions were identical for the methane/propane and the methane/hydrogen reference fuel tests, but slightly different values of equivalence ratio and $IMEP$ were used. The start of combustion was near TDC due to the low combustion duration. In-cylinder pressure was directly measured while temperature was computed as an isentropic compression process starting at T_{IVC}, which was calculated using the single-zone, trapped mass state equation. Temperature measurements will be discussed in more detail in the following chapters.

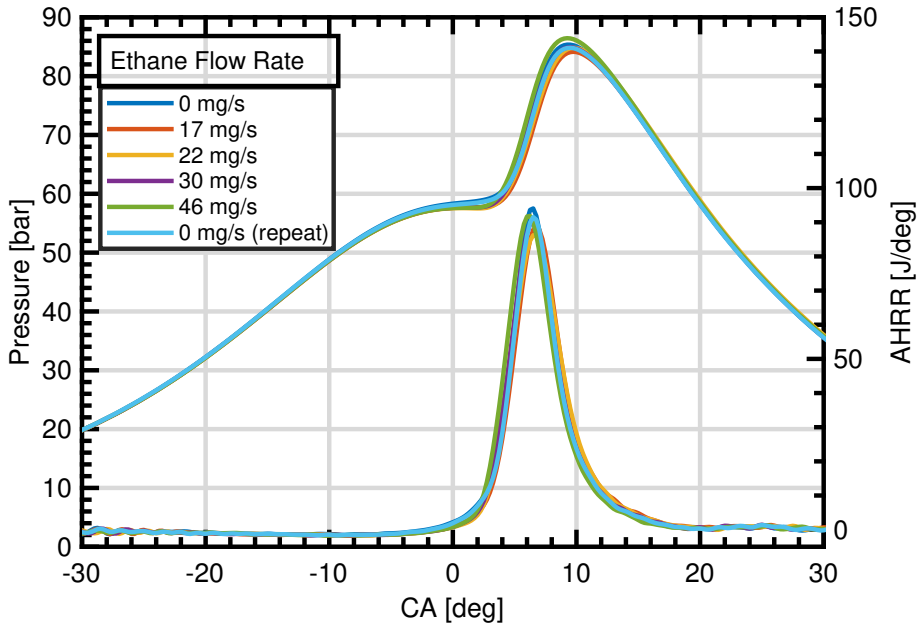

Figure 4.1: Pressure and apparent heat release rate with baseline fuels of methane/hydrogen and test fuel of ethane for operating condition 1.

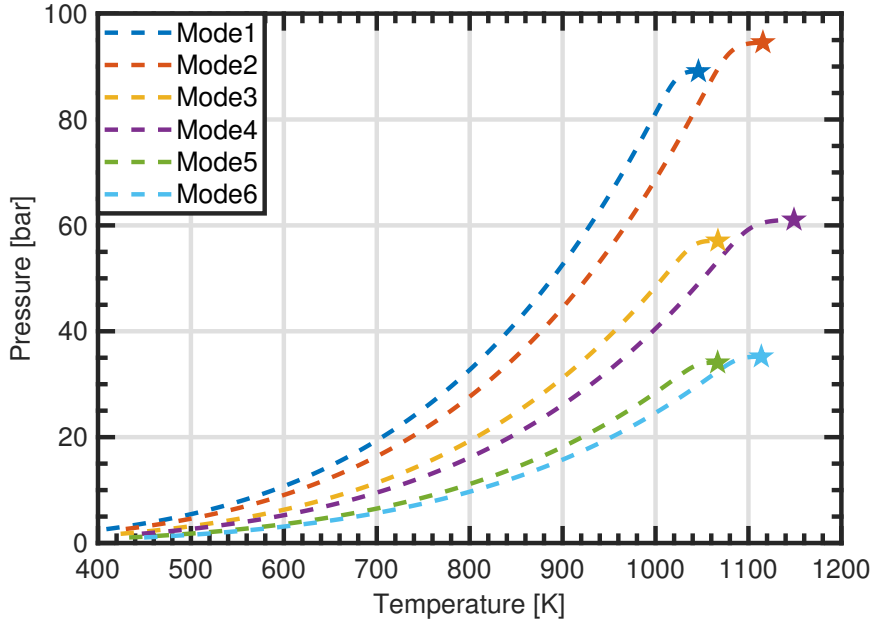

Figure 4.2: Pressure and temperature history for each operating condition up to TDC. Temperature was estimated as an isentropic compression process starting at IVC.

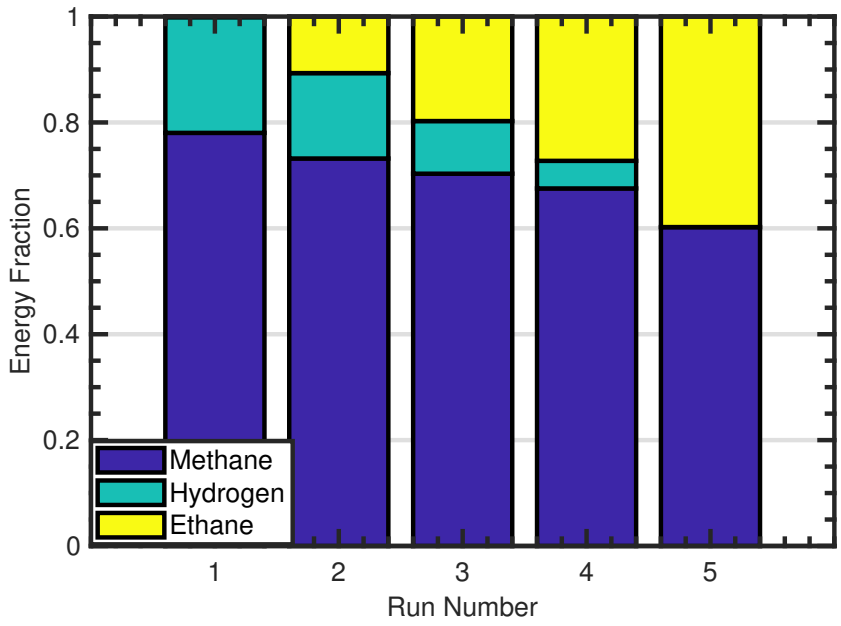

Figure 4.3: Energy fraction of all fuels for each run of the sweep.

4.2 Results

4.2.1 Hydrogen Index Sweeps

A representative example of the reference and test fuel fractions (by energy) for a fuel substitution sweep using methane/hydrogen as the reference fuels and ethane as the test fuel can be seen in Figure 4.3. The sweep was started with a binary mixture of the reference fuels; next, as the ethane fraction increased, the reference fuel fractions decreased. By looking at the relative energy fraction of the reference fuels, it can be seen that the ratio of methane to hydrogen changed as the test fuel fraction increased; this ratio change was required in order to keep combustion phasing constant.

By analyzing how the H_2/CH_4 ratio changed as a function of test fuel fraction, information is obtained about the relative reactivity of the test fuel relative to the two reference fuels. The test fuel can be described by a hydrogen index (HI), which is similar to a MN except that it represents the reactivity of the test fuel in terms of an equivalent percentage of H_2 in a mixture of H_2 and CH_4 (by energy); an HI of 0 corresponds to an

equivalent reactivity to pure methane, whereas an *HI* of 100 corresponds to an equivalent reactivity to pure hydrogen and an *HI* greater than 100 indicates a greater reactivity than hydrogen. The scale was defined in this manner so that a higher *HI* corresponds to a greater fuel reactivity. The overall mixture reactivity was assumed to be well described using a linear (by energy) blending rule,

$$HI_{mix} = HI_{TF} e_{tf} + HI_{ref}(1 - e_{tf}), \tag{4.1}$$

where HI_{mix} refers to the trapped mixture's global *HI*, HI_{ref} refers to the *HI* of the reference fuels as described by

$$HI_{ref} = \frac{e_{H2}}{e_{CH4} + e_{H2}} 100, \tag{4.2}$$

which was computed based on the measured mass flow rates, and e_{tf} refers to the test fuel energy fraction.

In Equation 4.1, there are two unknown values, HI_{mix} and HI_{tf}, both of which are independent of e_{tf}. Fitting the HI_{ref} vs. e_{tf} data to Equation 4.1 using a least squares approach for each test fuel and each different operating condition provided an estimate of HI_{tf} and its uncertainty. The results of a sweep for engine operating condition 3 with a test fuel of ethane can be seen in Figures 4.4.

The sweep started with a baseline fuel mixture of 22/78 (H_2/CH_4), as increasing amounts of ethane were added, it can be seen that the required H_2/CH_4 ratio decreased. This indicates that ethane was more reactive than the baseline mixture, and thus hydrogen had to be removed from the system as ethane was added in increasing amounts to maintain constant combustion phasing. The sweep ended at the limiting case when all of the hydrogen had been removed. At this point, if any more ethane were added to the system it would not be possible to maintain the desired combustion phasing. A fit of the data resulted in a calculated HI_{C2H6} of 55, indicating that at this operating condition

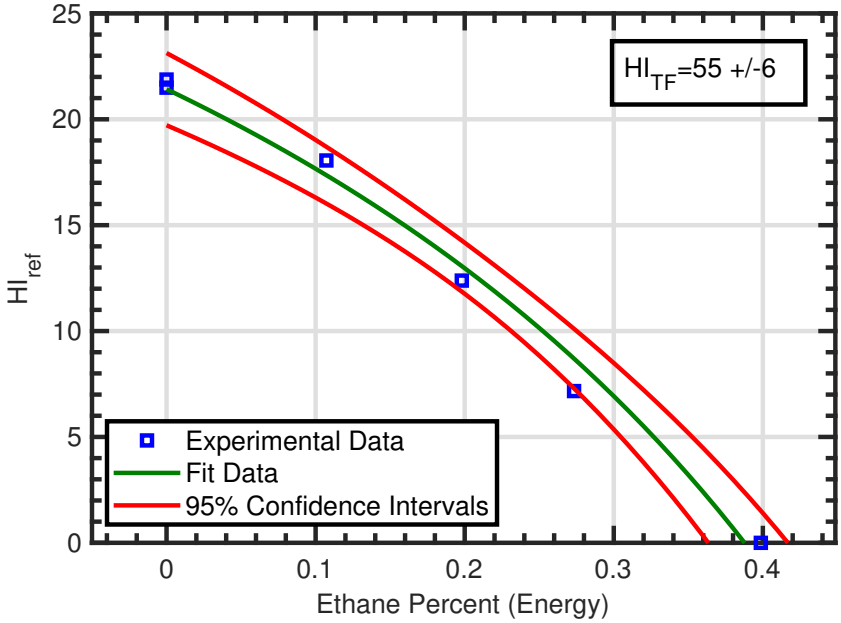

Figure 4.4: Reference fuel *HI* vs. ethane energy fraction for operating condition 3.

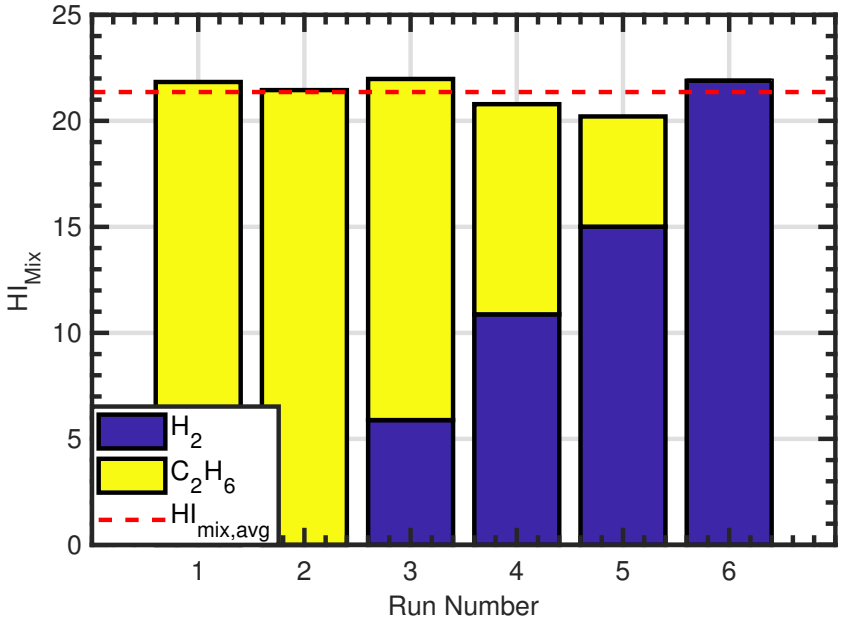

Figure 4.5: Total mixture *HI* contributions from each fuel with ethane as test fuel at operating condition 3.

ethane has an equivalent reactivity to a 55/45 H_2/CH_4 mixture. With HI_{C2H6} known, Equation 4.1 was used to back-calculate HI_{mix} for each test case of the sweep; this value should be constant for the entirety of the sweep and equal to the initial H_2 percent, i.e. 22. The individual fuel contributions to HI_{mix} can be seen in Figure 4.5; for the baseline condition (run twice), H_2 was the sole contributor, but as the ethane energy fraction increased the ethane contributed an increasingly larger amount to the total HI_{mix} up to the limiting case where no H_2 was left in the reference fuels and ethane was the sole contributor. For the previous case, the standard deviation of HI_{mix} was 0.7, showing that the energy-based blending accurately described the substitution sweep results.

The relationship between *HI* of the reference fuels and the test fuel fraction was different for different fuels; more-reactive fuels had a steeper slope than less-reactive fuels. Fuels with similar slopes exhibited similar reactivity at a given operating condition. It is interesting to note that different relative reactivity characteristics were seen as operating conditions vary. In Figure 4.6 (c) and (f), it can be seen that the test fuels' relative reactivities were much more similar at operating condition 6 as opposed to operating condition 3.

The operating conditions were chosen so that a 22/78 (H_2/CH_4) could be used for all baseline conditions. A fuel that had an equivalent reactivity to the baseline mixture would be represented by a horizontal line in Figure 4.6, because it could be substituted in for the baseline mixture on a 1:1 energy basis without changing the overall mixture reactivity. A fuel that had a lower reactivity than the baseline mixture would be represented by a line with a positive slope, because as it was substituted a higher percentage of hydrogen would be required to maintain the overall mixture reactivity. The negative slopes for all fuels in Figure 4.6 indicate that all of the fuels tested were more reactive than the baseline 22/78 (H_2/CH_4) mixture at all six operating conditions.

The results of all of the *HI* sweeps can be seen in Figure 4.7 and Table 4.2. As the size of the straight chain hydrocarbons increased, the calculated *HI* increased, indicat-

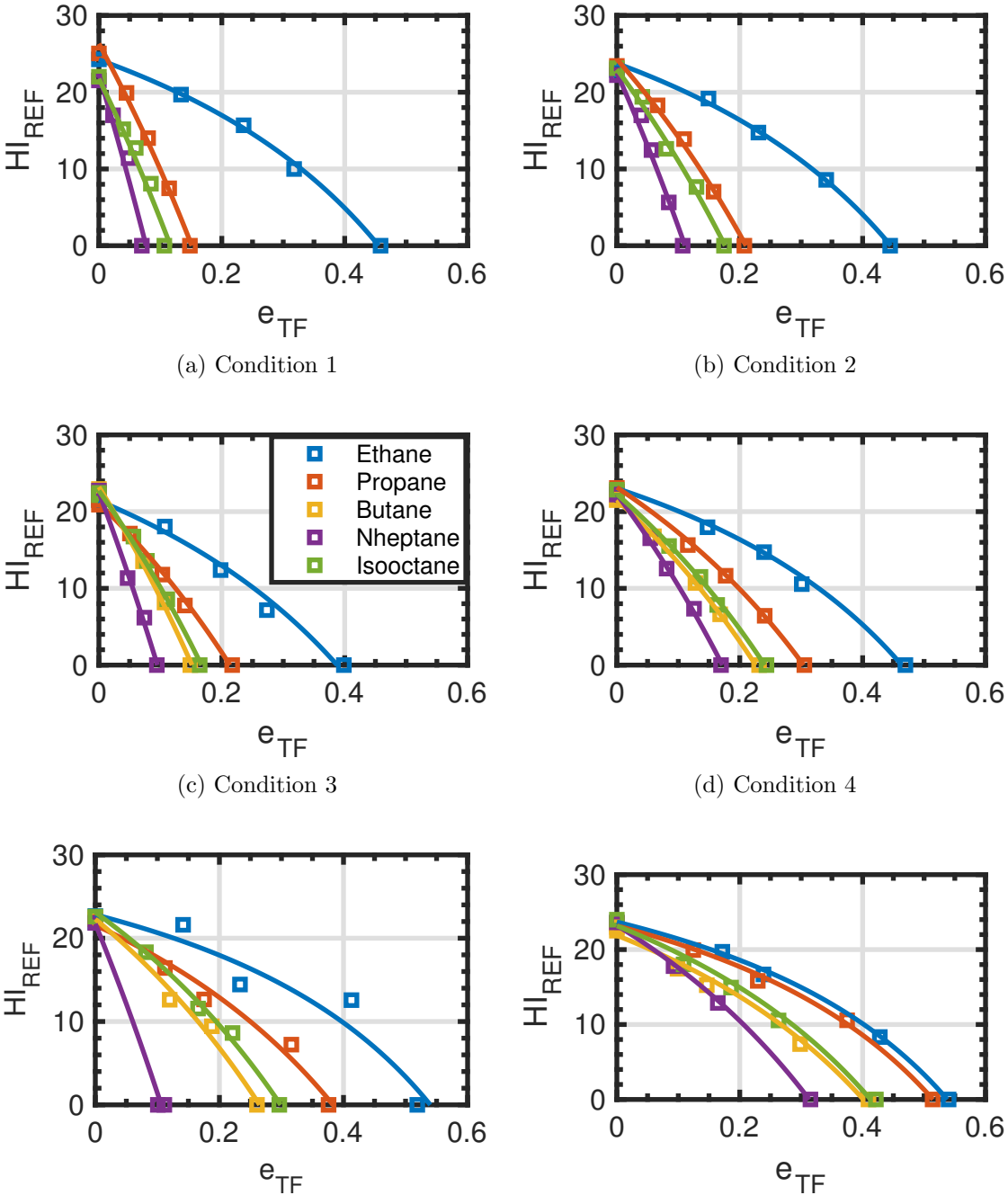

(a) Condition 1

(b) Condition 2

(c) Condition 3

(d) Condition 4

(e) Condition 5

(f) Condition 6

Figure 4.6: Reference fuel *HI* vs. e_{TF} for all operating conditions 1-6.

ing higher reactivity. Isooctane, the only branched hydrocarbon tested, showed similar reactivity to *n*-butane. It is interesting to note that for all of the fuels tested other than ethane, the *HI* changed substantially for different engine operating conditions. This

Table 4.2: Calculated *HI* for all experimental sweeps with uncertainty.

	1	2	3	4	5	6
Ethane	53±2	53±3	55±6	50±4	42±10	43±2
Propane	174±20	113±10	99±7	76±3	56±8	45±2
n-Butane			153±10	95±10	84±10	55±6
n-Heptane	290±100	203±40	236±30	129±7	204±50	74±7
Isooctane	187±50	130±10	136±10	93±6	77±6	56±6

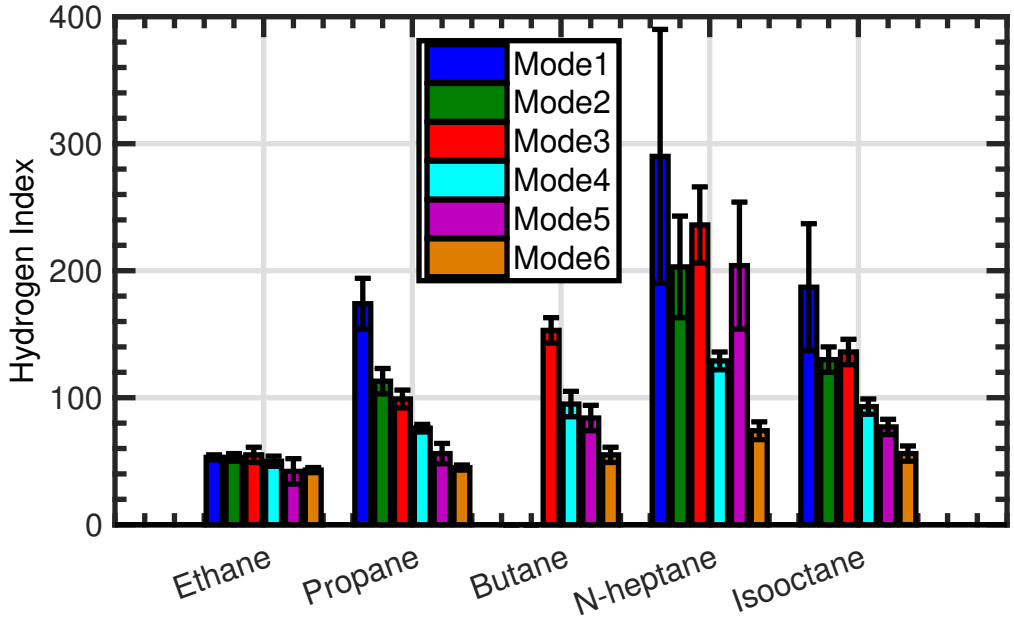

Figure 4.7: Calculated *HI* for each test fuel at all 6 operating conditions.

indicates that the higher hydrocarbon fuels have a reactivity relative to methane and hydrogen that is dependent on thermodynamic conditions. It is believed that this dependency is related to the fact that all of these higher hydrocarbon fuels exhibit negative temperature coefficient (NTC) behavior, whereas methane, hydrogen, and ethane do not. It is interesting to note that all of the higher hydrocarbon fuels exhibited similar trends in that the highest *HI* was for the high pressure, low temperature operating conditions (1 and 2) trending down to the lowest *HI* for the low pressure, high temperature operating conditions (5 and 6), see Table 4.1.

4.2.2 Propane Index Sweeps

In order to obtain an independent set of data for comparison and to remove the possibility of the high diffusivity of hydrogen changing the in-cylinder heat transfer, a similar method was used to obtain propane indexes (PI) for each fuel. The same engine operating conditions and fuel substitution strategy were used, except that the reference fuels now consisted of methane and propane. A PI of 100 refers to a reactivity of pure propane, whereas a PI of 0 refers to a reactivity of pure methane. The raw experimental data for all fuels tested at all operating conditions are shown in Figure 4.8. Similar to the HI sweep, the experiment started with a baseline mixture of propane and methane and then adjusted the quantities and ratios of the reference fuels as the test fuel was added in increasing amounts up to the limiting case of no propane (all fuels tested were more reactive than the baseline methane/propane mixture). From these data, the PI (analogous to HI in Equation 4.1) was calculated.

While the HI testing used a 22/78 (H_2/CH_4) mixture for all operating conditions, a higher percentage of propane was required for conditions 5 and 6 to achieve the desired combustion phasing. This is a result of hydrogen having a higher reactivity relative to propane at conditions 5 and 6; the operating conditions were chosen so that a 22/78 (H_2/CH_4) could be used for all conditions. As seen in Figure 4.8, all fuels tested had negative slopes, similar to the HI testing, indicating that all of the fuels tested were more reactive than the baseline fuel mixtures at all six operating conditions.

The results of all PI sweeps can be seen in Table 4.3 and Figure 4.9. The results showed a very different trend from the HI sweeps; now the smaller hydrocarbons, hydrogen, ethane and ethylene, showed a strong dependence on operating condition while the larger hydrocarbons appeared to be relatively insensitive to operating condition. The higher hydrocarbons showed a relatively constant reactivity compared to the reference fuels because their NTC behavior was similar to that of propane. The smaller hydrocarbons showed a sensitivity to operating condition different than propane's sensitivity

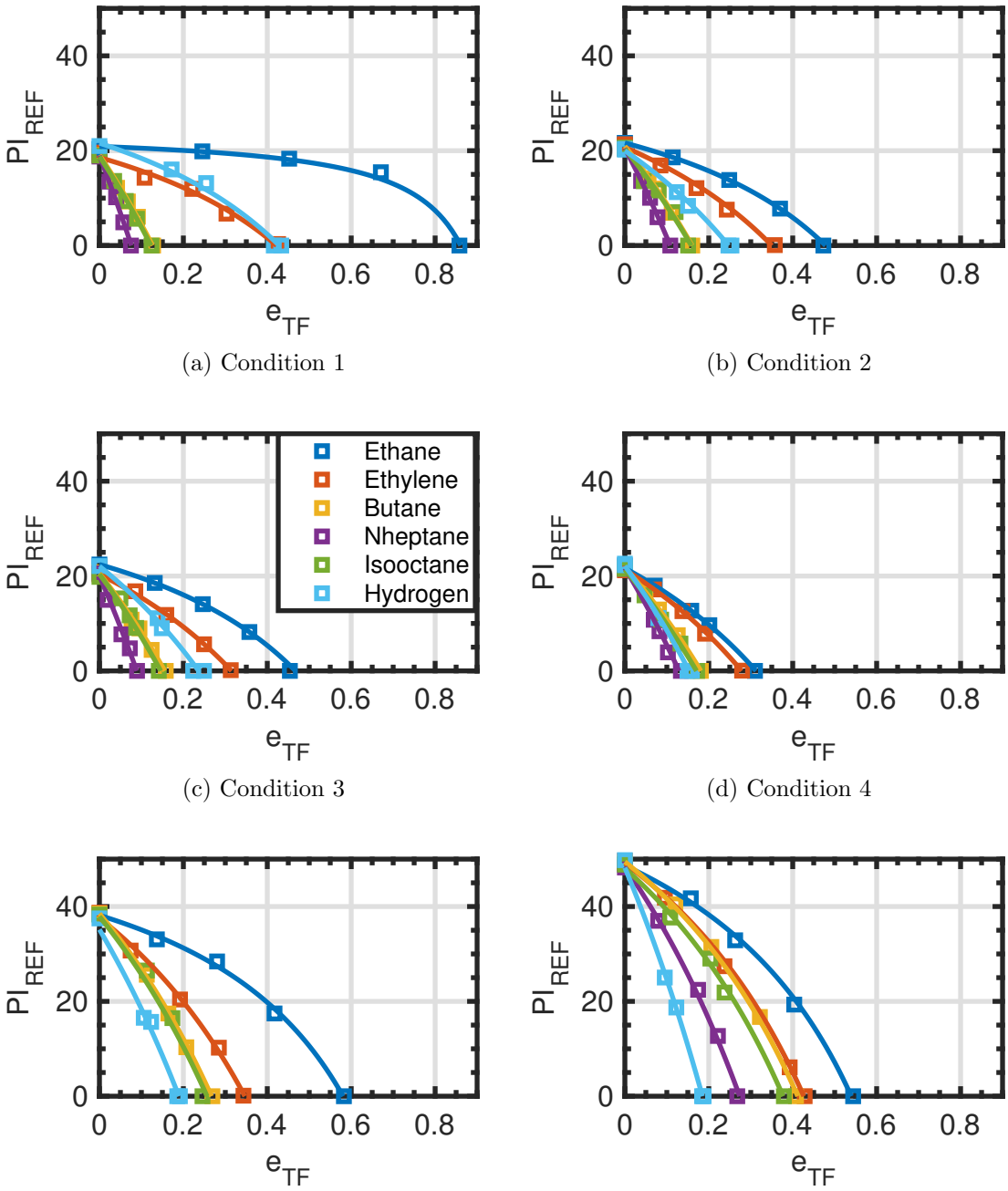

(a) Condition 1

(b) Condition 2

(c) Condition 3

(d) Condition 4

(e) Condition 5

(f) Condition 6

Figure 4.8: Reference fuel PI vs. e_{tf} for all operating conditions 1-6.

because they did not exhibit NTC behavior, which caused their relative reactivity to diverge with thermodynamic conditions.

Table 4.3: Calculated *PI* for all experimental sweeps with uncertainty.

	1	2	3	4	5	6
Hydrogen	50±5	81±6	93±10	145±10	186±30	261±20
Ethane	24±2	45±2	48±6	69±9	66±3	90±4
Ethylene	44±5	59±5	65±3	77±3	109±7	115±4
n-Butane	151±20	131±7	132±7	120±2	144±5	120±4
n-Heptane	249±20	190±6	224±30	168±20		177±10
Isooctane	153±7	128±30	140±20	125±8	148±30	127±8

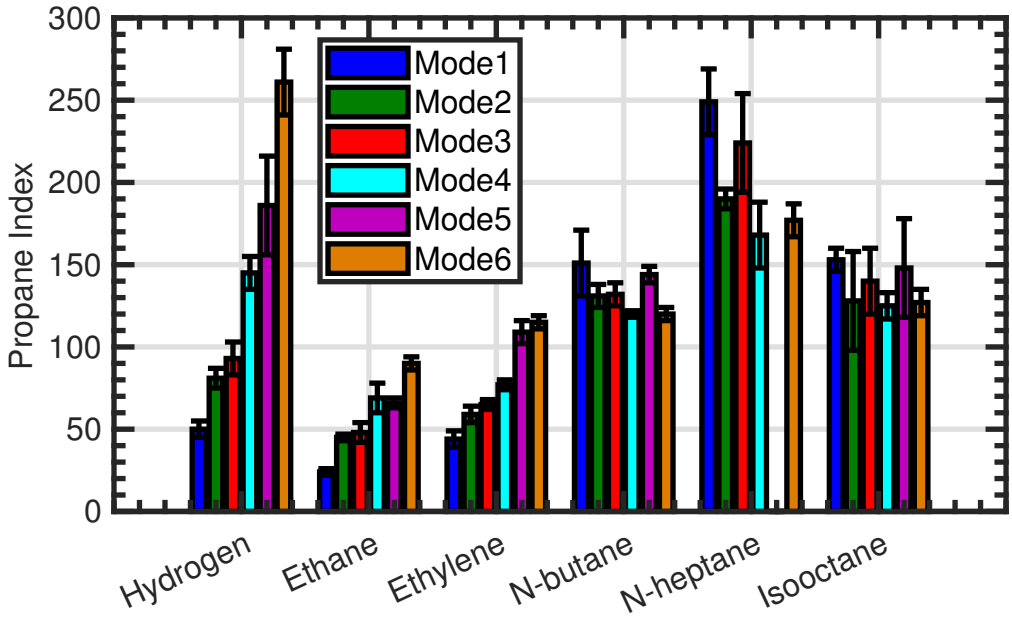

Figure 4.9: Calculated *PI* for each test fuel at all six operating conditions.

4.2.3 Propane Index and Hydrogen Index Comparison

In order to compare the calculated *HI* and *PI* for the test fuels, Equation 4.1 for the two different methods can be combined and simplified to the form in Equation 10.2.

$$PI_{tf} = 100 \times \frac{HI_{tf}}{HI_{C3H8}} \tag{4.3}$$

For example, the *HIs* for ethane and propane at operating condition 3 are 55 and 99, respectively, which results in a predicted *PI* of 56±7 for ethane at operating condition 3; the experimentally determined *PI* for ethane at operating condition 3 was 48±6. The predicted (from Equation 10.2) and experimentally derived *PI* for all fuels and conditions tested can be seen in Figure 4.10. The two main outliers were *n*-heptane and isooctane, both at operating condition 1; both of these fuels had low flow rates due to their high reactivity, so it is possible that their uncertainty was underestimated. Overall, it can be seen that the data showed a very strong 1:1 relationship. This validates that both a linear blending rule did appear to describe the autoignition properties of a fuel well and that either an *HI* or a *PI* could adequately describe the relative reactivity of a fuel for a given engine operating condition.

4.2.4 Multi-Component Gas Testing

Fuel substitution testing with both methane/propane and methane/hydrogen reference fuels was also performed using two pre-mixed hydrocarbon mixtures. The fuels consisted of a mixture of methane, ethane, propane, *n*-butane, and isobutane, and were blended to have MN65 and MN80. The compositions, both in energy and mole fractions, can be seen in Table 4.4. Both mixtures were representative of natural gas, consisting of mostly methane with the main highly reactive fuel being propane along with relatively small amounts of *n*- and isobutane.

The results of the *HI* and *PI* fuel substitution sweeps for both gas mixtures can be

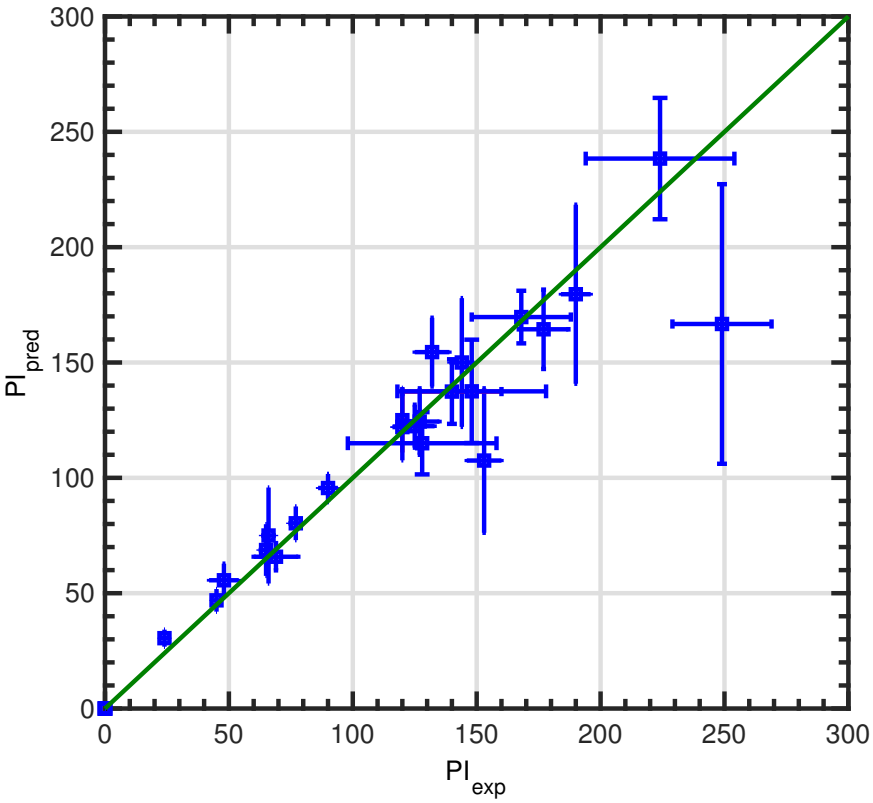

Figure 4.10: Predicted *PI* vs. experimentally found *PI* for all fuel substitution sweeps.

Table 4.4: Gas composition percentages, weighted by energy/moles.

	MN65	MN80
Methane	79.4/91.1	90.3/96.0
Ethane	0.6/0.4	0.7/0.4
Propane	15.1/6.8	6.8/2.9
N-butane	3.2/1.1	1.4/0.5
Isobutane	1.8/0.6	0.8/0.3

Table 4.5: Calculated *HI* and *PI* for MN65 and MN80 gas mixtures.

Fuel		1	2	3	4	5	6
MN65	PI	23±5	22±3	24±5	22±2	31±10	27±7
MN80	PI	10±5	11±4	13±4	14±2	17±4	16±5
MN65	HI	50±5	30±3	27±5	20±3	19±7	12±4
MN80	HI	27±4	14±4	17±6	12±2	16±6	8±2

seen in Figures 4.11 and 4.12 and Table 4.5. The experimental results showed trends similar to those seen with the single component test fuels. The *HI* was strongly dependent on operating condition, with the largest *HI* occurring at high pressure/low temperature condition (1) and the smallest *HI* occurring at low pressure/high temperature condition (6), while the *PI* was relatively constant across all operating conditions. These results indicate that the reactivity of the two gas mixtures relative to the methane/hydrogen reference fuels decreases as pressure decreases and temperature increases, while the reactivity relative to the methane/propane reference fuels stays relatively constant for all operating conditions. Because the main high reactivity fuel in the gas mixtures was propane, it follows that the gas mixtures would exhibit experimental trends similar to that of pure propane. Referring to Figure 4.7, propane showed the same trend in *HI* as a function of operating condition, while by definition the *PI* of a methane/propane mixture will be equal to a constant value that is independent of operating condition.

The results of the multi-component gas mixture testing were used to compare the predictive capability of the current work's linear energy-based blending rule,

$$HI_{pred} = \sum_{1}^{n} e_i HI_i, \tag{4.4}$$

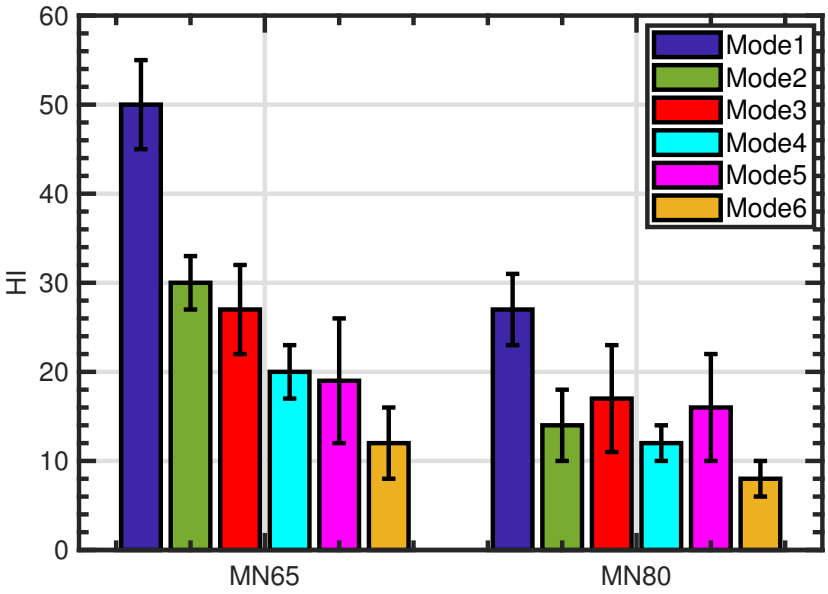

Figure 4.11: Results of *HI* testing and uncertainties for MN65 and MN80 gas mixtures.

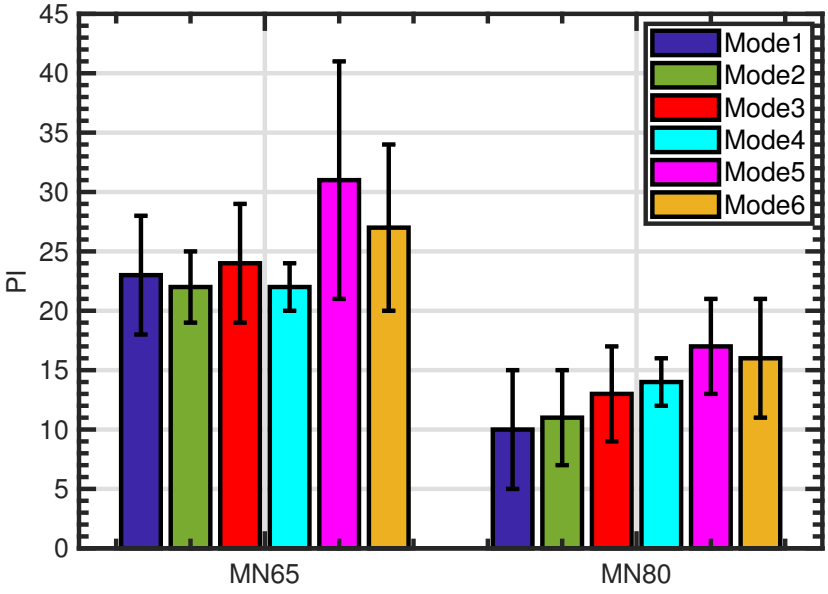

Figure 4.12: Results of *PI* testing and uncertainties for MN65 and MN80 gas mixtures.

to the industry-standard MN characterization,

$$HI_{pred} = 100\left(1 - \frac{MW_{CH4}LHV_{CH4}MN}{MW_{H2}LHV_{H2}(100 - MN) + MW_{CH4}LHV_{CH4}MN}\right). \tag{4.5}$$

The linear energy-based blending rule calculates the total mixture HI by summing the individual energy-weighted fuel HIs. Isobutane was not tested in the current work, so its HI values were assumed equal to n-butane; the potential inaccuracies involved with this assumption had a relatively small effect on the results due to the low energy/mole fraction of isobutane in both gas mixtures. An important note is the energy-fraction weighted, predicted HI value will have a dependency on operating condition because the individual fuel components have different HIs at different operating conditions. The MN-based rule directly calculates an energy-based HI from the molar-based MN; this value will be independent of operating condition.

A comparison of the predicted HIs for each method can be seen in Figure 4.13; it can be seen that the predicted HIs for both methods were similar for operating conditions 4 and 5 but grew increasingly further apart at the high pressure/low temperature conditions. Figure 4.14 shows the comparison between the HI values predicted by the two equations and the experimental HI values. As mentioned previously, the MN-based rule resulted in a single predicted HI for each gas mixture that was independent of operating condition, while the energy-based blending rule results varied with operating condition. Over the span of all test points, it is seen that the energy-based rule slightly over-predicted the HI compared to the experimental results. The MN-based rule matched the experimental results at the low pressure/high temperature condition (6), but poorly matched the experimental results at high pressure/low temperature condition (1). For example, for MN65 at condition 6, the energy-based rule predicted an HI of 10±1 while the MN-based rule predicted an HI of 14±1; both predicted values were relatively close to the experimental HI of 12±4. However, for MN65 at condition 1, the energy-based

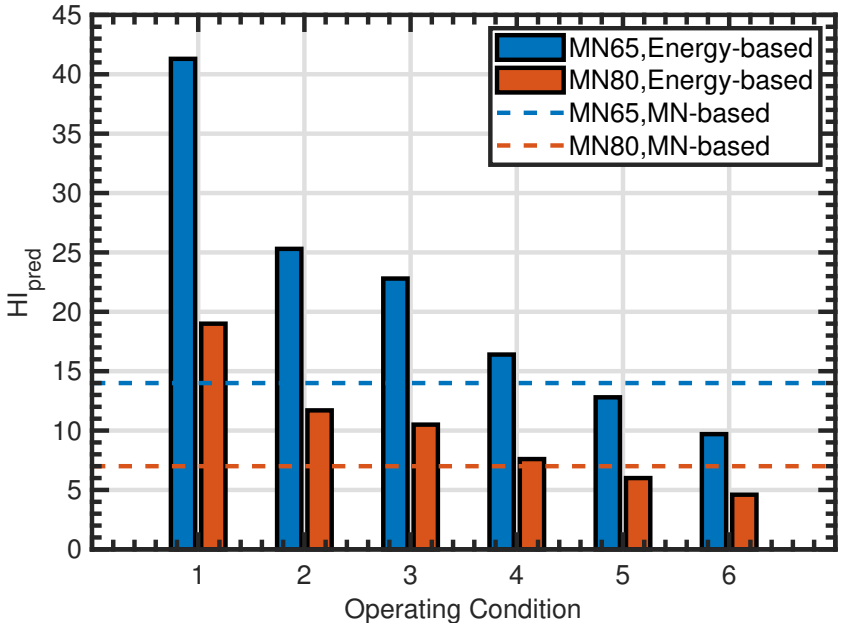

Figure 4.13: Predicted *HI* for MN65 and MN80 gas mixtures using the energy-based blending rule and *MN* characterization.

rule predicted an *HI* of 41±5 while the *MN*-based rule again predicted an *HI* of 14±1; the energy-based rule was much closer to the experimental *HI* of 50±5. This indicates that the *MN* classification for natural gas mixtures appears to be valid only for specific ranges of temperatures and pressures, whereas the energy-based blending rule appears to be reasonably valid over the entire range of temperatures and pressures tested. Additionally, the energy-based blending rule could have its thermodynamic range extended through further pure fuel substitution tests.

4.2.5 Baseline Sensitivity Testing

Two sets of experiments were performed to investigate the baseline operating point sensitivity: 1) the intake temperature was swept and the baseline propane concentration was adjusted to maintain CA_{50} and gross *IMEP* and 2) the baseline propane concentration was swept while all other intake conditions were fixed. The results of the intake temperature sweeps for all six operating conditions can be seen in Figure 4.15. There

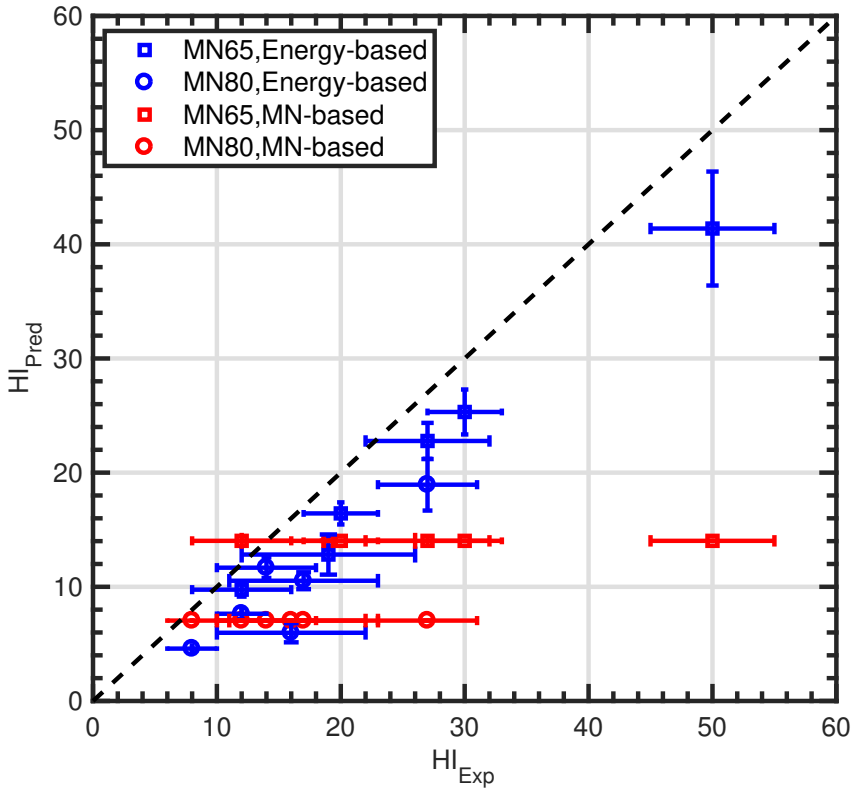

Figure 4.14: Predicted *HI* vs. experimental results for MN65 and MN80 gas mixtures using the energy-based blending rule and *MN* characterization.

was a strong relationship between the propane concentration required to maintain combustion phasing and load and T_{IVC}. The normalized slope of -5.3 indicates that the propane concentration had to change by >5% (absolute) for each 1% change in T_{IVC}. The experimental database of fuel substitution sweeps was built up over several years with multiple engine rebuilds between datasets. These sensitivity results indicate that if an operating condition required a similar baseline propane concentration to reach the same combustion phasing and load, there could be reasonable confidence that the thermodynamic conditions leading up to combustion were similar. The maximum variation in baseline propane concentration throughout the fuel substitution testing was around 2.5% (absolute), indicating a maximum change in T_{IVC} of 0.5%, or about 2 K. This high sensitivity suggests that the relative reactivity trends seen in the current work would be expected to be repeatable on different engine platforms by matching speed, TDC pressure, and equivalence ratio, and adjusting intake temperature until a similar baseline propane concentration resulted in matched combustion phasing.

The results of the propane concentration sweeps for all six operating conditions can be seen in Figure 4.16; there was a strong sensitivity of CA_{50} to changes in propane concentration. The slope of -0.9 indicates that there was an approximately 1:1 relationship between percent change in propane concentration (absolute) and degree change in combustion phasing. This result demonstrates the importance of maintaining constant combustion phasing throughout the fuel substitution sweep; any change in combustion phasing was an indication that global fuel reactivity was not constant and thus the HI or PI characterization would become invalid. However, if boundary conditions and combustion phasing remained fixed throughout a fuel substitution sweep, this result indicates that global fuel reactivity could be assumed to be relatively constant throughout the sweep. Maximum CA_{50} fluctuations during a fuel substitution sweep were around one degree, indicating an equivalent propane concentration change of about 1% (absolute).

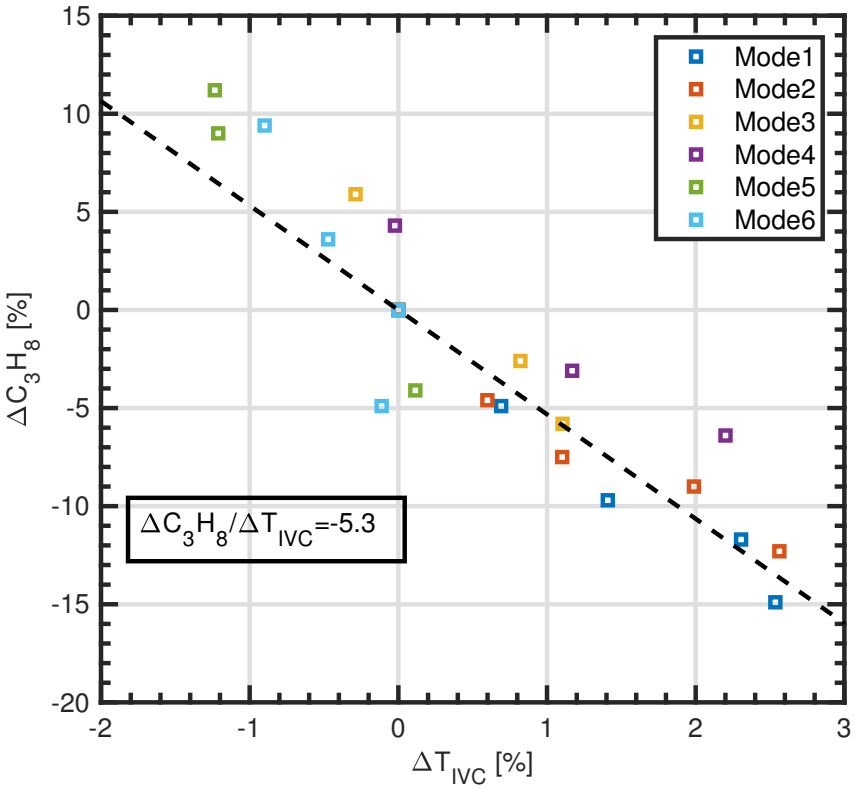

Figure 4.15: Results of T_{IVC} vs. C_3H_8% sensitivity testing.

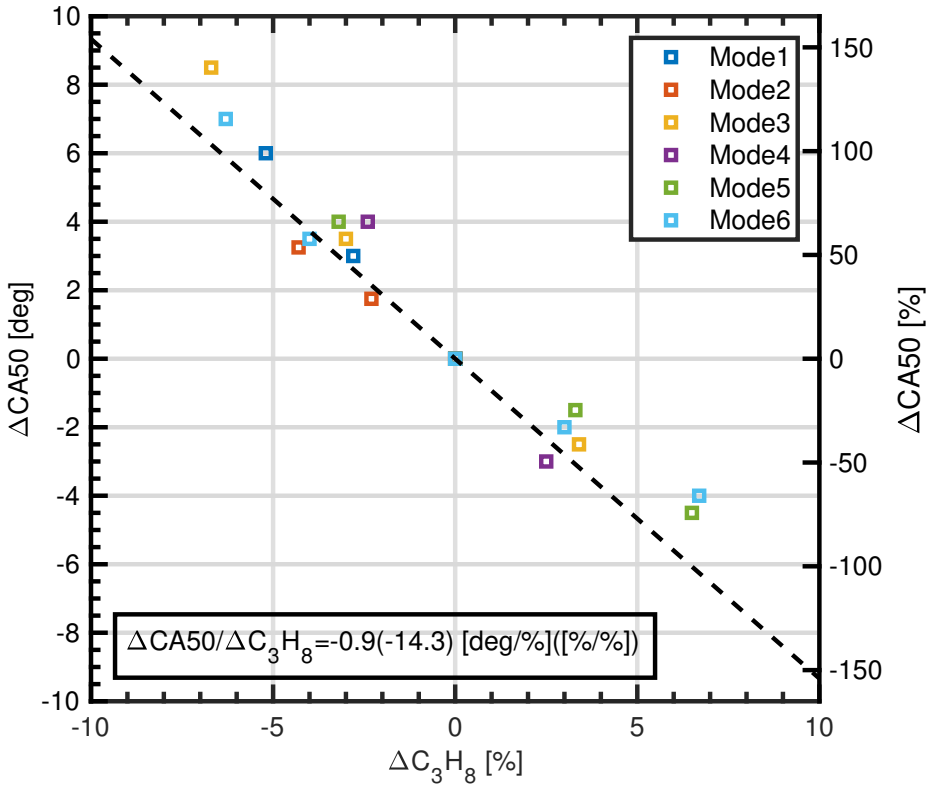

Figure 4.16: Results of C_3H_8% vs. CA_{50} sensitivity testing.

Table 4.6: Molecular weight and lower heating value for hydrogen and hydrocarbon fuels used in the current work.

Fuel	MW (kg/kmol)	LHV (MJ/kg)
Hydrogen	2.02	120.0
Methane	16.04	50.0
Ethane	30.06	47.8
Ethylene	28.04	47.2
Propane	44.08	46.4
n-Butane	58.1	45.8
n-Heptane	100.16	44.6
Isooctane	114.18	44.4

4.3 Energy-based Blending Rule Analysis

The previously mentioned work in [2] used a mass-weighted linear blending rule to calculate a mixture primary reference fuel number, PRF_{mix}, according to

$$PRF_{mix} = PRF_{tf} y_{tf} + PRF_{ref}(1 - y_{tf}), \tag{4.6}$$

where PRF_{tf} is the test fuel's equivalent PRF number, PRF_{ref} is the PRF number of the reference fuels, and y_{tf} is the test fuel mass fraction. While this was shown to adequately describe the overall mixture reactivity in the previous study for which all fuels tested had similar lower heating values (LHVs), this method was revised in the current work due to the complications stemming from the large LHV of hydrogen. Molecular weight (MW) and LHV value for all of the tested fuels are listed in Table 4.6. There is a wide range of MWs, with isooctane having a MW 57 times that of hydrogen. The LHVs are relatively similar for the hydrocarbons, but hydrogen has an LHV about 2.5 times larger than the hydrocarbon fuels.

While no generally accepted blending rule was found in literature, RON and MON testing use a weighting based on liquid volumes of the reference fuels (isooctane and *n*-heptane) while MN testing uses a weighting based on the gaseous volumes of the reference fuels (equivalent to mole-based for ideal gases). For RON and MON testing, the reference fuels' liquid densities are within 2% and the LHVs are within 0.3%, so the liquid

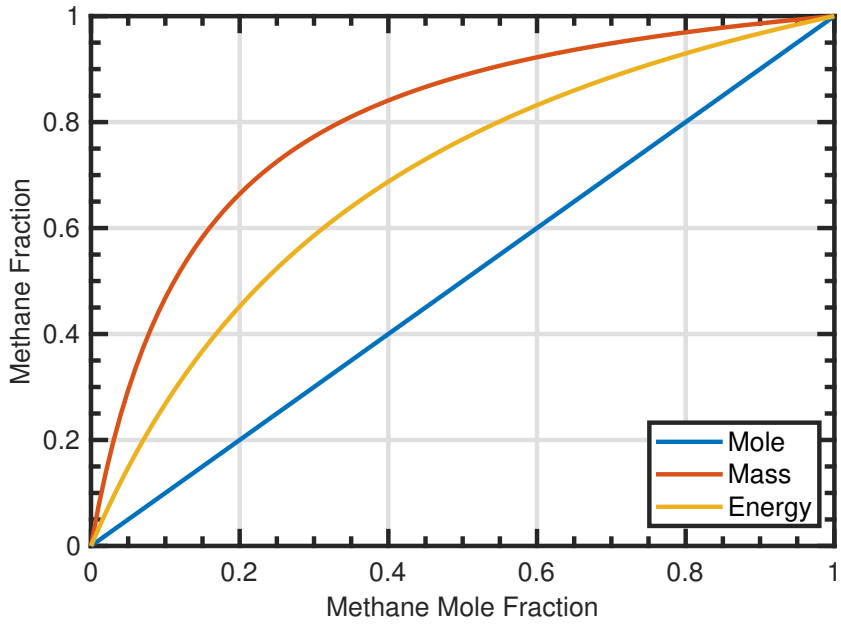

Figure 4.17: Methane mole, mass, and energy fraction vs. methane mole fraction in a binary mixture of methane and hydrogen.

volume weighting method is nearly identical to both mass-weighted and energy-weighted methods. Due to the large difference in MWs of the hydrocarbon fuels used in MN testing, the mole-weighted method used will be quite different from the mass-weighted or energy-weighted methods. Figure 4.17 shows the effect of the different methods of fraction weighting for a binary methane/hydrogen mixture; the differences exist due to the mismatch in MW and LHV for the two fuels. It is interesting to note that the differences between the three methods are relatively close near the end points when the mixture consists of a majority of one fuel, and the differences are the greatest when the mixture consists of a relatively even mixture of both fuels.

During fuel-substitution, RON/MON, or MN tests, the engine operating condition is fixed while test fuels are substituted for reference fuels. During tests, engine load is kept relatively constant, which means that total fuel energy (rather than total fuel mass or total fuel moles) is held constant. This points to the energy-weighted method as the most appropriate method to describe the overall fuel mixture.

Consider a hypothetical fuel substitution test. Using methane/hydrogen as the reference fuels and a test fuel that has the same LHV and MW as methane but an equivalent reactivity (or *HI*) as hydrogen. The baseline operating condition uses a 50/50 (by mole) mixture of methane/hydrogen, which is equivalent to 89/11 (by mass) and 77/23 (by energy). As the test fuel is introduced, in order to maintain engine load and overall mixture reactivity, hydrogen has to be removed at a 1/1 (by energy) rate as the test fuel is added. The limiting case occurs when no more hydrogen remains in the system, and the mixture is a 77/23 (by energy) binary mixture of methane/test fuel. Because the test fuel has the same LHV and MW as methane, the 77/23 (by energy) mixture is equivalent to a 77/23 (by mass) and 77/23 (by mole) mixture.

A summary of this hypothetical test can be seen in Figure 4.18; for all three methods of weighting, the blend composition of the two reference fuels (methane/hydrogen) changed from its initial value to pure methane as the test fuel was added and hydrogen was removed. The overall mixture reactivity was by

$$HI_{mix} = HI_{tf} f_{HI} + HI_{ref}(1 - f_{HI}), \tag{4.7}$$

where HI_{mix} refers to the trapped mixture's global *HI*, HI_{ref} refers to the *HI* of the two reference fuels as described by

$$\mathrm{HI}_{ref} = \frac{100 f_{H2}}{f_{H2} + f_{CH4}}, \tag{4.8}$$

and f_{TF} refers to the test fuel mole, mass, or energy fraction. It is important to note that all three sets of points shown in Figure 4.18 represent identical fuel amounts; the only difference is the weightings were calculated on a different basis.

In Equation 4.7, there are two unknown values, HI_{mix} and HI_{tf}, both of which are independent of f_{tf}. Fitting the HI_{ref} vs. f_{tf} data to Equation 4.7 using a least squares approach provides an estimate of the test fuel HI, HI_{tf}, which should be equivalent to the

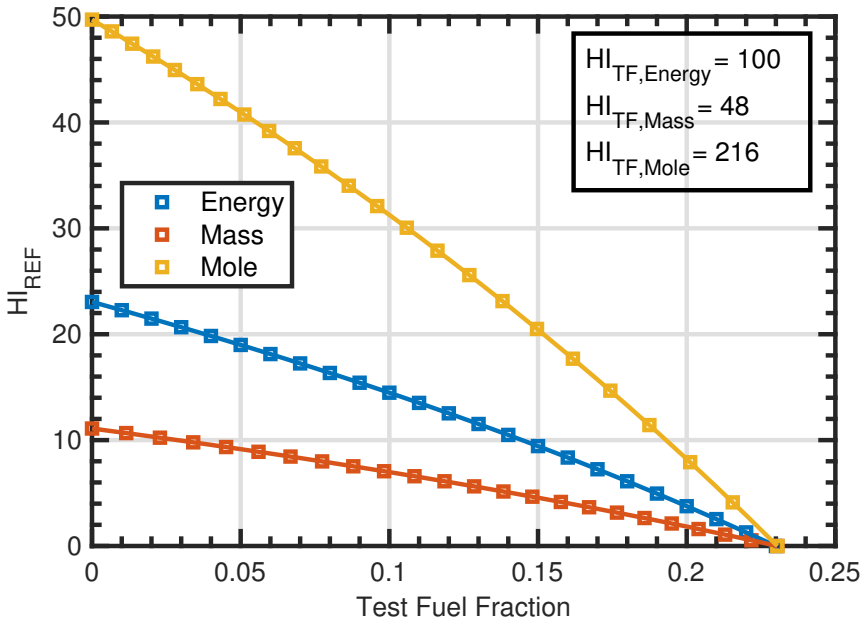

Figure 4.18: Hydrogen Index of the reference fuels as a function of test fuel fraction (both values calculated on an energy, mass, and molar basis).

HI of hydrogen, which is 100 (by definition). The fit results are shown in Figure 4.18; it can be seen that all three weighting methods are able to accurately fit the observed fueling trends. However, the mole-, mass-, and energy-based fits all give very different results for HI_{tf}, with the energy-based fit being the only method that results in a HI_{TF} that matched the true value for hydrogen, HI_{H2}=100. Therefore, while all three blending rules can accurately capture the behavior of fuel substitution sweeps (mathematically), when the test and reference fuels have relatively large differences in LHV or MW the energy-based blending rule results in the most physically meaningful results.

An important note is this characteristic is constrained to testing where the total fuel energy is held constant. These results suggest that the molar-based blending rule used for calculating the *MN* of natural gas mixtures would potentially have improved accuracy by switching to an energy-based blending rule; this is potentially one of the reasons that the *MN* calculations are not able to accurately extrapolate outside of small concentrations of heavier hydrocarbons such as propane, *n*-butane, and isobutane.

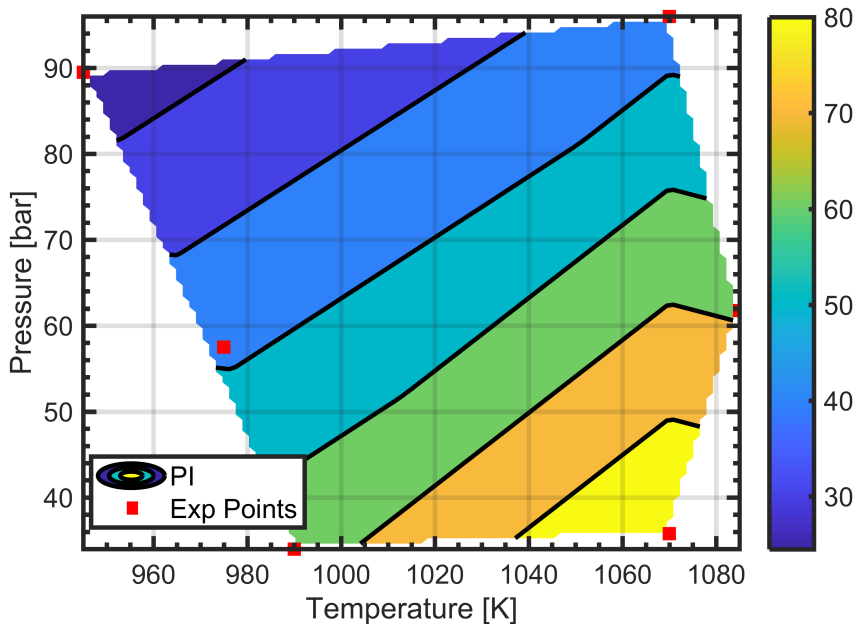

Figure 4.19: *PI* as a function of pressure and temperature for ethane.

4.3.1 Conclusions

Fuel substitution tests using reference fuels of methane/hydrogen and methane/propane were performed for the pure test fuels hydrogen, ethane, ethylene, propane, *n*-butane, *n*-heptane, and isooctane; it was seen that common hydrocarbon fuels show a strong sensitivity to temperature and pressure, and the reactivity relative to the reference fuels can change substantially at different operating conditions. For example, at operating condition 1 ethane has a similar reactivity to a mixture of 24/76 (C_3H_8/CH_4), while at operating condition 6 ethane has a similar reactivity to a mixture of 90/10 (C_3H_8/CH_4). A representative *PI* map as a function of temperature and pressure for ethane extrapolated from experimental data (six conditions) can be seen in Figure 4.19. A clear trend can be seen that when traversing from high pressure/low temperature to low pressure/high temperature conditions, ethane transitions from lower reactivity than propane to a quite similar reactivity compared to propane.

Fuel substitution tests were also performed with two multi-component *MN* gas mixtures. The results followed trends that were observed in the pure hydrocarbon fuel

testing, with the gas mixtures exhibiting similar sensitivity to that of propane relative to the reference fuels. The linear energy-based blending rule was used to predict the *HI* of each fuel mixture from the individual fuel components and seen to match experimental trends of increasing *HI* when traversing from the low pressure/high temperature condition (6) towards the high pressure/low temperature condition (1); however, predicted *HI* were lower than experimental *HI* across all operating conditions. The *MN* was also used to predict the *HI* of each fuel mixture and was seen to match experimental results at low pressure/high temperature conditions but not at high pressure/low temperature conditions.

The propane concentration change required to maintain combustion phasing as T_{IVC} was adjusted exhibited a strong sensitivity, indicating that operating conditions that were run with baseline propane concentrations within 2.5% (absolute) and combustion phasing fixed could be assumed to have in-cylinder temperatures within 0.5%. The change in combustion phasing as the propane concentration was adjusted also showed a strong sensitivity, indicating that if boundary conditions remained constant and CA_{50} was fixed within 1 degree throughout a fuel substitution sweep, global fuel reactivity could be assumed within 1% (absolute).

Chapter 5

Trapped Mass Temperature Measurements

The ideal gas state equation is one method often used to calculate the bulk in-cylinder gas temperature. The ideal gas law assumes that inter-molecular interactions are negligible, which is a valid assumption at the low pressure thermodynamic conditions near IVC. The thermodynamic state for an ideal gas can be defined by the mixture pressure and density, which allows the temperature at IVC to be calculated according to

$$T_{IVC} = \frac{P_{IVC} V_{IVC}}{MR}. \tag{5.1}$$

In order to fully quantify the uncertainty in T_{IVC} a rigorous analysis of each individual measurement that was involved in the values in this equation was necessary. Upon a review of the experimental setup, 14 parameters were found to be involved in the T_{IVC} calculation. Table 3.2 lists relevant sensor part numbers along with their corresponding measuring ranges and accuracies.

5.1 In-Cylinder Pressure Uncertainty

In-cylinder pressure was initially measured with a Kistler 6125B pressure transducer in series with a Kistler 5010 charge amplifier. The pressure was calculated by

$$P_{cyl} = P_{slope}(V - V_{peg}) + P_{peg}, \tag{5.2}$$

where P_{slope} is the calibrated transfer function between voltage and pressure, V is the measured voltage, V_{peg} is the average voltage during the pegging crank angle range, and P_{peg} is assumed to be the measured intake pressure at the time of pegging. The three parameters in this equation that must have their uncertainty quantified are: P_{slope}, V, and P_{peg}.

5.1.1 Pressure Transducer Transfer Function

The pressure-voltage relationship was calibrated in the lab using a dead weight tester. This involved using calibrated weights to apply a known pressure to the transducer and recording the voltage, which was measured by the DAQ system. The slope and 95% confidence interval, CI_{95}, were calculated by performing a linear fit on the data points. A more in-depth discussion of the calibration process related to engine experiments is found in [74].

5.1.2 Pressure Transducer Voltage

The precision uncertainty was quantified by acquiring 300 cycles of engine data and computing the CI_{95} for the mean value at each crank angle position by

$$CI_{95} = \bar{x} \pm \frac{t(N\text{-}1, 95)\sigma}{\sqrt{N}}, \tag{5.3}$$

where N is the number of cycles acquired, $\bar{x}$ is the sample mean, and σ is the sample standard deviation.

Because the difference between measured voltage and measured voltage at the pegging crank angle was the value of interest, it was assumed there were no accuracy biases associated with this measurement. One thing to note is that drift in the charge amplifier signal will cause an accuracy bias in the computed pressure value; this bias will have the smallest effect at the pegging crank angle and the largest effect at the crank angle just prior to pegging.

5.1.3 Pegging Pressure

The pegging pressure is ideally the absolute in-cylinder pressure measured at the pegging crank angle. Due to the complications of installing an absolute pressure transducer in the engine cylinder, this value is typically measured in the intake surge tank or the intake runner using either a low- or high-speed absolute pressure transducer. The pegging crank angle range is chosen near BDC during the intake stroke when the piston motion is minimal and the in-cylinder pressure is relatively steady. The majority of data were acquired with a low-speed pressure transducer installed in the intake surge tank. The precision was calculated with Equation 5.3, while the accuracy was verified in-house using a mechanical absolute pressure device, which was discussed in Chapter 3.

An additional source of uncertainty associated with using a low speed pressure transducer is that high speed pressure fluctuations in the intake runner can create bias errors. The pegging procedure assumes that the in-cylinder pressure at BDC during the intake stroke is equal to the measured intake pressure; however, a low-speed pressure transducer only measures the average intake pressure and cannot capture high-speed intake dynamics. A substantial pressure drop in the intake runner during the intake stroke may cause the in-cylinder pressure to have a lower value than the average measured intake pressure. To quantify this uncertainty, a high-speed absolute pressure transducer was installed in

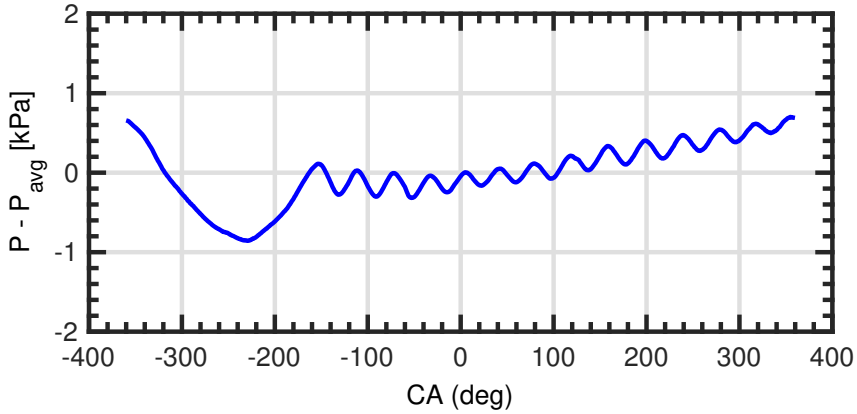

Figure 5.1: Difference between instantaneous and average intake runner pressure as a function of crank angle at 1000 RPM engine speed and 1.5 bar intake pressure.

the intake runner and intake and cylinder pressure data were acquired on a crank-angle time scale. Figure 5.1 shows the difference between measured intake pressure and mean intake pressure as a function of crank angle. While there was a drop in pressure during the initial portion of the intake stroke, the pressure started to recover towards the mean by BDC. The low-magnitude, high-frequency oscillations seen after the intake stroke was complete were due to wave dynamics in the intake runner. The deviation between the intake runner pressure at the pegging crank angle and the mean pressure was less than 0.5% of the mean pressure for all operating conditions.

5.1.4 Pressure Transducer Comparison

An AVL GU22CKA pressure transducer was used to verify pressure measurements after some discrepancies were seen in the repeatability of the Kistler 6125B pressure measurements taken over the span of several years. Figure 5.2 shows a comparison of the pressure data taken with each sensor; while the relative difference was small at TDC, the relative difference at IVC was 5-10% for all six operating conditions. As seen in Equation 5.1, the calculated temperature is directly proportional to the measured pressure, meaning that the T_{IVC} values calculated with the two sets of pressure data were substantially different.

Because the TDC pressures were relatively close, it is believed a dynamic hysteresis or drifting error occurred with the Kistler 6125B transducer, which caused relatively large errors during the gas exchange and early part of the compression stroke; it is noted that the Kistler 6125B transducer had been used in the DERC engine for >8 years, often under harsh operating conditions, while the AVL GU22CKA transducer was less than one year old.

Pressure trace analysis was performed on datasets from both sensors. Polytropic coefficients were fit to the logarithm pressure and logarithm volume data (base 10) for both the compression, from IVC to -40 deg aTDC, and expansion, from 40 deg aTDC to EVO, strokes. An example of the residuals from applying the curve-fits to motored data taken with each sensor is shown in Figure 5.3. The residuals of the curve-fit for the AVL sensor had a much smaller magnitude compared to the residuals for the Kistler sensor. The MSE of the curve-fit is very dependent on accurate volume estimation, which depends critically on the compression ratio and accurate crank angle assignment. Figure 5.4 shows the ratio of the curve-fit MSE of the Kistler/AVL sensors as a function of compression ratio and crank-angle shift. A value >1 indicates that the Kistler transducer had a larger MSE; it was seen that no matter what crank angle shift or compression ratio was used for the analysis, the Kistler sensor always had 4-6× larger MSE compared to the AVL sensor.

The difference between the polytropic coefficients calculated from the expansion and compression stroke were also compared between the two sensors. Due to heat transfer effects, the polytropic coefficient for the expansion stroke should be slightly larger than the polytropic coefficient for the compression stroke. Figure 5.5 shows the difference between the polytropic coefficients as a function of compression ratio and crank-angle shift. It was seen that the AVL sensor always had a positive difference, while the Kistler sensor always had a negative difference between the expansion and compression polytropic coefficients.

In addition to the two metrics from the motored trace analysis, the AVL transducer accuracy was verified by testing against another transducer on a different lab's engine platform, and was found to produce similar pressure data. For these reasons, the AVL sensor was used as the source of all pressure data and trapped mass calculations reported in the following chapters.

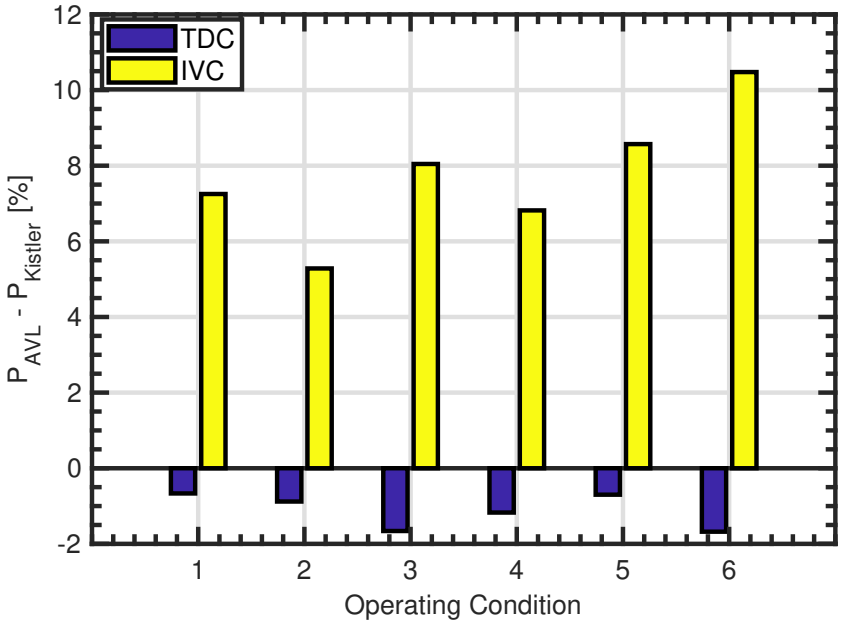

Figure 5.2: Relative difference between pressure data taken with AVL and Kistler pressure transducers at TDC and IVC for the six main operating conditions.

5.2 Volume Uncertainty

Engine volume was determined through the crank-slider equations

$$V = V_{TDC}\left[1 + \left(\frac{r_c - 1}{2}\right)\left(\frac{L}{a} + 1 - \cos\theta - z\right)\right], z = \sqrt{\left(\frac{L}{a}\right)^2 - \sin^2\theta}, \tag{5.4}$$

where V_{TDC} is the volume at TDC, r_c is the compression ratio, L is the connecting rod length, a is 1/2 of the stroke, and θ is the crank angle.

The connecting rod and stroke are measured dimensions and assumed accurate, so

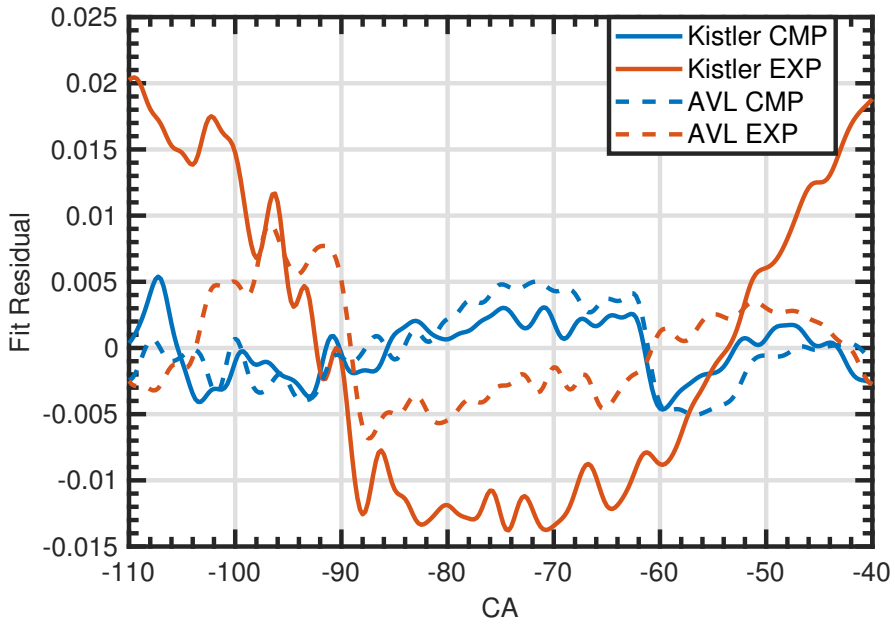

Figure 5.3: Residual between isentropic curve-fit pressure and measured pressure with the AVL GU22CKA and Kistler 6125B transducers.

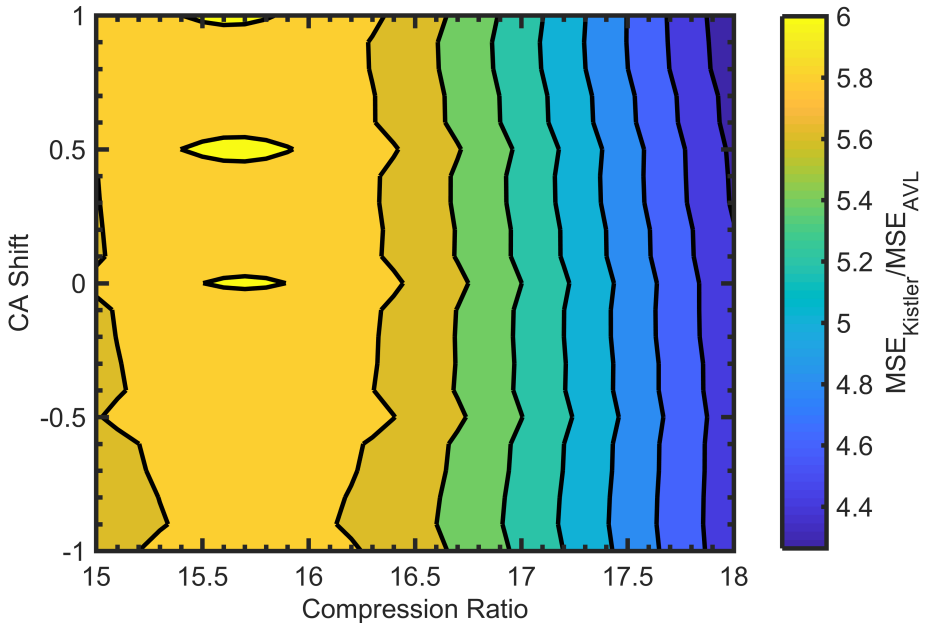

Figure 5.4: Ratio of the Kistler to AVL calculated MSEs for the difference between isentropic curve-fit pressure and measured pressure with each sensor.

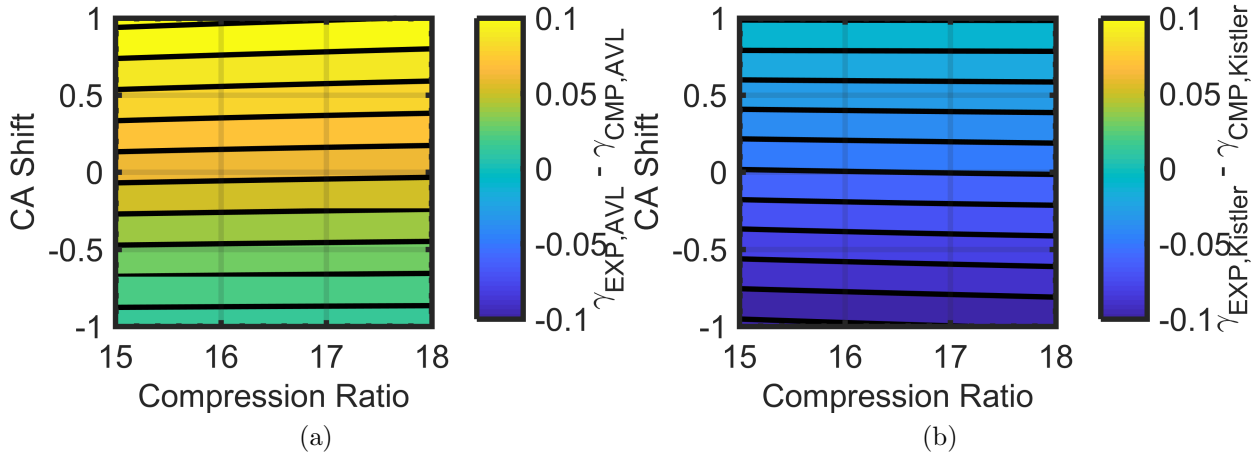

(a) (b)

Figure 5.5: Difference between expansion and compression polytropic coefficients for pressure data taken with the AVL (left) and Kistler (right) pressure transducers.

the uncertainty in this calculation comes from the V_{TDC} estimate and the crank angle measurement. There is also uncertainty associated with the compression ratio, but since compression ratio is a function of V_{TDC} it was not separately analyzed.

5.2.1 TDC Volume

The TDC volume had no precision associated with it, but there was an accuracy uncertainty involved with its measurement. There are two methods used to estimate TDC volume: the first involves a direct measurement of the piston and engine head clearance volume, while the second involves analysis of the in-cylinder pressure data taken during motoring conditions. Direct measurement of the TDC volume was difficult due to the complex geometry of both the piston and the engine head. Additionally, due to the high compression ratio of diesel engines, the TDC volume was quite small, approximately 30 cubic centimeters, which resulted in small absolute measurement errors having a large relative effect on the calculated TDC volume.

Pressure trace analysis involves fitting polytropic curves to the pressure data as described above. The 'correct' compression ratio was the one that resulted in the lowest mean squared error (MSE) between the pressure calculated from the polytropic curve-fits

and the pressure data.

Ideally, both the directly measured TDC volume and the TDC volume calculated from the pressure trace analysis will result in the same value; for the current work, the TDC volume calculated from the pressure trace analysis, 31.2 cm^3, was 4% higher than the directly measured TDC volume, 30.0 cm^3.

5.2.2 Crank Angle

The crank angle was measured through an optical encoder that was attached to the crankshaft. The resolution of the encoder was 0.25 degrees, which limited the minimum accuracy uncertainty to 0.125 degrees. The main accuracy uncertainty associated with this measurement was aligning the encoder's electrical TDC with the engine's mechanical TDC. This was performed by first manually rotating the engine to TDC, which was verified by flywheel angular markings and a dial indicator probe measuring piston height and then rotating the encoder until it reads TDC before tightening the coupler that fixes the encoder to the crankshaft. The electrical vs. mechanical alignment was then verified by motoring the engine and inspecting the crank angle where peak pressure occurred. Due to heat transfer, peak pressure will always occur slightly before TDC, typically 0.5-1.0 CAD [75]. A crank angle shift was applied to the encoder signal to fix peak pressure at 0.75 deg bTDC when motoring at a speed of 1000 RPM. This value was chosen to ensure that the bias associated with the CA measurement was limited to <1 degree. Figure 5.6 shows the normalized pressure near TDC for the six motored operating conditions used in the current work; the location of peak pressure was 0.75 CAD bTDC for five conditions and 1.0 CAD bTDC for the sixth condition.

The current work was focused on temperature estimation at IVC, where crank angle estimation has a relatively small effect on volume estimation and an uncertainty < 1 degree was acceptable. It is noted that many physical and thermodynamic simulation methods exist in the literature that could reduce this bias uncertainty, if necessary.

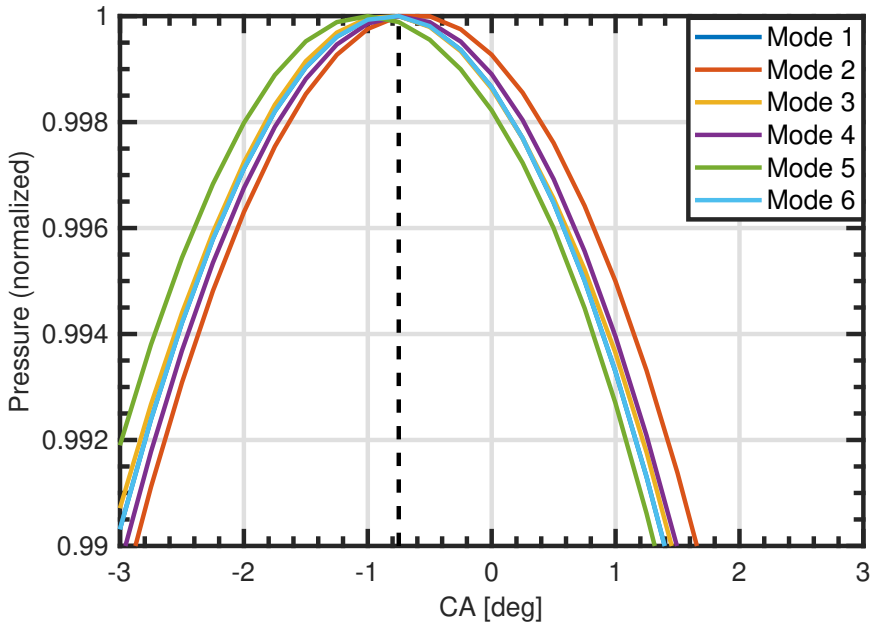

Figure 5.6: Normalized pressure for the six motored operating conditions.

5.3 Trapped Mass Uncertainty

Trapped mass is the term used for the total mass of the in-cylinder contents during the portion of the engine cycle when the valves are closed, assuming there is no blow-by. It was calculated by

$$M = \frac{\eta_{trap}(m_{air} + m_{fuel})}{1 - y_{res}}, \tag{5.5}$$

where η_{trap} is the engine trapping efficiency and y_{res} is the residual mass fraction.

There were three components that made up the in-cylinder mixture: fresh air, fuel, and internal residual combustion products from the previous cycle. External exhaust gas recirculation was not used for any of the experimental tests. Besides the measured air and fuel flow rates, the engine speed was used to convert flow rate measurements to a mass-per-cycle basis, and there was also a trapping efficiency that accounted for any fresh air and fuel flowing through the intake valves and escaping through the exhaust valves during valve overlap period, the portion of the engine cycle when both intake and exhaust valves were open. Trapping efficiency was also used to account for leaks in the

intake system; any metered air that was lost prior to entering the engine cylinder would affect the trapped mass calculation in the same way as short-circuiting during the valve overlap period.

5.3.1 Air Measurement

Airflow was measured using a set of calibrated choked flow orifices. When the pressure ratio across an orifice is above the critical ratio, the mass airflow is solely dependent on upstream conditions and can be calculated by

$$\dot{m} = C_d A \sqrt{\gamma \rho_u P_u \left(\frac{2}{\gamma+1}\right)^{\frac{\gamma+1}{\gamma-1}}}, \tag{5.6}$$

where C_d is the discharge coefficient, A is the cross-sectional area, γ is the specific heat ratio of air, and ρ_u and P_u are the density and pressure (respectively) of air upstream of the orifice.

By rearranging Equation 5.6 and substituting in the ideal gas relationship for density, it is seen in

$$\dot{m} = C_d A \sqrt{\gamma \frac{P_u^2}{T_u R} \left(\frac{2}{\gamma+1}\right)^{\frac{\gamma+1}{\gamma-1}}} \tag{5.7}$$

that mass flow is proportional to upstream pressure and inversely proportional to the square root of upstream temperature.

Over the range of normal operating conditions, all values in Equation 5.7 were constant except for pressure and temperature; therefore, by measuring pressure, temperature, and mass airflow a calibration equation was obtained

$$\dot{m} = C_{d,\text{lin}} \frac{P_u}{\sqrt{T_u}} + C_{d,\text{ofst}}, \tag{5.8}$$

where $C_{d,lin}$ and $C_{d,ofst}$ were the slope and y-intercepts of the calibrated curve fit. The calibration was performed using a Coriolis mass flow measurement device (Endress and

Hauser Promass 83M15) placed in series with the choked flow orifices as the reference air flow rate, which had an accuracy of 0.325 kg/hr. The accuracy uncertainty assigned to the slope and y-intercept values were determined by finding the CI_{95} of the linear curve fit coefficients.

Upstream Pressure Measurement

Upstream pressure was measured with a pressure transducer installed directly upstream of the choked flow orifices. Precision uncertainty was found by calculating the CI_{95} of the mean of the time-varying data, while accuracy uncertainty was calculated by performing an in-house calibration using a mechanical absolute pressure gage. Sensor part numbers, ranges, and accuracies are listed in Table 3.2.

Upstream Temperature Measurement

Prior to this uncertainty analysis, the temperature used in Equation 5.7 was assumed to be equivalent to the temperature measured by a thermocouple measuring lab ambient temperature. This introduced a possible bias that would result from the compressed air entering the choked flow orifices being a different temperature than the stagnant lab air; this bias would be especially pronounced when the engine had been running for a few hours and caused the lab ambient temperature to rise. This source of error was removed by installing a thermocouple in the air system directly upstream of the choked flow orifice. With the new thermocouple in place, the precision uncertainty was found by calculating the CI_{95} of the mean of the time-varying data, while the accuracy uncertainty was specified by the thermocouple manufacturer. The difference between lab and fresh air temperature was seen to be up to 5 K, with the largest errors occurring when the engine had been running for several hours, causing the lab ambient temperature to increase.

5.3.2 Fuel Measurement

Fuel flow rates were measured with a Coriolis mass flow measurement device. The output of the Coriolis meter was either a 4-20 mA analog current signal or a digital signal using the Hart Protocol. Initially, fuel flow data were acquired by sending the current output through a resistor and measuring the voltage across the resistor; this method was used because the lab did not have any DAQ devices capable of direct current measurement. In order to remove the uncertainty involved with this resistor measurement, a Hart Protocol modem was installed in the lab so that the digital output of the Coriolis device could be used. Using the digital output, the precision was found by calculating the CI_{95} of the mean of the time-varying data, while the accuracy uncertainty was specified by the manufacturer.

5.3.3 Engine Speed Measurement

Engine speed is required to convert the air and fuel flow rate measurements into a mass-per-cycle value according to

$$m = \frac{\dot{m} n_c}{N}, \tag{5.9}$$

where n_c is the number of revolutions per power stroke and N is the engine speed in revolutions per second. Engine speed was calculated by counting the encoder revolutions per unit of time, and the precision uncertainty was found by calculating the CI_{95} of the mean of the time varying calculated engine speeds.

5.3.4 Residual Gas Fraction

The residual exhaust mass from the previous cycle is a difficult value to quantify since it is not easy to directly measure. In order to minimize the amount of exhaust residual, and thus reduce its effect on the temperature calculation, the exhaust pressure was set as low as the lab setup allowed, near atmospheric pressure. There are a variety of different

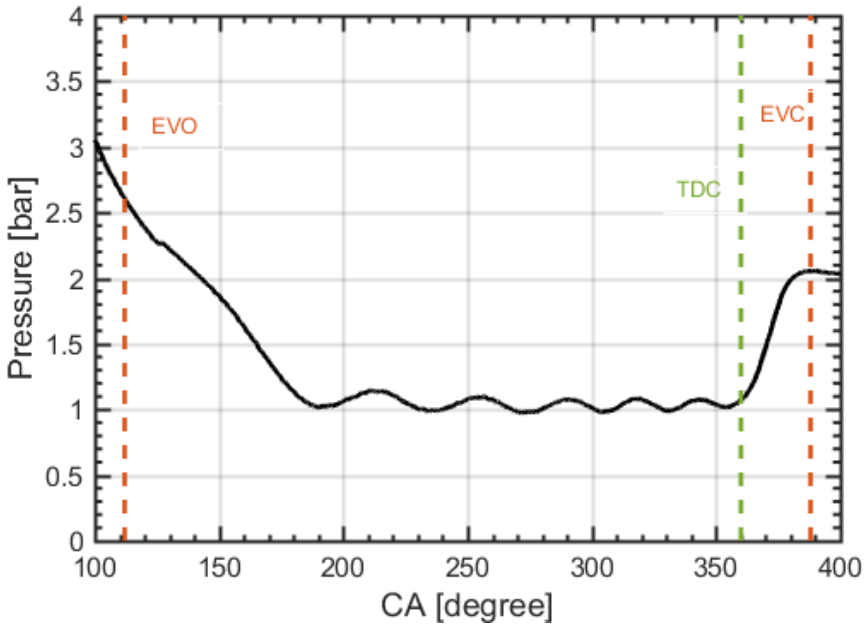

Figure 5.7: In-cylinder pressure during exhaust stroke.

methods that exist in literature to provide an estimate of the residual gas fraction. The method used in this study was a modified Yun and Mirsky method [76], which models the exhaust process as an isentropic expansion,

$$y_{\text{res}} = \frac{V_{\text{TDC}}}{V_{\text{EVO}}} \left(\frac{P_{\text{TDC}}}{P_{\text{EVO}}} \right)^{\frac{1}{\gamma}}. \tag{5.10}$$

The method typically considers an isentropic expansion from EVO to EVC, but was modified to use values at gas exchange TDC instead of EVC upon inspection of the pressure trace during this portion of the engine cycle. As seen in Figure 5.7, there was an increase in cylinder pressure between TDC and EVC when the intake valve opened and intake air entered the cylinder. Using the pressure at EVC caused the exhaust residual fraction to be overestimated. The volume and in-cylinder pressure uncertainties involved with this calculation have been described above. Alternative methods of estimating y_{res}, described in Chapter 2, were briefly investigated, but due to the low magnitudes of y_{res} none were found to have a large effect on the calculated temperature.

5.3.5 Trapping Efficiency

Trapping efficiency was a multiplier on the air and fuel flow rates that accounted for leaks in the intake system and fresh air and fuel short-circuiting through the engine during the valve overlap period. The nominal value of this multiplier was equal to 1, but it was useful to include in the uncertainty propagation analysis in order to evaluate how large of an effect these errors would have on the calculated temperature. The intake system was tested by pressurizing the system and measuring the mass flow rate with a Coriolis device. Because the engine intake valves were closed, any measured flow was air leaking out of the system. Intake pressure was swept and the leakage values were seen to be equivalent to an air flow rate error of less than 1/0.5% at an engine speed of 1000/2000 RPM.

The short circuiting was a bit more difficult to quantify. An experiment was performed with a varying pressure differential across the valves, which would be expected to drive the short circuiting flow; a larger positive difference between intake and exhaust pressure should cause more short circuiting. The engine was motored at 150 kPa intake pressure while exhaust pressure was swept from 120 kPa to 220 kPa and the calculated temperature at IVC was recorded at each point. As seen in Figure 5.8, calculated T_{IVC} was constant within 1 K throughout the sweep, suggesting that short-circuiting was minimal. A GT Power model, previously developed for the lab setup by Dr. Adam Dempsey, was also used to simulate the six main experimental operating conditions and no short-circuiting was seen in the model.

5.4 Gas Constant

The final value that appears in the temperature calculation is the gas constant, which was calculated by

$$R = \frac{R_{Univ}}{MW_{tot}} \tag{5.11}$$

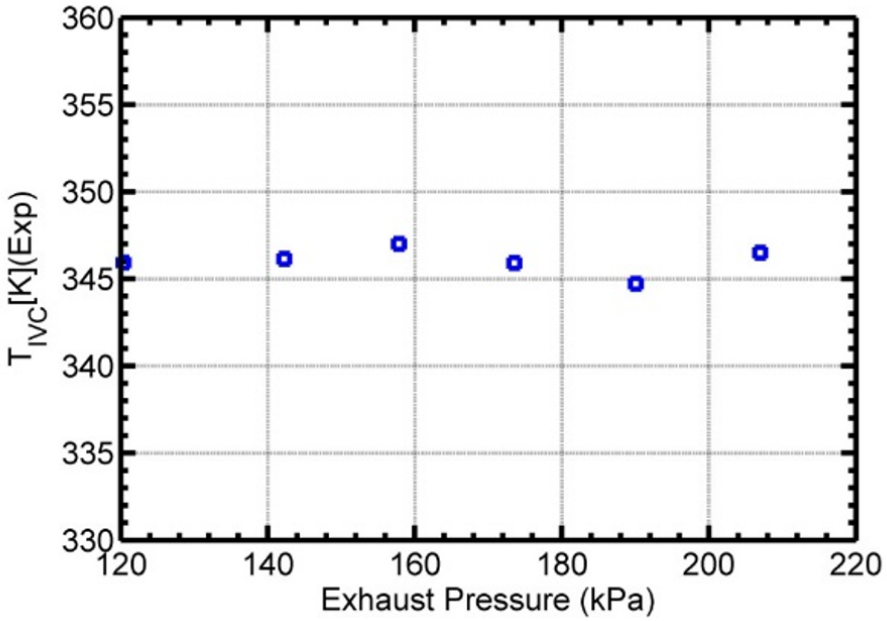

Figure 5.8: Trapped mass temperature at IVC as a function of exhaust pressure.

$$\mathrm{MW}_{tot} = \frac{\dot{m}_{air} + \dot{m}_{fuel} + y_{res}(\dot{m}_{air} + \dot{m}_{fuel})}{\frac{\dot{m}_{air}}{MW_{air}} + \frac{\dot{m}_{fuel}}{MW_{fuel}} + \frac{y_{res}(\dot{m}_{air}+\dot{m}_{fuel})}{MW_{y_{res}}}}. \tag{5.12}$$

Uncertainties of the air and fuel flow rates and the residual mass fraction have already been discussed, so the only additional uncertainty that must be quantified is that of the MW_{yres}, which is calculated from emissions measurements. The precision uncertainty was determined by finding the CI_{95} of the time-varying exhaust emissions data and the accuracy uncertainty comes from the individual emissions analyzers' calibrations. The emissions calibrations were performed using two gases with known concentrations, one with the full scale concentration of the emission species of interest and the other was pure nitrogen. A gas divider that allowed the ratio of the two gases to be varied in discrete steps was used to vary the concentration of the emission species. Negligible differences were seen between MW_{yres} calculated from the emissions measurements and MW_{yres} calculated using the assumption of complete combustion. The MW_{yres} calculated assuming complete combustion was used for experimental tests that did not have emissions data available.

5.5 Uncertainty results

A summary of the uncertainty for the parameters previously discussed can be seen in Table 5.1. The values were divided into three categories: precision refers to random error occurring during the measurements such as due to data acquisition uncertainty, sensor calibration bias refers to accuracy estimation bias of each sensor either calibrated in-house or from manufacturer datasheets, and conceptual bias refers to other sources of bias uncertainty. A conceptual bias example for the residual mass fraction was the uncertainty involved with the assumption that the exhaust followed an isentropic process. Boxes that are empty have negligible uncertainty associated with that category. Precision and accuracy uncertainty for each parameter were calculated and propagated through to a temperature uncertainty by

$$\sigma_{\text{prec,tot}}^2 = \sum \sigma_{\text{prec,n}}^2 \tag{5.13}$$

$$\sigma_{\text{bias,tot}}^2 = \sum \sigma_{\text{bias,n}}^2 \tag{5.14}$$

$$\sigma_{\text{tot}} = \sqrt{\sigma_{\text{prec,tot}}^2 + \sigma_{\text{bias,tot}}^2}, \tag{5.15}$$

where σ_n corresponds to the temperature uncertainty associated with parameter n.

The results for the temperature uncertainty throughout the compression and expansion strokes can be seen for all six operating conditions in Figure 5.9. There was an estimated absolute temperature uncertainty of 7-9 K at IVC that increased to about 20-30 K at TDC. The normalized uncertainty was less than 2% at IVC and less than 3% at TDC. Tables 5.2 and 5.3 show a summary of the calculated IVC temperatures with uncertainty for the main six motored and fired conditions.

One benefit of performing the full uncertainty propagation is that one can quantify the relative contributions of each parameter. The relative contributions were used to provide insight as to which parameters warranted further investigation in order to limit the overall temperature uncertainty. Figure 5.10 shows the uncertainty contributions

Table 5.1: Uncertainty estimates for trapped mass temperature calculation.

	Precision	Sensor Calibration Bias	Conceptual Bias
P_{peg}	$\frac{t(N,95)\sigma}{\sqrt{N_{\text{cyc}}}}$	0.5[%]	0.5[%]
P_{upstream}	$\frac{t(N,95)\sigma}{\sqrt{N_{\text{cyc}}}}$	0.5[%]	
MW_{res}	$\frac{t(N,95)\sigma}{\sqrt{N_{\text{cyc}}}}$	1[%]	
$P_{\text{cyl,volt}}$	$\frac{t(N,95)\sigma}{\sqrt{N_{\text{cyc}}}}$	0.11[%]	
T_{upstream}	$\frac{t(N,95)\sigma}{\sqrt{N_{\text{cyc}}}}$	2.2[K]	
Fuel Flow	$\frac{t(N,95)\sigma}{\sqrt{N_{\text{cyc}}}}$	0.5[%]	
RPM	$\frac{t(N,95)\sigma}{\sqrt{N_{\text{cyc}}}}$		
Cd_{lin}		1[%]	
Cd_{ofst}		0.0015[kg/min]	
$\text{P}_{\text{cyl,slope}}$		0.1[%]	
η_{trap}			1[%]
y_{res}			20[%]
V_{TDC}			2[%]
CA		0.125[°]	0.5[°]
γ			5[%]

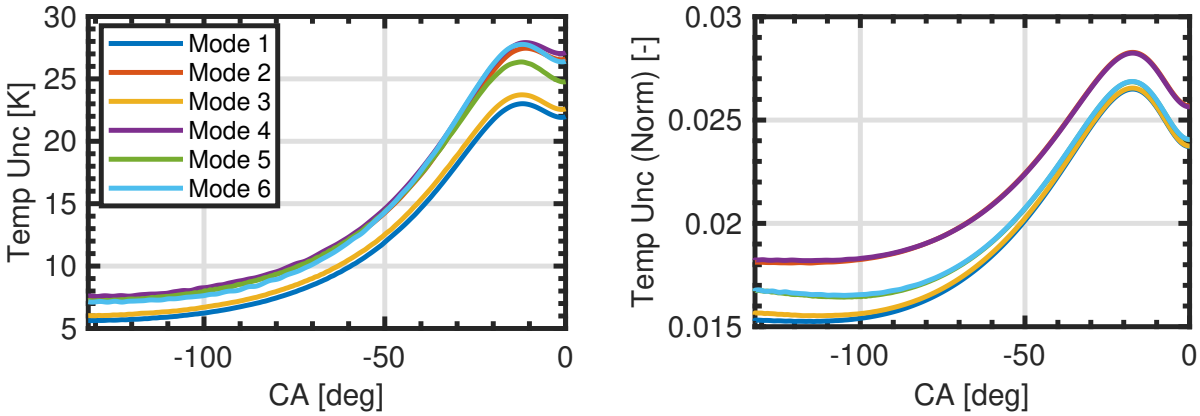

(a) (b)

Figure 5.9: Total trapped mass temperature uncertainty as a function of crank angle.

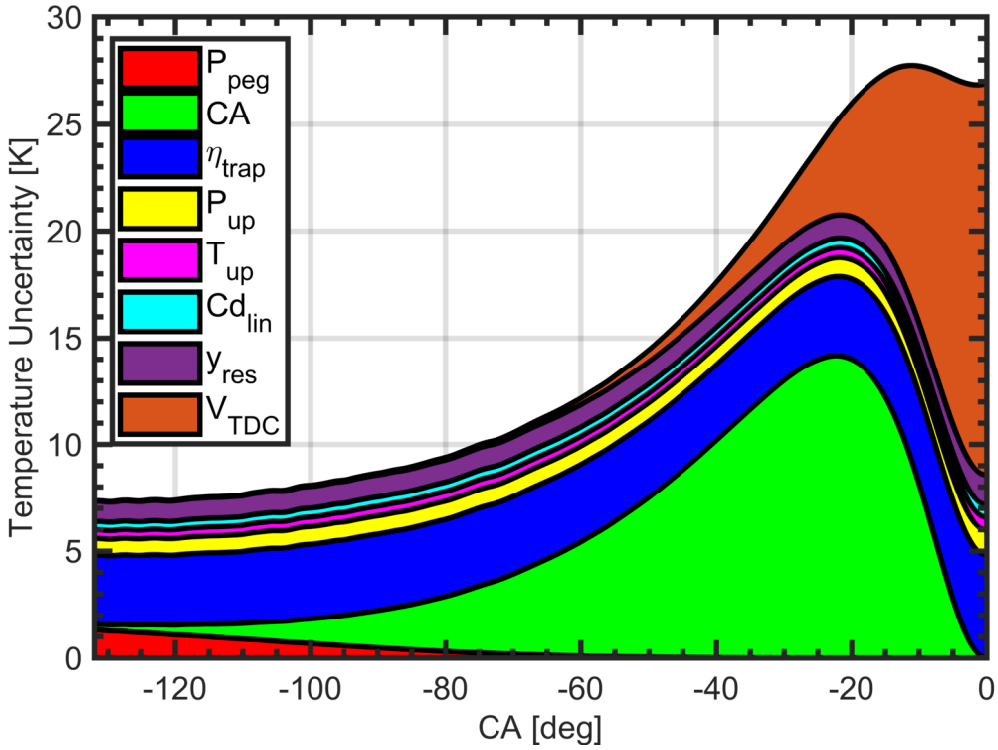

Figure 5.10: Temperature uncertainty contributions as a function of crank angle.

of each parameter as a function of crank angle throughout the compression stroke for operating condition 1. Only parameters that had a relative contribution >2% were included in the graph.

It is interesting to note how the relative contributions changed from IVC to TDC. For example, at IVC the trapping efficiency and pegging pressure had the largest contributions, whereas at TDC the TDC volume dominated the temperature uncertainty. The trapping efficiency uncertainty resulted in a constant trapped mass uncertainty so its relative contribution stayed almost constant, whereas pegging pressure was a constant pressure uncertainty that only had a significant effect at low in-cylinder pressures, and TDC volume was a constant volume uncertainty that only had a large effect at low in-cylinder volumes. This graph is useful to guide future work for improving the in-cylinder temperature estimation accuracy. Improvements made to reduce the uncertainty in trapping efficiency, pegging pressure, residual mass fraction, and the upstream air pressure

Table 5.2: Temperature estimation at IVC with uncertainties for motored conditions.

Speed [RPM]	1000	2000	1000	2000	1000	2000
Intake Pressure [bar]	2.25		1.5		0.90	
Intake Temperature [K]	383	383	423	423	423	423
Trapped Mass [K]	386±7	406±8	404±8	423±8	409±9	419±9

Table 5.3: Temperature estimation at IVC with uncertainties for fired conditions.

Speed [RPM]	1000	2000	1000	2000	1000	2000
Intake Pressure [bar]	2.25		1.5		0.90	
Intake Temperature [K]	383	383	423	423	463	453
Trapped Mass [K]	399±7	427±8	425±8	446±8	438±9	455±9

will reduce temperature uncertainty at IVC; improvements made to reduce the uncertainty in TDC volume, trapping efficiency, residual mass fraction, and the upstream air pressure will reduce temperature uncertainty at TDC.

5.6 Conclusions

A rigorous analysis was performed on the uncertainty in trapped mass temperature. There were 14 parameters involved in the trapped mass calculation, all of which individually contributed to the total temperature uncertainty. The total uncertainty at IVC was ±7-9 K, or about 2%. Trapping efficiency, residual gas fraction, and pegging pressure were the main contributors to the temperature uncertainty at IVC. Temperature is a critical factor in chemical kinetics simulations; in an effort to reduce the uncertainty and obtain additional temperature estimations, two other temperature measurement methods were utilized which will be discussed in the following chapters.

Chapter 6

Spectroscopy Temperature Measurements

Water absorption spectroscopy is a non-intrusive method that can be used to measure in-cylinder temperature. A MEMS-VCSEL (Thorlabs, SL1310V1-SP4) laser was used as a swept light source over the wavenumber range from 7300 to 7600 cm^{-1} at a 10 kHz repetition rate. The laser wavelength was measured with a characterized athermal etalon (Primanex PETL1-211T21200). Data were acquired at 200 MHz using an independent DAQ system (Gage CSE1642). By applying the Beer-Lambert law [77] to the recorded data, the water absorbance as a function of frequency was calculated on a crank angle basis. The 10 kHz rate gave a crank angle resolution of 0.6/1.2 degrees at 1000/2000 RPM.

6.1 Experimental Setup

An engine probe that could be installed in the direct-injector bore was designed by Dr. Scott Melin and part of the work for his dissertation [78]. A custom piston with a polished surface finish was installed in the engine to provide a means to reflect the light back to the probe. A model of the probe and a picture of the piston can be seen in

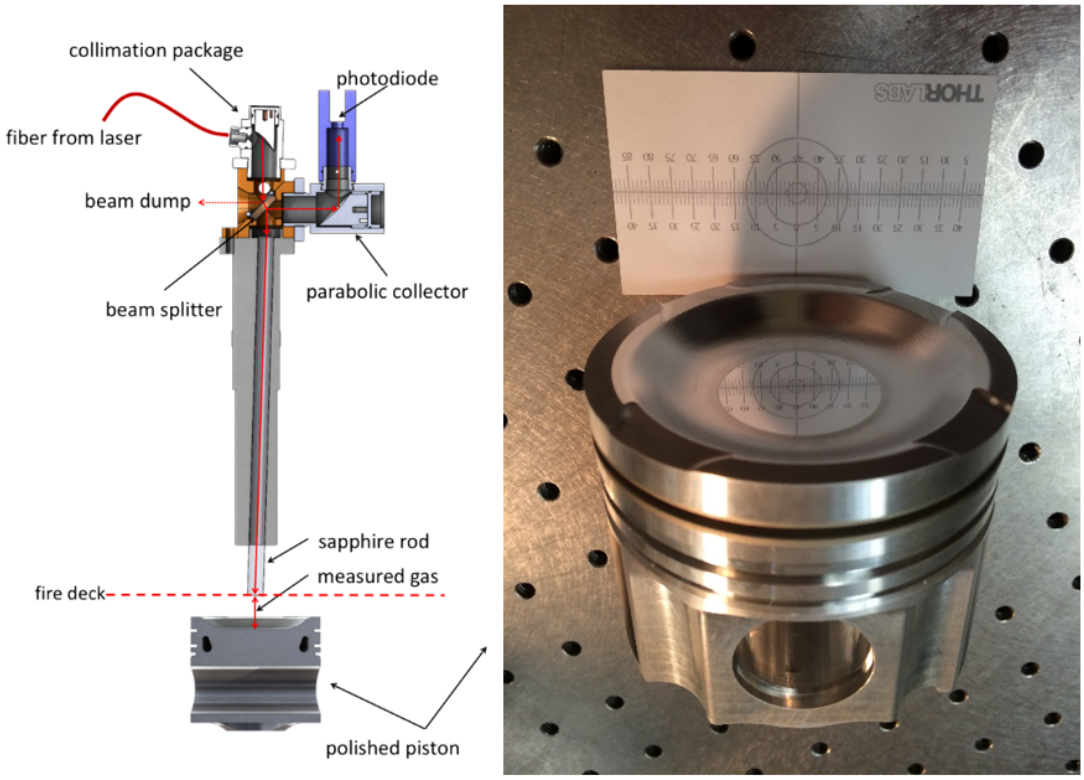

Figure 6.1: Model of the engine probe (left), taken from [78] and custom piston (right).

Figure 6.1. The absorbance signal strength was dependent on the concentration of water in the signal path; a water seeder was used to add water to the dry building air in order to achieve intake water mole fractions between 1.5 and 3% for all operating conditions. The water mole fraction was verified with an hygrometer (GE OptiSonde 1111H). A detailed description of the optical setup can be found in Chapter 7 of [78], where a similar study was performed on an optical engine. All of the spectroscopy temperature experiments were performed in cooperation with Dr. Scott Melin; Dr. Melin's focus was the spectroscopy data acquisition, while the author's focus was engine operation and engine data acquisition.

The operating conditions were chosen to cover a wide range of intake temperatures in addition to the intake temperatures used for operating conditions 1-4 during the fuel substitution testing. Motoring conditions were run with intake temperatures varying

Table 6.1: Motored operating conditions for spectroscopic temperature measurements.

Speed [RPM]	1000		2000	
Intake Pressure [bar]	1.47	2.2	1.45	220
Intake Temperature [K]	323-423	368-383	323-423	368-383

Table 6.2: Fired operating conditions for spectroscopic temperature measurements.

Speed [RPM]	1000		2000	
Intake Pressure [bar]	1.47	2.2	1.45	2.2
Intake Temperature [K]	393-423	368-383	393-423	368-383

from 323 K to 423 K, while firing conditions with methane/propane mixtures were run with intake temperatures varying from 368 K to 423 K. Firing conditions could not be run at lower intake temperatures due to fuel reactivity limits. A full summary of motoring and firing conditions can be seen in Tables 6.1 and 6.2. The pressure was reduced from 1.5 and 1.47 to 1.47 and 1.45 bar, respectively, at higher intake temperatures to match TDC pressures from previous fuel substitution testing. This intake pressure reduction was required due to a slight increase in compression ratio with the custom piston.

6.2 Data Processing

During testing, the DAQ system recorded the incident, I_0, and transmitted, I, light, which were used to calculate absorbance, A, as a function of frequency according to

$$A = -\ln\left(\frac{I}{I_0}\right). \tag{6.1}$$

A reference clock signal set to 20 kHz was used to synchronize laser measurements and engine crank angle. The result was a dataset of absorbance vs. wavenumber at each crank angle location, as seen in Figure 6.2 for -132 (IVC) and -60 CAD, taken at 2000 RPM, 2.21 bar intake pressure, and 393 K intake temperature.

While the main focus of this work was on temperature estimation at IVC conditions, -60 CAD was also investigated to ensure that the processing method also worked at

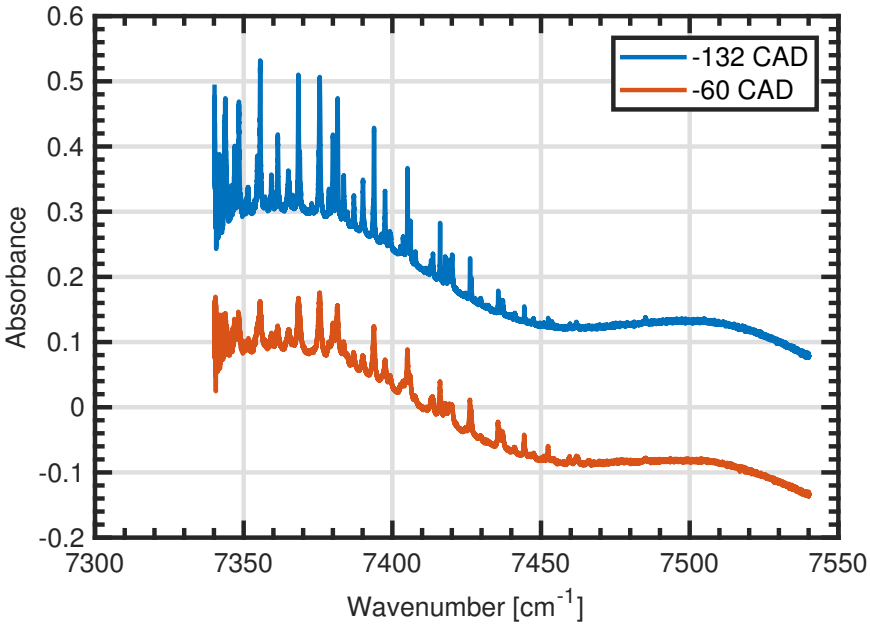

Figure 6.2: Raw absorbance vs. wavenumber at -132 and -60 CAD.

elevated temperatures and pressures. The main difference between the two datasets other than a smoothing of the peaks at -60 CAD due to pressure broadening effects, was a large offset that exists between the two datasets. The offset was a result of the spectral baseline artifacts and illustrates the need for a robust method to remove the baseline; this will be discussed in more detail in Section 6.2.3. The absorbance data were processed to reduce noise and remove the baseline artifacts, and compared to a simulation database; BT2 [29], HITEMP [30], and HITRAN [31] were all utilized as databases to generate simulated absorbance datasets at fixed temperature and pressure broadening conditions. The process of using the databases to generate absorbance datasets is described in more detail in [78]. By finding the simulation condition that was the closest match to the experimental data, the in-cylinder temperature was estimated.

A data processor that was originally created in Labview by Dr. Scott Melin [78], based on a band-shape processing method, was re-created in Matlab in the current work and used to calculate temperature from the absorbance data. Band-shape refers to the method of analyzing the absorbance data over a wide wavenumber range as opposed

to looking at a few specific wavenumber locations. The processing method is divided into five main steps: (1) import the raw data, (2) apply a de-noising filter, (3) compute and subtract the baseline artifact, (4) apply a smoothing filter, and (5) calculate the temperature fit. Each step in the process involved a number of selectable parameters that could affect the final processed temperature. Eight main parameters were identified as critical and investigated to find their optimal values and calculate uncertainty as detailed in the following sections.

6.2.1 Importing Raw Data

The first step when processing the absorbance data was to import the raw absorbance data, A_{raw}, into the processing program. Wavelength was assigned to the absorbance data by matching characterized wavenumber locations to peaks of the etalon signal, as seen in Figure 6.3. The etalon signal was calibrated using the wavelength axis from an external cavity diode laser. There were two tunable parameters involved in this process, $\omega_{1,raw}$, the starting wavenumber, and $\Delta\omega_{raw}$, the wavelength shift. The starting wavenumber of the data is, ideally, the starting wavenumber of the frequency scan. Absorbance data were available starting at 7340 cm^{-1}, but Figure 6.4 shows that there was significant noise at the low-wavenumber end of the spectrum. Figure 6.5 shows the difference between the raw and filtered data as well as I_0, an indication of the laser power. It is seen that the high noise levels correlated with low laser power. There is a large reduction in the noise level by 7344 cm^{-1}. Therefore, 7345 cm^{-1} was chosen as the starting location to avoid the high-noise portion of the data. As there was little absorbance information at the high-wavenumber portion of the spectrum, the ending wavenumber location was not a critical parameter and was set to 7550 cm^{-1} for all cases. Figure 6.6 shows an example of the percent change in processed temperature as $\omega_{1,raw}$ was changed from its nominal value; over the range of values swept there was $<0.1\%$ change from the nominal temperature.

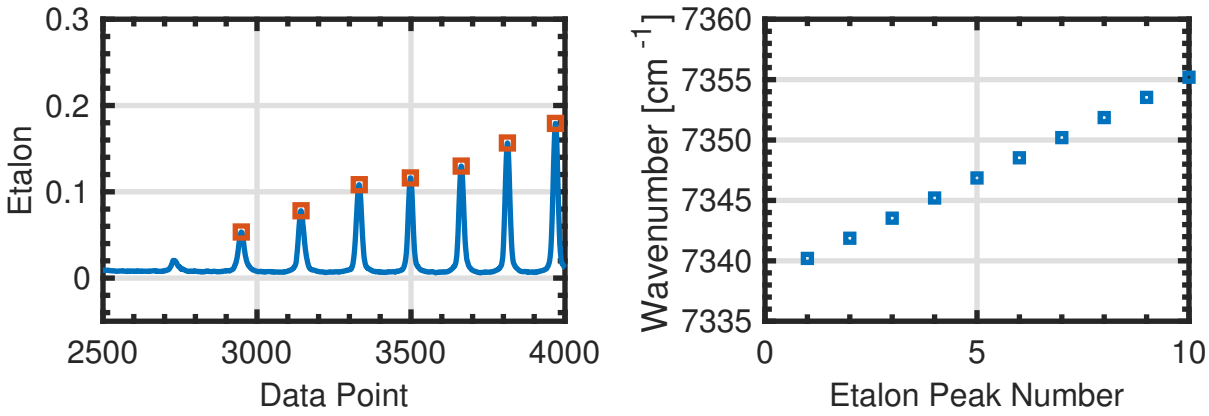

(a) (b)

Figure 6.3: Etalon vs. data point (left) and characterized wavenumber vs. etalon peak (right).

It is interesting to note that small discontinuities occurred for the -132 CAD dataset near 7342, 7344, and 7348 cm^{-1}. Referring to Figure 6.4, these regions occurred when $\omega_{1,raw}$ was near a peak in the absorbance data. Edge effects from filtering will occur when $\omega_{1,raw}$ is too close to a peak; therefore, the value of $\omega_{1,raw}$ should be chosen in a relatively flat region of the absorbance data. This effect was less severe for the -60 CAD case because the peak heights were smaller due to pressure broadening effects.

The wavenumber shift applied to the experimental data, $\Delta\omega_{raw}$, was intended to make up for a global wavenumber vs. absorbance mismatch between the experimental data and the simulation database. The optimal value for this parameter was calculated by computing the cross-correlation between the experimental data and simulated dataset according to

$$CC_{\Delta w_{raw}} = \sum_{i=1}^{N} A_{exp}(\omega_i) A_{sim}(\omega_i + \Delta\omega_{raw}), \tag{6.2}$$

where A_{exp} is the experimental absorbance and A_{sim} is the simulated absorbance. The value of $\Delta\omega_{raw}$ that resulted in the maximum cross-correlation value was taken as the optimal wavenumber shift. Figure 6.7 shows the result of cross correlation as a function of $\Delta\omega_{raw}$; the maximum value occurred when $\Delta\omega_{raw}$= -0.03 cm^{-1}. Figure 6.8 shows

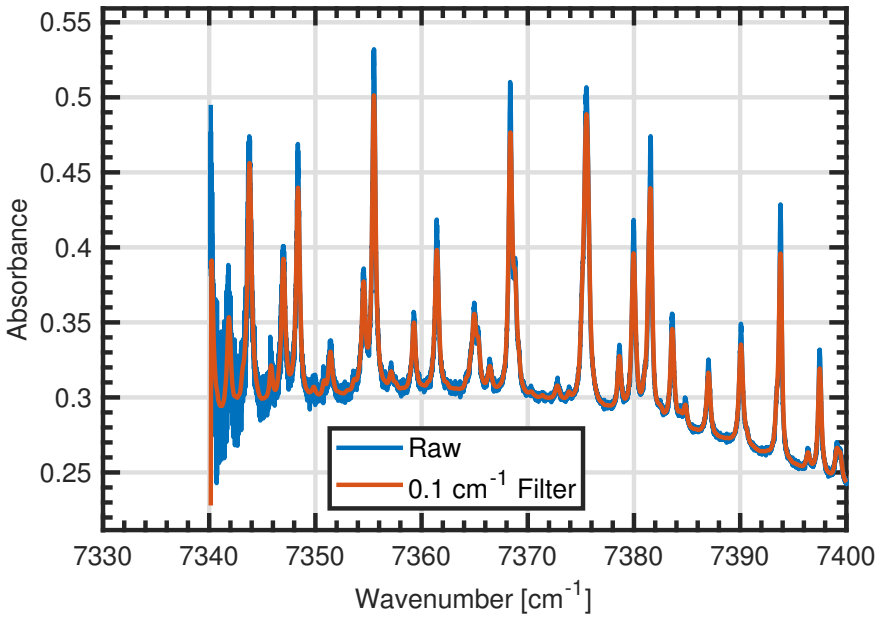

Figure 6.4: Raw and filtered absorbance for a representative data set near IVC.

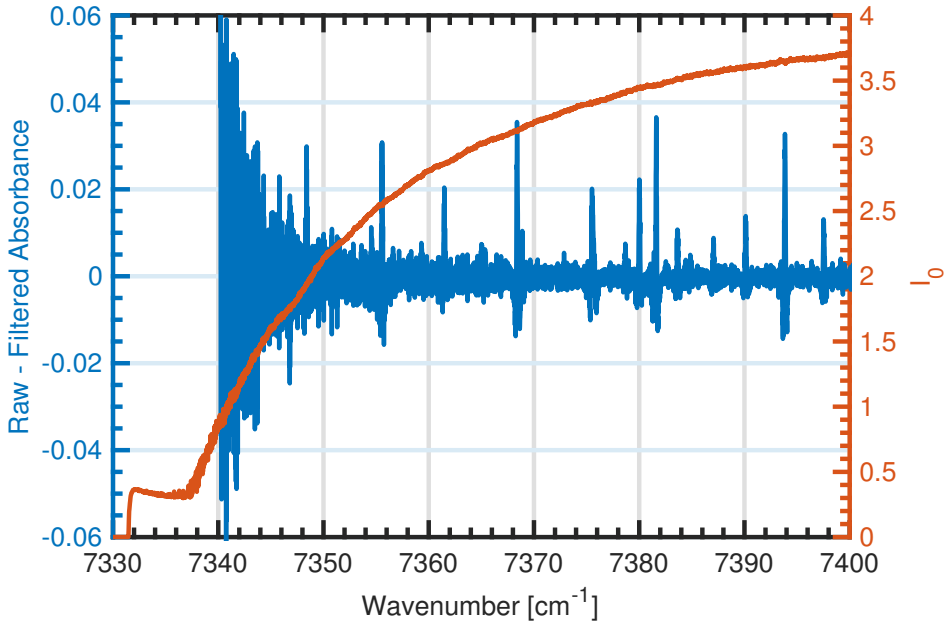

Figure 6.5: Difference between raw and filtered absorbance for a representative data set near IVC along with I_0, an indication of laser power.

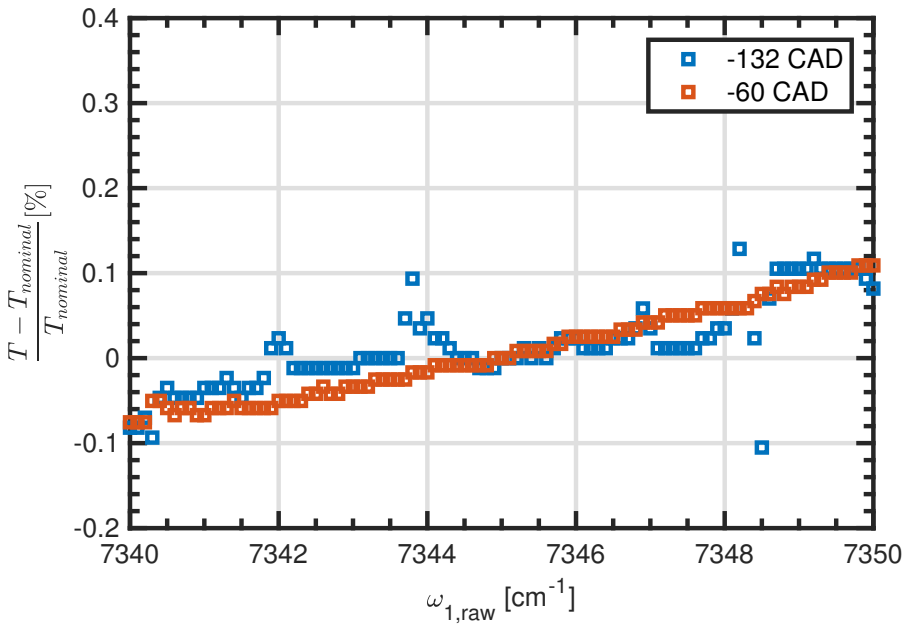

Figure 6.6: Sensitivity of processed temperature to starting wavenumber location, $\omega_{1,raw}$, for the raw absorbance data.

a zoomed in portion of the raw and shifted experimental absorbance along with the simulated absorbance. After the wavenumber shift was applied, the experimental and simulated absorbance peaks were well aligned. Figure 6.9 shows an example of the change in processed temperature as $\Delta\omega_{raw}$ was changed from its nominal value; there existed a moderate sensitivity to this wavenumber shift that was consistent for both datasets, indicating that care must be taken to align the experimental and simulated datasets.

6.2.2 De-noising Filter

The second step in the processing algorithm was to apply a filter with width $\Delta\omega_{DN}$ to decrease the noise on the signal; this step was necessary because noise in the dataset will affect the baseline removal process. The goal of the filter was to decrease noise while minimally affecting the absorbance data. The filtering was applied using a Gaussian convolution filter with a full-width half-max (FWHM) equal to $\Delta\omega_{DN}$. Figure 6.10 shows the results for three different filter widths with offsets applied for clarity, and the difference

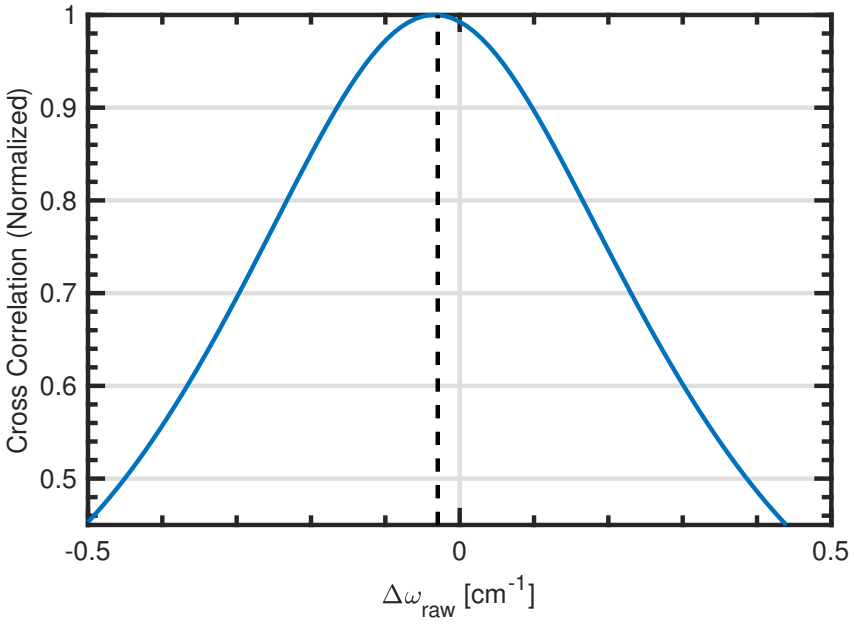

Figure 6.7: Cross correlation (normalized) as a function of wavenumber shift.

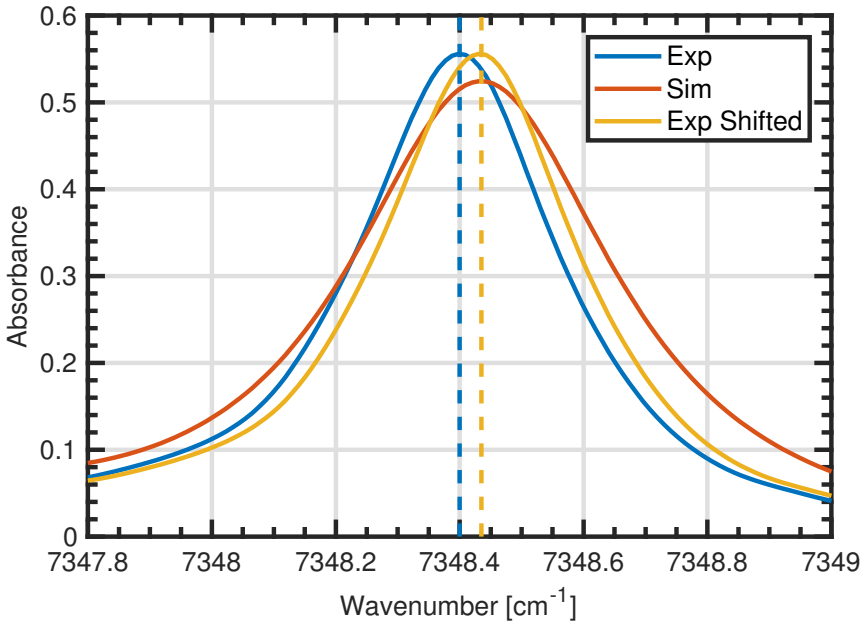

Figure 6.8: Experimental data and simulation data with and without wavenumber shift applied. Data are zoomed to show a single absorption feature.

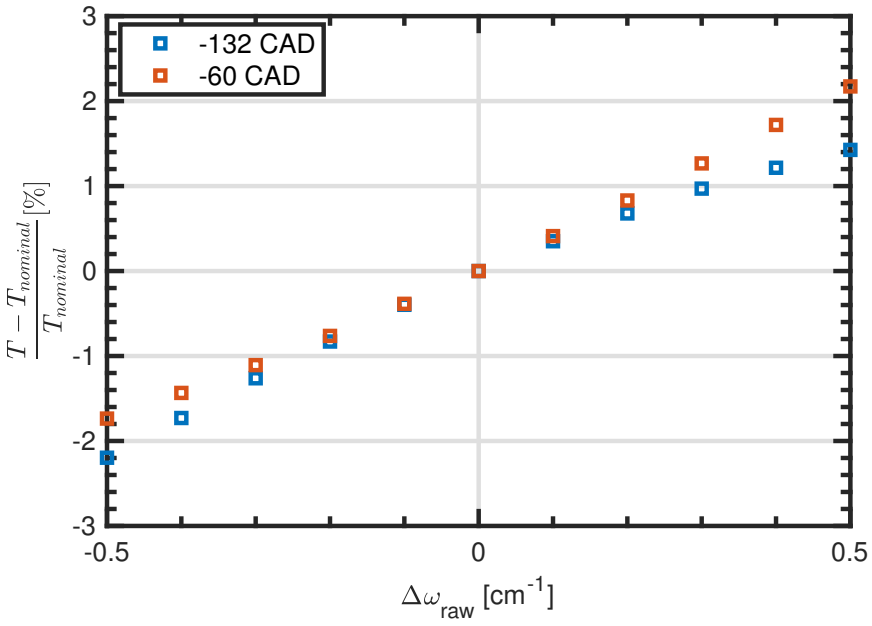

Figure 6.9: Sensitivity of processed temperature to raw wavenumber shift, $\Delta\omega_{raw}$.

between the filtered and raw absorbance values can be seen in Figure 6.11. It can be seen from the flat portions of absorbance data that too small of a filter did not adequately remove the measurement noise. Too large of a filter, however, affected the absorbance peak heights. A filter width of 0.1 cm^{-1} was chosen for these experiments as a compromise between adequately removing noise but not overly attenuating the absorbance peaks. Figure 6.12 shows an example of the sensitivity of the processed temperature to the value chosen for $\Delta\omega_{DN}$. There was a relatively large temperature change associated with overly small filter values, and a general downward trend of processed temperature as $\Delta\omega_{DN}$ increased, but the sensitivity was relatively low near the nominal value of 0.1 cm^{-1}.

6.2.3 Baseline Removal

The experimental absorbance dataset will always have a baseline associated with it due to wavelength-dependent, non-gas-phase absorption throughout the pathlength and on surfaces. It is assumed that the baseline is well behaved, meaning that it does not

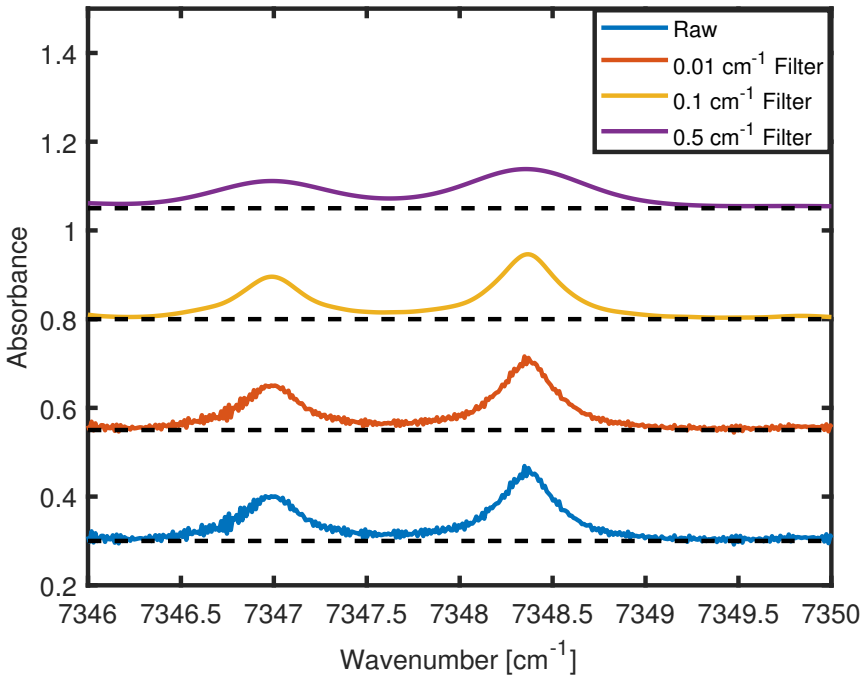

Figure 6.10: Raw and filtered absorbance data for several filter widths, offset for clarity.

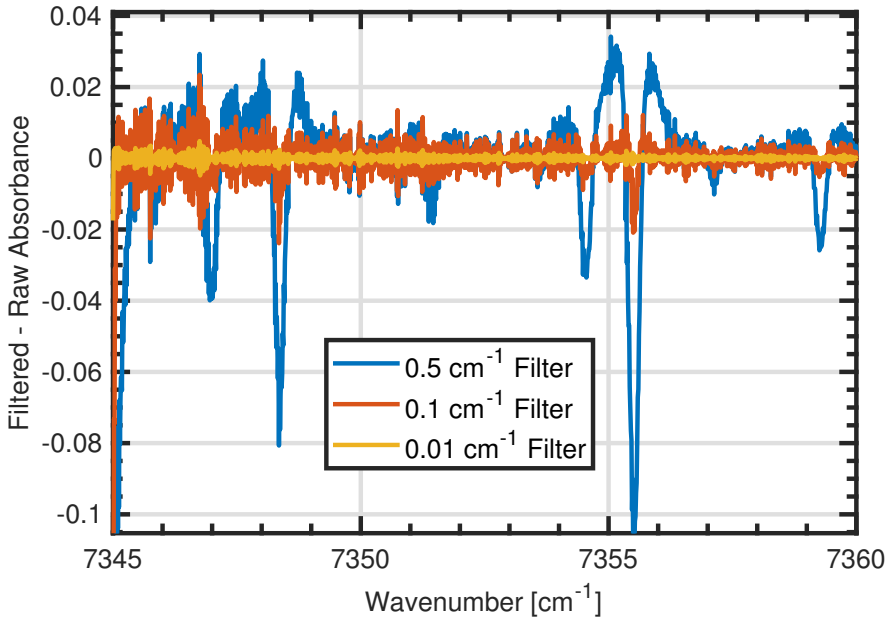

Figure 6.11: Difference between raw and filtered absorbance data (right) for several filter widths.

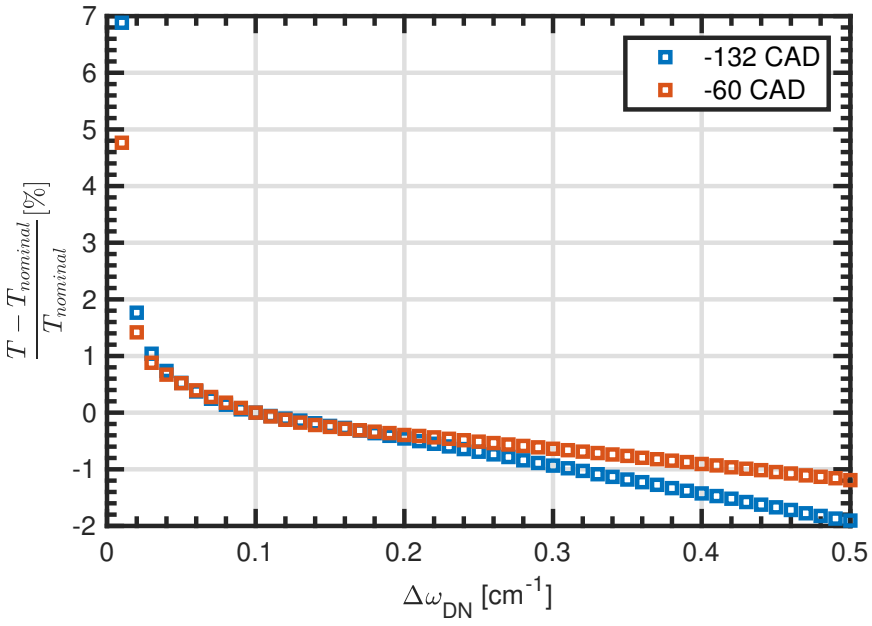

Figure 6.12: Sensitivity of processed temperature to de-noising filter width, $\Delta\omega_{DN}$.

contain high frequency fluctuations. This assumption allows the baseline to be estimated through an iterative filtering procedure. First the raw data were filtered with a 2nd order Butterworth filter having a width $\Delta\omega_{base}$. At each wavenumber location, if the raw absorbance was greater than the filtered absorbance the baseline was set to the filtered value, but if the raw absorbance was less than the filtered absorbance the baseline was set to the raw value. The first iteration of this process is shown in Figure 6.13. The process was then repeated N_{iter} times, with each iteration using the baseline from the previous iteration as the raw data. In order to cancel out any non-baseline signal removal related changes to the absorbance data by the iterative filtering process, the process was applied to both the experimental and simulated datasets. The baseline evolution as the number of iterations increased is shown in Figure 6.14. At N_{iter}=10, the baseline contained high frequency content from individual absorbance peaks; this will cause issues if the experimental and simulation datasets have slightly different pressure broadening values or peak wavenumber locations. At an extremely high number of filter iterations, for example the N_{iter}=10000 case shown in Figure 6.14, the calculated baseline appears

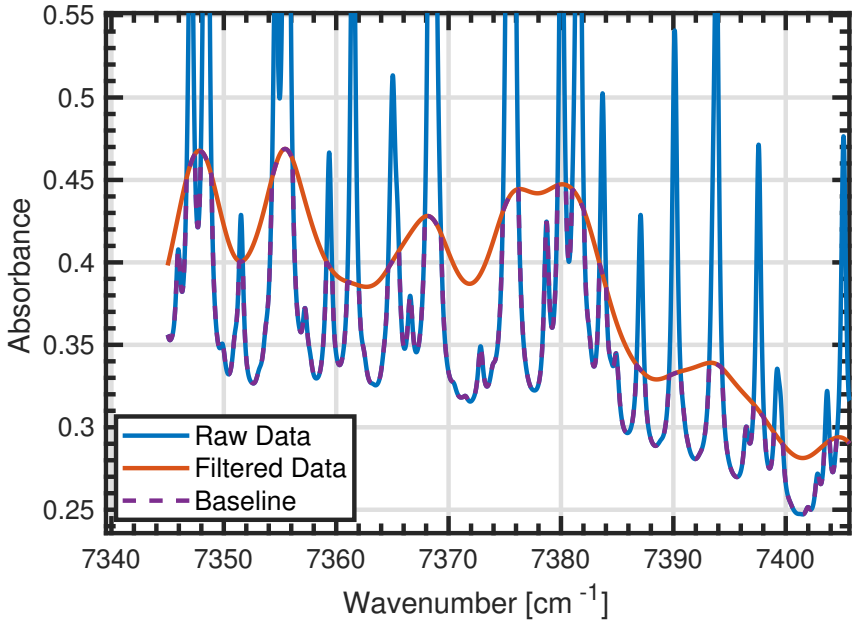

Figure 6.13: 1st iteration of iterative baseline filtering process.

over-smoothed and not representative of the actual baseline for the absorbance data. Therefore, efforts were made to find a metric that could be used to identify the optimal number of filter iterations.

An important note is that N_{iter} and $\Delta\omega_{base}$ must both be analyzed together as they have an interaction effect on the processed temperature. A two-dimensional sweep of N_{iter} and $\Delta\omega_{base}$ was performed with all other parameters kept at their nominal values. Contour plots of the resultant temperature and mean squared error (MSE) between the experimental and simulation datasets are shown in Figures 6.15 and 6.16; a wide spread of temperatures can be seen with sharp gradients in several locations, indicating the importance of the proper selection of these parameter values. The MSE contour plot indicates that the best match between the experimental and simulated data occurred generally at values of $\Delta\omega_{base}$ below 10 cm^{-1} and was relatively independent of N_{iter}, except that lower values of N_{iter} resulted in lower MSE as $\Delta\omega_{base}$ increases. Figures 6.17 and 6.18 show the contour plots zoomed-in on the low MSE region. It is seen that the temperature was relatively stable over the entire region of parameter pairs where the

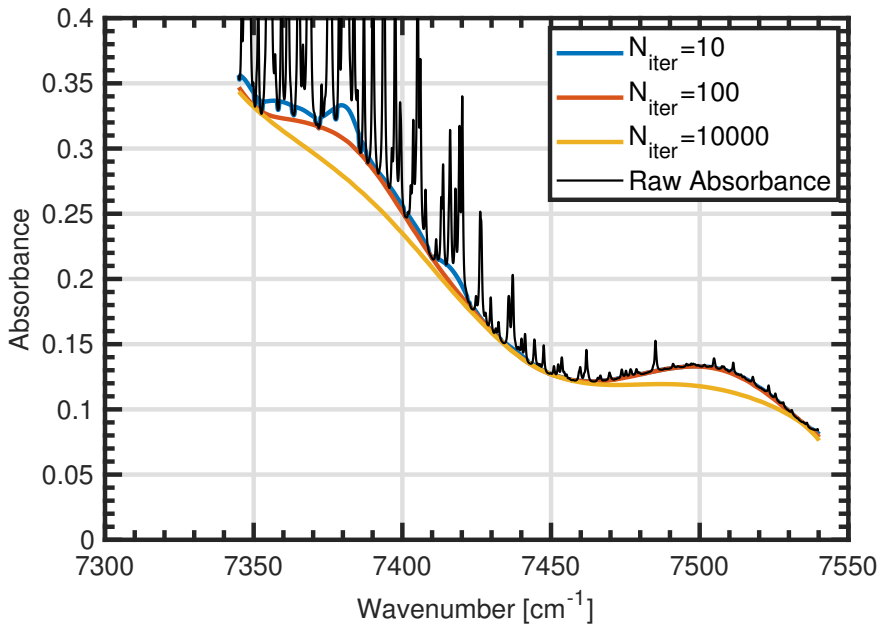

Figure 6.14: Baseline after 10, 100, and 10000 iterations.

lower MSE values occurred; nominal values of 30 filter iteration and a filter width of 9 cm^{-1} were chosen due to their proximity to the minimum MSE region. Figures 6.19 and 6.20 show similar zoomed in contour plots for the -60 CAD dataset. Similar trends were seen, although the minimum MSE region occurred at slightly lower values for $\Delta\omega_{base}$ and higher values for N_{iter}; due to the small sensitivity of temperature around these regions and the focus of the current work on IVC conditions, the parameters chosen for the -132 CAD dataset were used for all of the data processing. It is noted that the same investigation should be repeated at elevated temperatures and pressures beyond -60 CAD to ensure that the baseline filter parameters show similar performance.

An important note is that while this metric will find the number of iterations and filter width region near which the experimental dataset matched closest with a simulation dataset, it did not guarantee that the result was the most accurate baseline or that the processed temperature was the 'correct' value. Future work could involve more investigation into this baseline fitting procedure.

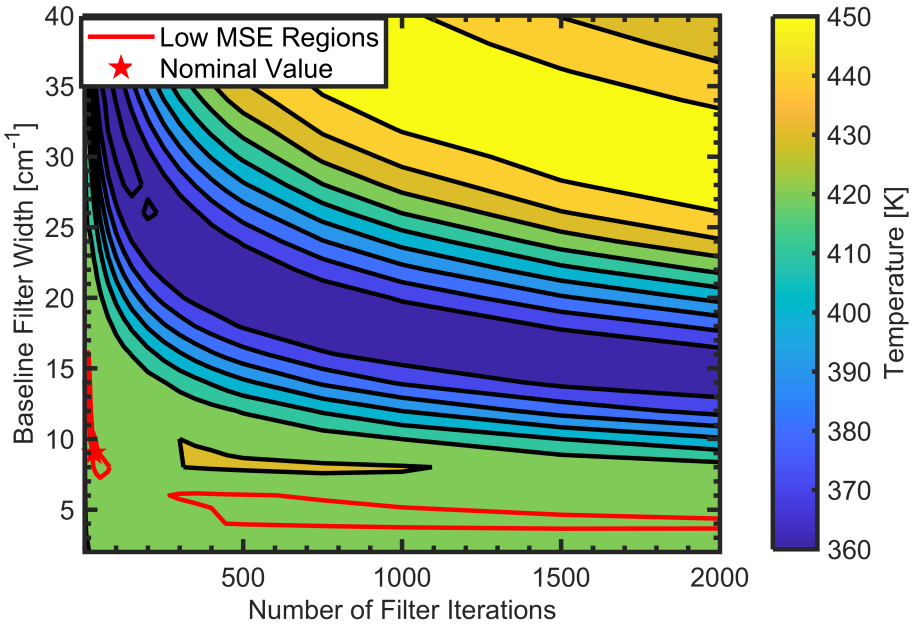

Figure 6.15: Processed temperature as a function of filter width and iterations at -132 CAD.

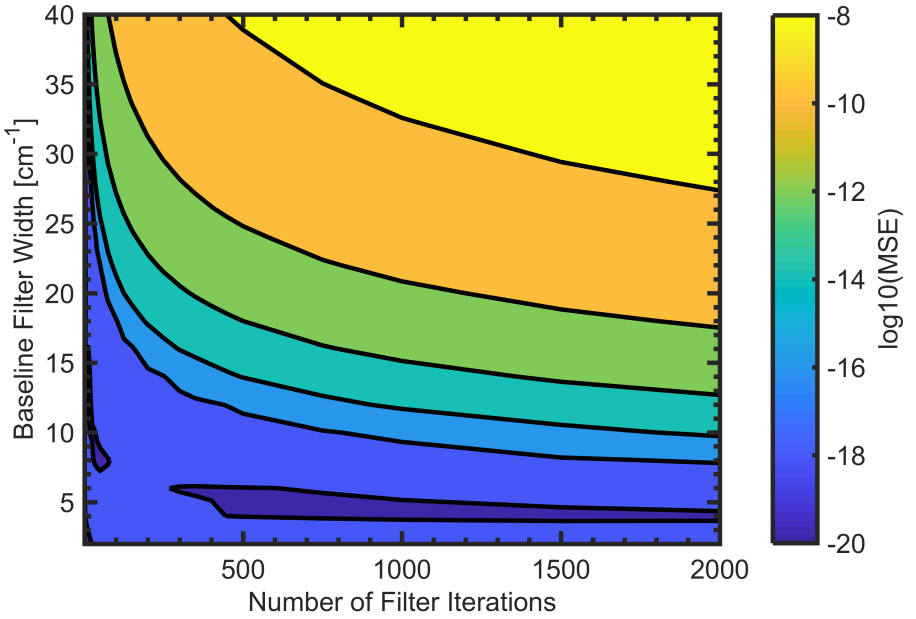

Figure 6.16: MSE as a function of filter width and iterations at -132 CAD.

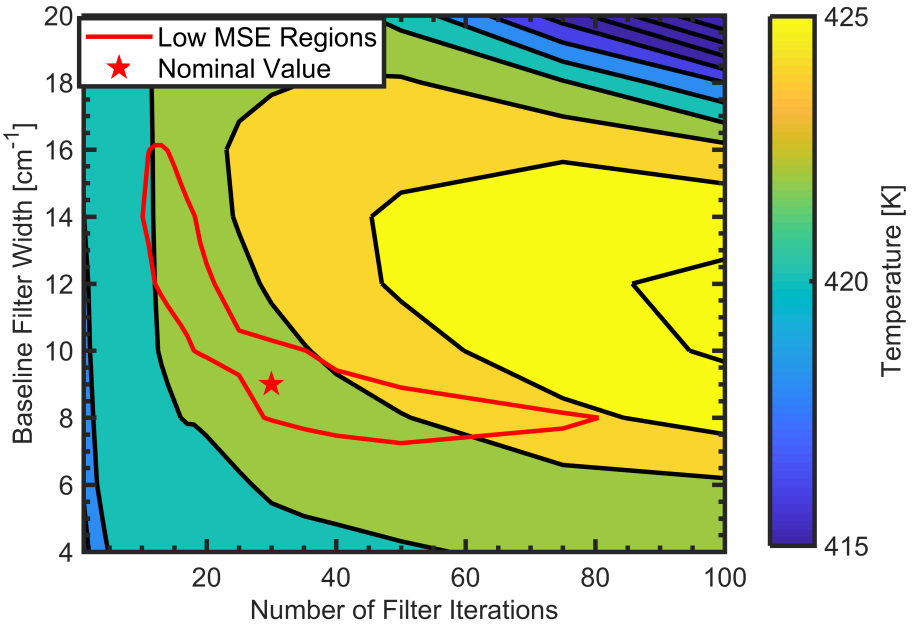

Figure 6.17: Processed temperature as a function of filter width and iterations at -132 CAD, zoomed in.

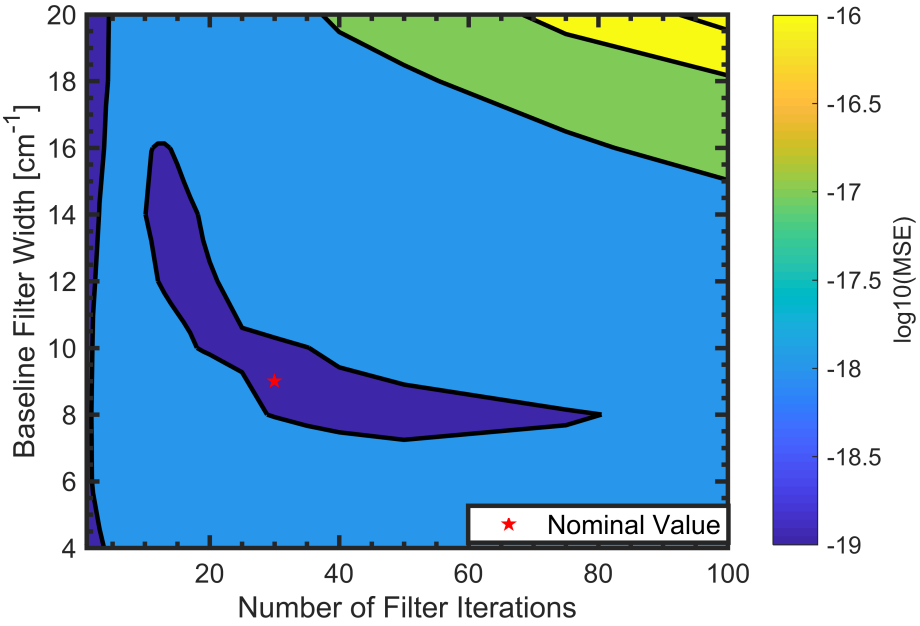

Figure 6.18: MSE as a function of filter width and iterations at -132 CAD, zoomed in.

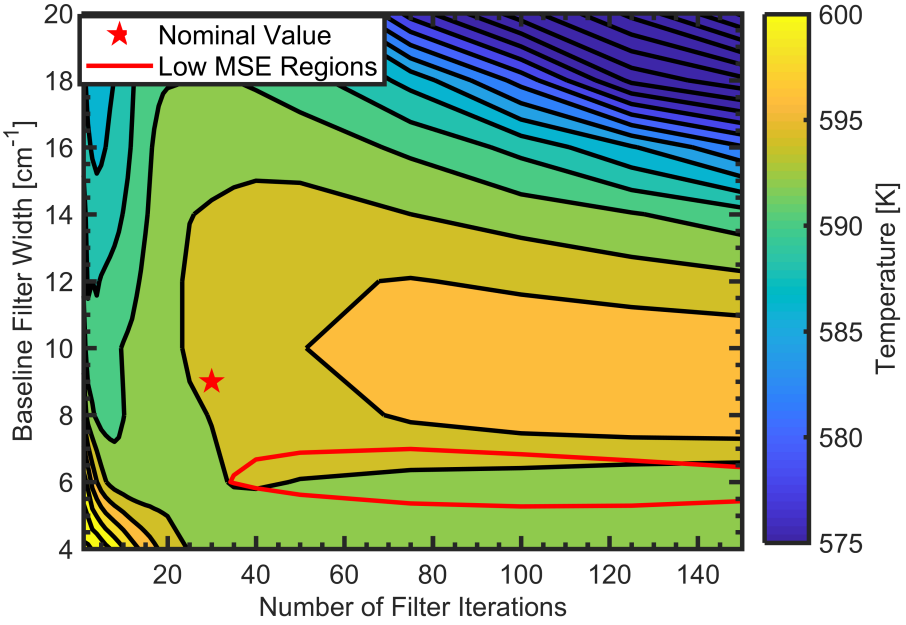

Figure 6.19: Processed temperature as a function of filter width and iterations at -60 CAD.

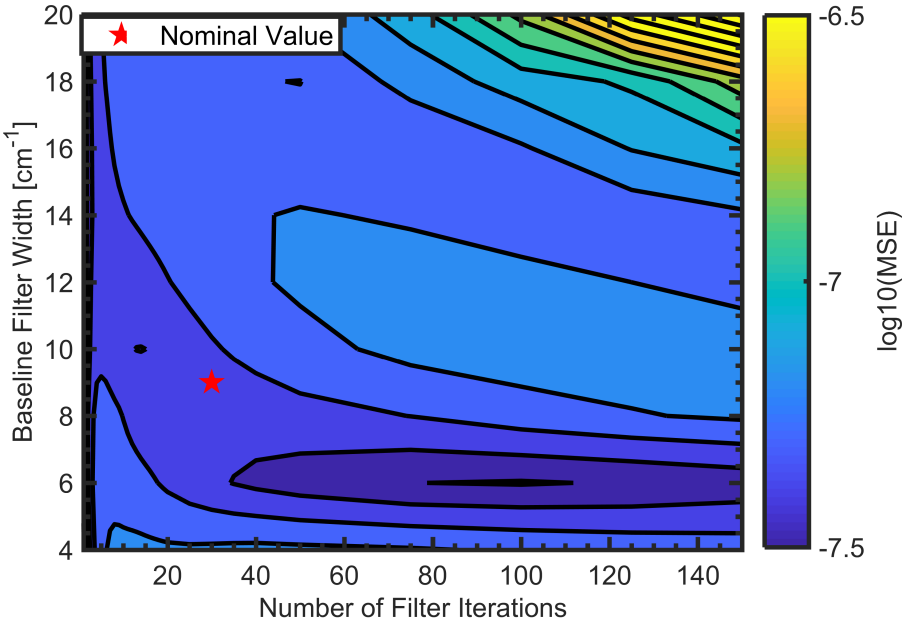

Figure 6.20: MSE as a function of filter width and iterations at -60 CAD.

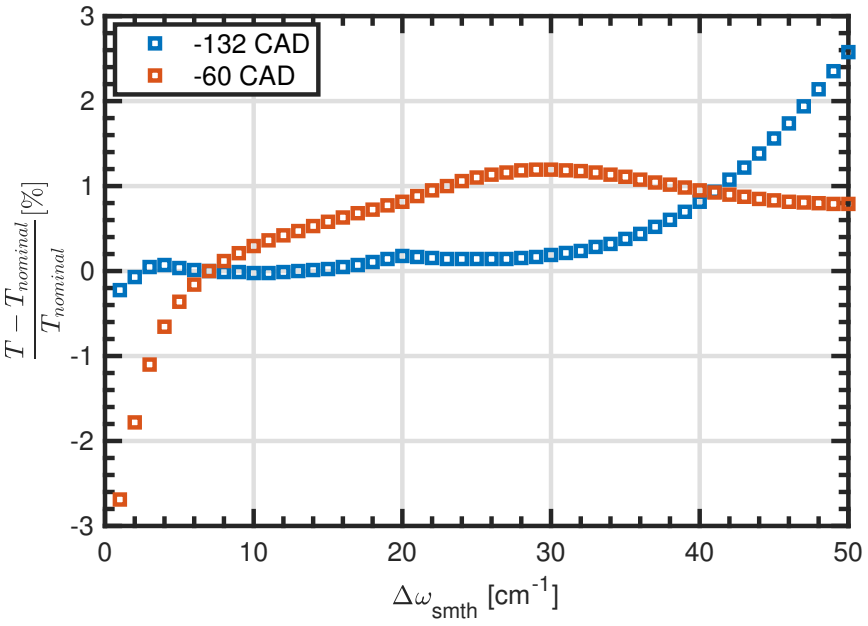

Figure 6.21: Final processed temperature as a function of smoothing filter width.

6.2.4 Smoothing Filter

Once the experimental baseline was removed, the experimental data were directly compared to the simulation database. A Gaussian smoothing filter with a FWHM of $\Delta\omega_{smth}$ was applied to both the experimental and simulation datasets in order to reduce the effects of database errors in linecenter frequency and collisional broadening coefficients. Figure 6.21 shows the final temperature solution as a function of $\Delta\omega_{smth}$. At the lowest values of filter width, small errors in the experimental data and simulated spectrum result in large differences in the calculated temperature. Once the filter width was greater than about 5 cm^{-1} there was a relatively small change in temperature, about 0.2%, for the -132 CAD dataset as the width continued to increase until $\Delta\omega_{smth}$ reached values of 30 cm^{-1}; further increases in $\Delta\omega_{smth}$ above 30 cm^{-1} resulted in a rapid divergence of the temperature. A filter value of 6.5 cm^{-1} was chosen for these experiments to avoid the high sensitivity region at low pressure conditions; for the -60 CAD dataset it appeared that a slightly larger value should be used.

In addition to the smoothing filter width, the start, $\omega_{1,smth}$, and end, $\omega_{2,smth}$, wave-

lengths where the experimental and simulation data are compared must be chosen. As seen in Figure 6.22, the majority of the absorbance information occurred in the wavenumber range from 7350-7450 cm^{-1}, but there was a trend of more absorbance data occuring at higher wavenumbers at elevated temperatures. For this reason, instead of a fixed wavenumber location for $\omega_{2,smth}$, a more robust method was developed by setting the ending wavenumber location to a fraction of the cumulative sum of the absorbance. Figure 6.23 shows the processed temperature as a function of the cumulative sum fraction; it is seen that there was a large sensitivity for low numbers because a large portion of the absorbance information was not being used, but a relatively stable region exists from 0.8 to 0.98 for both datasets.

The starting point, $\omega_{1,smth}$, was a sensitive parameter because the majority of the absorbance data was located at the low-wavenumber range, especially at cooler temperatures. While ideally the starting location will be as early as possible to include the maximum amount of absorbance information, care must be taken to avoid edge effects of the baseline and smoothing filters. For this reason, a starting location of 7370 cm^{-1} was used for these experiments. For future testing, it would be useful to use a laser source that can produce low-noise absorbance data at a lower wavenumber range to improve the lower temperature data fidelity.

6.3 Temperature Fit

The final step in the process was to compute a best-fit line for the experimental data vs. each simulation dataset. The simulation temperature and pressure broadening that resulted in the linear fit with minimum MSE were the final processed experimental temperature and pressure broadening. Figure 6.25 shows an example of a 'good' and 'bad' fit between the simulated and experimental absorbance values. The simulated data at 390 K had a linear relationship with the experimental data while the simulated data at 590

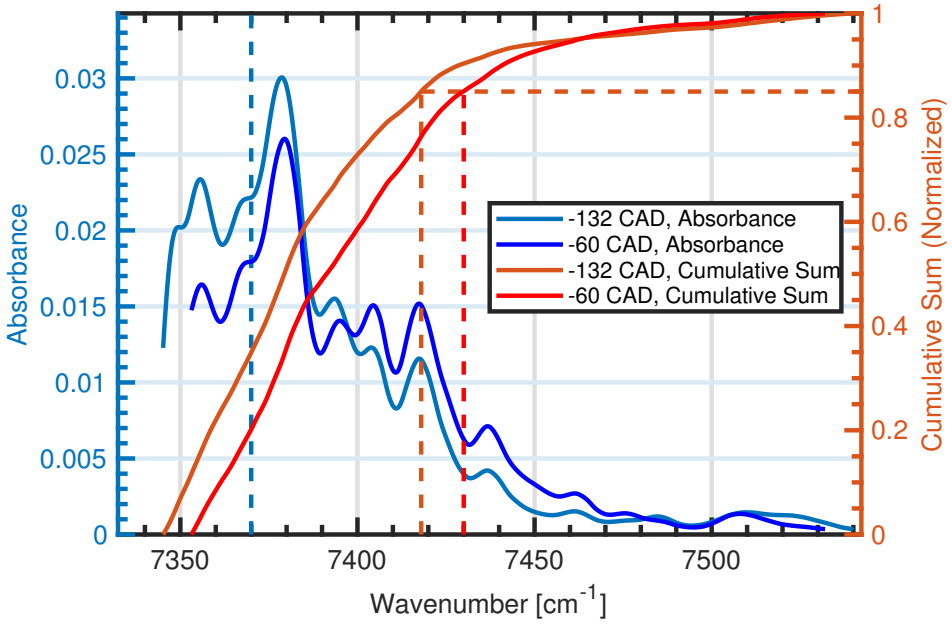

Figure 6.22: Experimental data with smoothing filter applied. Cumulative data used to define window for data and simulation comparison.

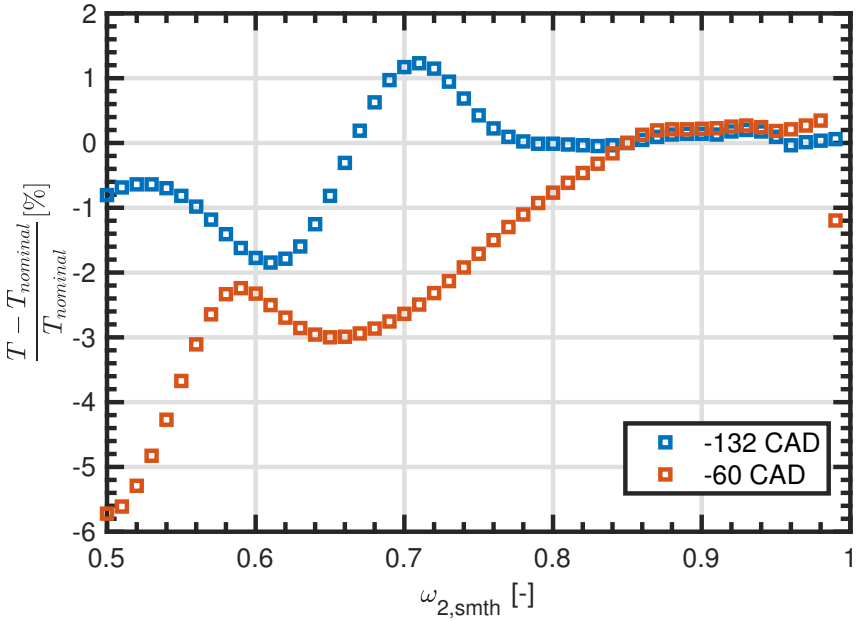

Figure 6.23: Final processed temperature as a function of ending wavenumber.

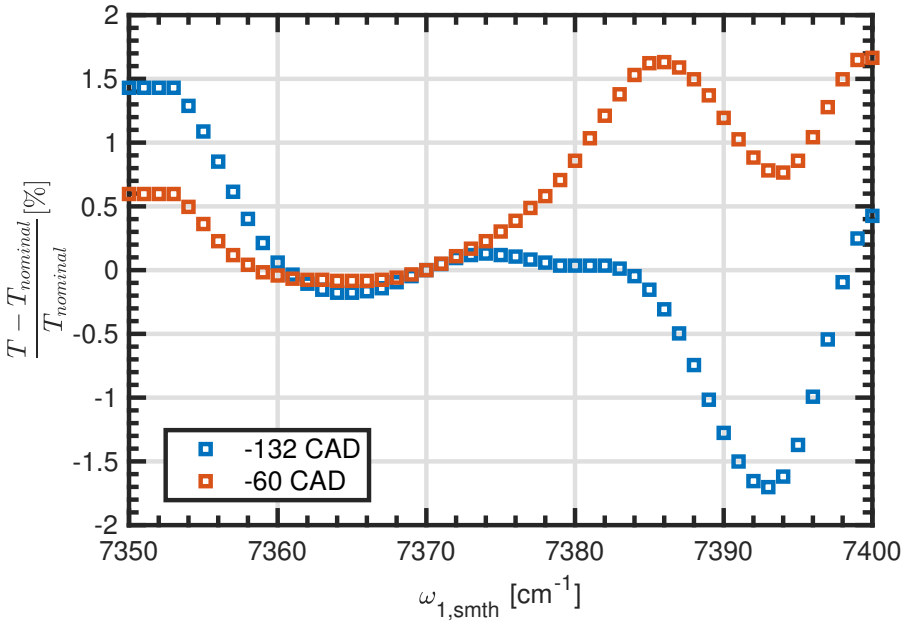

Figure 6.24: Final processed temperature as a function of starting wavenumber.

K was much less linear. The reason a linear curve fit was applied rather than directly computing the MSE between the simulation and experimental data is that the difference in water mole fraction and path length between the datasets cause a scaling difference. Figure 6.26 shows an example of typical MSE trends when calculating the fit between a single experimental dataset and a range of simulation temperatures and pressures; a global minimum is seen at approximately 595 K and the nominal pressure. To ensure that the temperature solution was not limited to the resolution of the simulation database, an interpolation was performed on the MSE vs. temperature data at the pressure that resulted in the lowest MSE to solve for the exact minimum of the MSE vs. temperature curve.

An important note is that at different simulated pressures, there were different temperatures that resulted in the lowest MSE; as seen in Figure 6.26, the temperature at which the MSE is a relative minimum varied from 577-615 K. Therefore, it is important to have enough pressure resolution in the simulation database to achieve the desired temperature accuracy. An alternative method could be to find the temperature at each

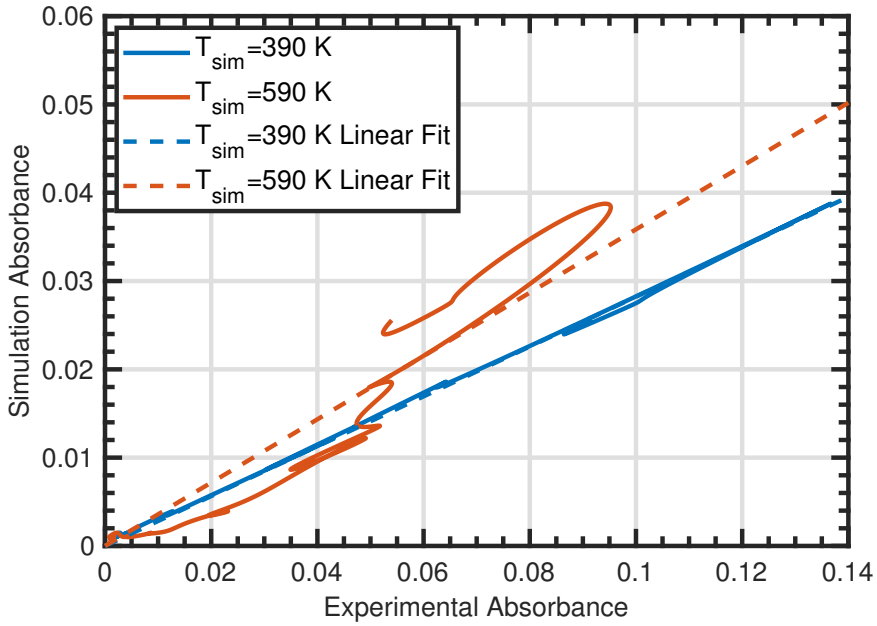

Figure 6.25: Linear curve fit for two simulation temperatures.

pressure that resulted in the relative minimum MSE and spline fit these temperature minima vs. MSE results; but this was not studied in the current scope of work.

An important note about the HITRAN and HITEMP databases is that even though they were defined in terms of pressure, whereas the BT2 database was defined in terms of a constant pressure broadening coefficient, it was not expected that the best-fit simulation pressure will match the experimentally measured pressure due to errors in the broadening coefficients. The current practice is to assume that the simulation pressure that results in the global minimum MSE between the simulated and experimental data is the correct pressure. An alternative method is to perform the MSE calculation between the experimental dataset and simulation database over a range of temperatures and pressure broadening values prior to applying the final smoothing filter; the simulation pressure broadening that results in the global minimum MSE between the experimental dataset and simulation dataset is then used in the final MSE calculation once the datasets are smoothed. This should ensure an accurate estimate of the correct pressure broadening value to use before the individual peak height and width information is lost due to the

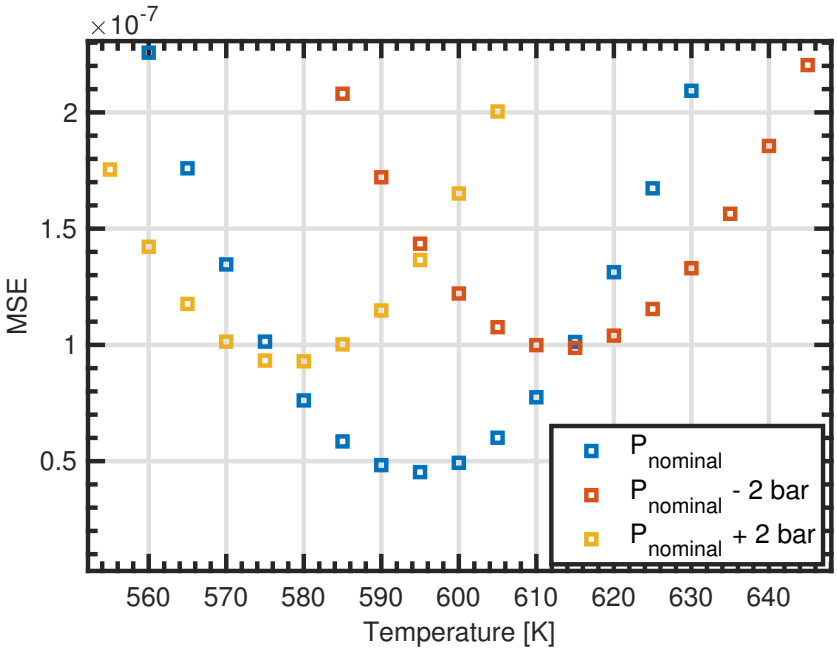

Figure 6.26: Curve fit MSE over a range of temperatures for several pressures.

smoothing filter application.

6.4 Uncertainty Analysis

Analyzing the uncertainty of the processed temperature proved to be a difficult process due to the large number and non-linear behavior of the factors involved. Sources of error were categorized as measurement precision, bias of each processing parameter, and biases involved with errors in the simulation database.

Measurement Precision

Measurement precision was estimated by calculating the 95% CI for the temperature at each crank angle. Three sets of 6-7 consecutive engine cycles were recorded for tests at 1000 RPM, while three sets of 13-14 consecutive engine cycles were recorded for tests at 2000 RPM. The precision uncertainty includes the effects of random measurement noise and cycle-to-cycle temperature variations. Figure 6.27 shows the mean temperature along

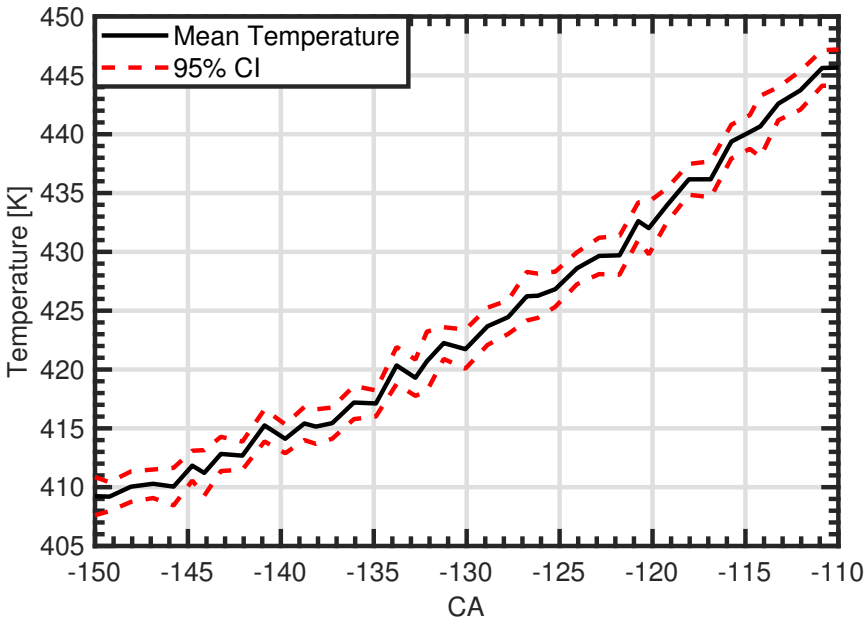

Figure 6.27: Mean temperature vs. CAD with 95% CI for a 2000 RPM, 2.21 bar intake pressure, 383 K intake temperature condition.

with 95% CI for an unfiltered representative dataset; the 95% confidence uncertainty bounds of the sampled mean near IVC was 0.5%, or 1-2 K, for all cases.

Processing Parameter Bias

There was no straightforward method to directly calculate the temperature uncertainty associated with the value chosen for each processing parameter. Estimations of reasonable upper and lower bounds were selected for each process parameter, and the processing program was run with the full factorial design of experiments (DOE) combination of these bounded values to obtain a range of final temperatures; the nominal values along with upper and lower bounds can be seen in Table 6.3. Figure 6.28 shows the main effects of the eight parameters investigated, along with the only non-negligible interaction, baseline filter width and number of filter iterations. For both datasets, no parameters had an effect larger than about 0.5%, indicating that there was only moderate temperature sensitivity over the range of parameters investigated. Figure 6.29 shows a histogram and cumulative

Table 6.3: Nominal values and upper and lower bound for important processing parameters.

Feature	Units	Nominal Value	Lower Bound	Upper Bound
N_{iter}	-	75	50	150
$\Delta\omega_{base}$	cm^{-1}	12	6	24
$\omega_{1,raw}$	cm^{-1}	7345	7342	7350
$\omega_{1,smth}$	cm^{-1}	7370	7365	7375
$\omega_{2,smth}$	cm^{-1}	7500	7450	7500
$\Delta\omega_{raw}$	cm^{-1}	0	-0.05	0.05
$\Delta\omega_{dn}$	cm^{-1}	0.1	0.05	0.3
$\Delta\omega_{smth}$	cm^{-1}	6.5	5	9

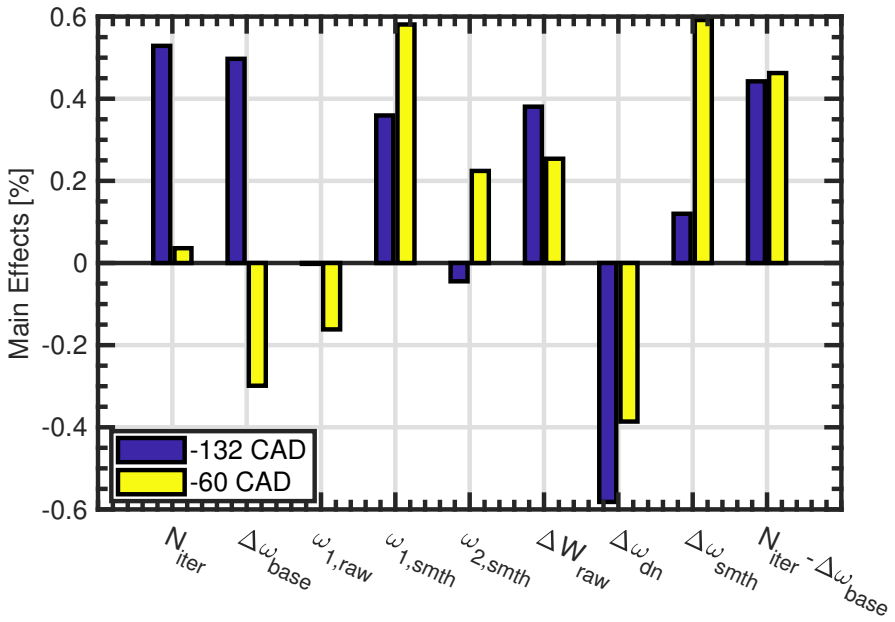

Figure 6.28: Bar chart showing main effects and baseline filter interaction.

fraction of the DOE results; it can be seen that the total temperature spread was about ±1.5% from the nominal. The parameter ranges were chosen to be on the high side for the processor, so the uncertainty estimate due to processing parameters is thought to be conservative.

Simulation Database and Processing Errors

The bias associated with either the simulation database being inaccurate or the processing method being flawed, even if the optimal values for each processing parameter were

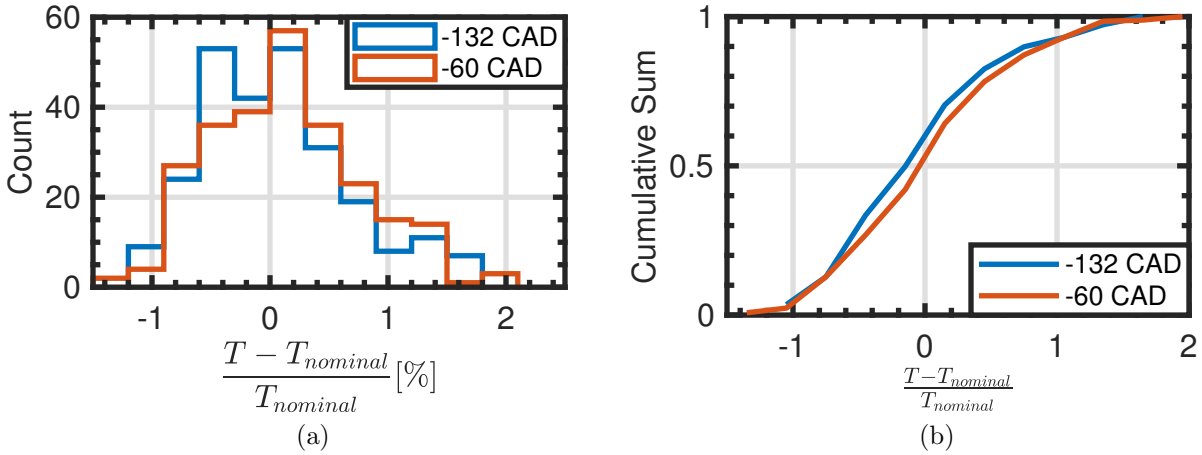

Figure 6.29: Histogram showing results of full factorial parameter DOE (left) and cumulative fraction of histogram data (right).

chosen, is by far the most difficult uncertainty to estimate. For future work it would be useful to obtain a more accurate estimate of this value through testing in a pressure-controlled environment at a known temperature.

An estimation for the accuracy biases due to database error was obtained by using three separate simulation databases, BT2, HITEMP, and HITRAN. HITEMP and HITRAN were used as the experimental data, with a representative baseline from actual experimental data added in, while BT2 was used as the simulation database. An absolute temperature error was calculated for a range of temperatures and pressures since the true experimental temperature, *i.e.*, the temperature used to create the HITEMP/HITRAN spectrum, was known. Results of this processing can be seen in Figures 6.30 and 6.31. At representative IVC conditions, corresponding to the lower left portion of the graphs, there was reasonable agreement between all three databases with an error of approximately 1-2%; however, as pressure increased the processed (HITRAN or HITEMP) temperature was increasingly higher than the true temperature. The database uncertainty is interpolated from the data points used to generate Figure 6.30.

An important note is that using this method to estimate uncertainty associated with database accuracy will be inaccurate if all three databases are incorrect. For example, if

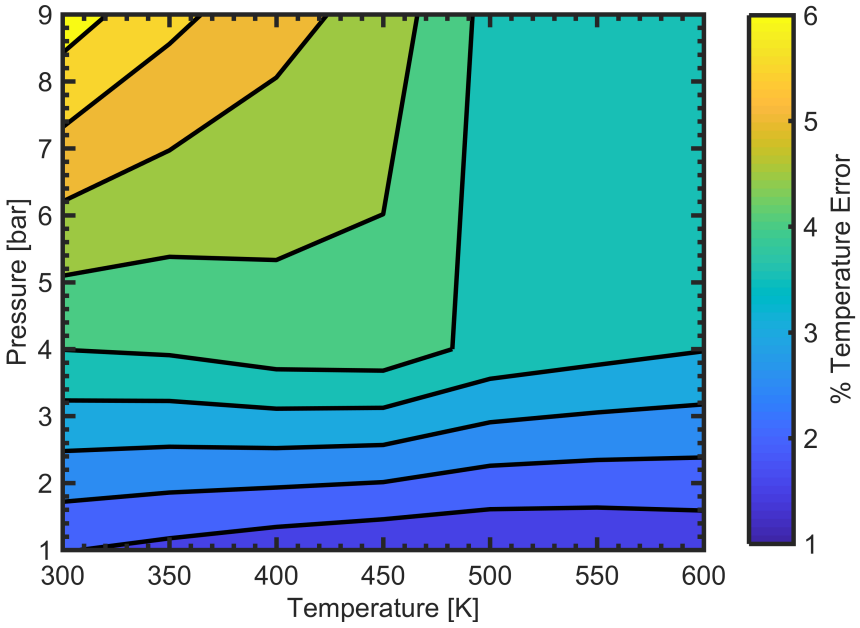

Figure 6.30: Processed temperature error when using HITRAN as the experimental data and BT2 as the simulation database.

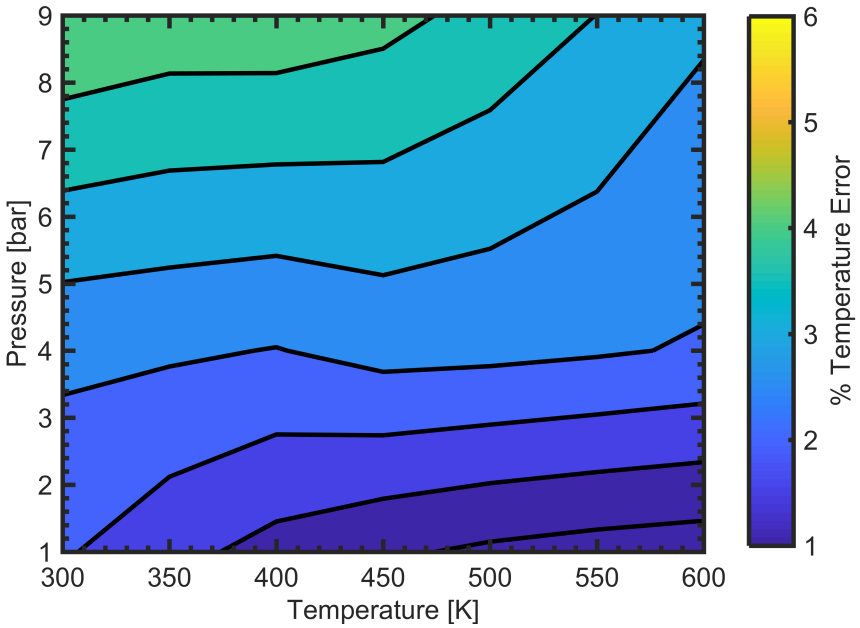

Figure 6.31: Processed temperature error when using HITEMP as the experimental data and BT2 as the simulation database.

Table 6.4: Temperatures at IVC with uncertainties for motored and fired conditions.

Speed [RPM]	1000	2000	1000	2000
Intake Pressure [bar]	2.25		1.5	
Intake Temperature [K]	383	383	423	423
Motored T_{IVC} [K]	403±9	421±10	422±10	439±10
Fired T_{IVC} [K]	411±9	432±10	433±10	453±10

the BT2, HITEMP, and HITRAN absorbance data at 450 K and 1 bar are identical this method will estimate that the bias associated with the processing method and database errors to be 0 K. The simulation databases' absorbance data could actually correspond to 425 K, a bias of 25 K, but it would be impossible to find this bias without experimental testing in a controlled temperature environment. Dr. Scott Melin performed tests at atmospheric pressure in a controlled furnace environment with a wide range of temperatures and found that simulations using the BT2 database matched within the experimental uncertainty bounds of ±0.5%, while simulations using the HITEMP database showed a negative bias of 2-3% compared to the experimental uncertainty bounds [78].

Final uncertainty was calculated by combining these three uncertainties in quadrature, with the main contributions coming from the uncertainty in the processing parameters and database accuracy. Figure 6.32 shows the single-sided 95% confidence uncertainty contributions for the 2000 RPM, 2.21 bar intake pressure, 383 K intake temperature operating condition. Table 6.4 lists a summary of the temperature results with uncertainty for motored and fired conditions.

6.5 Conclusions

Water absorption spectroscopy was used to obtain crank-angle resolved, in-cylinder temperature estimates for both motored and fired conditions over a range of intake pressures and temperatures. The datasets were very repeatable, with low precision uncertainty, and no obvious differences were seen in the data quality for motored vs. fired conditions. The final processed temperature showed moderate sensitivity to many of the processing

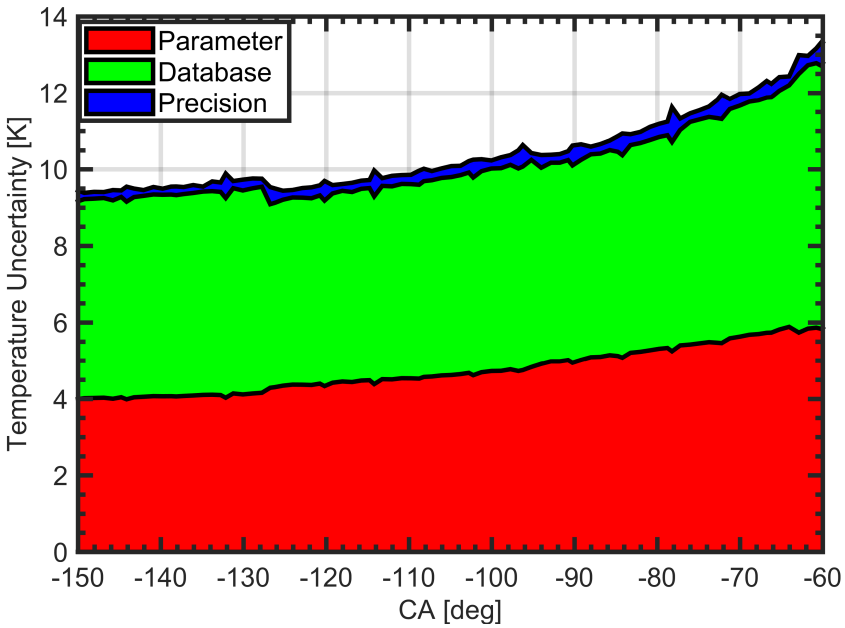

Figure 6.32: Uncertainty contributions from processing parameters, simulation database, and precision for a 2000 RPM, 2.21 bar intake pressure, 383 K intake temperature operating condition.

parameters, indicating that selection of the parameters values is non-trivial. Database accuracy was also a source of uncertainty, with some disagreement being seen between the three databases investigated. Further testing in a controlled environment where the measured temperature is known would be a useful tool for reducing some of these sources of uncertainty.

Another method that was briefly investigated in the current work was to calculate the differences between the experimental data and the simulation data that resulted in the minimum MSE. This involved quantifying differences such as peak warping, pressure broadening, and peak magnitudes. These peak warping, pressure broadening, and peak magnitudes were then randomly applied to a simulated set of data where the true temperature was known, and the temperature error distribution gave an estimate of the uncertainty due to differences between the experimental and simulation data. Preliminary results showed that peak warping had a small effect on the temperature error distribution, while pressure broadening had a large effect on the temperature error distri-

bution. A more rigorous analysis using this method was outside the scope of the current work, but would be a useful area for future work.

Chapter 7

Thermocouple Temperature Measurements

7.1 Experimental Setup

Two K-type thermocouples, purchased from Medtherm (Models TCFW202-05K05T and TCFW202-05K10T), were used to provide an additional method of measuring in-cylinder temperatures. The manufacturer datasheet can be found in Appendix A. A holder for the thermocouple was designed by another student, James Cherry, and was installed in the injector bore. A model of the full assembly can be seen in Figure 7.1. The thermocouple was installed 3 mm below the engine head surface; this height was chosen to place the thermocouple outside the wall boundary layer. The thermocouples were classified by their wire diameters; TC_1 had a diameter of 0.0127 mm and TC_2 had a diameter of 0.0254 mm.

A thermocouple amplifier (Analog Devices AD595C) was used to convert the thermocouple output to an analog voltage that was read by the NI DAQ hardware. Temperature data were acquired with 0.25 CAD resolution for 300 cycles at each operating point.

Operating points were selected to match operating conditions 1-6 used for the *HI/PI*

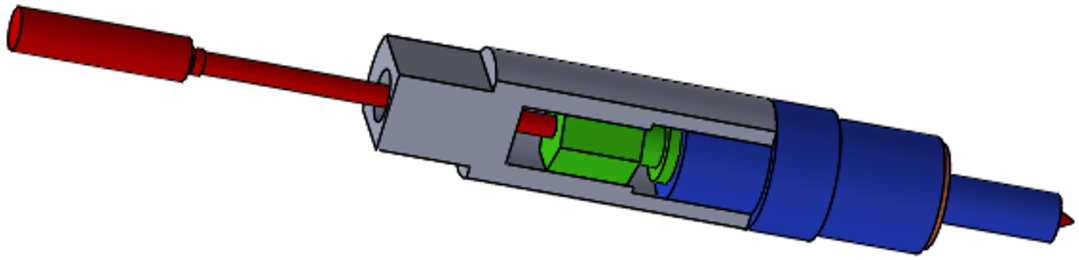

Figure 7.1: Model of the thermocouple holder assembly, created by James Cherry.

Table 7.1: Motored operating conditions for thermocouple testing.

Speed [RPM]		1000	2000	1000	2000	1000	2000
Intake Pressure [bar]		2.25		1.5		0.9	
Intake Temperature [K]	TC_1		323-348	303-423	323-423		
	TC_2	323-383	348-383	303-423	323-423	348-423	303-423

testing while covering a similar range of intake temperatures as the spectroscopy testing. A full summary of the operating conditions can be seen in Table 7.1. Two thermocouples were used for the testing. The first thermocouple, TC_1, failed during testing at 2000 RPM and 2.25 bar intake pressure. It is believed that the thermocouple failure was due to the high velocity flow during the intake process. The second thermocouple, TC_2, failed during testing at firing conditions. Several datasets were acquired under firing conditions before the second thermocouple failed; however, inconsistencies were seen in the fired data that were believed to have been caused by high temperature oxidation of the thermocouple.

7.2 Data Processing

The smallest thermocouple size available from Medtherm was initially selected to minimize the response time, but due to the short engine time scales, the thermocouple time

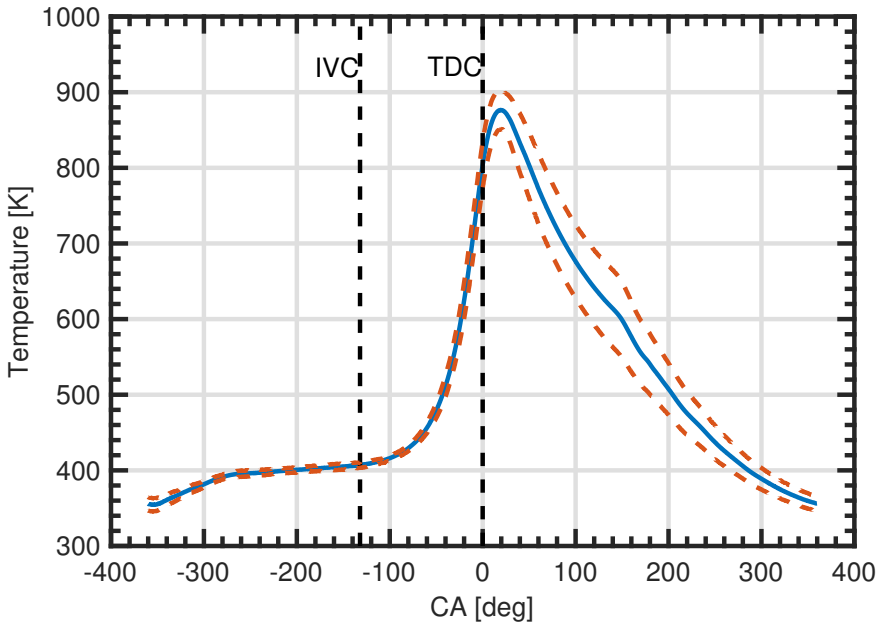

Figure 7.2: Motored raw temperature (solid) with dashed lines representing the 95% prediction interval at 1000 RPM with a 423 K intake temperature and 1.5 bar intake pressure.

constant was still long enough to introduce a significant bias. An example of the raw thermocouple temperature, averaged for 300 cycles is shown in Figure 7.2. The standard deviation was quite low (<3 K) at IVC and rose to ∼15 K at TDC. It is believed that the uncertainty increase during the expansion stroke is due to growth of the cold boundary layer in the expansion stroke and turbulent mixing of the cold boundary layer fluid with the rest of the in-cylinder gases. The effect of the thermocouple time constant can clearly be seen by the location of maximum temperature being well after TDC.

A correction was applied to the raw temperature data by using the first-order approximation

$$T_{\text{corr}} = T_{\text{raw}} + \tau \frac{dT_{\text{raw}}}{dt}. \tag{7.1}$$

This lumped capacitance approximation is valid for Biot numbers <<1; the Biot number

is the resistance to conduction divided by the resistance to convection, given by

$$Bi = \frac{hL_c}{k}, \tag{7.2}$$

where h is the convection coefficient, L_c is the characteristic length, defined as the volume to area ratio for a sphere, and k is the thermocouple conductivity. The Biot numbers for each thermocouple had estimated values less than 0.005 over the full engine cycle for all operating conditions. The smaller thermocouple, TC_1, which had a diameter of 0.0127 mm, was specified by Medtherm as having a time constant of 5 ms/4 ms in low/high gas velocity conditions, while the larger thermocouple, TC_2, with a diameter of 0.0254 mm, had a reported time constant of 10 ms/7 ms in low/high gas velocity conditions, see Appendix A. These approximate values were not sufficient for correcting the raw data as the gas flow conditions specified by Medtherm were unknown. Additionally, the time constant was expected to vary with density and temperature throughout the engine cycle due to their influence on the convective heat transfer coefficient.

7.2.1 Time Constant Calculation: Physical Parameter Estimation

The time constant was approximated by Equations 2.12, 2.13, and 2.14. The velocity was assumed to be equal to the average cylinder velocity from computation fluid dynamics simulations, which are described in more detail in the following chapter; this value was generally ∼25% higher than the mean piston speed. The physical properties of pure nickel were assumed for the thermocouples.

An example of the calculated time constant for TC_1 at 1000 RPM, 423 K, and 1.5 bar intake temperature and pressure is shown in Figure 7.3. The time constant scaled inversely with cylinder pressure and temperature; therefore, it was relatively constant near IVC. One important note is that the constant-velocity assumption introduces errors

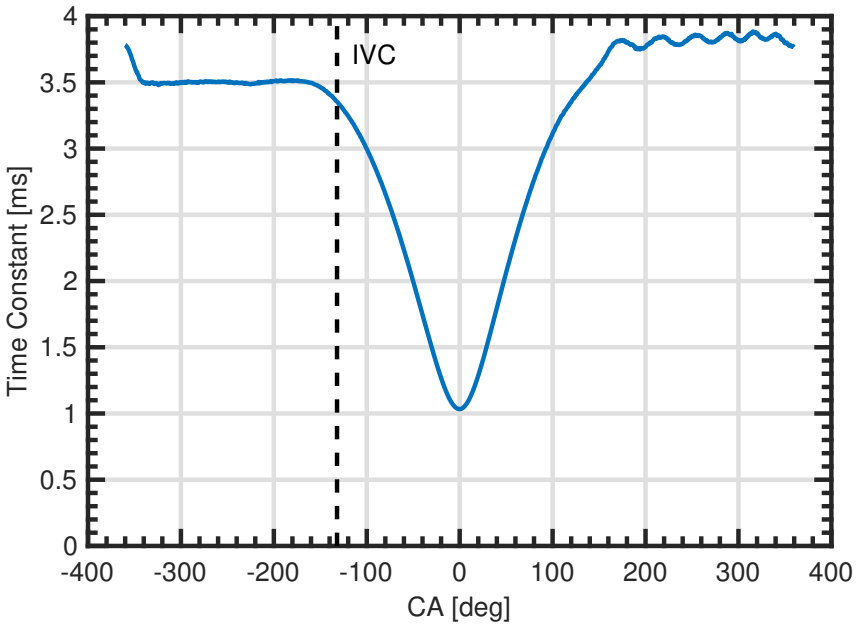

Figure 7.3: Time constant for TC_1 as a function of CA.

when the instantaneous velocity deviates from this average value; this had the potential to cause errors in the correction estimation, especially during the initial portions of the intake and exhaust strokes when the gas velocity was large.

A constant scaling factor, X, was applied to the time constant to account for inaccuracies in the parameters used in the time constant calculation. The metric for calculating the optimal value for X was the mean squared error (MSE) given by

$$MSE = \frac{1}{N}\sum(T_{corr} - T_{isen})^2. \tag{7.3}$$

First, the isentropic temperature, T_{isen}, was calculated assuming an isentropic compression process starting at IVC. The temperature at IVC was re-calculated for each time constant value. The MSE was calculated between T_{corr} and T_{isen} from IVC to -50 CAD. An example of the MSE as a function of X is shown in Figure 7.4; the value of X that resulted in the minimum MSE was taken as the optimal value. The optimal multipliers for both thermocouples at all conditions tested are shown in Figure 7.5. While there was

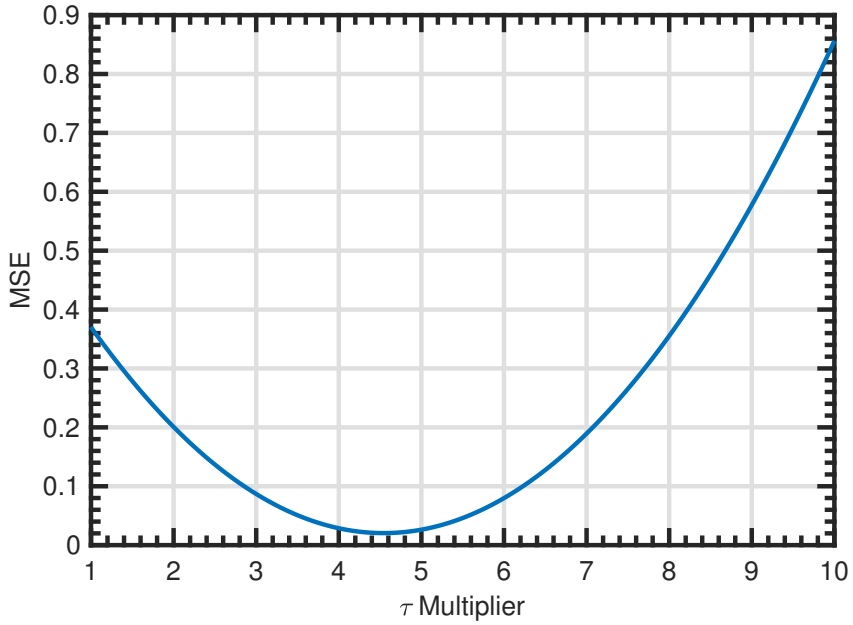

Figure 7.4: MSE as a function of the time constant multiplier for TC_1 at 1000 RPM, 423 K, and 1.5 bar intake temperautre and pressure.

Table 7.2: Optimized time constant for TC_1 and TC_2 at IVC for each operating condition.

Speed [RPM]		1000	2000	1000	2000	1000	2000
Intake Pressure [bar]		0.9		1.5		2.25	
τ [ms]	TC_1		10.2	15.4	12.1		
	TC_2	24.4	18.9	28.5	22.3	33.8	26.9

some variance in the data, especially for TC_2, the results were relatively constant for each thermocouple for all conditions tested. The average optimal multiplier was 4.6 for TC_1 and 8.5 for TC_2. The thermocouple response near IVC was of the greatest interest for the current work; the calculated time constant with the optimal multiplier at IVC for each thermocouple for all conditions is shown in Table 7.2. The time constant for TC_2 changed by 75% from the high intake pressure to the low intake pressure conditions, indicating the magnitude of errors that could occur from assuming a constant value. It is also interesting to note that the calculated time constants at IVC conditions were all 2-3 times larger than the reported time constants from Medtherm.

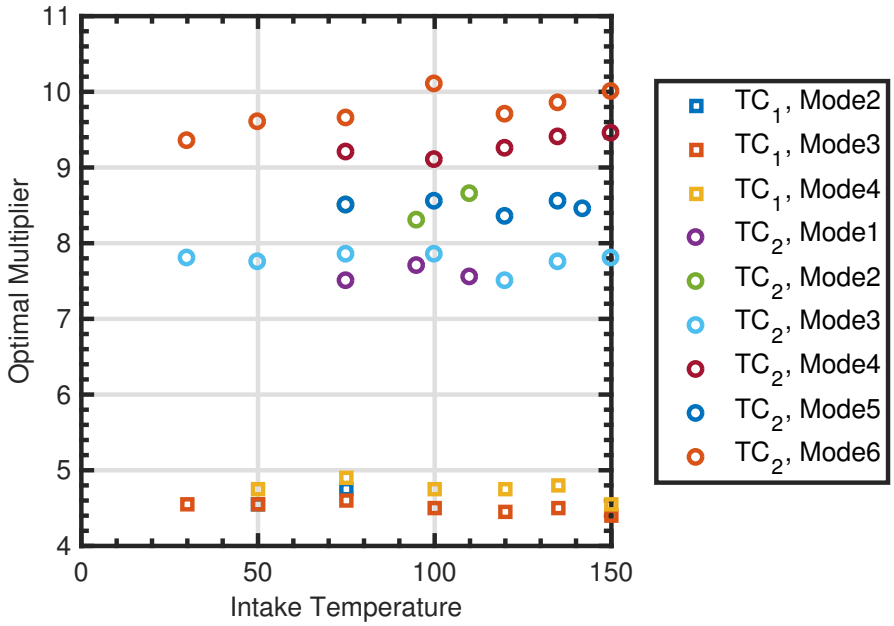

Figure 7.5: Optimal value of the time constant multiplier for both thermocouples at all conditions tested.

7.2.2 Time Constant Calculation: Two-Thermocouple Probe Technique

An independent technique was utilized to obtain a second estimate for the thermocouples' time constants. The data from two or more thermocouples measuring the same gas temperature can be combined to directly calculate each thermocouple's time constant without any knowledge of either thermocouple's physical parameters, as discussed in Section 2.2.3. The error between the compensated temperature for each thermocouple is calculated with the assumption that the time constants are not time-varying. While this assumption was not valid over the entire engine cycle, Figure 7.3 showed that the time constant was not expected to vary much near IVC. Equations 2.19, 2.20, and 2.21 were used to directly solve for the average time constants, τ_1 and τ_2, over the specified CAD window, using only the raw thermocouple data. Figure 7.6 shows the resultant average time constant as a function of crank angle for three different window lengths; it was seen that too small of a window had a large variance in the calculated time constant,

Table 7.3: Time constant used for compensating TC_1 and TC_2 at IVC for each operating condition.

Speed [RPM]		1000	2000	1000	2000	1000	2000
Intake Pressure [bar]		0.9		1.5		2.25	
τ [ms]	TC_1		7.7	11.6	9.1		
	TC_2	18.3	14.2	21.4	16.7	25.4	20.2

whereas too large of a window resulted in a single value that was independent of crank angle. Figure 7.7 shows the calculated time constant for both thermocouples at IVC as a function of window length for the intake temperature sweep run at 2000 RPM and 1.5 bar. The calculated time constants for each thermocouple were relatively constant in the window range of 30-80 CAD. When these values were compared to the physical time constant calculations, listed in Table 7.2, it is seen that this two-thermocouple method resulted in values around 25% lower at IVC. Figure 7.8 shows the comparison of calculated time constants at IVC with each method for TC_1 and TC_2 at 2000 RPM and both 1.5 and 2.25 bar intake pressures; the two-thermocouple method was not able to produce reasonable results for the 1000 RPM and 1.5 bar intake pressure. Because the two-thermocouple method involved multiple datasets taken with two independent thermocouples and required less assumptions compared to the physical time constant calculation method, the time constants calculated using this method were believed to be more accurate. However, the two-thermocouple method only works when the time constant is relatively constant and could not be used during the parts of the engine cycle when conditions are rapidly changing, so the 25% reduction at IVC, seen in Figure 7.8, was applied to the physical time constant calculations over the entire engine cycle. The resulting time constants for each thermocouple at IVC are shown in Table 7.2. The 25% difference between the time constants calculated with each method was used as an estimate of the uncertainty bias associated with the time constant correction. Table 7.3 lists the final time constants for both thermocouples for all operating conditions at IVC.

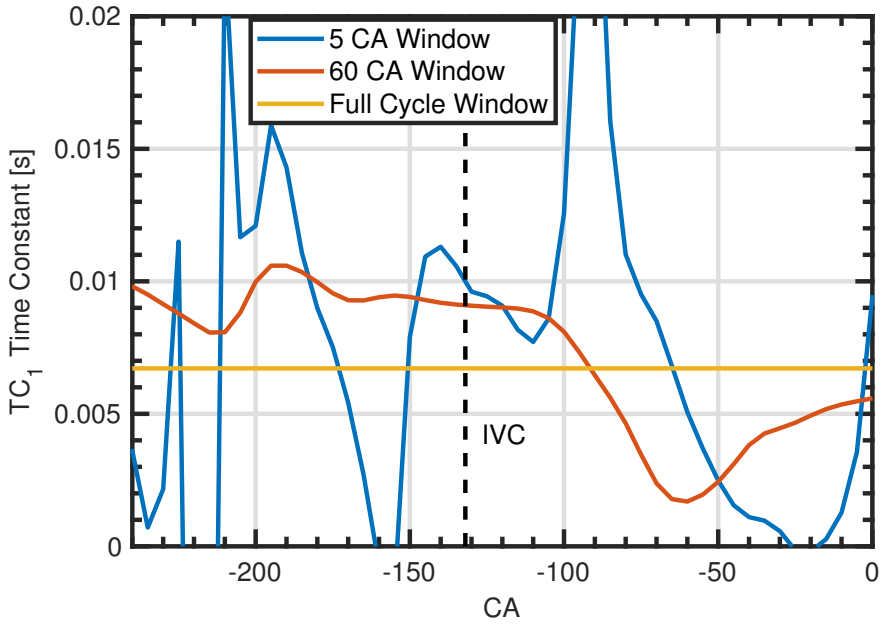

Figure 7.6: Calculated time constant for TC_1 (solid) and TC_2 (dashed) vs. CA for several window lengths at 2000 RPM and 1.5 bar intake pressure.

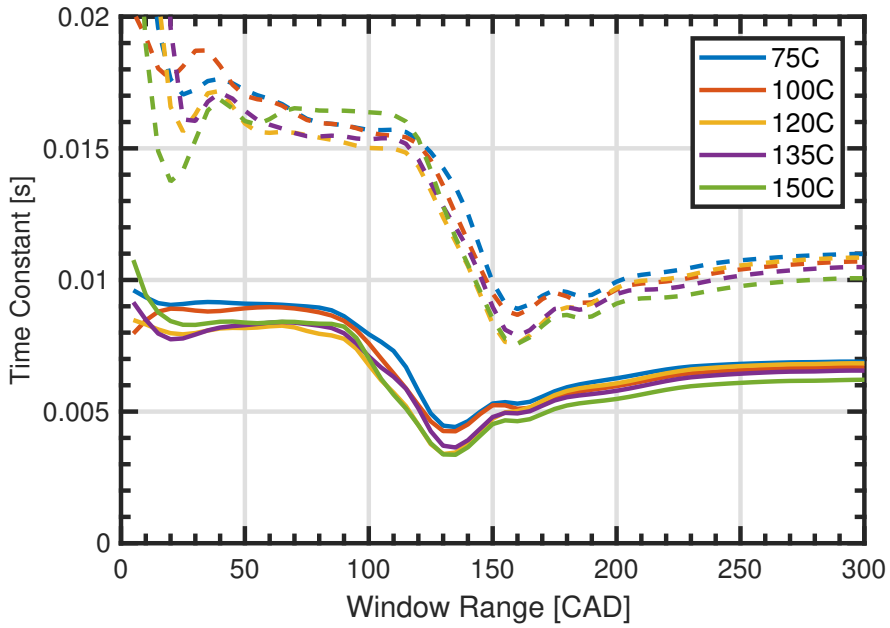

Figure 7.7: Calculated time constant at IVC vs window lengths at 2000 RPM and 1.5 bar intake pressure.

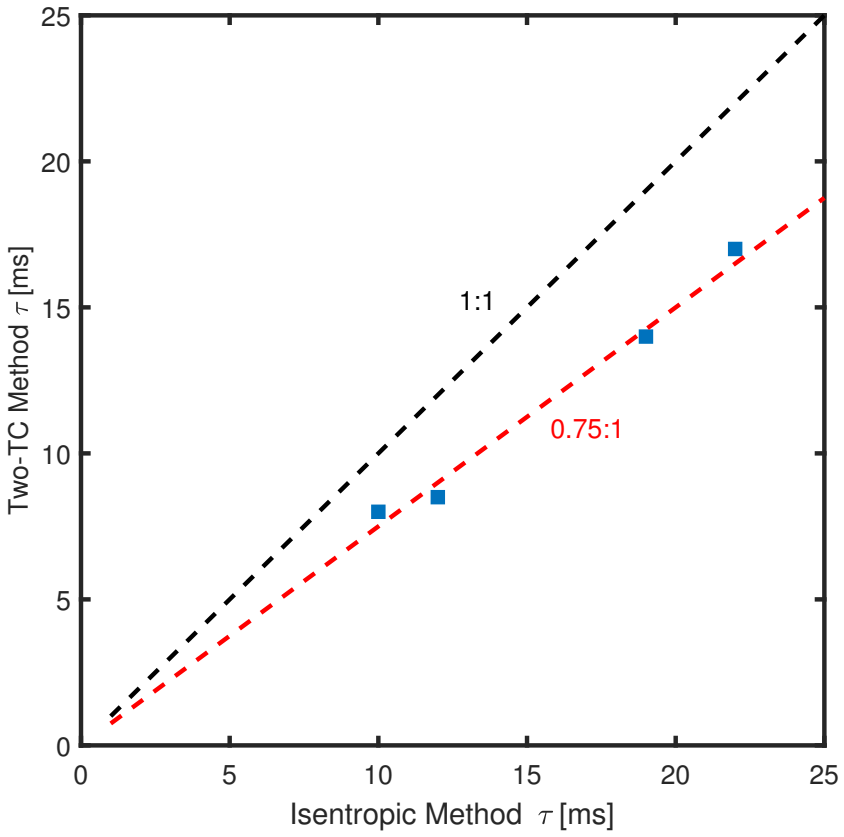

Figure 7.8: Two-TC method time constants vs. isentropic method time constants for TC_1 and TC_2 at 2000 RPM, 1.5 and 2.25 bar intake pressure along with 1:1 and 0.75:1 reference lines.

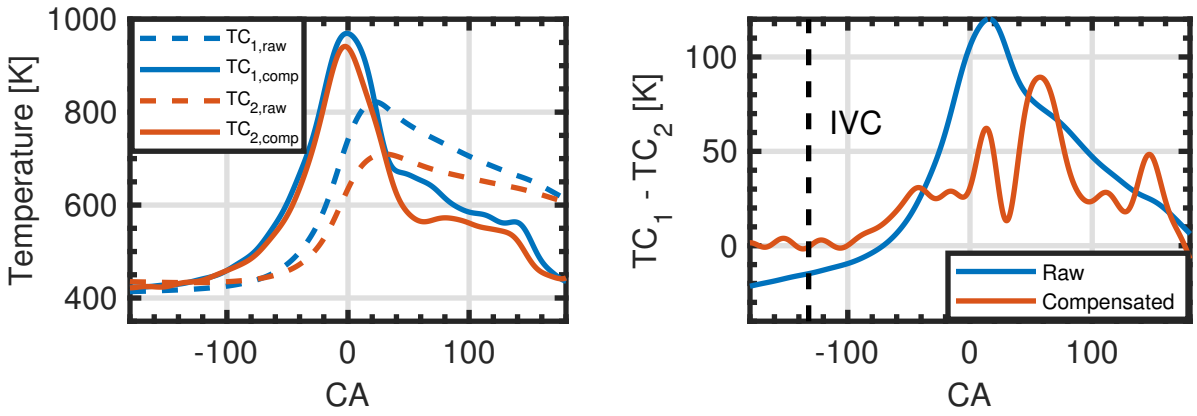

(a) (b)

Figure 7.9: Raw (dashed) and corrected (solid) temperatures (left) and temperature residuals (right) at 2000 RPM and 1.5 bar intake pressure.

7.2.3 Time Constant Correction Results

The results of the time constant correction using the physical time constant method reduced by a 25% are shown in Figure 7.9, where the dashed lines are the raw temperature and the solid lines are the corrected temperature; data from both thermocouples for the same operating condition are shown. The left plot shows that the corrected temperatures had the expected location of maximum temperature near TDC, and that there was relatively good agreement between the two compensated temperatures, while the right plot shows the temperature difference between TC_1 and TC_2 for both the raw and compensated temperatures. A comparison of both thermocouples' corrected temperatures at IVC for all operating conditions is shown in Figure 7.10; there was excellent agreement for all conditions tested, with an average MSE of <2 K and no outliers.

7.3 Uncertainty Analysis

The 95% confidence interval for the mean of the 300 cycles of raw temperature data was calculated according to Equation 5.3, discussed in Chapter 5. The main biases associated with the thermocouple measurement were divided into three main categories: material

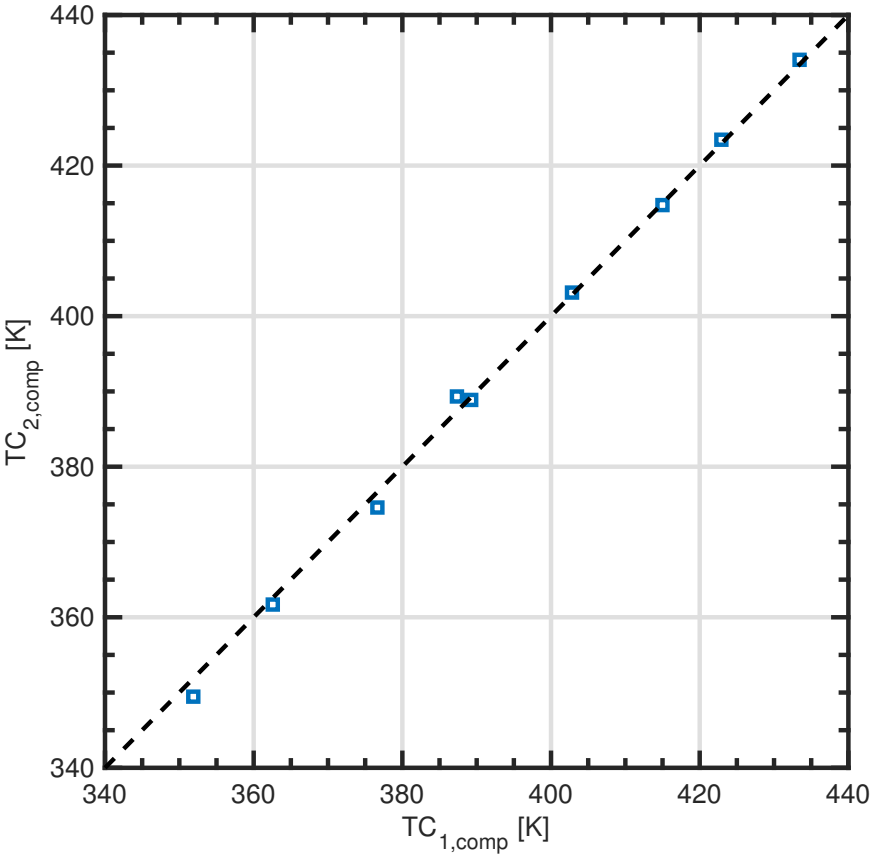

Figure 7.10: Comparison of compensated thermocouple temperatures for all conditions at IVC.

accuracy, radiation bias, and time constant bias. Due to the large length-to-diameter ratio of thermocouple, the bias due to conduction was assumed to be negligibly small. The material accuracy for the type K thermocouples was 2.2 K or 0.75% (whichever value is greater). The radiation bias was calculated according to Equation 2.17. The wall emissivity, ϵ_w, was assumed to be 1 and the wall temperature, T_w, was set to the coolant temperature for a worst-case estimate. The T^4 radiation dependence makes the radiation bias more significant at higher temperatures. The bias associated with the time constant was calculated by re-calculating T_{corr} with a 25% smaller or larger time-scaled time constant.

The total temperature uncertainty and relative contributions of each bias are shown in Figure 7.11. The time constant uncertainty dominated the temperature uncertainty at all crank angles, indicating the importance of accurately estimating this parameter. Trends were similar between the 1000 and 2000 RPM conditions. While the temperature uncertainty reached values of over 50 K near TDC, the uncertainty near IVC was much smaller with values of 3-4 K; calculated temperature uncertainties for both thermocouples for all operating conditions at IVC can be seen in Table 7.4. One interesting note is that the uncertainty due to the time constant only affects the results for non-zero gradients of T_{raw}; therefore, the time constant bias uncertainty contribution approached zero at the minimum and maximum values of T_{raw}. The maximum value occurred near 20 CAD. While uncertainty due to radiation started to have a larger effect at elevated temperatures, the thermocouple temperature at this time was expected to be relatively accurate. Unfortunately, there were other biases introduced at this point in the engine cycle due to temperature stratification in the cylinder, which will be discussed in more detail in the next chapter. T_{raw} also is expected to match the true local temperature where it reached a minimum value, near -250 CAD. While the temperature at this CAD during the intake stroke was not extremely useful, a useful method to improve IVC temperature estimation accuracy would be to use a thermocouple with a longer time constant that would

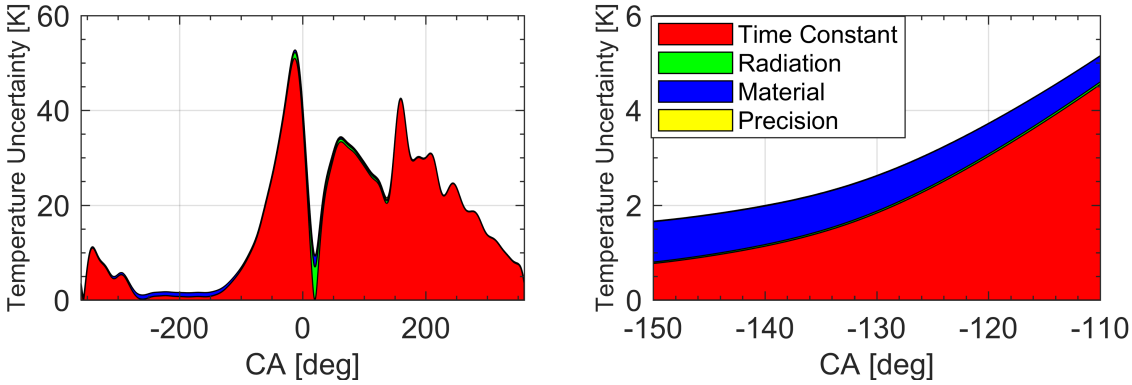

Figure 7.11: Total uncertainty and relative contributions at 1000 RPM and 1.5 bar intake pressure for TC_1.

Table 7.4: Thermocouple temperature with uncertainty for TC_1 and TC_2 for the six main operating conditions.

Speed [RPM]		1000	2000	1000	2000	1000	2000
Intake Pressure [bar]		0.9		1.50		2.25	
Intake Temp [K]		383		423		423	
IVC Temperature [K]	TC_1			417.9±4.0	433.4±4.9		
	TC_2	394.2±4.1	411.8±3.3	412.7±4.0	434.1±3.1	409.7±3.8	428.9±3.2

have its minimum value later in the intake stroke, near IVC. This approach would likely increase the uncertainty throughout the compression stroke, but would have the effect of reducing uncertainty near IVC. This effect can be seen by comparing the uncertainty between TC_1 and TC_2 at 2000 RPM and 1.5 bar intake pressure in Table 7.4; TC_2 had a smaller uncertainty despite its larger time constant at this operating condition. Figure 7.12 shows the raw temperature data for both thermocouples; the minimum temperature for TC_1 occurred at -228 CAD, while the minimum temperature for TC_2 occurred at -136 CAD due to its longer time constant.

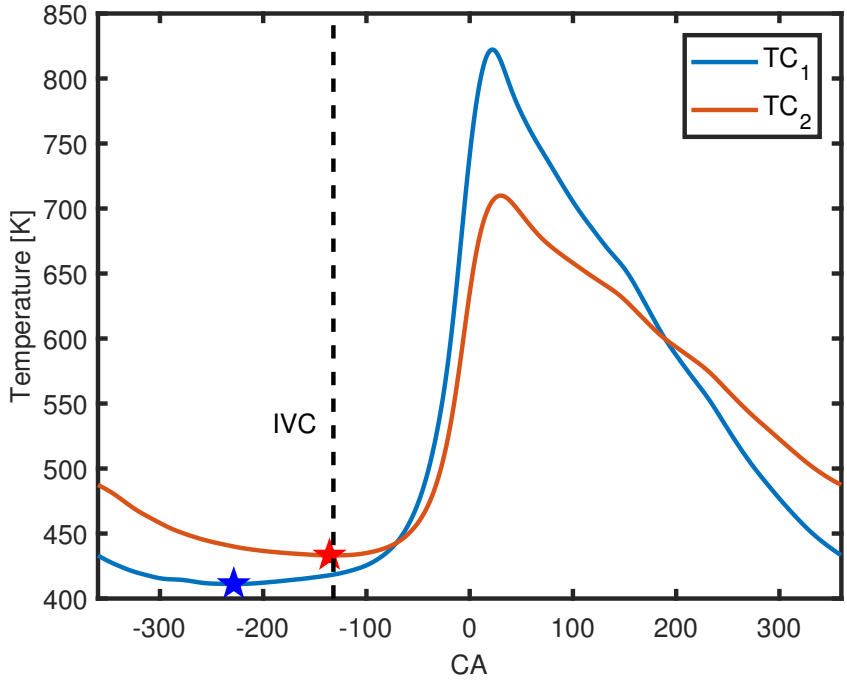

Figure 7.12: Raw temperatures along with locations of minimum raw temperature at 1000 RPM and 1.5 bar intake pressure for TC_1 and TC_2.

Chapter 8

Temperature Comparison

8.1 Introduction

This chapter covers several topics that were used to combine the temperature measurement methods discussed in the previous three chapters into a final experimental temperature that was used as a metric to evaluate the engine simulations. First, CFD analysis was performed to gain insight into in-cylinder properties that are difficult to experimentally measure, such as exhaust residual stratification, temperature stratification, and local gas velocities. The CFD simulations were used to obtain an estimate for the possible biases that could arise for the different temperature measurement methods. Next, temperatures for each method are compared for all operating conditions. Finally, the temperatures were combined into a single temperature and a corresponding uncertainty that was used in the following chapters for evaluating the kinetics mechanisms.

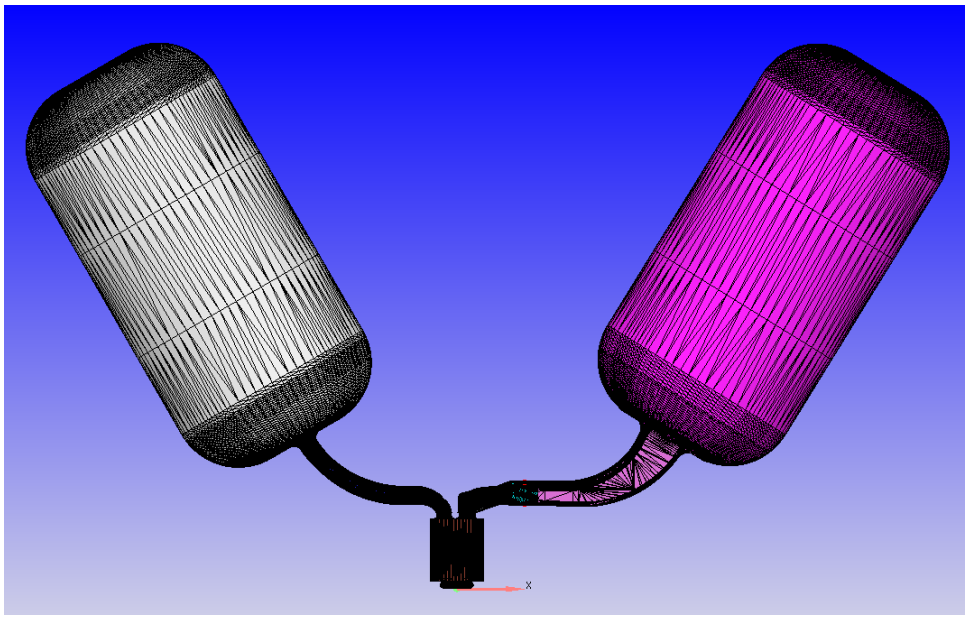

Figure 8.1: DERC engine model in Converge.

8.2 Converge Simulations

8.2.1 Simulation Setup

Full-cycle CFD simulations were performed by another student, Arun Ravindran, using Converge CFD code [79]. The simulations were performed to provide an estimate of the in-cylinder temperature stratification and to estimate the biases associated with the different temperature measurement methods. The full engine geometry was modeled in Converge, including intake and exhaust runners, surge tank, and the combustion chamber as seen in Figure 8.1.

Three consecutive engine cycles were run so that the simulation could reach a steady operating condition. Pressure varied by less than 1.5% and temperature varied by less than 0.1% throughout the compression stroke from the 2nd cycle to the 3rd cycle. There was no inlet air flow to the intake surge tank, which caused it to slowly empty as each intake stroke occurred; this was the main reason that the pressure varied slightly from the 2nd to the 3rd cycles, but temperature stayed relatively constant. Mass-averaged thermodynamic data were acquired for the entire simulation, while spatially-resolved

Table 8.1: Motored operating conditions for Converge simulations.

Speed [RPM]	1000	2000	1000	2000	1000	2000
Intake Pressure [bar]	2.25		1.5		0.9	
Intake Temperature [K]	383	383	298:423	298:423	423	423

Table 8.2: Fired operating conditions for Converge simulations.

Speed [RPM]	1000
Intake Pressure [bar]	1.50
Intake Temperature [K]	423

data were acquired for the 3rd cycle at 10 CAD intervals. The Converge simulations were used to gain insight and validate assumptions for several in-cylinder properties that are difficult to measure experimentally: exhaust residual concentration and stratification, gas velocity, and temperature stratification.

Intake temperature sweeps were performed for both motoring and firing cases at conditions representative of the main six experimental operating conditions. Tables 8.1 and 8.2 list the conditions tested. For all cases, combustion chamber wall temperatures were set to 361 K to match the coolant temperature of the engine experiments and intake/exhaust runner wall temperatures were set to match intake air temperatures. Due to the increased computational cost of running fired simulations, only one condition was run. The Aramco mechanism was used for the chemical kinetics solver.

8.2.2 Exhaust Residuals

The internal exhaust residual concentration from the simulation for a fired condition was calculated by comparing the ratio of CO_2 concentrations after combustion and after the intake stroke. The in-cylinder CO_2 mass fraction for the second cycle is seen in Figure 8.2. Combustion occurred near TDC, which caused the CO_2 mass fraction to rapidly increase; the level stayed constant until the intake valve opened and fresh air diluted the combustion products. The ratio of CO_2 after the intake stroke to CO_2 after combustion, which represents the residual fraction, was equal to 0.019. Exhaust residuals

were expected to be low due to the positive pressure difference between the intake and exhaust; this was intentional to minimize the effect of the residuals. It is interesting to note that the residual concentration was a bit lower than that seen in engine experiments, with the engine experiments having a calculated value near 0.033. Applying the Yun and Mirsky correlation described in Section 5.3.4 resulted in a calculated residual fraction of 0.031, which was a very close match to the value calculated in the engine experiments.

Because the intake was a closed system in the simulation, the true residual concentration was also calculated for a motored condition with

$$y_{res,motor} = \frac{m_{intake,i} - m_{intake,f}}{m_{cyl}}, \tag{8.1}$$

where $m_{intake,i}$ and $m_{intake,f}$ were the intake runner and surge tank total air masses before and after the intake stroke, and m_{cyl} was the trapped mass in the cylinder once the intake stroke was complete. The true residual concentration was 0.0275, much smaller than the value calculated with the Yun and Mirsky correlation of 0.057. This could be an indication that the Yun and Mirsky method provides an overestimation of the exhaust residual fraction, especially for motored conditions, which would cause the trapped mass to be overestimated and the trapped mass temperature to be underestimated.

While the average exhaust residual was a useful tool for comparing to the correlations used in engine experiments to estimate the exhaust residuals, the spatially resolved data revealed additional information. Figure 8.3 shows the maximum, minimum, and average exhaust residual concentration throughout the compression stroke. A wide spread of exhaust residual concentrations is seen at IVC, from a minimum of near 0 to a maximum of about 2.5 times the average. This spread gradually decreased as mixing continued throughout the compression stroke.

One theory early in the engine experiments was that locally high concentrations of hot residuals would trigger the start of combustion. Figure 8.4 shows the joint PDF of temper-

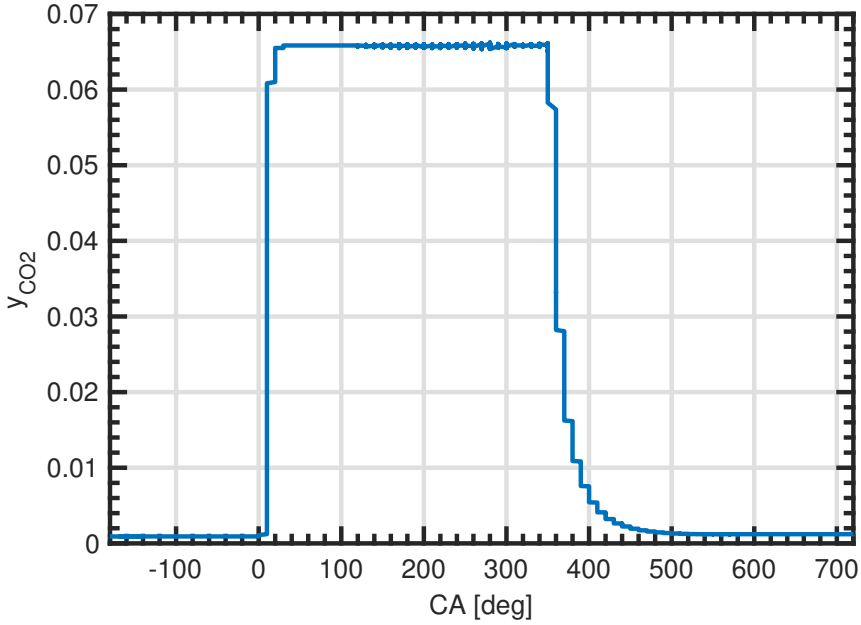

Figure 8.2: CO2 mass fraction as a function of crank angle.

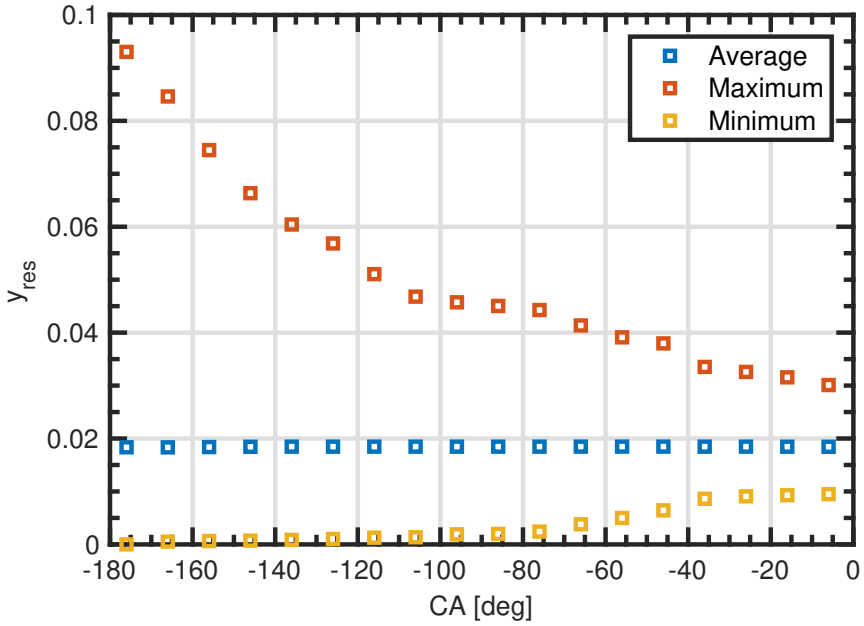

Figure 8.3: Average, minimum, and maximum exhaust residual fractions during the compression stroke.

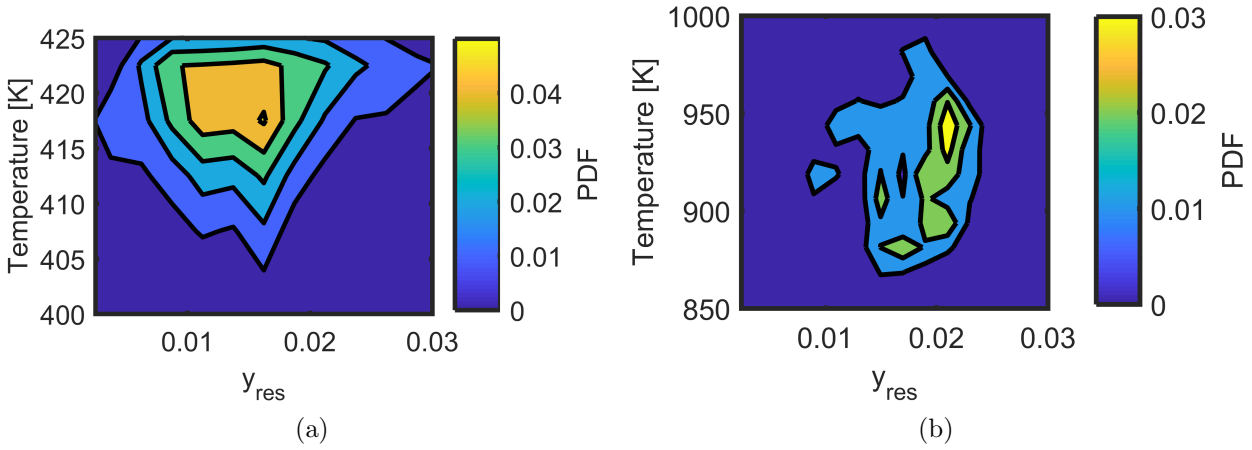

Figure 8.4: Temperature as a function of residual concentration at IVC (left) and TDC (right).

ature and residual concentration. While it is seen that there is maybe a weak correlation between temperature and y_{res} at IVC, the areas with highest residual concentrations do not have a higher temperature than the areas with average residual concentrations. At TDC, there is no correlation seen between temperature and residual concentration; the spread of residuals was also much smaller compared to IVC. Because there were no hot spots caused by local pockets of high residual concentrations, it is expected that the residual stratification during the early part of the compression stroke did not affect temperature estimations. The low average value and low spread in residual concentrations near TDC indicated that assuming a homogeneous air/fuel/residual mixture is a valid assumption for the chemical kinetics simulations.

8.2.3 Velocity Estimation

In-cylinder gas velocity at the thermocouple location is required in the calculation of the thermocouple time constant. Figure 8.5 shows the velocity magnitude for two different engine speeds for motored and fired conditions. Cylinder-averaged velocity was relatively constant in time and approximately equal to 4.5(8.5) m/s at 1000(2000) RPM. These numbers were relatively close to the mean piston speeds of 3(6) m/s. The gas velocity

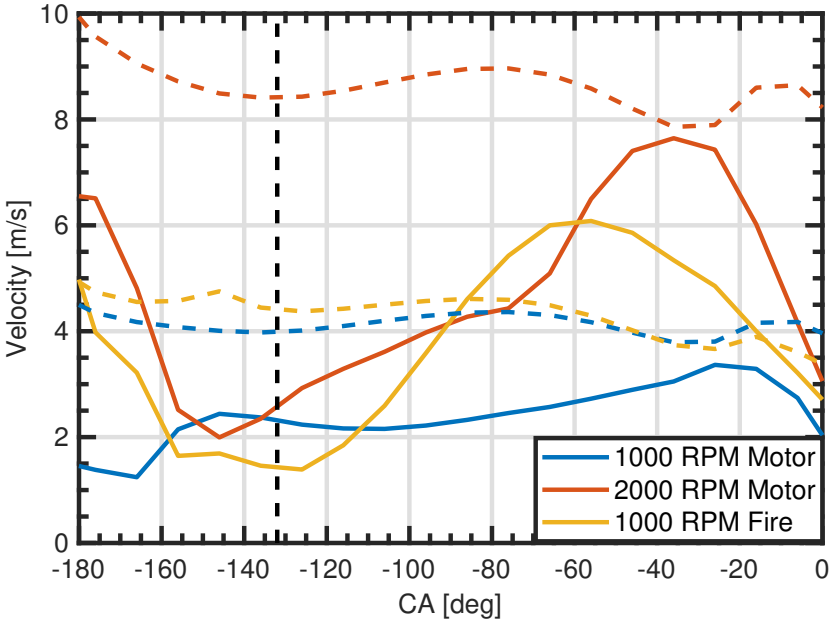

Figure 8.5: Velocity at thermocouple location (solid) and mass-averaged (dashed) for motored and fired conditions.

at the thermocouple location varied quite a bit during the compression stroke. Due to uncertainties in the grid resolution accuracy for the velocity at the thermocouple location, the cylinder-averaged velocity, which was effectively constant throughout the compression stroke, was selected for use in the thermocouple time constant calculation. The bias associated with uncertainties in the velocity values used for calculating the thermocouple time constants was accounted for in the time constant uncertainty, discussed in the previous chapter.

8.2.4 Temperature Bias Estimation

The temperature distributions at IVC and TDC are shown in Figure 8.6, with the dashed vertical lines showing the mass-averaged temperature. At IVC, the temperature distributions skewed towards the wall temperature on one side and was quite close (<5 K) to the mean temperature on the other side. At TDC, there was a much larger spread in temperature that again skewed towards wall temperature on the low temperature side

and was about 30-50 K higher than the mean temperature on the high temperature side.

This spatially resolved temperature information was used to estimate the biases associated with the different experimental temperature measurement methods used in the engine experiments. The mass-averaged temperature was the equivalent of the experimental temperature calculated using the estimated trapped mass and ideal gas law. Mass is fixed in the experimental calculation, which is valid only during the closed portion of the engine cycle. The temperature path used for the spectroscopy testing was estimated by taking the mass-averaged temperature of a centrally located cylinder of gas with a radius of 3.5 mm. The cylinder radius was set to match the optical probe's physical dimensions. The temperature at the location of the thermocouple was set equal to the temperature 3 mm below the engine head surface. The temperature of the inner core was calculated by taking the mass-averaged temperature of the hottest 10% of the cylinder contents (by mass). Figure 8.7 shows a pictorial representation of the different temperature estimation methods.

These four different temperatures and the differences between the different temperatures and the inner core temperature at 1000 RPM, 150 kPa intake pressure, and 423 K intake temperature for motored conditions are seen in Figure 8.8. The trapped mass, spectroscopy, and thermocouple temperatures are within 7 K of the inner core temperature throughout the early portion of the compression stroke. This result suggests that the biases of the temperatures measured at IVC relative to the inner core temperature would be expected to be within 7 K for the engine experiments at this operating condition. An important note is that for the spectroscopy testing a flat piston was used in the experiments as opposed to the stock bowl piston used in the Converge simulation; as the piston nears TDC the simulation results may vary from the experimental results due to different boundary conditions. Another important note is that wall temperatures in the simulation were set to the coolant temperature, 361 K, as a worst-case bias estimate. Figure 8.9 shows the estimated biases as a function of the difference between

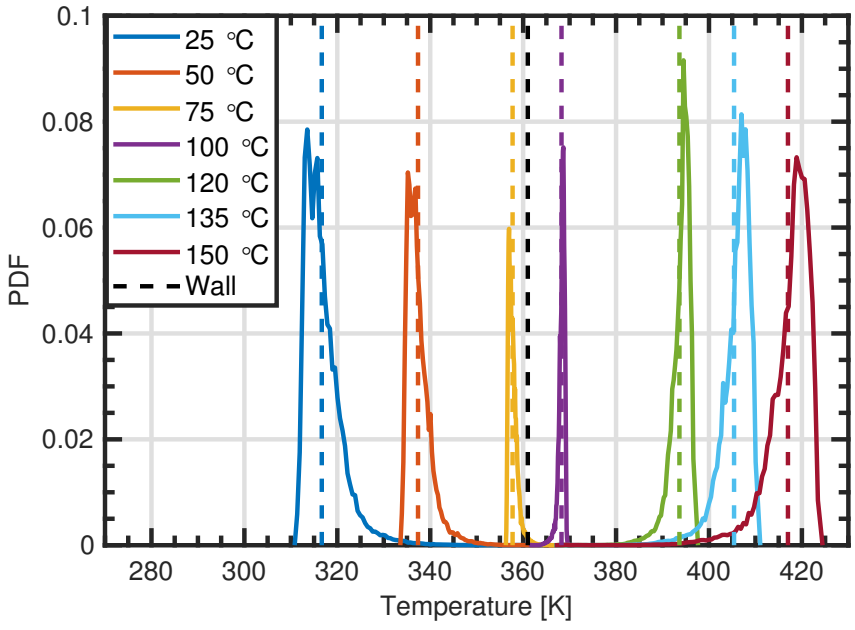

(a)

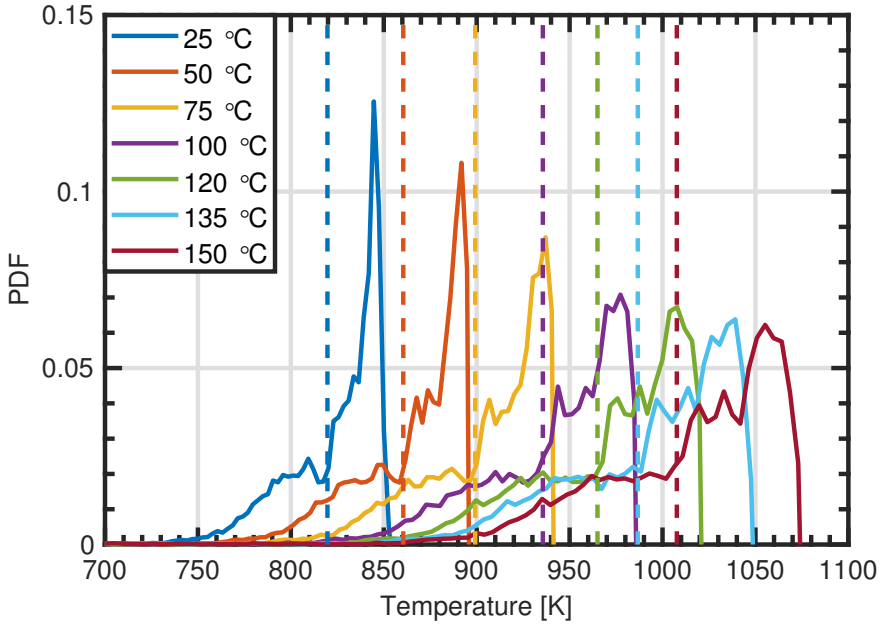

(b)

Figure 8.6: PDF of in-cylinder temperature at -IVC (a) and TDC (b) for the intake temperature sweep at 1000 RPM and 1.5 bar intake pressure. Dashed lines indicate the mass-averaged mean temperature.

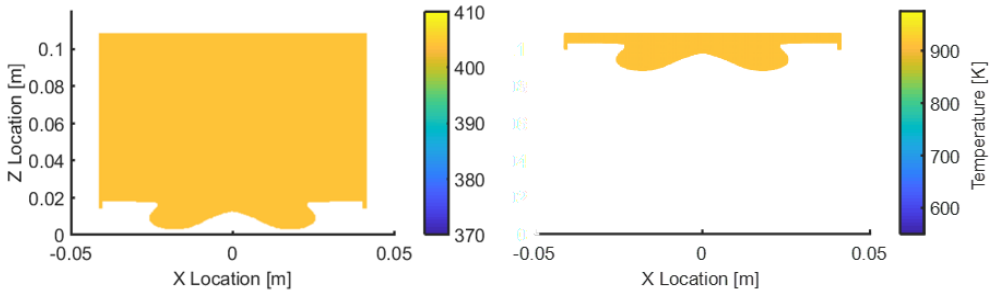

(a) Mass-Averaged

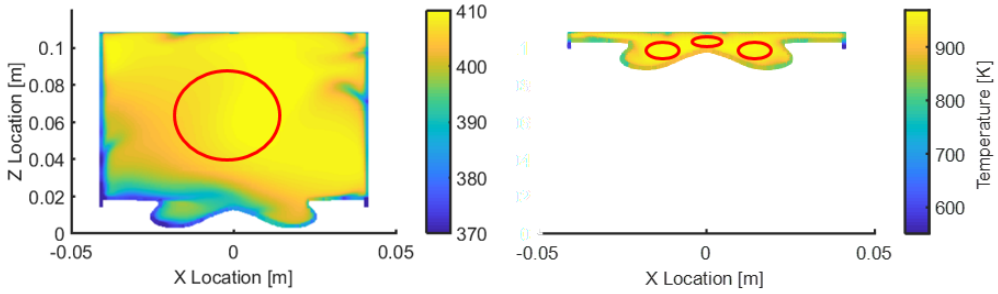

(b) Inner Core

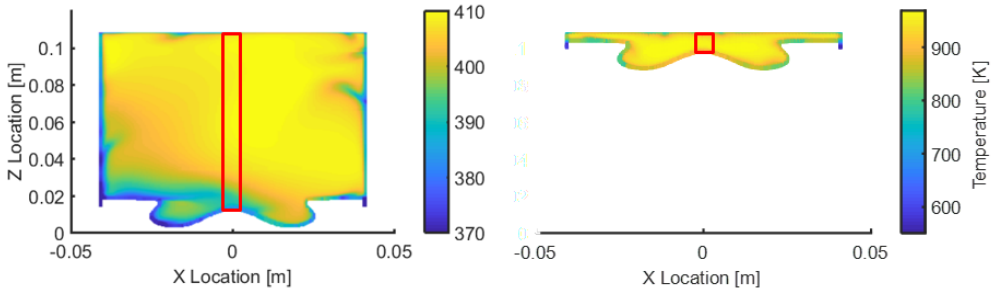

(c) Spectroscopy

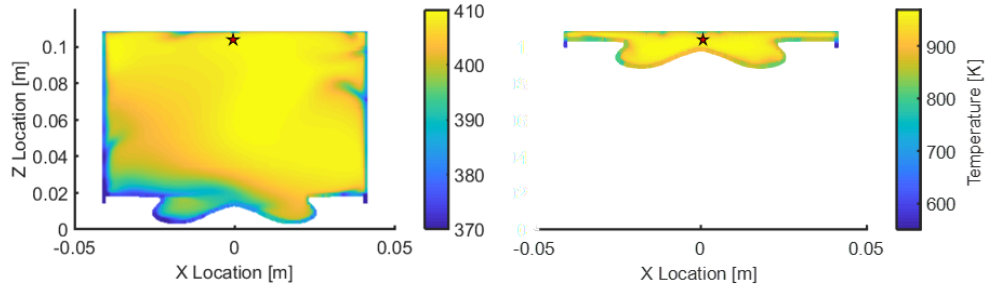

(d) Thermocouple

Figure 8.7: From top to bottom: mass-averaged (a), inner core (b), spectroscopy (c), and thermocouple (d) temperature locations at IVC (left) and TDC (right) for a motored cycle at 1000 RPM, 1.5 bar intake pressure, and 423 K intake temperature.

the intake and wall temperature at motored conditions. It was seen that the biases were proportional to the difference between the intake and wall temperature. Therefore, the simulations were expected to be a worst-case estimate for the biases, especially for fired conditions where the wall temperatures were expected to be substantially higher than the coolant temperature and thus relatively close to the elevated intake temperatures. A summary of the worst-case estimated biases at IVC for each temperature estimation method are seen in Table 8.3.

When the wall temperature is close to the intake temperature, the biases associated with the different temperature measurement methods approaches zero at IVC. Due to the elevated intake temperatures used for the main six operating conditions, 383-463 K, wall temperatures are expected to be relatively close to the intake temperatures. A bias correction was not applied to the temperature estimation methods due to the uncertainty in estimating wall temperatures combined with uncertainty in the absolute accuracy of the Converge simulations. There is, however, an additional uncertainty associated with these potential biases, which was conservatively set to 50% of the worst case bias listed in Table 8.3 and was combined with each previously discussed temperature uncertainty in quadrature. The reported temperatures from the previous sections combined with the uncertainties, now modified with the method bias uncertainty, are used as the reported values for the rest of the chapter.

The effect of thermocouple height location was also investigated to validate the placement location; Figure 8.10 shows that any height >2 mm was not greatly influenced by the wall boundary layer and matched closely with the inner core temperature.

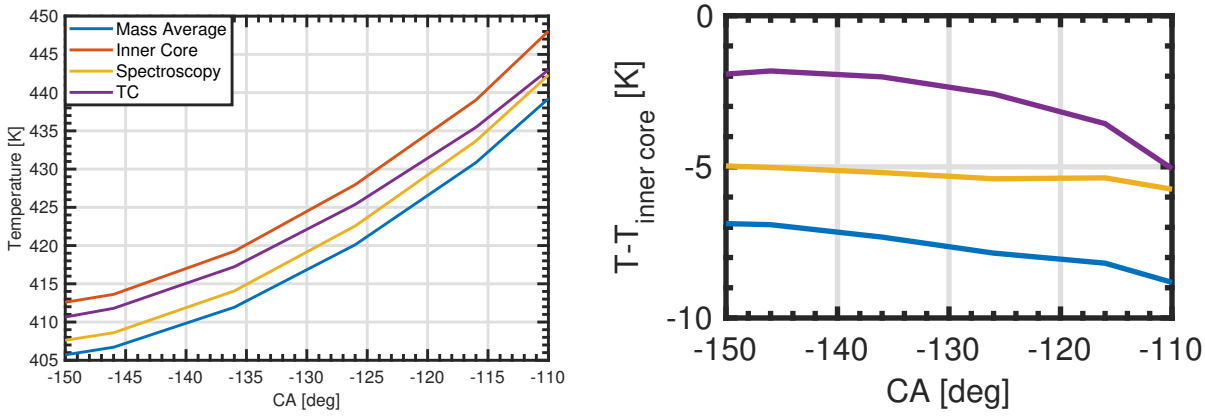

(a) (b)

Figure 8.8: Temperature (left) and temperature difference from inner core method (right) for all temperature measurement methods for motored conditions at 1000 RPM, 423 K intake temperature, and 1.5 bar intake pressure.

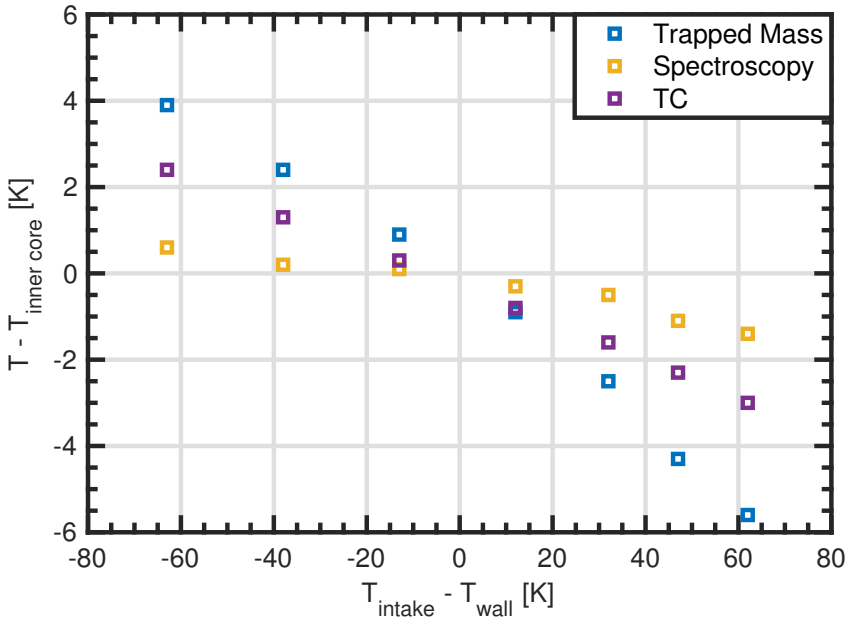

Figure 8.9: Comparison of the difference between trapped mass, spectroscopy, and thermocouple measurement methods and the inner core temperature for motored conditions at IVC as a function of the difference between the intake temperature and the wall temperature.

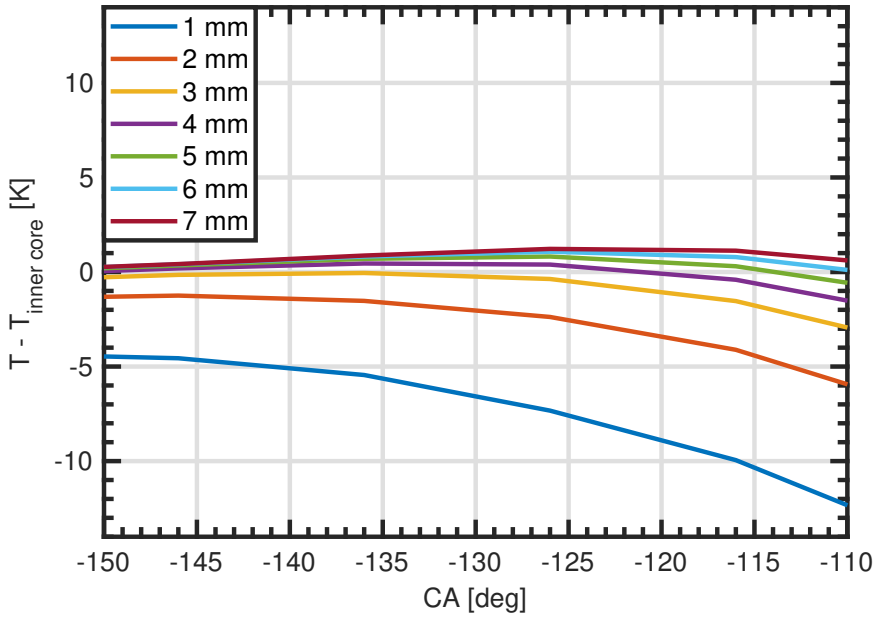

Figure 8.10: Impact of thermocouple placement on the measured temperature relative to the inner-core temperature, determined from Converge simulations.

Table 8.3: Summary of worst case temperature measurement bias at IVC, where the bias is the difference between each temperature method and the inner core temperature.

	Motored						Fired
Speed [RPM]	1000	2000	1000	2000	1000	2000	1000
Intake Pressure [bar]	2.25		1.5		0.90		1.5
Intake Temperature [K]	383	383	423	423	423	423	423
Trapped Mass Bias [K]	-0.6	-0.7	-5.2	-4.6	-7.7	-5.8	-4.7
Spectroscopy Bias [K]	-0.1	-0.5	-1.0	-1.4	-3.6	-2.0	-1.5
Thermocouple Bias [K]	-0.5	-1.5	-2.6	-6.8	-7.1	-7.1	-4.5

8.3 Experimental Temperature Comparison

8.3.1 Motored Conditions

Experimental results were compared for the three temperature measurement methods for motored conditions. Figures 8.11 and 8.12 show a comparison of the temperature estimation methods with uncertainty for all motored conditions at 1000 and 2000 RPM. Overall there was reasonable agreement between all methods, with both the spectroscopy temperatures and thermocouple temperatures consistently higher than the trapped mass temperatures. Figure 8.13 shows difference between the thermocouple/spectroscopy temperatures and the trapped mass temperatures at the high intake temperatures representative of the fuel substitution testing. There is reasonable agreement within the uncertainty bounds of each measurement method. Relative to the trapped mass temperatures, the most commonly used method for temperature measurements, the thermocouple temperatures were approximately 5-10 K higher and the spectroscopy temperatures were approximately 15 K higher. The uncertainty bounds overlapped for all three methods for a majority of the conditions. Due to the thermocouple temperatures having the lowest uncertainty bounds, it appears that the spectroscopy temperatures were biased slightly high and the trapped mass temperatures were biased slightly low.

8.3.2 Fired Conditions

Results were also compared for the spectroscopy and trapped mass measurement methods for fired conditions, as seen in Figures 8.15 and 8.16. Thermocouple data were not available for fired conditions. Results were similar to the motored conditions, with the temperature uncertainty bounds overlapping for all conditions except one case at 1000 RPM. The spectroscopic temperature was again consistently higher than the trapped mass temperatures by about 5-10 K. Figure 8.16 shows the difference between the spectroscopic temperatures and the trapped mass temperatures at the high intake tempera-

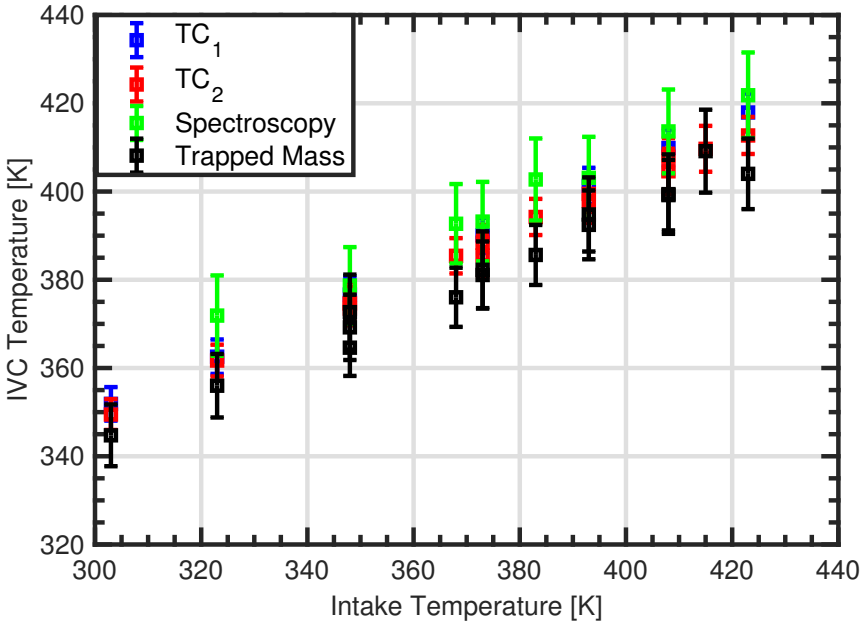

Figure 8.11: Comparison of thermocouple, spectroscopy, and trapped mass measurement methods at IVC as a function of intake temperature at 1000 RPM and 2.25, 1.5, and 0.9 bar intake pressure for motored conditions.

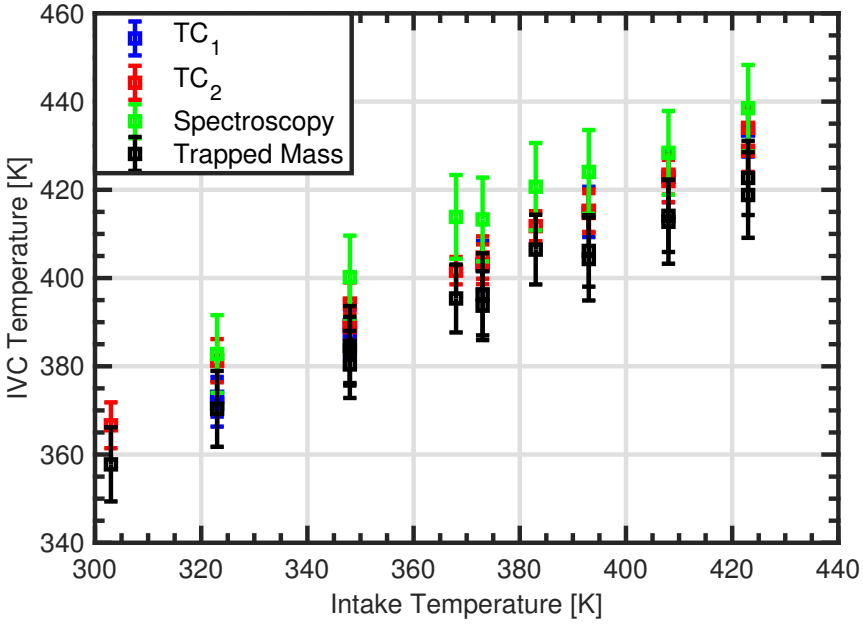

Figure 8.12: Comparison of thermocouple, spectroscopy, and trapped mass measurement methods at IVC as a function of intake temperature at 2000 RPM and 2.25, 1.5, and 0.9 bar intake pressure for motored conditions.

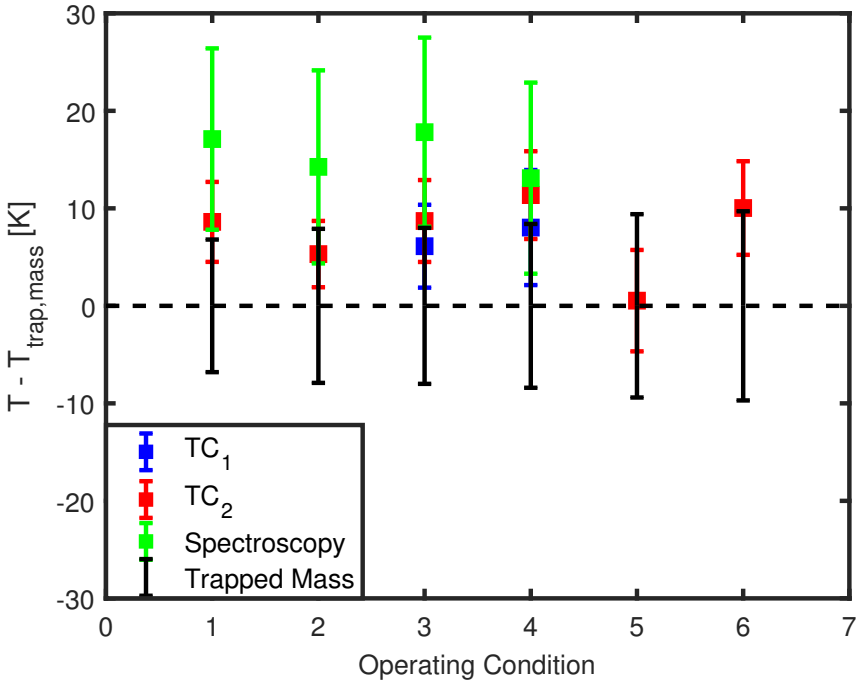

Figure 8.13: Comparison of thermocouple, spectroscopy, and trapped mass measurement methods at IVC as a function of motored operating condition.

tures representative of the fuel substitution testing; reasonable agreement is seen for all four conditions.

8.3.3 Combining Estimation Methods

For the fired conditions, the spectroscopy and trapped mass measurements with their respective uncertainties were combined into a single temperature value by

$$T_{final} = \frac{\sum_{i=1}^{N} w_i T_i}{\sum_{i=1}^{N} w_i} \tag{8.2}$$

$$CI_{95} = T_{final} \pm \sqrt{\frac{1}{\sum_{i=1}^{N} w_i}} \tag{8.3}$$

$$w_i = \frac{1}{\sigma_i^2}, \tag{8.4}$$

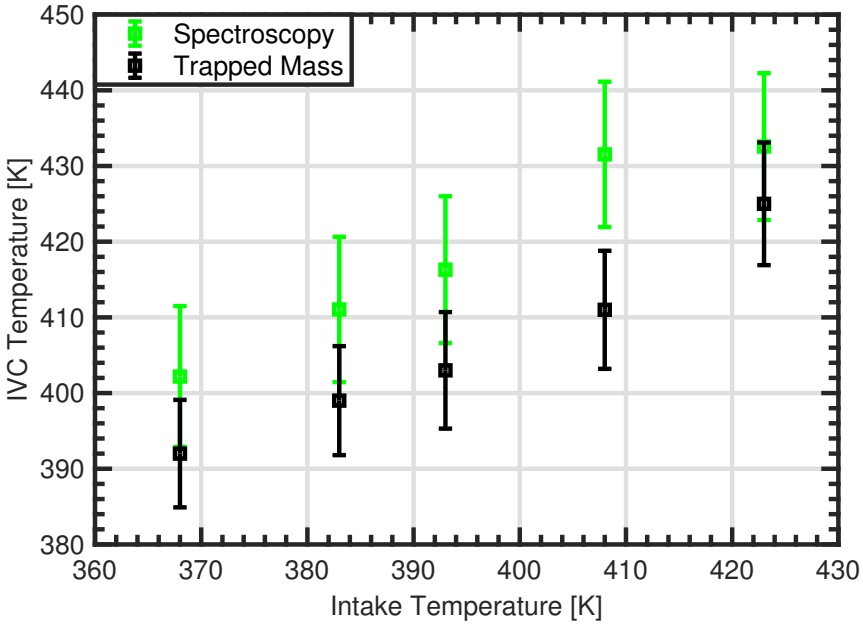

Figure 8.14: Comparison of spectroscopy and trapped mass measurement methods at IVC as a function of intake temperature at 1000 RPM and 2.25, 1.5, and 0.9 bar intake pressure for fired conditions.

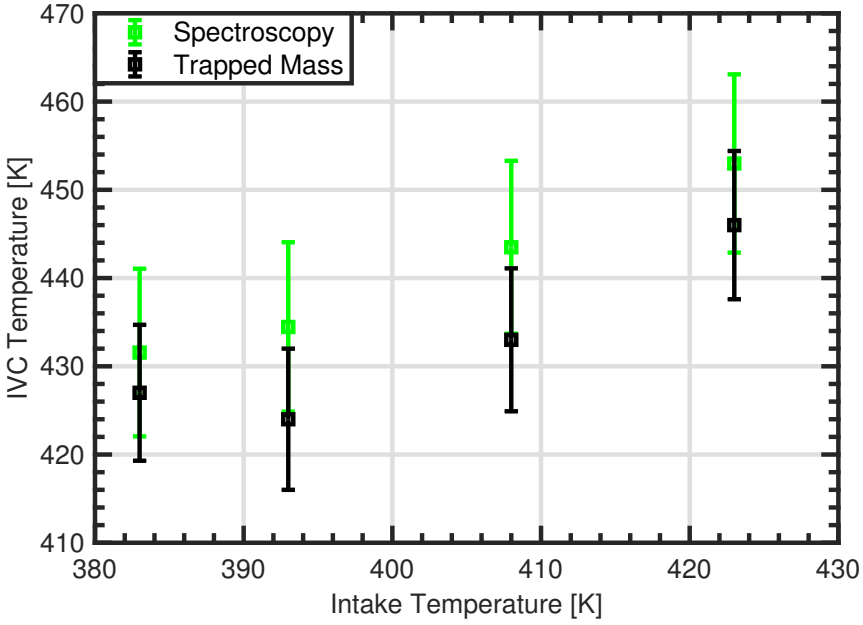

Figure 8.15: Comparison of spectroscopy and trapped mass measurement methods at IVC as a function of intake temperature at 2000 RPM and 2.25, 1.5, and 0.9 bar intake pressure for fired conditions.

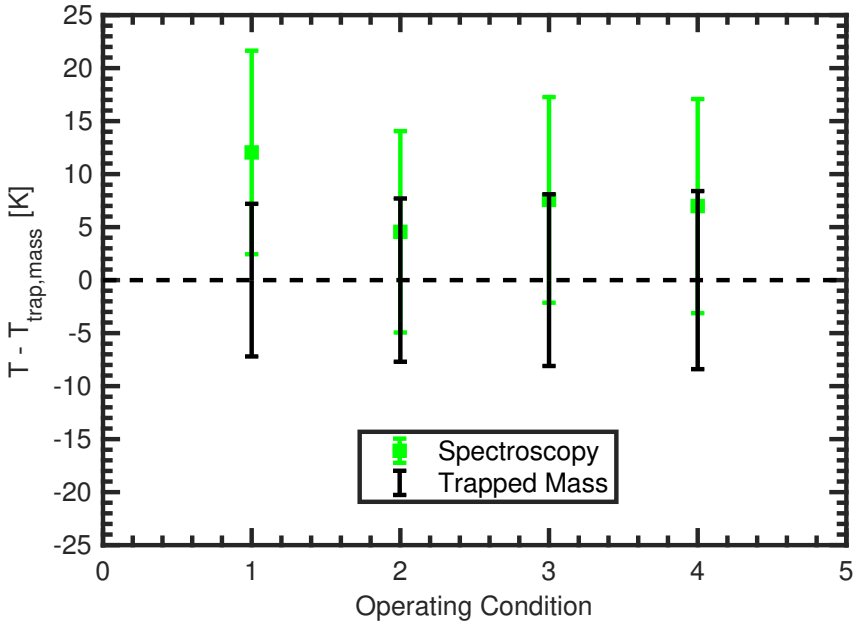

Figure 8.16: Comparison of spectroscopy and trapped mass measurement methods at IVC as a function of fired operating condition.

where T_{final} is the weighted average temperature, T_i is each individual temperature estimation, CI_{95} is the weighted 95% confidence intervals, and σ_i is each individual temperature uncertainty. The weighting is proportional to the inverse uncertainty squared, which gives more weight to the methods that have the lowest uncertainty. The different temperature estimation methods along with the weighted average for motored and fired conditions are shown in Tables 8.4 and 8.5. The spectroscopic and trapped mass weighted temperatures were available for fired operating conditions 1-4, spectroscopy was not available for operating conditions 5-6 so the weighted temperature was set equal to the trapped mass temperature for those conditions. The weighted temperatures and respective uncertainties shown in Table 8.5 were used for all fired experimental temperatures shown in the following chapters.

Table 8.4: Combined temperature measurement with uncertainties for motored conditions.

Speed [RPM]	1000	2000	1000	2000	1000	2000
Intake Pressure [bar]	2.25		1.5		0.90	
Intake Temperature [K]	383	383	423	423	423	423
Trapped Mass [K]	386±7	406±8	404±8	423±8	409±9	419±10
TC_1 [K]			418±4	433±6		
TC_2 [K]	394±4	412±3	413±4	434±5	410±5	429±5
Spectroscopy [K]	403±9	421±10	422±10	439±10		
T_{final} [K]	393±3	412±3	415±3	433±3	410±5	427±4

Table 8.5: Combined temperature measurement with uncertainties for fired conditions.

Speed [RPM]	1000	2000	1000	2000	1000	2000
Intake Pressure [bar]	2.25		1.5		0.90	
Intake Temperature [K]	383	383	423	423	463	453
Trapped Mass [K]	399±7	427±8	425±8	446±8	438±9	455±9
Spectroscopy [K]	411±10	432±10	433±10	453±10		
T_{final} [K]	403±5	429±5	428±5	449±6	438±9	455±9

8.4 Conclusions

CFD simulations were performed to gain insight into the in-cylinder conditions. A fairly large spread in y_{res} was seen at IVC conditions, which decreased throughout the compression stroke; however, this residual gas stratification did not appear to cause temperature stratification. Disagreement was seen between the true residual mass fraction and the calculated residual mass fraction using the Yun and Mirsky correlation, with the Yun and Mirsky correlation producing artificially high values, especially at motored conditions. Mass-averaged cylinder velocity was seen to be fairly constant throughout the compression stroke and slightly larger than mean piston speed. The amount of in-cylinder temperature stratification at IVC was proportional to the difference between intake temperature and wall temperature, while the amount of in-cylinder temperature stratification at TDC was proportional to the intake temperature. The worst-case biases for the three different estimation methods were <5 K for all cases, and decreased to 0 K as the intake temperature approached the wall temperature.

For both motored and fired conditions, the spectroscopy temperatures were consis-

tently higher than the trapped mass temperatures, with the uncertainty bounds of each measurement overlapping for most cases. For motored conditions, the thermocouple measurements, which had the lowest uncertainty, were in-between the spectroscopy and trapped mass temperatures. These results suggest that the spectroscopy temperatures are likely biased slightly high and the trapped mass temperatures are likely biased slightly low. For fired conditions, the spectroscopy and trapped mass temperatures were combined to form a single estimated temperature, T_{final} with a corresponding CI_{95} for each condition.

Chapter 9

Absolute Reactivity Simulations

The focus of the last several chapters was obtaining reliable estimates of the in-cylinder thermodynamic conditions. The objective of the work outlined in this chapter was to evaluate each kinetics mechanism based on its ability to match the engine experiments on an absolute basis. The in-cylinder thermodynamic conditions required in the engine simulation to match the experimental combustion metrics were compared to the experimental thermodynamic conditions. The baseline engine cases for each of the six operating conditions using reference fuel mixtures of both methane/propane and methane/hydrogen were used for this evaluation. Cantera was selected as the simulation tool for these experiments for its solution speed and simplicity compared to a full CFD program such as Converge.

9.1 Single-zone Model

The first model investigated was a single-zone engine simulation from IVC to EVO. The reactor was initialized at IVC with the experimentally measured pressure, temperature, and mole fractions. The main model parameters that were allowed to vary included compression ratio, heat transfer multiplier, and wall temperature. The heat transfer multiplier is a global multiplier used to scale the calculated heat transfer. The Annand

correlation [80],

$$h = C\frac{k}{D}Re^{0.7} \tag{9.1}$$

was used to estimate the convective heat transfer coefficient h; C is a constant coefficient, k is the conductivity of air, D is the bore, and Re is the Reynolds number. The heat transfer coefficient is utilized in Newton's law of cooling,

$$\dot{Q} = hA(T - T_w), \tag{9.2}$$

where A is the combustion chamber surface area, and T and T_w are the gas and wall temperatures. The mean piston speed was used as the characteristic velocity and combustion chamber bore as the length scale in the Reynolds number calculation. The Annand correlation was chosen for its ease of implementation and wide use in engine literature.

Experimental motoring cases were simulated first in order to calibrate the model without the complications of combustion. Compression ratio, heat transfer multiplier, and wall temperature were swept in a full factorial DOE to find the values that resulted in a minimum MSE between the simulated and experimental pressure traces for all six operating conditions in the range of -100 to 100 CAD. The compression ratio and global heat transfer multiplier were constrained to be the same for all operating conditions while wall temperature was allowed to vary independently for each condition. The parameter values that resulted in the lowest MSE can be seen in Table 9.1. Figures 9.1 and 9.2 show the experimental (solid) and simulated (dashed) pressures and relative pressure differences as a function of crank angle. Excellent agreement was achieved for all six operating conditions, with pressure residuals <1% throughout the compression stroke.

With the compression ratio and heat transfer multipliers selected, wall temperatures were optimized to match the firing pressure traces. The range of -30 to -10 CAD was chosen to ensure that pressure was closely matched near the start of combustion but prior to any heat release. The wall temperatures that resulted in the minimum MSE

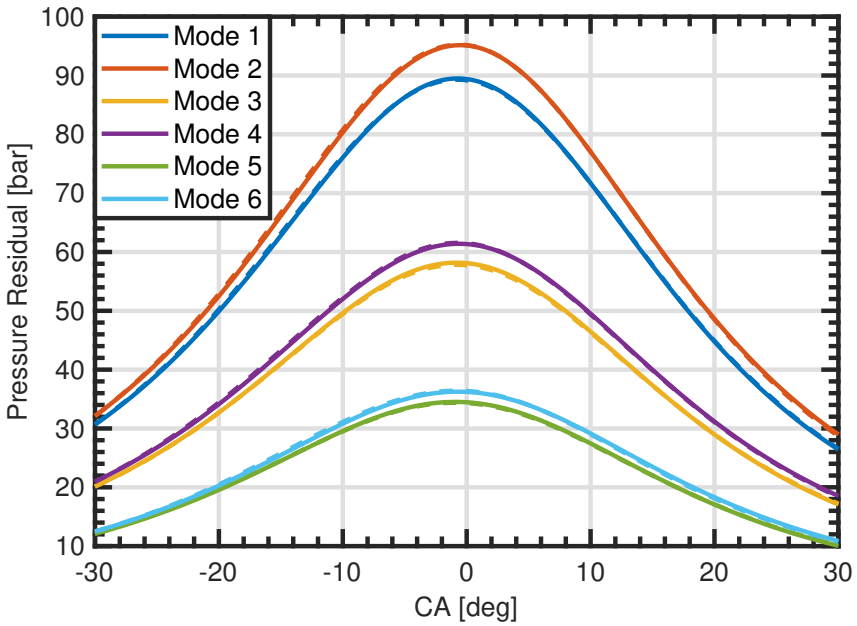

Figure 9.1: Experimental (dashed) and simulated (solid) pressure as a function of CA for motored conditions using single-zone model. Note that the experimental data are difficult to discern as they lie almost directly on top of the simulated curves.

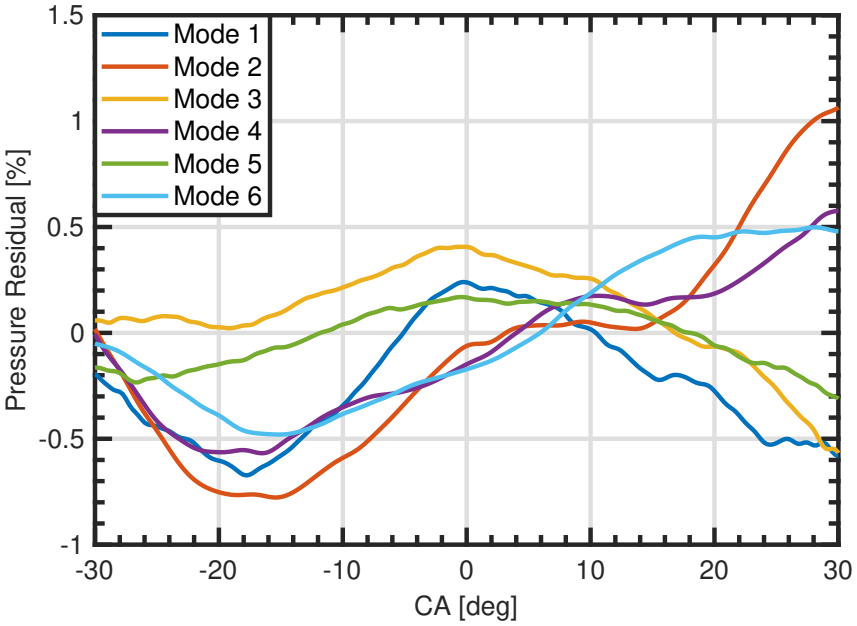

Figure 9.2: Difference between experimental and simulated compression pressure as a function of CA for motored conditions.

Table 9.1: Summary of motoring conditions and model parameters.

		1	2	3	4	5	6
Engine Speed	RPM	1000	2000	1000	2000	1000	2000
Intake Pressure	bar	2.25		1.5		0.90	
Compression Ratio	-	16.4	16.4	16.4	16.4	16.4	16.4
Heat Transfer Multiplier	-	1	1	1	1	1	1
Motored Wall Temperature	K	350	474	378	464	406	484
Fired Wall Temperature	K	410	560	425	560	485	560

between experimental and simulated pressure are shown in Table 9.1. It should be noted that wall temperatures were unreasonably high, especially for the 2000 RPM operating conditions. The wall temperatures were used as a model calibration tool that compensated for simplifications of the model such as neglecting crevice volume and blow-by; the desired outcome was to accurately match the experimental pressure rather than obtaining physically meaningful wall temperatures. Figures 9.3 and 9.4 show the comparison between experimental and simulated pressures from -30 to -10 CAD; similar to the motored conditions, excellent agreement for all six operating conditions was achieved, with a maximum difference of 1%. No combustion was seen in the simulation cases because the chemistry solver was disabled in order to reduce solution time.

Simulations were run for all baseline CH4/C3H8 mixtures with the chemical kinetics mechanisms listed in Table 2.2. With all other conditions fixed, temperature at IVC was adjusted in the simulation until $CA_{50,sim}$ matched $CA_{50,exp}$. The required $T_{IVC,sim}$ was substantially higher than $T_{IVC,exp}$ for all mechanisms other than the UBC mechanism, requiring temperatures 40-120 K higher than the experimental temperatures, well outside the experimental temperature uncertainty bounds.

The Converge CFD simulations (see Section 8.2) were used to investigate the amount of temperature stratification near SOC. Figure 9.5 shows the difference in temperature between the hottest 10% of the cylinder contents and the average temperature. The single-zone model would be expected to match the average temperature, causing the inner core temperature to be underestimated by up to 60 K.

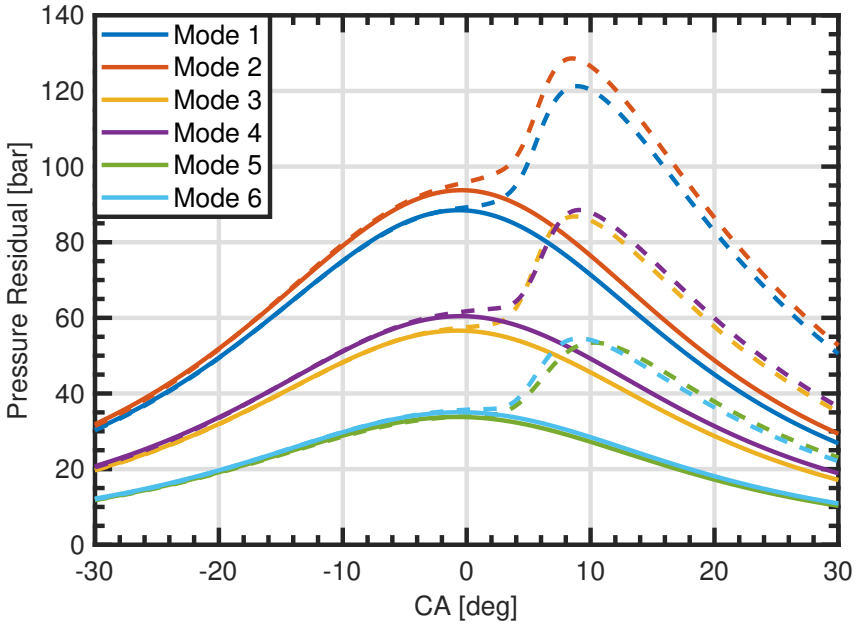

Figure 9.3: Experimental (dashed) and simulated (solid) pressure as a function of CA for fired conditions.

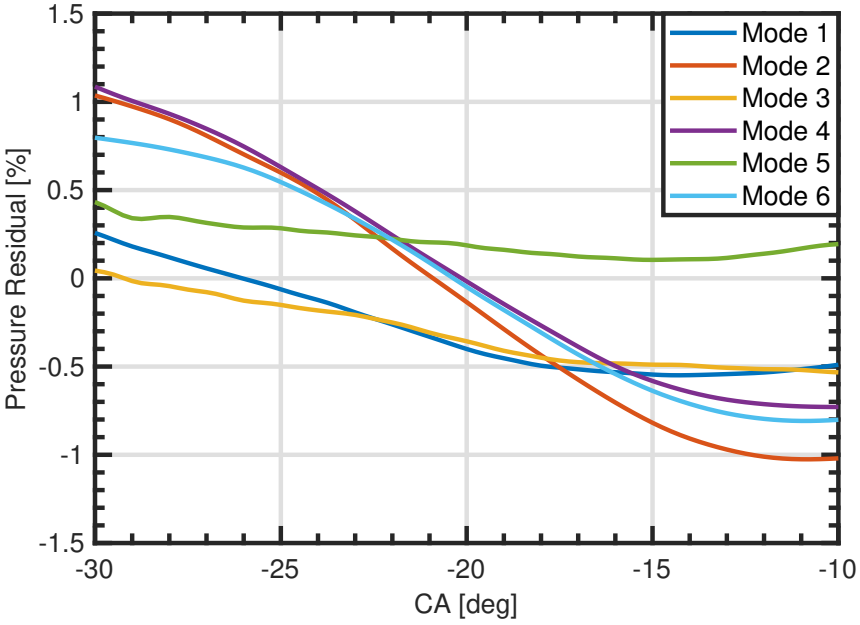

Figure 9.4: Difference between experimental and simulated compression pressure as a function of CA for fired conditions.

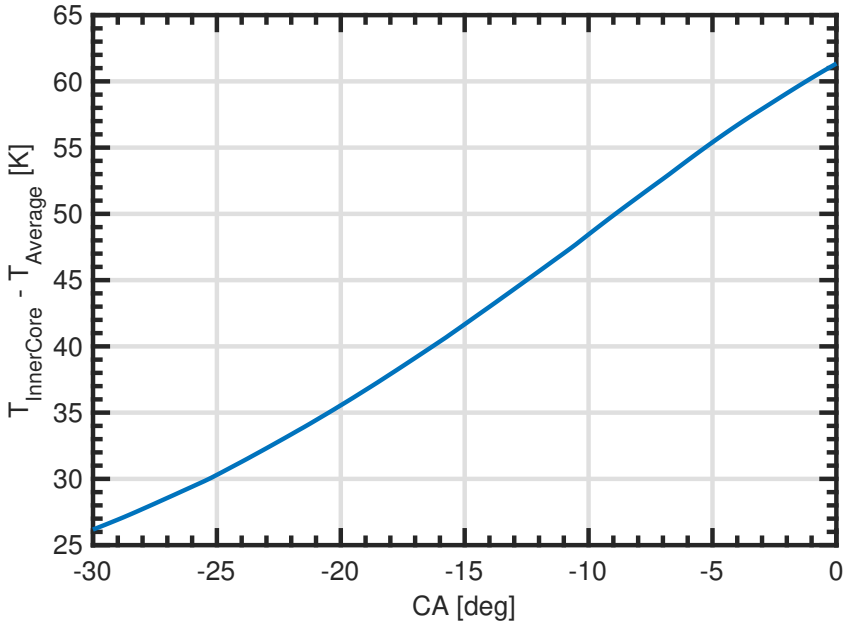

Figure 9.5: Inner core vs. mean temperature as a function of crank angle.

9.2 Two-zone Model

Combustion is expected to begin in the hottest, inner-core region. A two-zone model was created in Cantera so that the inner-core was accounted for. The main, outer zone was identical to the single-zone model, except that the volume was set equal to 90% of the total IVC volume. The T_{IVC} for the outer zone was fixed at the experimental T_{IVC}. The inner-zone volume was set equal to 10% of the total IVC volume, and it was also identical to the single-zone model except that it was adiabatic. No mass transfer occurred between zones, but pressure was equilibrated between the two zones via a movable wall. The inner-core volume of 10% was chosen to represent the initial 10% of combustion; when comparing to experimental data $CA_{50,sim,core}$ was compared to $CA_{10,exp}$. It is noted that technically $CA_{50,sim,core}$ should be compared to $CA_{5,exp}$, but $CA_{10,exp}$ was seen to be more consistent throughout the experimental data sets. Alternatively, the inner-core volume could be set to 20% of the total IVC volume and compared to $CA_{10,exp}$; this method resulted in a difference in $T_{IVC,sim,core}$ of <0.5 K compared to when the inner-

core volume was set to 10 % of the total IVC volume. In order to reduce the effect of the inner-core volume on the main, outer zone which was tuned to match experimental pressures, the inner-core volume of 10% was used for all reported simulation results in the current work. $CA_{50,sim,core}$ was calculated by

$$AHRR_{core} = \frac{\gamma}{\gamma - 1} P \frac{dV_{core}}{d\theta} + \frac{1}{\gamma - 1} V_{core} \frac{dP}{d\theta} \tag{9.3}$$

$$CHR_{core} = \int_{-50}^{80} AHRR_{core} d\theta, \tag{9.4}$$

with a constant value of 1.34 used for γ to replicate the process used to calculate $CA_{10,exp}$ from the experimental data. When comparing the two-zone, inner-core temperature to the mean temperature it was seen that the Cantera simulation showed a similar trend to the Converge simulation, see Figure 9.6. It is noted that a difference of approximately 5 K is seen between the Cantera and Converge simulations at TDC; this difference was small compared to other experimental and simulation uncertainties and the root cause was not investigated further in the current work.

An additional benefit of using the two-zone model is that the inner core is isentropically compressed so that its temperature is somewhat independent of the outer-zone temperature. By fixing the heat transfer multiplier, wall temperatures, and $T_{IVC,outer}$ for the outer zone, the simulation pressure can consistently match the experimental pressure. Figure 9.7 shows the pressure and temperature at TDC for the inner core and the outer zone; the inner core IVC temperature was adjusted by 100 K in each direction while the TDC pressure changed by less than 0.5% from its nominal value. With the single-zone model it was seen that as $T_{IVC,sim}$ was increased, heat transfer also increased which caused the simulation pressure to decrease below the experimental pressure, which required a wall temperature adjustment to recover the pressure match. Also, using a two-zone model effectively eliminated the large source of temperature uncertainty near TDC due to V_{TDC} estimation uncertainty; the inner-core's isentropic compression was only

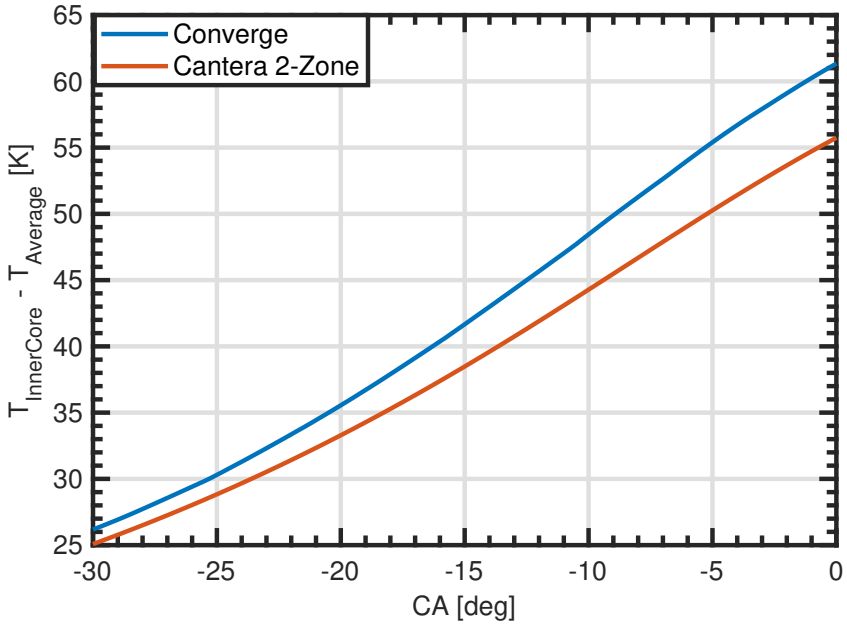

Figure 9.6: Inner core vs. average temperature as a function of crank angle from Converge and Cantera simulations.

dependent on the simulated pressure, which was matched to the experimental pressure, and independent of volume.

Combustion performance of the inner core was the focus of this simulation, so chemistry was turned off for the outer zone to reduce simulation time. This had an additional benefit of allowing $T_{IVC,core}$ to be set lower than $T_{IVC,outer}$ for simulations with mechanisms that over-predicted the fuel reactivity compared to the engine experiments. With chemistry turned on in the outer zone, $T_{IVC,outer}$ would need to be reduced to avoid premature combustion in the outer zone, which would affect heat transfer rates and cause a mismatch between simulated and experimental compression pressures.

9.3 Ignition Delay Calculations

Constant pressure ignition delay simulations for the various fuels and mechanisms of interest were also computed in Cantera. Temperature, pressure, test fuel, and equivalence ratio were specified for each test case. A representative example of an ignition delay

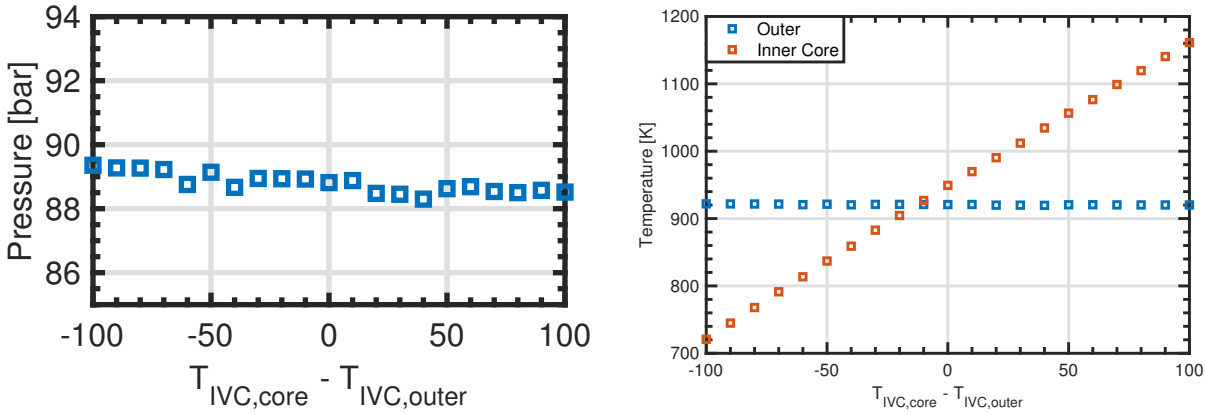

(a) (b)

Figure 9.7: TDC pressure (left) and core and outer TDC temperatures (right) as a function of the difference between core and outer IVC temperatures.

simulation is shown in Figure 9.8, where temperature and OH concentration are plotted as a function of time. Temperature started to rise around 2 ms, with a 100 K increase by 3.25 ms, while the rapid increase in OH concentration did not occur until after 3.5 ms. Specifying an ignition delay criteria is a non-trivial matter; two methods were investigated, one tracking the gradient of the OH concentration and the other tracking the temperature rise.

Figure 9.9 shows an example of the OH gradient ignition delay method. First the location and value of the maximum gradient was found. Next, a line with slope equal to the maximum gradient was extended from the location of maximum gradient. The ignition delay was defined as the time at which the line intersects zero on the ordinate. Alternatively, the ignition delay can be defined as the time where the maximum gradient occurs; for this case the difference between these two methods was <1%. Referring to Figure 9.8, it is seen that the OH concentration had a sharp increase near the end of the temperature rise, indicating that this method will produce a conservative estimate of the ignition delay.

The ignition delay can also be defined as the time at which the temperature crosses a threshold value. Figure 9.10 shows an example of normalized temperature as a function

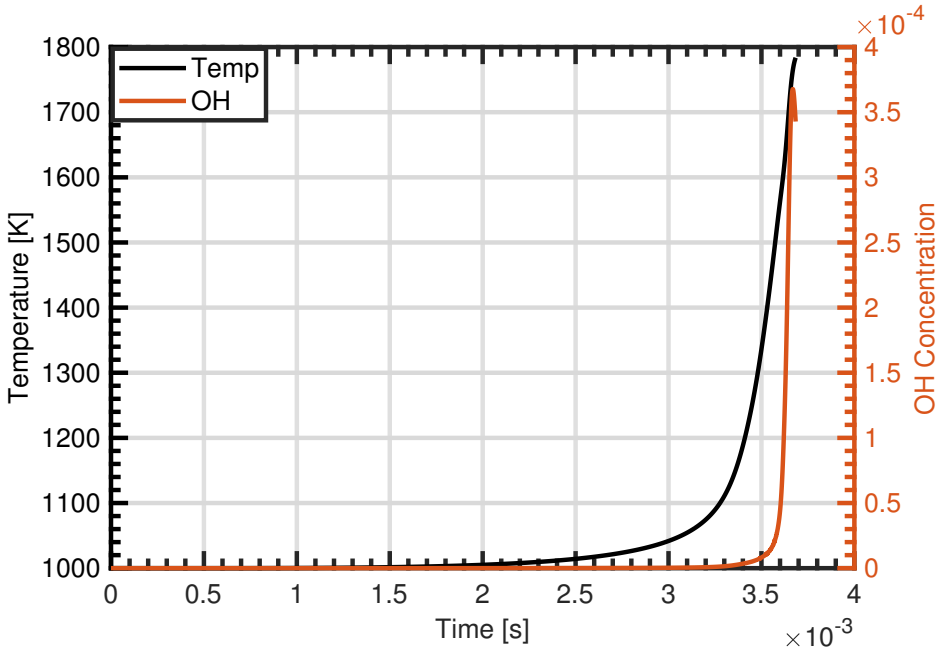

Figure 9.8: Temperature and OH concentration vs. time for a constant pressure ignition delay simulation using the C5-49 mechanism with ethane at 1000 K temperature, 60 bar pressure, and 0.35 equivalence ratio.

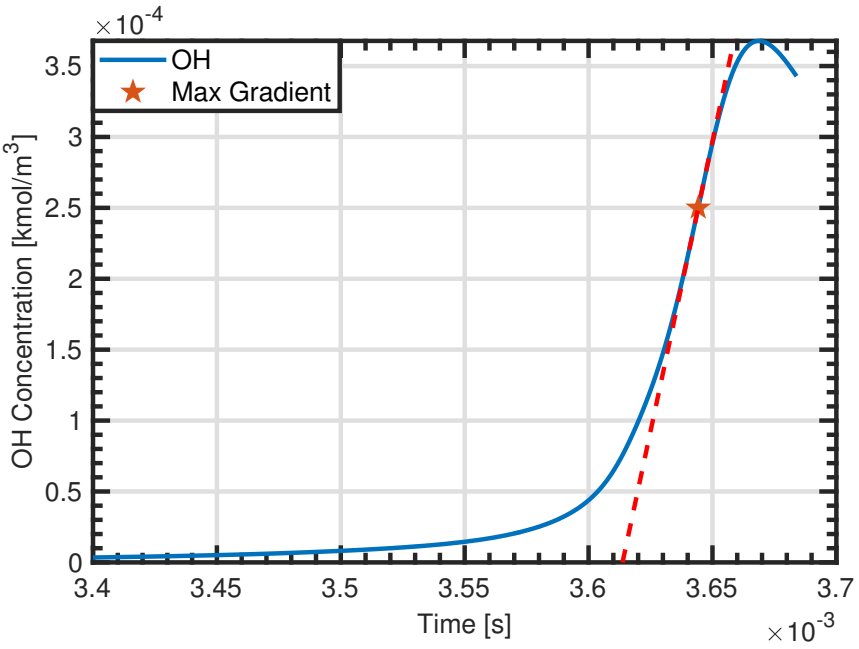

Figure 9.9: OH concentration vs. time. The location of maximum gradient and a line with slope equal to the maximum gradient passing through the location of maximum gradient are also shown.

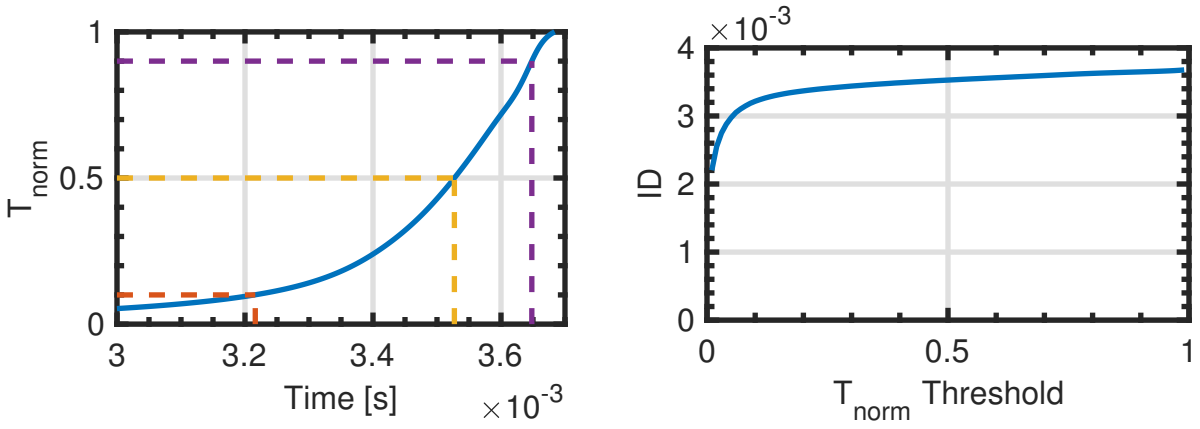

(a) (b)

Figure 9.10: Normalized temperature vs. time plotted with thresholds of 0.1, 0.5, and 0.9 (left). Ignition delay as a function of normalized temperature threshold.

of time along with threshold values of 0.1, 0.5, and 0.9. The normalized temperature is defined as

$$T_{norm} = \frac{T - T_0}{T_f - T_0}, \tag{9.5}$$

where T_0 is the initial temperature and T_f is the final temperature after ignition; the normalized temperature can be thought of as the fractional temperature rise from the initial temperature to the adiabatic flame temperature. The ignition delay showed a strong dependence on the temperature threshold. Figure 9.11 shows the ignition delay, normalized by the maximum ignition delay, as a function of the normalized temperature threshold for several hydrocarbon fuels. The ignition delay trends were fuel dependent, with ethane and propane showing similar trends, but *n*-butane and methane showing different behavior. This is an important result, because it means the relative ratio of ignition delay between the different fuels will vary as the temperature threshold varies.

An important part of the current work involved comparing the ignition quality of a variety of fuels, which means selecting a meaningful method for defining ignition delay was critical. Due to the high sensitivity of the ignition delays to low temperature thresholds, the OH-gradient method was used for all ignition delays shown in the following

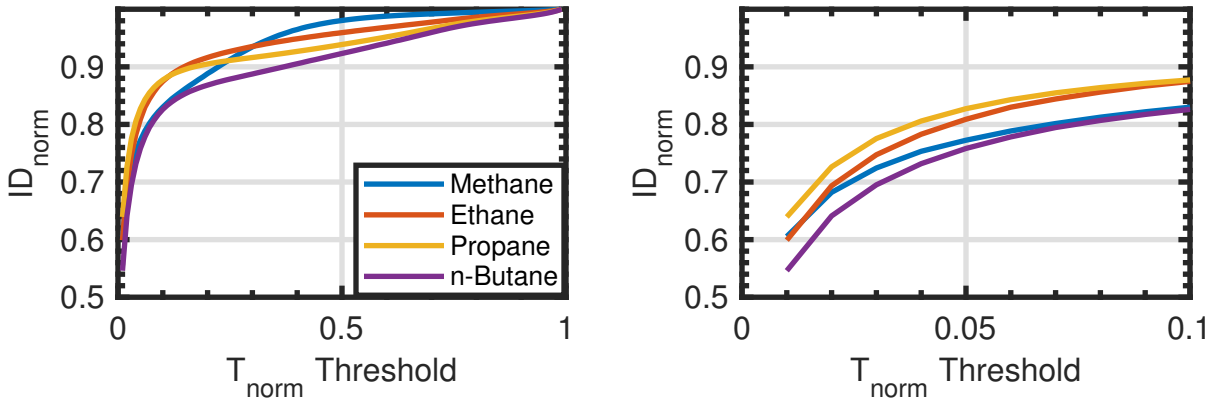

(a) (b)

Figure 9.11: Normalized ignition delay as a function of normalized temperature threshold for methane, ethane, propane, and *n*-butane (left) and zoomed in version (right).

sections. An important note is that this method works well for fuels that have minimal low temperature chemistry, such as methane, ethane, and hydrogen, which are the main focus of the current work.

9.4 Baseline Condition Simulations

9.4.1 Methane/Propane Baseline Conditions

Simulations were run for all baseline CH_4/C_3H_8 and CH_4/H_2 mixtures. With all other conditions fixed, $T_{IVC,sim,core}$ was adjusted in the simulation until $CA_{50,sim,core}$ matched $CA_{10,exp}$. The results of the baseline CH_4/C_3H_8 simulated cases with all mechanisms can be seen in Figures 9.12 and 9.13 and Table 9.2. A detailed discussion of the different mechanisms investigated can be found in Section 2.4. There was excellent agreement between $T_{IVC,exp}$ and $T_{IVC,sim,core}$ using the LLNL mechanism, with only operating condition 1 falling outside the uncertainty bounds of the experimental temperatures. Simulated results with the Aramco and C5-49 mechanisms were also reasonably close, within 20 K of the experimental temperatures and within 10 K of the uncertainty bounds, with the C5-49 performing slightly better than the Aramco mechanism. The GRI mechanism

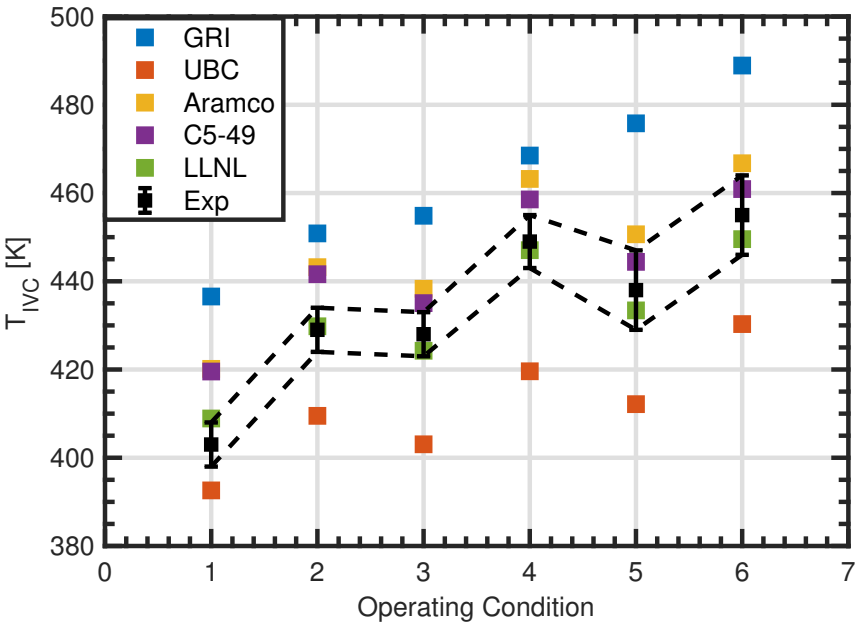

Figure 9.12: Comparison of simulated core T_{IVC} required to match experimental combustion phasing for CH_4/C_3H_8 baseline conditions and the experimental values.

required substantially higher core temperatures, between 20 and 40 K, for all conditions while the UBC mechanism required lower core temperatures, between 10 and 30 K, for all operating conditions.

9.4.2 Methane/Propane Ignition Delay Comparison

Figure 9.14 shows the ignition delays along the isentropic pressure-temperature curves for operating conditions 1 (left) and 6 (right) for fuel mixtures of 80/20 (energy) methane/propane

Table 9.2: Summary of simulated and nominal experimental temperatures at IVC required to match combustion phasing for CH_4/C_3H_8 baseline conditions.

		1	2	3	4	5	6
Engine Speed	RPM	1000	2000	1000	2000	1000	2000
Intake Pressure	bar	2.25		1.5		0.90	
Exp	K	403	429	428	449	438	455
GRI	K	437	451	455	469	476	489
UBC	K	393	410	403	420	412	430
Aramco	K	420	443	438	463	451	467
C5-49	K	420	442	435	459	444	461
LLNL	K	409	430	424	447	433	450

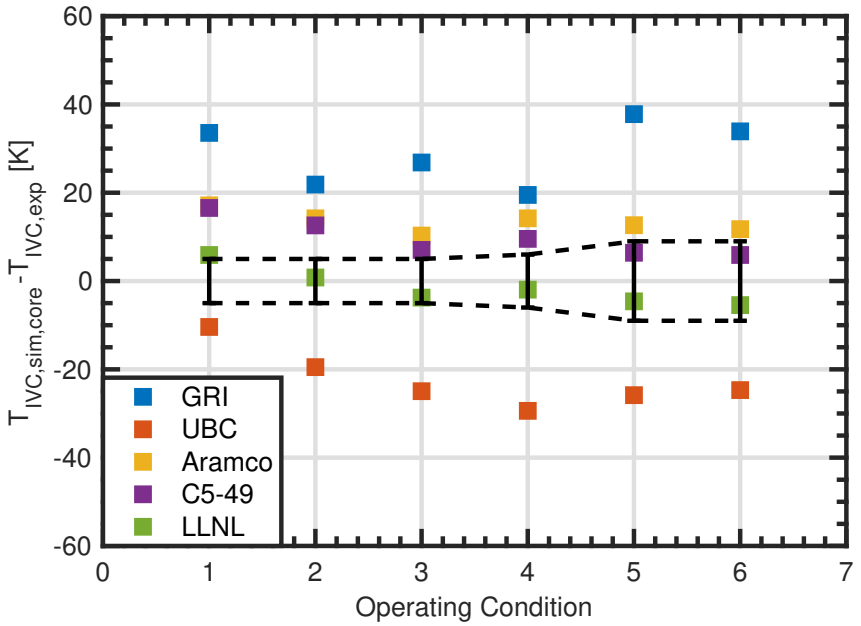

Figure 9.13: Difference between simulated core T_{IVC} required to match experimental combustion phasing and experimental T_{IVC} for CH_4/C_3H_8 baseline conditions.

(a, b), pure methane (c, d), and pure propane (e, f) at an equivalence ratio of 0.35. The isentropic curves were generated by starting at the $T_{IVC,sim,core}$ required to matched the experimental combustion phasing for the LLNL mechanism. Operating condition 1 had the highest pressure and lowest temperature, while operating condition 6 had the lowest pressure and highest temperature. The ignition delays for the baseline CH_4/C_3H_8 mixture show similar trends to those seen in Figure 9.13 where the relative $T_{IVC,sim}$ required for each mechanism correlated with that mechanism's ignition delays. Relative to the C5-49 mechanism, the Aramco mechanism was nearly identical, the LLNL mechanism had slightly lower ignition delays, the UBC mechanism had much lower ignition delays, and the GRI mechanism had much greater ignition delays. It is interesting to note the GRI mechanism's ignition delays were much closer to the Aramco and C5-49 mechanisms' ignition delays at elevated temperatures.

The ignition delays of pure methane were nearly identical for the C5-49, Aramco, and LLNL mechanisms. The UBC mechanism's ignition delays for pure methane were

substantially smaller than the other mechanisms. The GRI mechanism's ignition delays for pure methane were the highest of all mechanisms for temperatures below 1000 K, but became lower than the C5-49, Aramco, and LLNL mechanisms for temperatures above 1000 K.

The ignition delays of propane for all mechanisms other than the GRI mechanism were similar for temperatures above 800 K, with the LLNL and UBC mechanism having slightly lower values for operating condition 6. The GRI mechanism produced a substantially higher ignition delay for propane over all temperatures and pressures.

From these results, it appears that the lower $T_{IVC,sim}$ required by the UBC mechanism relative to the other mechanisms was mainly driven by its methane chemistry, and the higher $T_{IVC,sim}$ required by the GRI mechanism relative to the other mechanisms was mainly driven by its propane chemistry. The smaller differences in $T_{IVC,sim}$ required for the Aramco, C5-49, and LLNL mechanisms appear to be driven mainly by differences in their respective propane chemistry.

9.4.3 Methane/Hydrogen Baseline Conditions

The results of the baseline CH_4/H_2 simulated cases are seen in Figures 9.15 and 9.16 and Table 9.3. The results were very consistent between all mechanisms other than the GRI mechanism, with temperatures within the uncertainty bounds of the experimental temperatures for conditions 2-6, and < 5 K outside the uncertainty bounds for condition 1. The temperature required with the UBC mechanism was consistently lower than the other mechanisms by about 10 K, and was within the uncertainty bounds for conditions 1-3 and approximately 5 K outside the uncertainty bounds for conditions 4-6.

9.4.4 Methane/Hydrogen Ignition Delay Comparison

Figure 9.17 shows the ignition delays along the isentropic pressure-temperature curves for operating conditions 1 (left) and 6 (right) for fuel mixtures of 75/25 (energy) methane/hydrogen

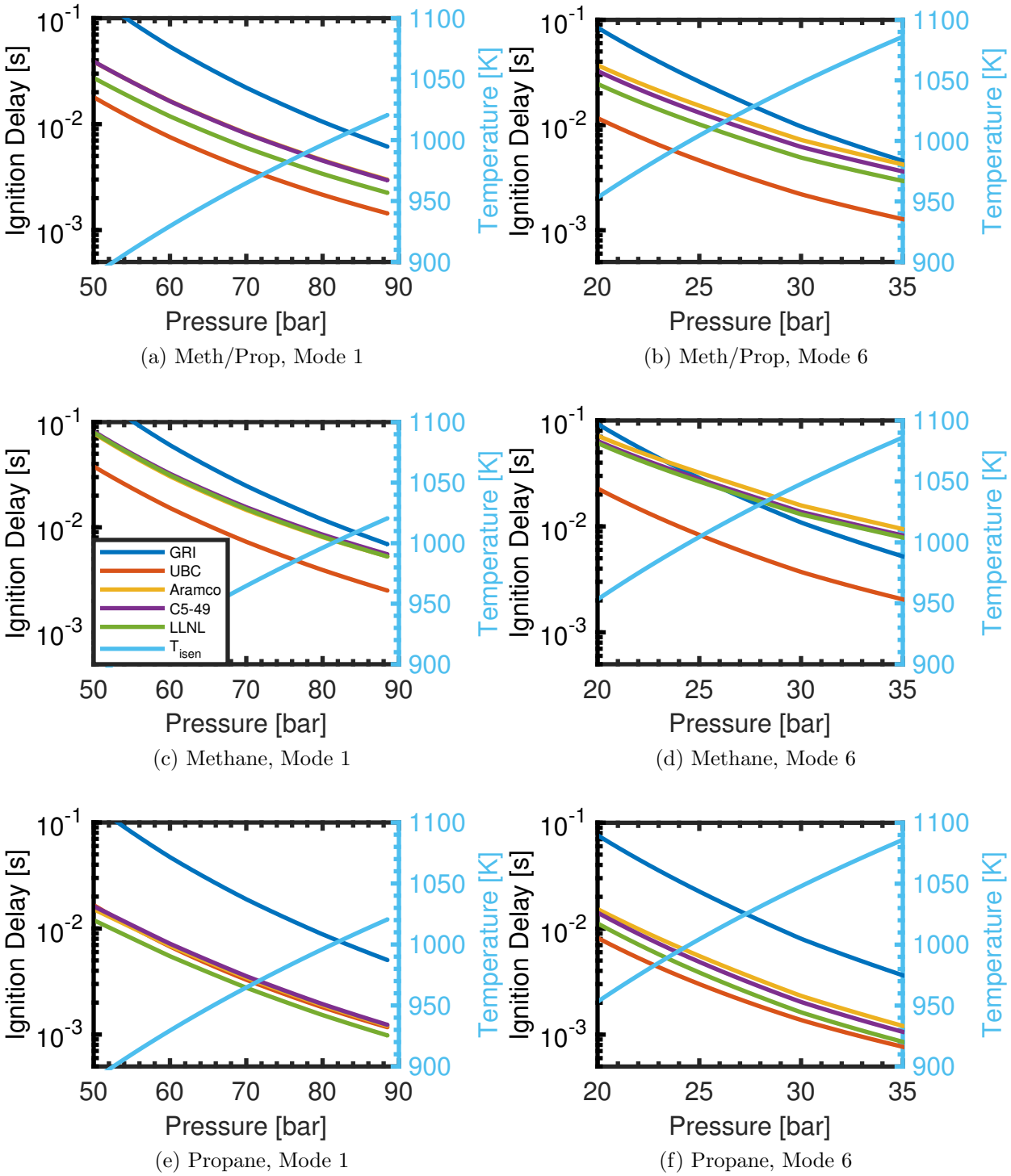

(a) Meth/Prop, Mode 1

(b) Meth/Prop, Mode 6

(c) Methane, Mode 1

(d) Methane, Mode 6

(e) Propane, Mode 1

(f) Propane, Mode 6

Figure 9.14: Constant pressure ignition delay for pressure-temperature curves for operating conditions 1 (left) and 6 (right) for 80/20 methane/propane (a,b), methane (c,d), and propane (d,f) at an equivalence ratio of 0.35.

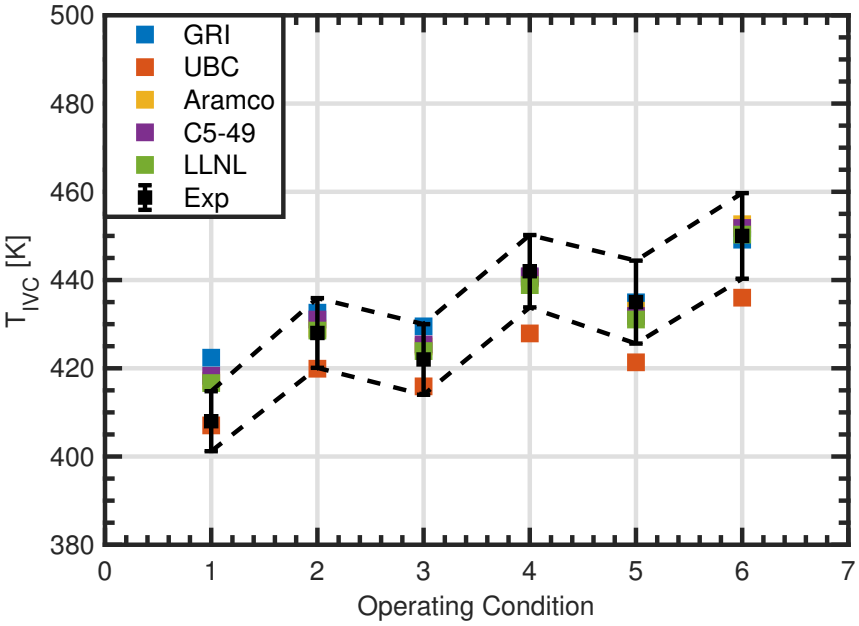

Figure 9.15: Simulated core T_{IVC} required to match experimental combustion phasing for CH_4/H_2 baseline conditions along with the experimental T_{IVC}.

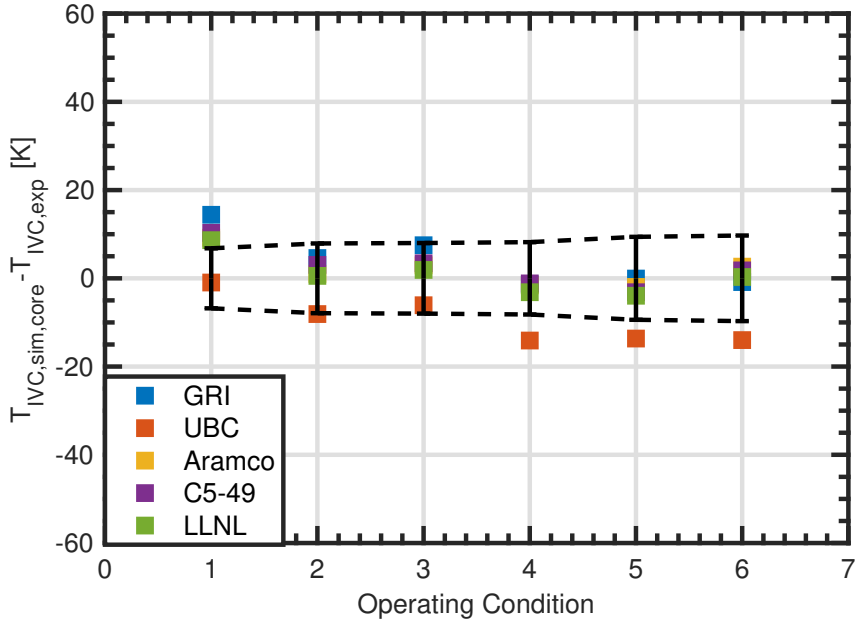

Figure 9.16: Difference between simulated core T_{IVC} required to match experimental combustion phasing along with the experimental T_{IVC} for CH_4/H_2 baseline conditions.

Table 9.3: Summary of simulated and nominal experimental temperatures for CH_4/H_2 baseline conditions.

		1	2	3	4	5	6
Engine Speed	RPM	1000	2000	1000	2000	1000	2000
Intake Pressure	bar	2.25		1.5		0.90	
Exp	K	408	428	422	442	435	450
GRI	K	422	433	430	441	435	449
UBC	K	407	420	416	428	421	436
Aramco	K	417	429	425	440	433	453
C5-49	K	418	431	425	441	432	452
LLNL	K	416	429	424	439	431	450

(a, b), pure methane (c, d), and pure hydrogen (e, f) at an equivalence ratio of 0.35. The ignition delays for the baseline CH_4/H_2 mixture show trends consistent with the $T_{IVC,sim}$; at the high pressure, low temperature condition 1, the C5-49, Aramco, and LLNL mechanisms' ignition delays were nearly identical, while the GRI mechanism produced slightly longer ignition delays and the UBC mechanism produced slightly shorter ignition delays. At the low pressure, high temperature condition 6, the UBC mechanism again produced the shortest ignition delays, while the other mechanisms had similar ignition delays.

The methane ignition delays were substantially shorter for the UBC mechanism compared to the other four mechanisms. At low temperatures the GRI mechanism had a longer ignition delay for methane compared to the C5-49, Aramco, and LLNL mechanisms, but a crossover temperature exists at both the high and low pressure conditions where the GRI began to have shorter ignition delays. Hydrogen ignition delays were very similar for all mechanisms, with the GRI mechanism producing slightly longer ignition delays for all conditions.

From these results, it appears that the $T_{IVC,sim}$ differences for the baseline methane/hydrogen cases were mainly driven by the methane chemistry rather than the hydrogen chemistry. Referring to Figure 9.16, the UBC mechanism required a lower $T_{IVC,sim}$ than the other mechanisms due to its shorter methane ignition delays. The GRI mechanism required slightly higher $T_{IVC,sim}$ relative to the C5-49, Aramco, and LLNL mechanisms at the low temperature conditions and a slightly lower $T_{IVC,sim}$ at the high temperature conditions;

this behavior matches the trend of its methane ignition delays become shorter relative to the other mechanisms as temperature increases.

9.4.5 Methane/Propane and Methane/Hydrogen Baseline Conditions Comparison

The difference between the temperature required for the CH_4/H_2 baseline conditions and the corresponding experimental temperature vs. the same temperature difference required for the CH_4/C_3H_8 baseline conditions is shown in Figures 9.18 and 9.19, where Figure 9.19 is normalized by the experimental temperature uncertainty, σ_{exp}, for each operating condition

$$T_{norm} = \frac{T_{IVC,sim} - T_{IVC,exp}}{\sigma_{exp}}. \tag{9.6}$$

Points that fall within the vertical ± 1 lines were within the experimental uncertainty range for the methane/propane cases, and points that fall within the horizontal ± 1 lines were within the experimental uncertainty range for the methane/hydrogen cases. Mechanisms that exhibited consistent relative reactivity errors for both CH_4/H_2 and CH_4/C_3H_8 would be expected to have their points fall on the 45 degree dashed line. Large errors in the experimental temperature estimation would likewise shift data points up or down the 45 degree line, errors in the mechanisms' ability to capture the kinetics of propane would shift the data points in the horizontal direction, and errors in the mechanisms' ability to capture the kinetics of hydrogen would shift the data points in the vertical direction.

The LLNL mechanism appears to match closest with the experimental data, with all data points within the experimental uncertainty bounds for the CH_4/C_3H_8 baseline conditions and only one condition outside the uncertainty bounds for the CH_4/H_2 baseline conditions. The Aramco and C5-49 mechanisms both show similar results, closely matching the CH_4/H_2 baseline conditions, but requiring higher temperatures for the

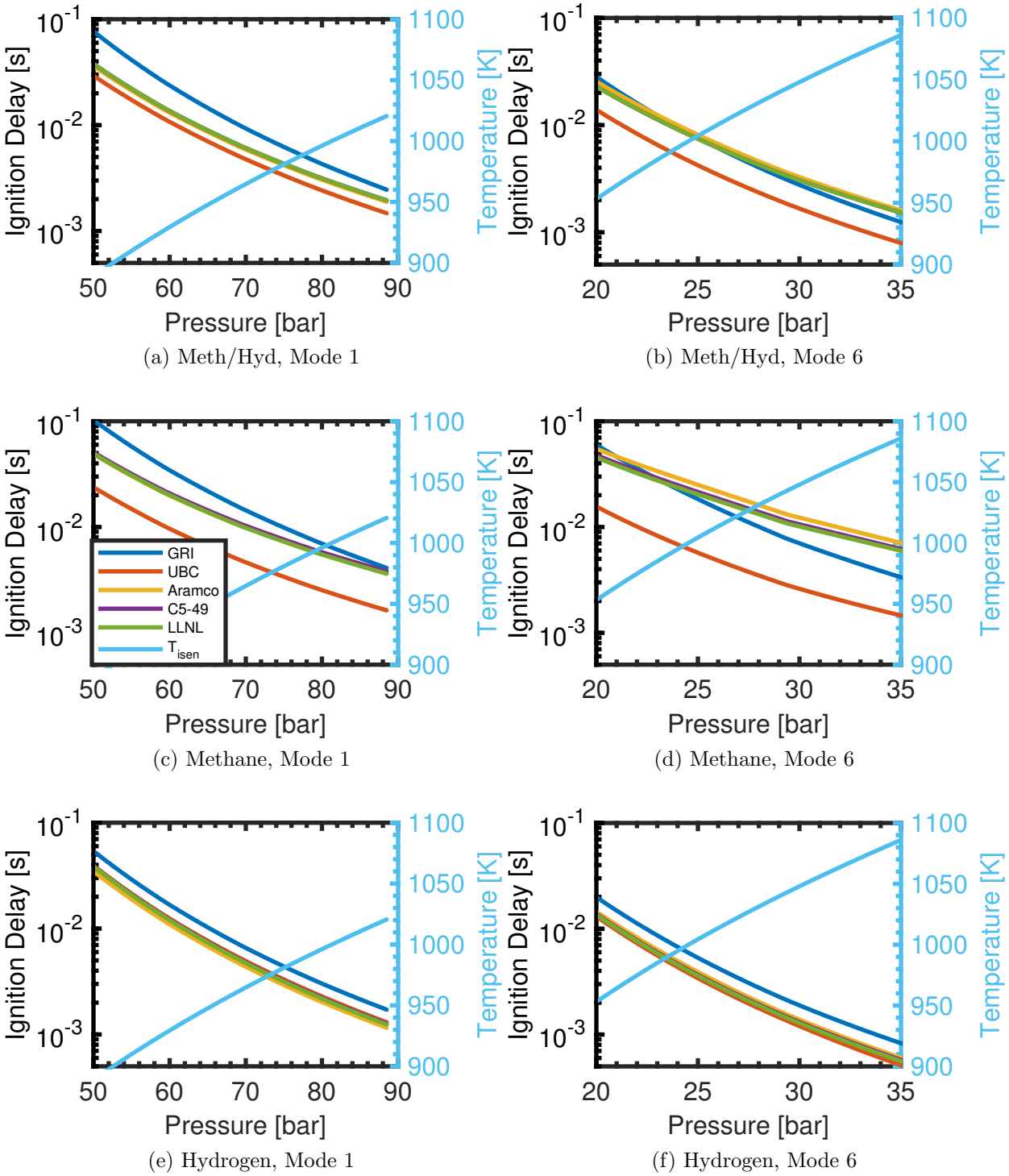

(a) Meth/Hyd, Mode 1

(b) Meth/Hyd, Mode 6

(c) Methane, Mode 1

(d) Methane, Mode 6

(e) Hydrogen, Mode 1

(f) Hydrogen, Mode 6

Figure 9.17: Constant pressure ignition delay for pressure-temperature curves for operating conditions 1 (left) and 6 (right) for 75/25 methane/hydrogen (a,b), methane (c,d), and hydrogen (d,f) at an equivalence ratio of 0.35.

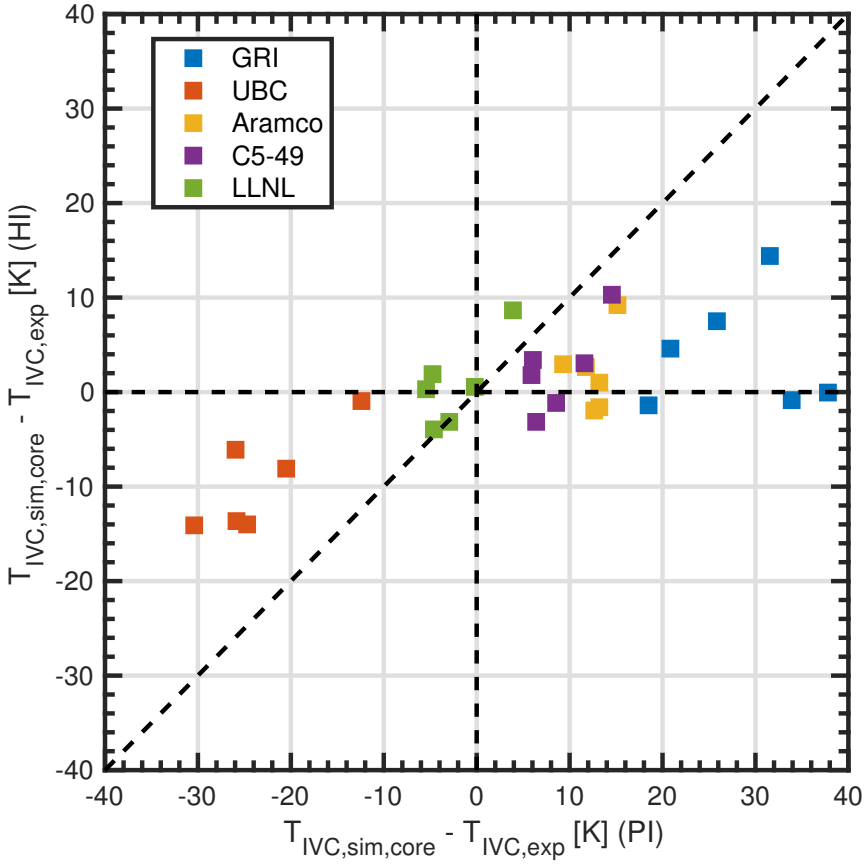

Figure 9.18: Difference between simulation core IVC temperature and experimental IVC temperature required for CH_4/H_2 baseline conditions vs. the same temperature difference for CH_4/C_3H_8 baseline conditions.

CH_4/C_3H_8 baseline conditions. The GRI mechanism also matches the CH_4/H_2 baseline conditions for most conditions, but requires much higher temperatures for the CH_4/C_3H_8 baseline conditions. The UBC mechanism was reasonably close for the CH_4/H_2 baseline conditions, but required much lower temperatures for the CH_4/C_3H_8 baseline conditions.

9.5 Summary

Experimental motored and fired pressures were well matched using a Cantera two-zone engine model. The two-zone model's isentropic, inner-core temperature was seen to reasonably match the inner-core temperature in Converge full-cycle CFD simulations. The

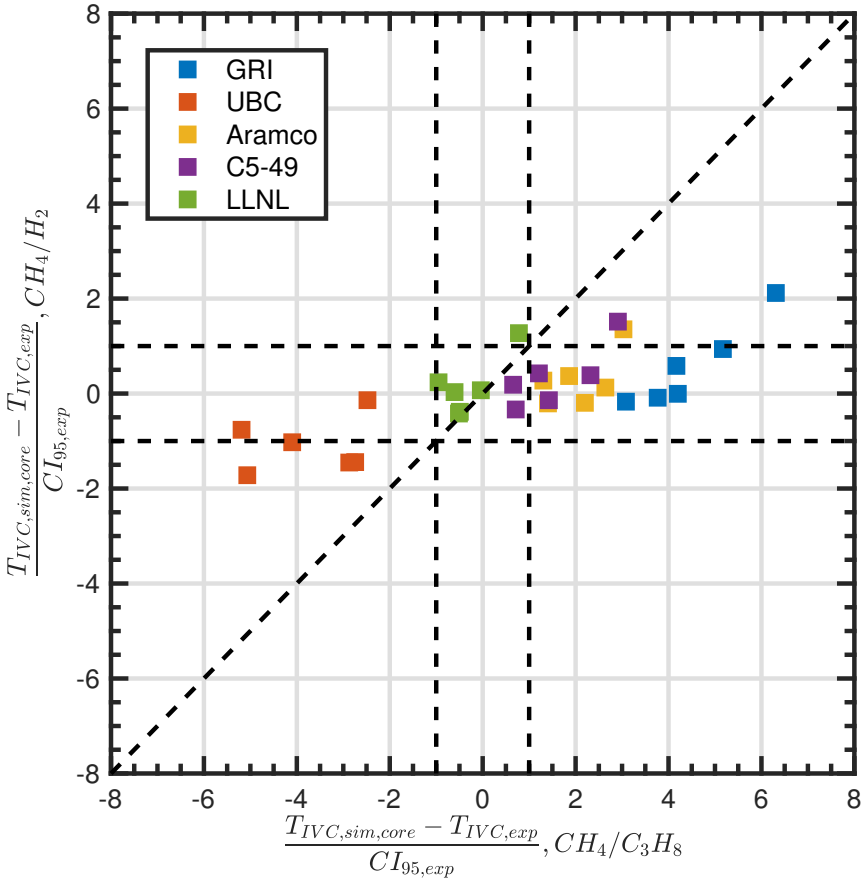

Figure 9.19: Difference between simulation core IVC temperature required and experimental IVC temperature for CH_4/H_2 baseline conditions vs. the same temperature difference for CH_4/C_3H_8 baseline conditions, normalized by the experimental temperature uncertainty at each condition.

six baseline methane/propane and methane/hydrogen operating conditions were simulated using five different mechanisms, and the simulation IVC temperature was adjusted until $CA_{50,sim}$ of the inner core matched $CA_{10,exp}$. Table 9.4 shows a generalized summary of the results with each mechanism for both sets of baseline conditions.

For the methane/propane baseline conditions, the $T_{IVC,sim,core}$ for the LLNL closely matched $T_{IVC,exp}$, the $T_{IVC,sim,core}$ for the Aramco and C5-49 mechanisms were slightly higher than the experimental uncertainty bounds, the $T_{IVC,sim,core}$ for the GRI mechanism was consistently higher, and the $T_{IVC,sim,core}$ for the UBC mechanism was consistently lower.

For the methane/hydrogen baseline conditions, all of the $T_{IVC,sim,core}$ values matched reasonably well with the $T_{IVC,exp}$. The $T_{IVC,sim,core}$ for the Aramco, C5-49, LLNL, and GRI mechanisms were all quite close to the experimental temperatures, with only one of the six conditions requiring a $T_{IVC,sim,core}$ outside the experimental uncertainty bounds. The UBC mechanism required a lower $T_{IVC,sim,core}$ than the other mechanisms for all conditions, with four of the six conditions requiring a $T_{IVC,sim,core}$ outside the experimental uncertainty bounds.

Individual fuels' ignition delays were investigated along the simulated temperature-pressure conditions; it appeared that the GRI mechanism required a greater $T_{IVC,sim}$ for the methane/propane cases relative to the C5-49, Aramco, and LLNL mechanisms mainly due to differences in its propane chemistry, which showed longer ignition delays than the other mechanisms. The UBC mechanism required a lower $T_{IVC,sim}$ for the methane/propane cases relative to the C5-49, Aramco, and LLNL mechanisms mainly due to differences in its methane chemistry, which showed abnormally short ignition delays. The hydrogen ignition delays for all fuels were relatively similar, indicating that the differences in $T_{IVC,sim}$ for the methane/hydrogen cases were mainly due to differences in methane chemistry. The ignition delays for methane using the GRI mechanism relative to the C5-49, Aramco, and LLNL mechanisms decreased with increasing temperature;

Table 9.4: General comparison of simulated core T_{IVC} required to match experimental combustion phasing for methane/propane and methane/hydrogen baseline conditions and the experimental T_{IVC}, where ⇑(⇓) indicates the reactivity was over(under)-predicted, ⇑⇑(⇓⇓) indicates the reactivity was substantially over(under)-predicted, and = indicates the reactivity was reasonably well predicted. In general, T_{IVC} errors >20 K were classified as substantially over- or under-predicted.

	GRI	UBC	Aramco	C5-49	LLNL
Methane/Hydrogen	=	⇑	=	=	=
Methane/Propane	⇓⇓	⇑⇑	⇓	⇓	=

below 1000-1050 K the GRI mechanism had longer ignition delays for methane while above 1000-1050 K the GRI mechanism had shorter ignition delays for methane.

Chapter 10

Relative Reactivity Simulations

10.1 Introduction

The first part of this chapter focuses on Cantera engine simulations of the experimental fuel substitution studies using the same model discussed in the previous chapter. Two simulation methods are used: fixed fuel concentrations with a variable $T_{IVC,core}$, and a constant $T_{IVC,core}$ with variable fuel concentrations. The results of both simulation methods are compared to the experimental results and used to evaluate the kinetics mechanisms' accuracy when predicting the relative reactivity of each fuel relative to the methane/propane and methane/hydrogen reference fuels. Ignition delays generated using each kinetics mechanism are also investigated to gain insight on the root cause of the differences seen in predicted relative fuel reactivities.

The second part of this chapter investigates an alternative method to fuel substitution simulations to characterize relative fuel reactivity. Instead of simulating a fuel substitution sweep with a full engine simulation, constant pressure ignition delays were used to obtain a PI for each test fuel. The ignition delay PIs are compared to the engine simulation PIs. A benefit of the ignition delay method for characterizing relative fuel reactivity is that it is a generic method that is independent of a specific engine geometry

or combustion strategy, and it can be used to generate a *PI* map over a wide range of temperatures and pressures, including conditions that are difficult to reach using the fuel substitution procedure on either a real or virtual engine.

10.2 Simulation of Fuel Substitution Cases: Fixed Fuel Concentrations, Varying $T_{IVC,core}$

The two-zone, adiabatic-core Cantera model described in the previous chapter was used to simulate all of the experimental fuel substitution cases. The reactor was initialized at IVC with the experimentally measured pressures and mole fractions, while $T_{IVC,core}$ was adjusted for each case until $CA_{50,sim,core}$ matched $CA_{10,exp}$.

Figure 10.1 shows the required simulation temperature as a function of ethane energy fraction when simulating the *PI* testing using the C5-49 mechanism for all six operating conditions. In Chapter 4, it was shown that IVC temperature was held constant for each fuel substitution sweep; therefore, the required simulation temperature as a function of ethane energy fraction should be constant if ethane's reactivity relative to the methane/propane reference fuels' reactivities is accurately captured by the C5-49 mechanism. Figure 10.2 shows the same data, with the temperatures normalized by the baseline temperature for each operating condition,

$$T_{norm} = \frac{T - T_{base}}{T_{base}} 100, \tag{10.1}$$

where T_{base} is the $T_{IVC,sim,core}$ required to match the experimental combustion phasing with the baseline methane/propane mixtures. The slope of the normalized temperature vs. ethane energy fraction is an indication of how well the relative reactivity of ethane predicted by the C5-49 mechanism compares to the experimental results. A slope of 0 indicates a perfect match; a positive slope indicates that the relative reactivity of ethane

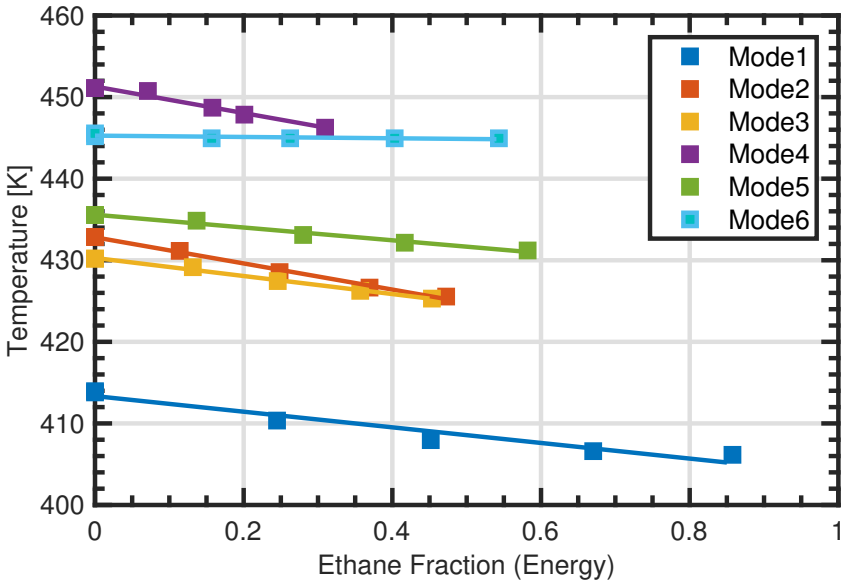

Figure 10.1: IVC temperature required in simulation to match experimental combustion phasing as a function of ethane energy fraction when simulating the *PI* testing using the C5-49 mechanism for all six operating conditions.

is under-predicted, because a higher temperature is required in the simulation as the ethane fraction increases, while a negative slope indicates that the relative reactivity of ethane is over-predicted, because a lower temperature is required in the simulation as the ethane fraction increases. The C5-49 mechanism over-predicts the reactivity of ethane relative to methane/propane for all operating conditions. It is interesting to note that the magnitude of over-prediction was seen to depend on operating condition, with the least amount of over-prediction occurring at the low pressure, high temperature condition (6).

The amount of under- or over-prediction for each test fuel at each operating condition can be quantified by a single value by applying a linear-curve fit to the individual temperature vs. test fuel points for each condition. Examples of the curve-fits can be seen in Figures 10.1 and Figure 10.2. All data with the Aramco, C5-49, and LLNL mechanisms were well described with a linear fit, indicated by the small 95% confidence intervals. There are two main ways to compare these data: comparing the curve-fit slopes of all mechanisms for a single fuel, and comparing the curve-fit slopes for all fuels for a single

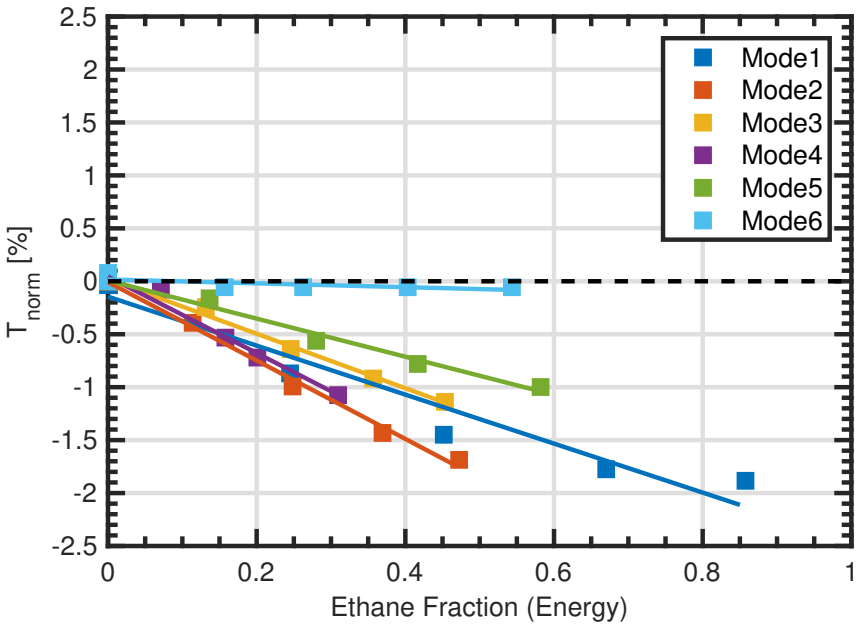

Figure 10.2: Normalized IVC temperature required in simulation to match experimental combustion phasing as a function of ethane energy fraction when simulating the *PI* testing using the C5-49 mechanism for all six operating conditions.

mechanism.

Figure 10.3a shows the curve-fit slopes for ethane over all operating conditions using all five mechanisms, while Figure 10.3b shows the data with just the Aramco, C5-49, and LLNL mechanisms. The GRI and UBC mechanisms showed inconsistent results for several of the test fuel simulations, which resulted in very large 95% confidence intervals. The results reported for the remainder of this chapter focus only on the Aramco, C5-49, and LLNL mechanisms due to this inconsistent behavior. Further, the results of the previous chapter showed that the absolute accuracy of the GRI and UBC mechanisms were substantially worse compared to the other mechanisms. Figure 10.4 shows an example of the curve-fit slopes for all fuels over all operating conditions using the C5-49 mechanism. Different test fuels had varying amounts of over- or under-prediction, with the magnitudes of over- or under-prediction for each test fuel having some dependency on operating condition.

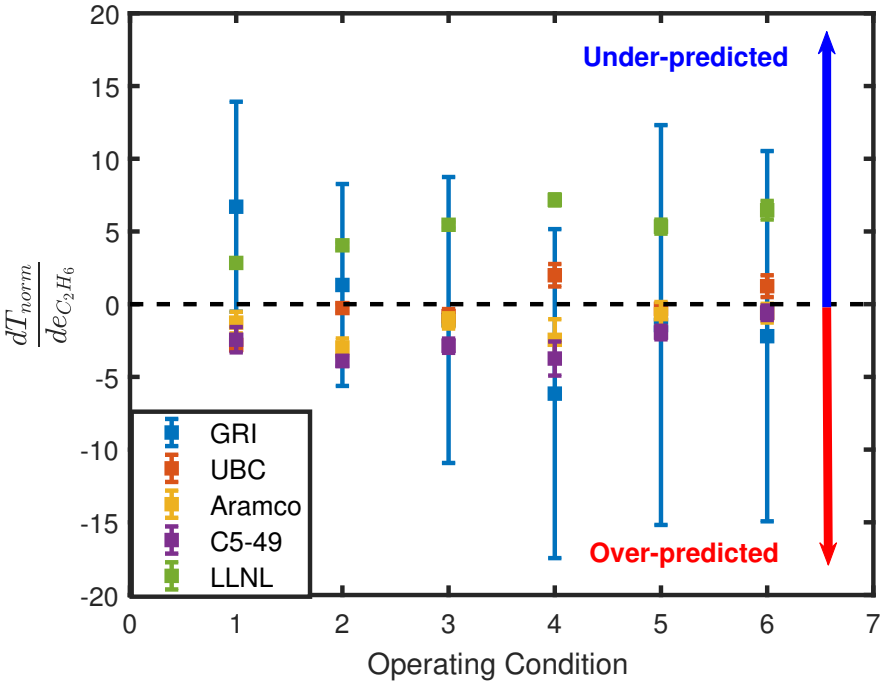

(a)

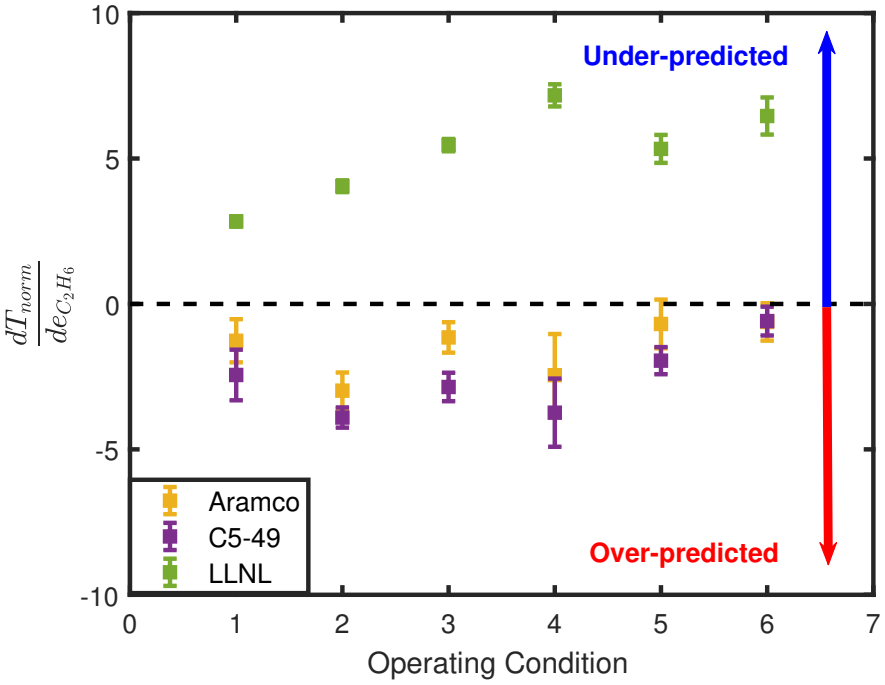

(b)

Figure 10.3: Slope of linear curve-fit with 95% confidence intervals applied to each set of normalized temperature vs. ethane energy fraction for all operating conditions of *PI* fuel substitution testing using all mechanisms (a) and only the Aramco, C5-49, and LLNL mechanisms (b).

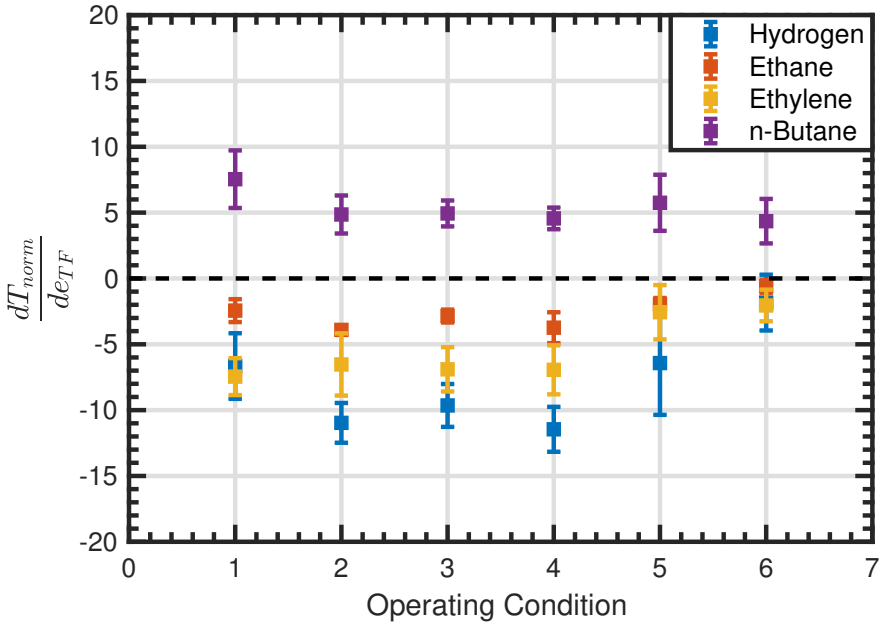

Figure 10.4: Slope of linear curve-fit with 95% confidence intervals applied to each set of normalized temperature vs. test fuel energy fraction for all fuels and operating conditions of *PI* fuel substitution testing using the C5-49 mechanism.

10.3 Simulated Fuel Substitution Sweep: Fixed $T_{IVC,core}$, Varying Fuel Concentrations

An alternative simulation method is to directly simulate a fuel substitution sweep. The simulation procedure was nearly identical to the experimental procedure described in Chapter 4. With a baseline fuel mixture containing only methane/propane, the temperature at IVC was adjusted until $CA_{50,sim,core}$ was 4.5 degrees aTDC, per the experiments. Next, with $T_{IVC,core}$ fixed, increasing amounts of the test fuel were added, while the total fuel energy was held constant, and the methane/propane fuel ratio was adjusted to keep $CA_{50,sim,core}$ constant. The results of a simulated sweep can be seen in Figure 10.5; as the ethane energy fraction increased, propane was removed from the fuel mixture in order to keep combustion phasing constant. This was necessary because ethane was more reactive than the baseline methane/propane fuel mixture. A fit was applied to the data, as described in Chapter 4, to calculate a *PI* for ethane at this operating condition. The

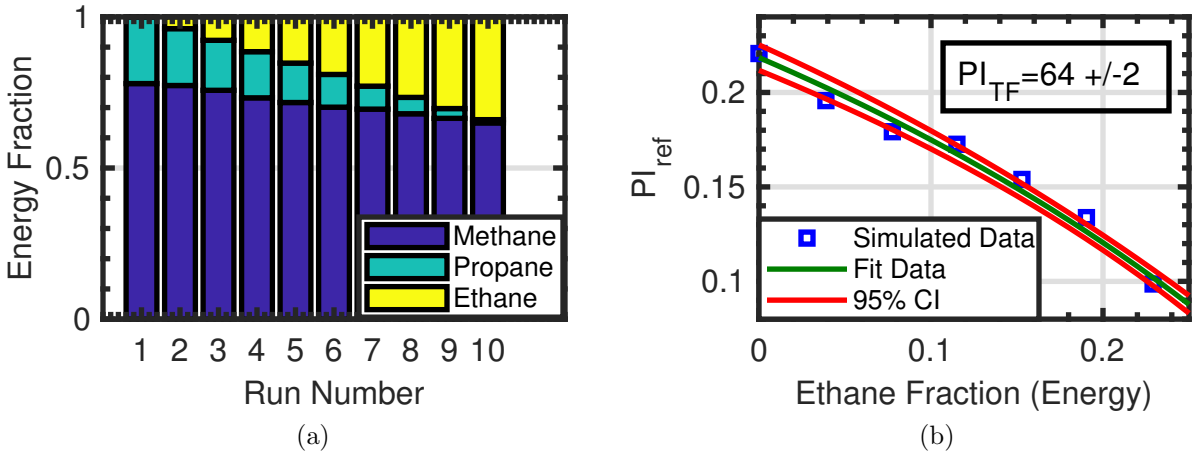

Figure 10.5: Fuel energy fractions (left) and reference fuel *PI* as a function of ethane energy fraction along with non-linear fit and 95% confidence intervals for a simulation at operating condition 1 using the C5-49 mechanism.

C5-49 mechanism predicted that ethane had a *PI* of 64±2, *i.e.* an equivalent reactivity to a mixture of 64% propane and 36% methane (by energy), at this operating condition. The low value for the 95% *CI* of the fit validates the ability of the energy blending rule to describe the overall fuel mixture reactivity.

The calculated *PI* for all fuels, operating conditions, and mechanisms can be directly compared to the experimentally found *PI*s. The focus of this comparison is limited to the Aramco, C5-49, and LLNL mechanisms because they were the most accurate at matching the experimental IVC temperatures, as discussed in the previous chapter. Figure 10.6 shows the comparison of the simulated and experimental *PI*s. The C5-49 mechanism showed the greatest over-prediction of the *PI*, while the LLNL mechanism showed the greatest under-prediction. An interesting note is the negative *PI* seen with the LLNL mechanism at operating condition 1, indicating that ethane is predicted to be less reactive than methane at this condition.

Figure 10.7 shows the difference between experimental and simulated *PI*s, *i.e.*, PI_{exp}-PI_{sim}, for ethane at each operating condition. A perfect match between experimental and simulated *PI*s would fall on the horizontal dashed line, while values >0 indicate the

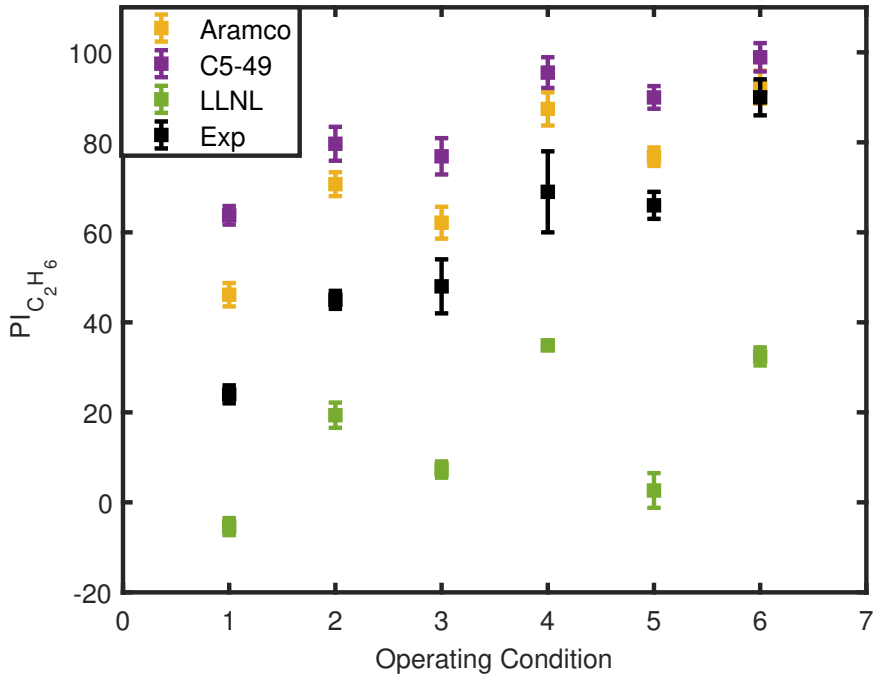

Figure 10.6: Simulated and experimental *PI*s with uncertainty for ethane at all operating conditions using the Aramco, C5-49, and LLNL mechanisms.

simulation is under-predicting the relative reactivity of ethane, and values <0 indicate that the simulation is over-predicting the relative reactivity of ethane. The difference was defined in this way to have positive (negative) values correspond to under-(over)-prediction trends, similar to the temperature slope trends from the previous section.

10.4 Individual Fuel Investigations

10.4.1 Methane

Methane was used as the low reactivity reference fuel for both *PI* and *HI* testing, and thus any differences in its kinetics between mechanisms will potentially affect all results. Figure 10.8 shows the ignition delays for methane at an equivalence ratio of 0.35 along the isentropic pressure-temperature curves for the high pressure, low temperature conditions 1 (left) and the low pressure, high temperature condition 6 (right). The ignition delays for

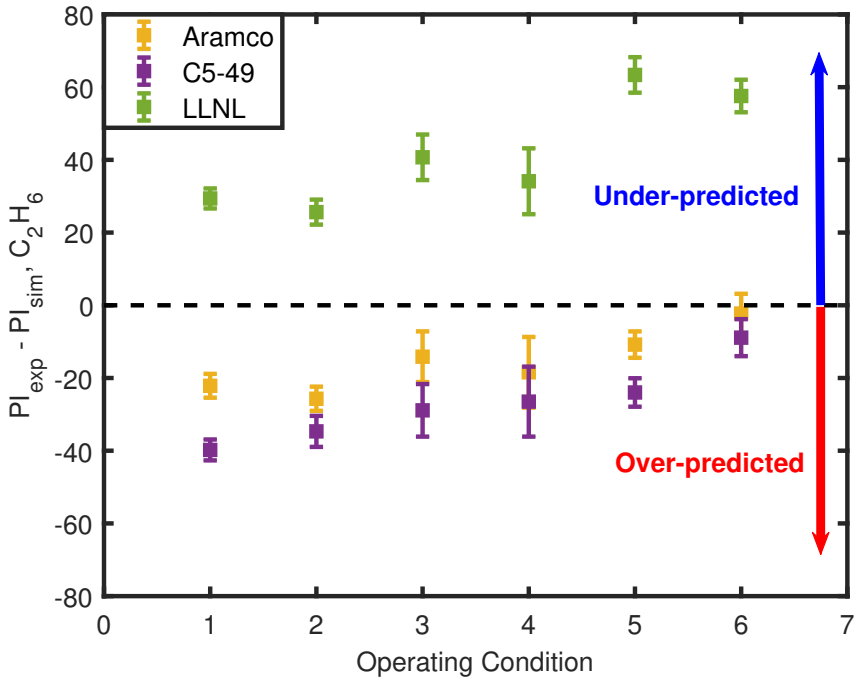

Figure 10.7: Difference between experimental and simulated *PI*s with uncertainty for ethane at all operating conditions using the Aramco, C5-49, and LLNL mechanisms.

methane with the Aramco, C5-49 and LLNL mechanisms are very similar at condition 1, while the Aramco mechanism has a slightly longer ignition delay at condition 6. Because the ignition delays are similar with all three mechanisms, methane chemistry is not expected to impact the relative reactivity results when comparing between mechanisms.

10.4.2 Hydrogen

Figure 10.9 shows the slope of normalized temperature vs. test fuel energy fraction (left) and the difference between experimental and simulated *PI*s with uncertainty (right) for all operating conditions of the *PI* fuel substitution testing with hydrogen, using the Aramco, C5-49, and LLNL mechanisms. Both simulation methods show consistent trends. The reactivity of hydrogen relative to methane/propane is well matched with the LLNL mechanism for operating conditions 1-4 and slightly under-predicted for operating conditions 5 and 6. Both the C5-49 and Aramco mechanisms strongly over-predict the

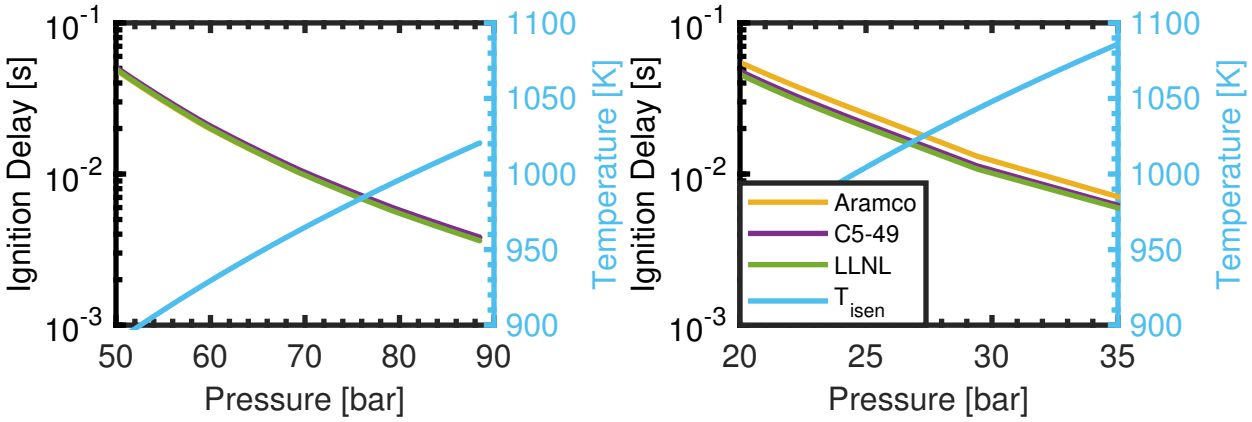

Figure 10.8: Constant pressure ignition delay for pressure-temperature curves for operating conditions 1 (left) and 6 (right) for methane.

relative reactivity of hydrogen, with the the Aramco mechanism having slightly larger magnitudes of over-prediction compared to the C5-49 mechanism.

Figure 10.10 shows the ignition delays along the isentropic pressure-temperature curves for operating conditions 1 (left) and 6 (right) for hydrogen at an equivalence ratio of 0.35. The ignition delays for hydrogen with the Aramco, C5-49, and LLNL mechanisms are nearly identical, which strongly suggests that the differences in the reactivity of hydrogen relative to methane/propane seen in Figure 10.9 are caused by differences in their propane and methane chemistry rather than their hydrogen chemistry. This will be discussed more in the discussion section following the individual fuel results.

10.4.3 Propane

Figure 10.11 shows the slope of normalized temperature vs. test fuel energy fraction (left) and the difference between experimental and simulated *HI*s with uncertainty (right) for all operating conditions of the *HI* fuel substitution testing with propane using the Aramco, C5-49, and LLNL mechanisms. The reactivity of propane relative to methane/hydrogen was well-matched with the LLNL mechanism at conditions 2-6, but showed under-prediction at condition 1. The Aramco and C5-49 mechanisms showed

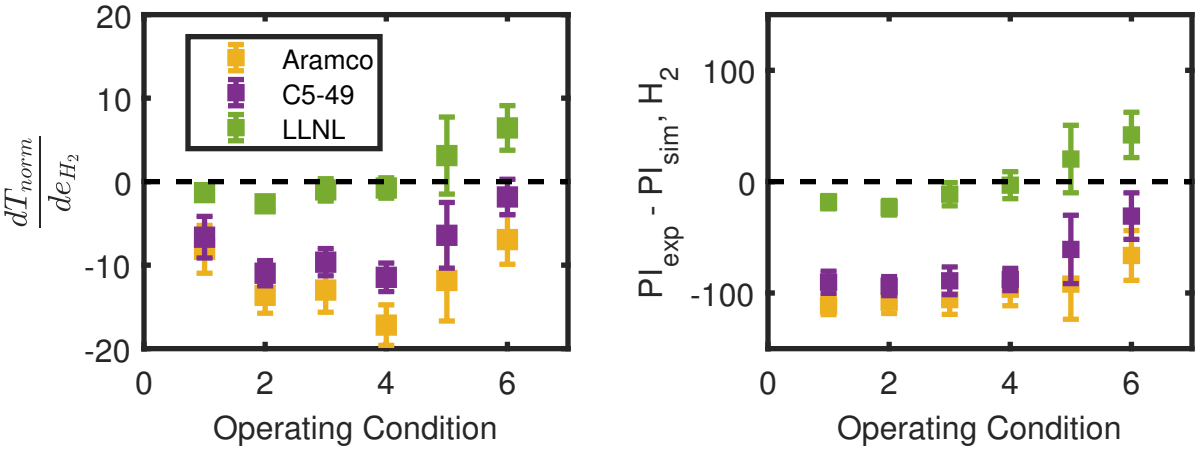

(a) (b)

Figure 10.9: Slope of linear curve-fit with 95% confidence intervals applied to each set of normalized temperature vs. test fuel energy fraction (left) and difference between experimental and simulated PIs with uncertainty (right) for all operating conditions of PI fuel substitution testing with hydrogen.

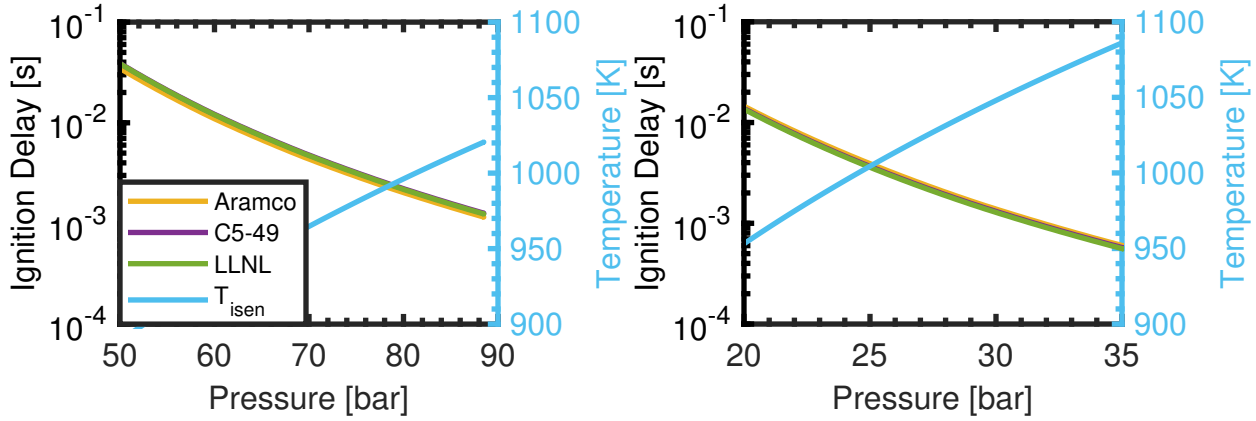

(a) (b)

Figure 10.10: Constant pressure ignition delay for pressure-temperature curves for operating conditions 1 (left) and 6 (right) for hydrogen.

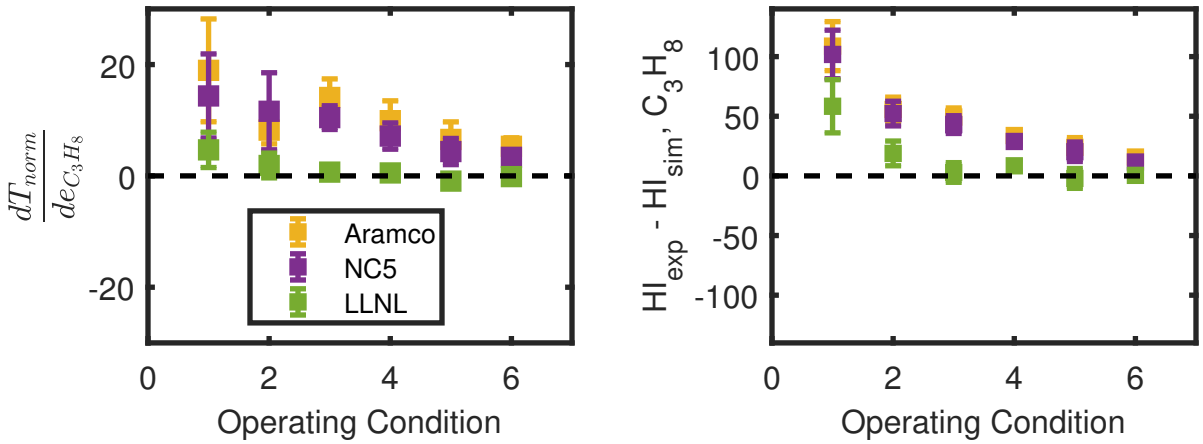

(a) (b)

Figure 10.11: Slope of linear curve-fit with 95% confidence intervals applied to each set of normalized temperature vs. test fuel energy fraction (left) and difference between experimental and simulated *HI*s with uncertainty for all operating conditions of *HI* fuel substitution testing with propane.

similar amounts of under-prediction, and gave the largest under-prediction at the high pressure conditions (1 and 2).

Figure 10.12 shows the ignition delays along the isentropic pressure-temperature curves for operating conditions 1 (left) and 6 (right) for propane at an equivalence ratio of 0.35. The ignition delays are nearly identical for the C5-49 and Aramco mechanisms at condition 1, while the Aramco mechanism has slightly longer ignition delays at condition 6. The LLNL mechanisms had consistently shorter ignition delays at both conditions. These ignition delay results are consistent with the trends seen in the constant temperature and constant fueling simulations. Because all three mechanisms had relatively similar ignition delays for methane and hydrogen, the differences in the reactivity of propane relative to methane/hydrogen seen in Figure 10.11 are most likely caused by differences in their propane chemistry.

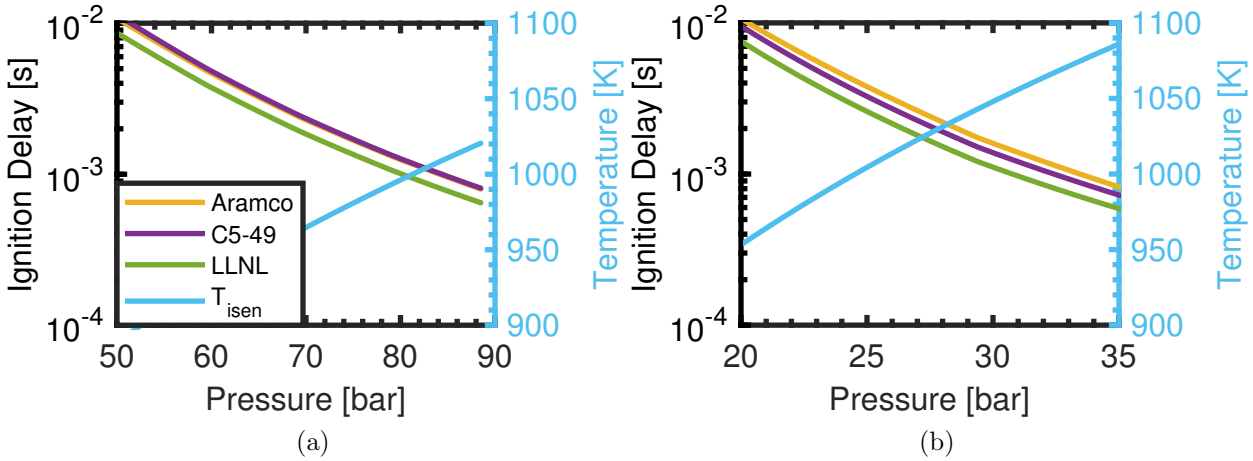

Figure 10.12: Constant pressure ignition delay for pressure-temperature curves for operating conditions 1 (left) and 6 (right) for propane.

10.4.4 Ethane

Figure 10.13 shows the slope of normalized temperature vs. test fuel energy fraction (left) and the difference between experimental and simulated *PI*s with uncertainty (right) for all operating conditions of the *PI* fuel substitution testing with ethane, using the Aramco, C5-49, and LLNL mechanisms. Both simulation methods show consistent trends. The reactivity of ethane relative to methane/propane is slightly over-predicted with the Aramco and C5-49 mechanisms, while it is under-predicted with the LLNL mechanism. The C5-49 mechanism has a slightly greater magnitude of over-prediction compared to the Aramco mechanism. The Aramco and C5-49 mechanisms show much closer matches to the experimental tests at low pressure conditions (5 and 6), almost perfectly matching at operating condition 6.

Figure 10.14 shows the slope of normalized temperature vs. test fuel energy fraction (left) and the difference between experimental and simulated *HI*s with uncertainty (right) for all operating conditions of the *HI* fuel substitution testing with ethane, using the Aramco, C5-49, and LLNL mechanisms. The reactivity of ethane relative to methane/hydrogen is slightly under-predicted for all conditions, with the C5-49 mechanism having the smallest amount of under-prediction. The Aramco and LLNL mecha-

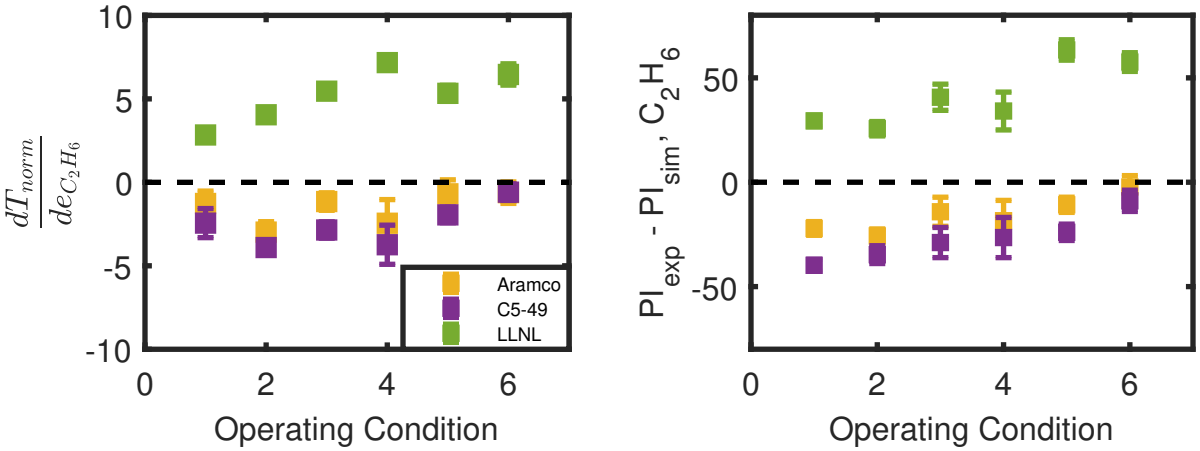

(a) (b)

Figure 10.13: Slope of linear curve-fit with 95% confidence intervals applied to each set of normalized temperature vs. test fuel energy fraction (left) and difference between experimental and simulated PIs with uncertainty (right) for all operating conditions of PI fuel substitution testing with ethane.

nisms' amount of under-prediction for ethane are similar.

Figure 10.15 shows the ignition delays along the isentropic pressure-temperature curves for operating conditions 1 (left) and 6 (right) for ethane at an equivalence ratio of 0.35. The ignition delays for ethane with the Aramco and LLNL mechanisms are similar, with the Aramco mechanism being slightly shorter at the high pressure condition (1). The ignition delays for the C5-49 mechanism are shorter at both the low and high pressure conditions.

The differences in the reactivity of ethane relative to methane/propane seen in Figure 10.13 are most likely due to differences in the propane chemistry between the LLNL and C5-49/Aramco mechanisms and differences in the ethane chemistry between the C5-49 and Aramco/LLNL mechanisms. The differences in propane chemistry appeared to have a larger effect, seen by the large difference between the LLNL and C5-49/Aramco results. The differences in the reactivity of ethane relative to methane/hydrogen appear to be mainly caused by differences in ethane chemistry between C5-49 and LLNL/Aramco, with the differences between Aramco and LLNL caused by small differences in methane,

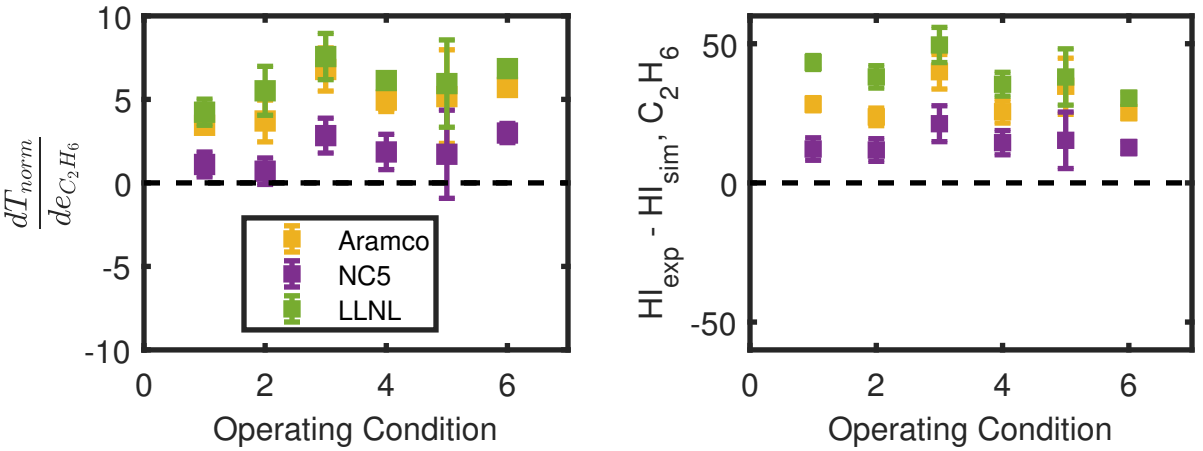

(a) (b)

Figure 10.14: Slope of linear curve-fit with 95% confidence intervals applied to each set of normalized temperature vs. test fuel energy fraction (left) and difference between experimental and simulated *HI*s with uncertainty for all operating conditions of *HI* fuel substitution testing with ethane.

hydrogen, and ethane chemistry.

10.4.5 Ethylene

Figure 10.16 shows the slope of normalized temperature vs. test fuel energy fraction (left) and the difference between experimental and simulated *PI*s with uncertainty (right) for all operating conditions of the *PI* fuel substitution testing with ethylene, using the Aramco, C5-49, and LLNL mechanisms. All three mechanisms over-predicted the reactivity of ethylene relative to methane/propane, with the Aramco mechanisms showing the largest amount of over-prediction and the LLNL mechanism showing the smallest amount of over-prediction.

Figure 10.17 shows the ignition delays along the isentropic pressure-temperature curves for operating conditions 1 (left) and 6 (right) for ethylene at an equivalence ratio of 0.35. The LLNL mechanisms shows the shortest ignition delays for ethylene at both conditions, so one would expect the LLNL mechanism to show the largest amount of over-prediction for the reactivity of ethylene. However, Figure 10.17 shows that the

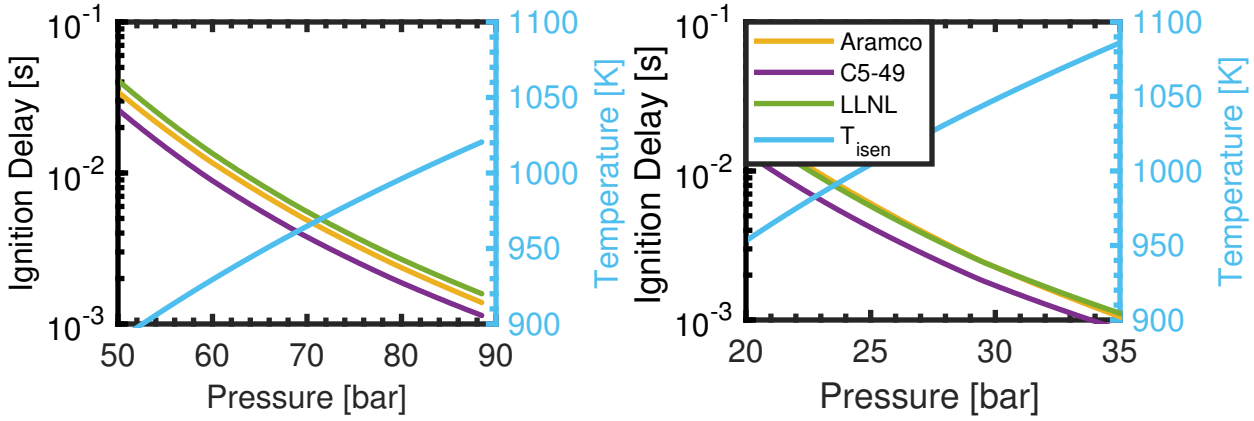

Figure 10.15: Constant pressure ignition delay for pressure-temperature curves for operating conditions 1 (left) and 6 (right) for ethane.

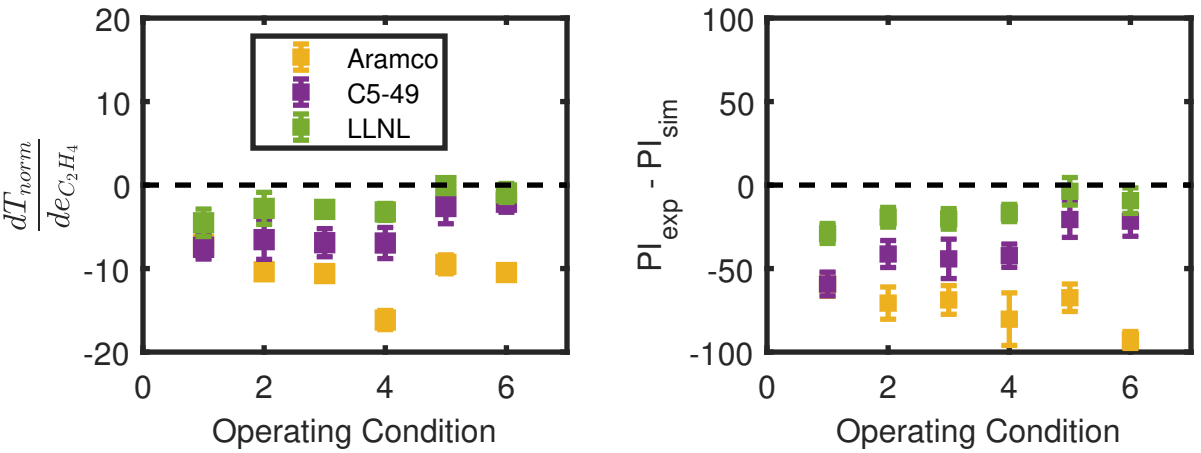

Figure 10.16: Slope of linear curve-fit with 95% confidence intervals applied to each set of normalized temperature vs. test fuel energy fraction (left) and difference between experimental and simulated PIs with uncertainty (right) for all operating conditions of PI fuel substitution testing with ethylene.

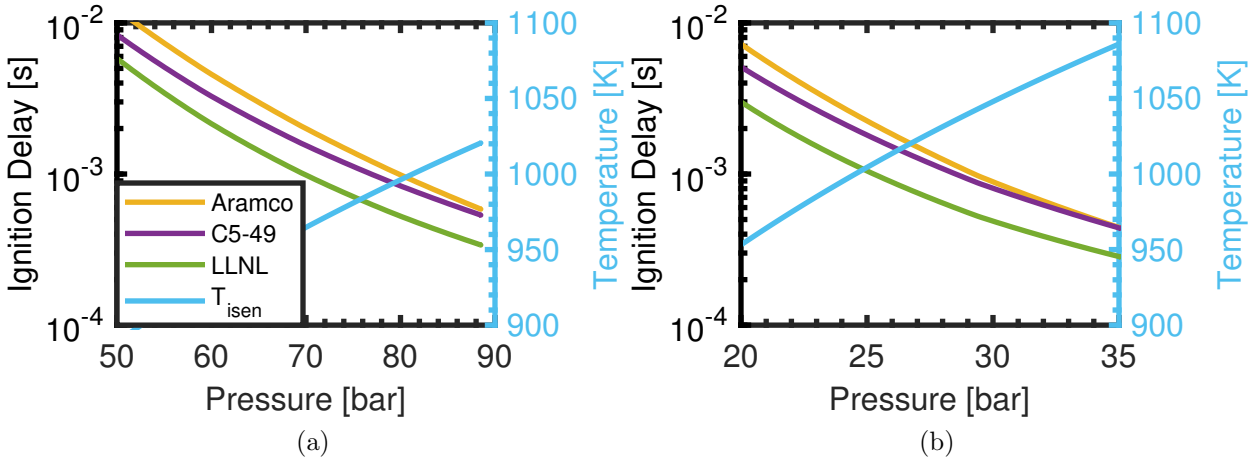

Figure 10.17: Constant pressure ignition delay for pressure-temperature curves for operating conditions 1 (left) and 6 (right) for ethylene.

LLNL mechanism has the smallest amount of over-prediction for ethylene. This seemingly contradictory behavior is most likely caused by the LLNL mechanism also having shorter ignition delays for propane. Even though the LLNL mechanism has the shortest ignition delay for ethylene, ethylene's reactivity, relative to methane and propane, is still lower than with the C5-49 and Aramco mechanisms.

10.4.6 *n*-Butane

Figure 10.18 shows the slope of normalized temperature vs. test fuel energy fraction (left) and the difference between experimental and simulated *PI*s with uncertainty (right) for all operating conditions of the *PI* fuel substitution testing with *n*-butane, using the C5-49 and LLNL mechanisms. The Aramco mechanism's largest hydrocarbon is propane, so the following simulations could only be carried out with the C5-49 and LLNL mechanisms. Both the C5-49 and LLNL mechanisms under-predict the reactivity of *n*-butane relative to methane/propane, with the LLNL showing a larger amount of under-prediction.

Figure 10.19 shows the slope of normalized temperature vs. test fuel energy fraction (left) and the difference between experimental and simulated *HI*s with uncertainty (right) for all operating conditions of the *HI* fuel substitution testing with *n*-butane, using

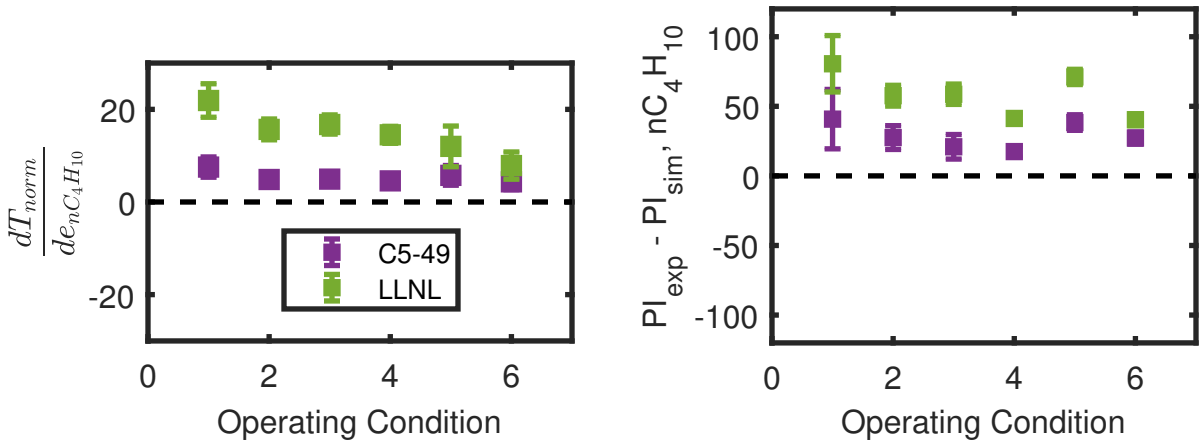

(a) (b)

Figure 10.18: Slope of linear curve-fit with 95% confidence intervals applied to each set of normalized temperature vs. test fuel energy fraction (left) and difference between experimental and simulated *PI*s with uncertainty (right) for all operating conditions of *PI* fuel substitution testing with *n*-butane.

the C5-49 and LLNL mechanisms. Both mechanisms show nearly identical amounts of under-prediction relative to methane/hydrogen. Experimental data were not available for conditions 1 and 2.

Figure 10.20 shows the ignition delays along the isentropic pressure-temperature curves for operating conditions 1 (left) and 6 (right) for *n*-butane at an equivalence ratio of 0.35. The ignition delays are nearly identical with the C5-49 and LLNL mechanisms, with the C5-49 being marginally longer at elevated temperatures and pressures. Figure 10.19 showed similar amounts of under-prediction for the reactivity of *n*-butane relative to methane/hydrogen, while Figure 10.18 showed larger magnitudes of under-prediction for the reactivity relative to methane/propane with the LLNL mechanism. This discrepancy for the *PI* results is most likely due to the longer ignition delays for propane with the C5-49 mechanism compared to the LLNL mechanism.

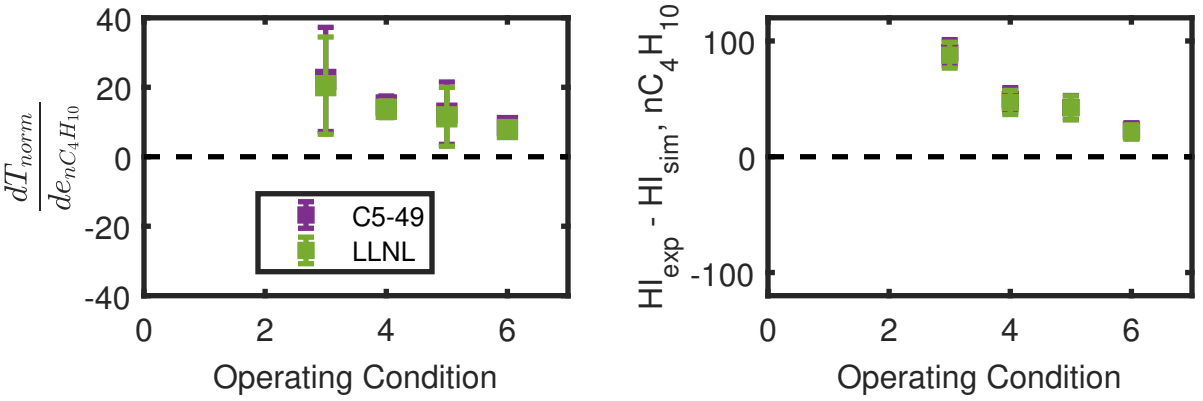

(a) (b)

Figure 10.19: Slope of linear curve-fit with 95% confidence intervals applied to each set of normalized temperature vs. test fuel energy fraction (left) and difference between experimental and simulated *HI*s with uncertainty (right) for all operating conditions of *HI* fuel substitution testing with *n*-butane.

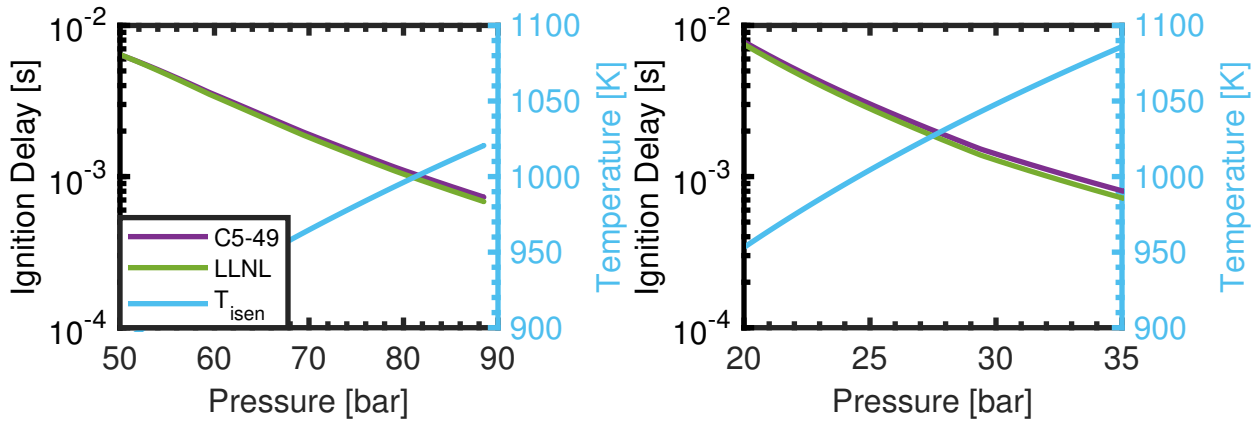

(a) (b)

Figure 10.20: Constant pressure ignition delay for pressure-temperature curves for operating conditions 1 (left) and 6 (right) for *n*-butane.

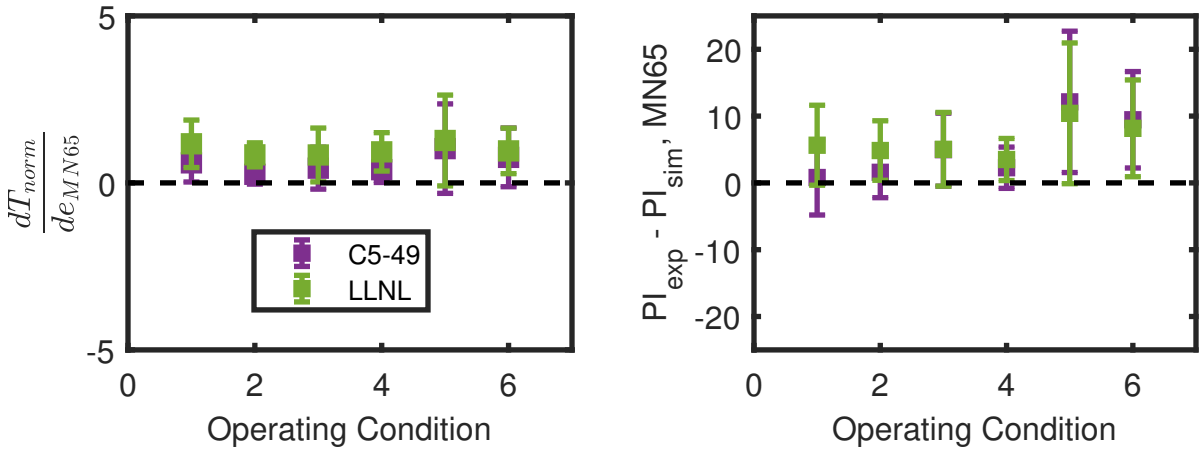

(a) (b)

Figure 10.21: Slope of linear curve-fit with 95% confidence intervals applied to each set of normalized temperature vs. test fuel energy fraction (left) and difference between experimental and simulated *PI*s with uncertainty (right) for all operating conditions of *PI* fuel substitution testing with MN65.

10.4.7 MN65

Figure 10.21 shows the slope of normalized temperature vs. test fuel energy fraction (left) and the difference between experimental and simulated *PI*s with uncertainty (right) for all operating conditions of the *PI* fuel substitution testing with MN65, using the C5-49 and LLNL mechanisms. Both mechanisms show a small amount of under-prediction relative to methane/propane, but most operating conditions fall within the uncertainty bounds of matching the experimental data. The MN65 mixture consists of mostly methane and propane, so it follows that its reactivity relative to methane/propane would be accurately predicted with each mechanism.

Figure 10.22 shows the slope of normalized temperature vs. test fuel energy fraction (left) and the difference between experimental and simulated *HI*s with uncertainty (right) for all operating conditions of the *HI* fuel substitution testing with MN65, using the C5-49 and LLNL mechanisms. The reactivity of MN65 relative to methane/hydrogen is under-predicted at the high pressure conditions (1 and 2) and matches the experimental data within the uncertainty bounds at the low pressure conditions (5 and 6) for both

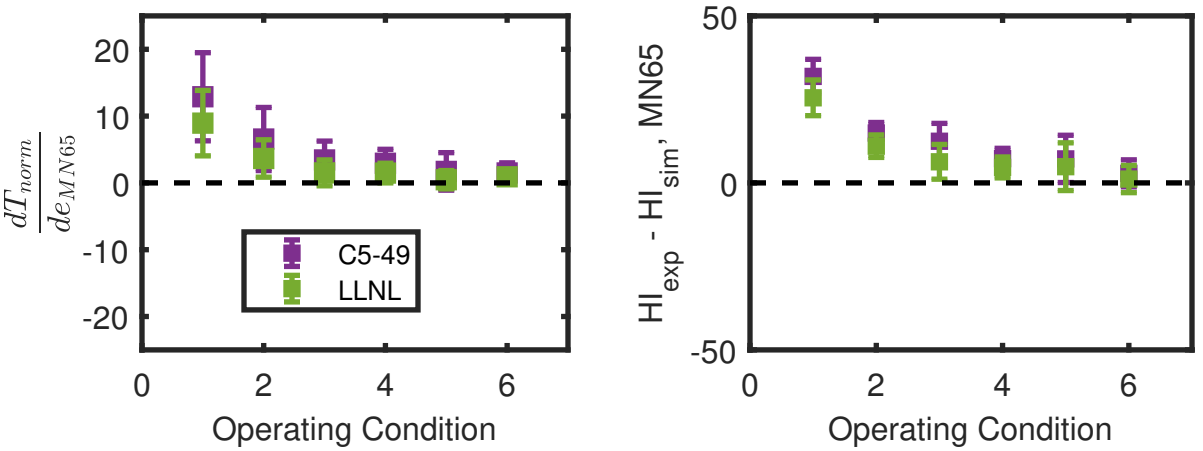

(a) (b)

Figure 10.22: Slope of linear curve-fit with 95% confidence intervals applied to each set of normalized temperature vs. test fuel energy fraction (left) and difference between experimental and simulated *HI*s with uncertainty for all operating conditions of *HI* fuel substitution testing with MN65.

mechanisms. The C5-49 mechanism is seen to have a slightly higher magnitude of under-prediction compared to the LLNL mechanism. The larger magnitude of under-prediction at high pressure conditions (1 and 2) is consistent with the results from simulating *HI* testing with pure propane, seen in Figure 10.11.

Figure 10.23 shows the ignition delays along the isentropic pressure-temperature curves for operating conditions 1 (left) and 6 (right) for MN65 at an equivalence ratio of 0.35. The ignition delays for MN65 are slightly shorter with the LLNL mechanism compared to the C5-49 mechanism. The difference is most likely caused by the propane contained in the mixture, which was also seen to have a shorter ignition delay with the LLNL mechanism. This difference in ignition delays is likely the reason for the slightly greater amount of reactivity under-prediction relative to methane/hydrogen with the C5-49 mechanism that was seen in Figure 10.22.

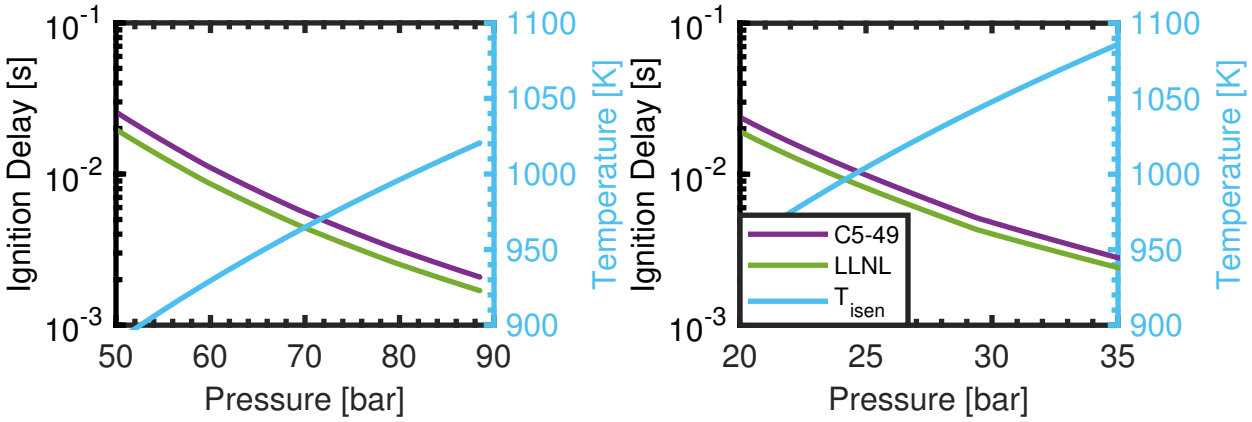

(a) (b)

Figure 10.23: Constant pressure ignition delay for pressure-temperature curves for operating conditions 1 (left) and 6 (right) for MN65.

10.4.8 MN80

Figure 10.24 shows the slope of normalized temperature vs. test fuel energy fraction (left) and the difference between experimental and simulated *PI*s with uncertainty (right) for all operating conditions of the *PI* fuel substitution testing with MN80, using the C5-49 and LLNL mechanisms. Both mechanisms showed consistent trends of very small amounts of under-prediction of the reactivity of MN80 relative to methane/propane. This is consistent with the results seen with MN65, with the main difference between the two fuel mixtures being smaller amounts of propane for the MN80 mixture.

Figure 10.25 shows the slope of normalized temperature vs. test fuel energy fraction (left) and the difference between experimental and simulated *HI*s with uncertainty (right) for all operating conditions of the *HI* fuel substitution testing with MN80, using the C5-49 and LLNL mechanisms. The results with both mechanisms showed that the reactivity of MN80 relative to methane/hydrogen was under-predicted at the high pressure condition (1) and slightly under-predicted at the remaining conditions.

Figure 10.26 shows the ignition delays along the isentropic pressure-temperature curves for operating conditions 1 (left) and 6 (right) for MN80 at an equivalence ratio of 0.35. The ignition delay trends were similar to those seen with MN65, with slightly

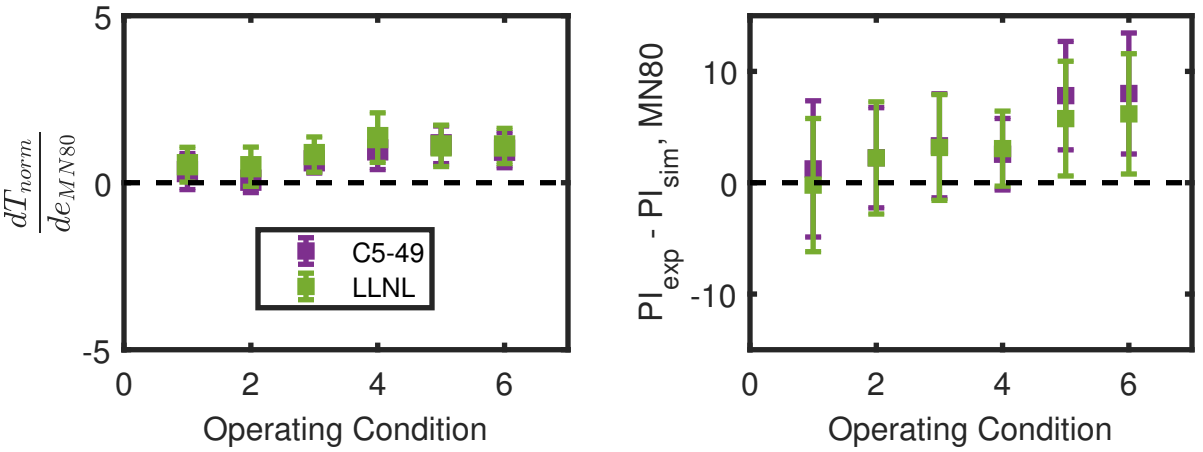

(a) (b)

Figure 10.24: Slope of linear curve-fit with 95% confidence intervals applied to each set of normalized temperature vs. test fuel energy fraction (left) and difference between experimental and simulated *PI*s with uncertainty (right) for all operating conditions of *PI* fuel substitution testing with MN80.

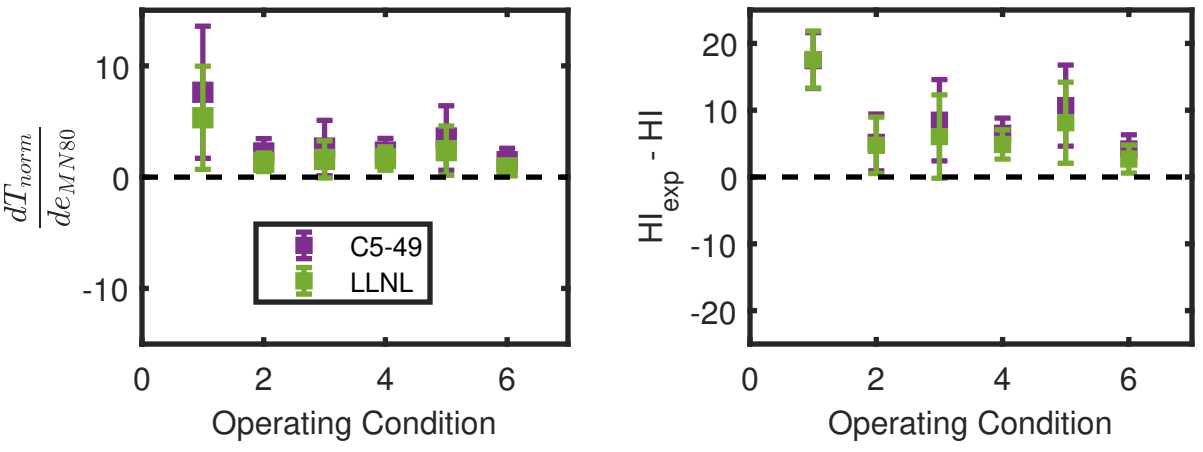

(a) (b)

Figure 10.25: Slope of linear curve-fit with 95% confidence intervals applied to each set of normalized temperature vs. test fuel energy fraction (left) and difference between experimental and simulated *HI*s with uncertainty for all operating conditions of *HI* fuel substitution testing with MN80.

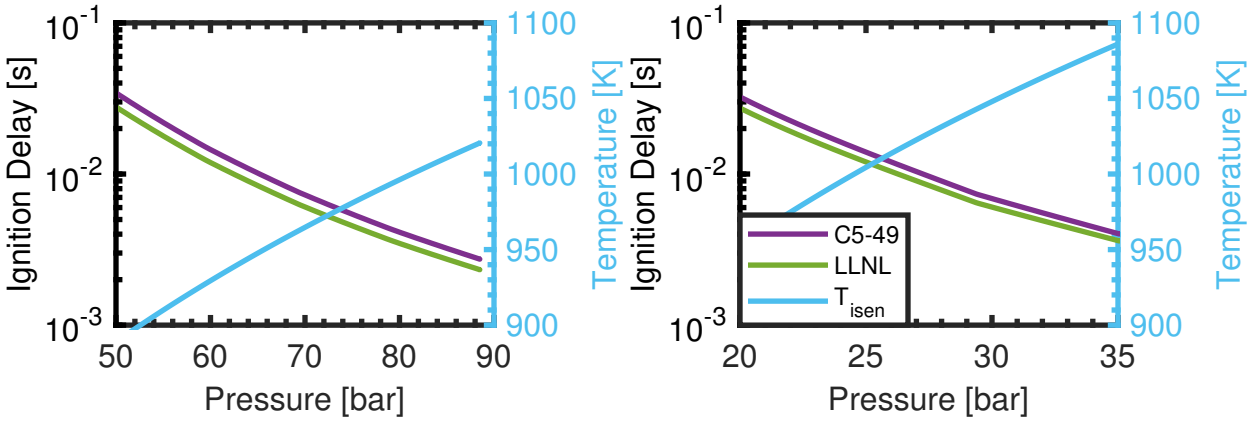

(a) (b)

Figure 10.26: Constant pressure ignition delay for pressure-temperature curves for operating conditions 1 (left) and 6 (right) for MN80.

shorter values for both conditions with the LLNL mechanism.

10.4.9 *n*-Heptane

Figure 10.27 shows the slope of normalized temperature vs. test fuel energy fraction (left) and the difference between experimental and simulated *PI*s with uncertainty (right) for all operating conditions of the *PI* fuel substitution testing with *n*-heptane, using the LLNL mechanism. No other mechanism considered in this work contains chemistry for *n*-heptane or isooctane, so results could only be simulated with the LLNL mechanism. The reactivity of *n*-heptane relative to methane/propane was under-predicted at all conditions.

Figure 10.28 shows the slope of normalized temperature vs. test fuel energy fraction (left) and the difference between experimental and simulated *HI*s with uncertainty (right) for all operating conditions of the *HI* fuel substitution testing with *n*-heptane, using the LLNL mechanism. The reactivity of *n*-heptane was under-predicted relative to methane/hydrogen at all conditions, although the amount of under-prediction was lower at the medium and low pressure, higher temperature conditions (4 and 6).

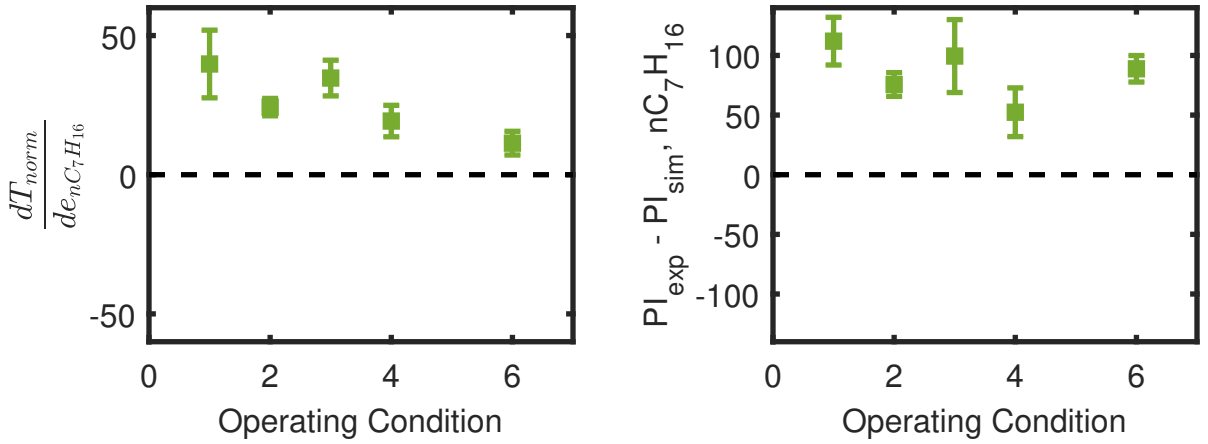

(a) (b)

Figure 10.27: Slope of linear curve-fit with 95% confidence intervals applied to each set of normalized temperature vs. test fuel energy fraction (left) and difference between experimental and simulated PIs with uncertainty (right) for all operating conditions of PI fuel substitution testing with n-heptane.

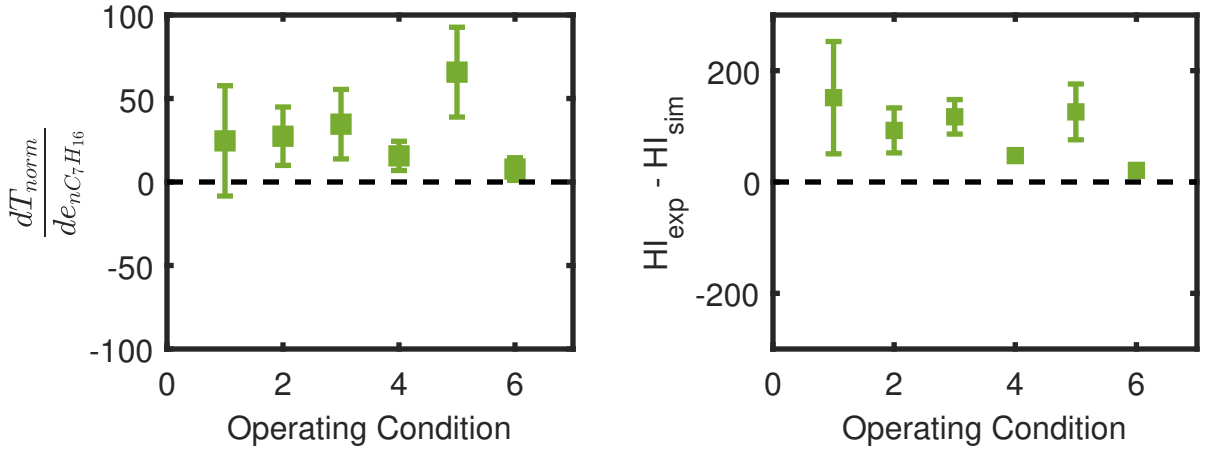

(a) (b)

Figure 10.28: Slope of linear curve-fit with 95% confidence intervals applied to each set of normalized temperature vs. test fuel energy fraction (left) and difference between experimental and simulated HIs with uncertainty for all operating conditions of HI fuel substitution testing with n-heptane.

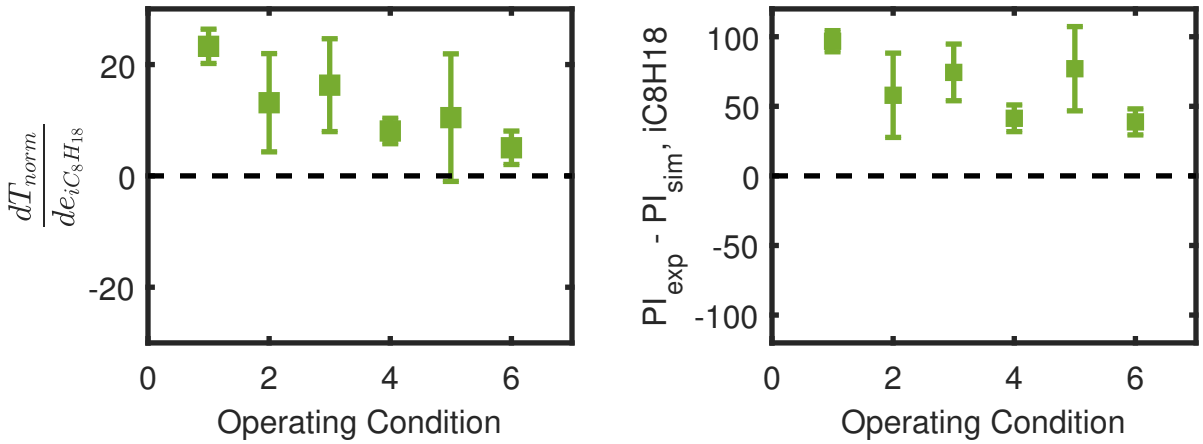

(a) (b)

Figure 10.29: Slope of linear curve-fit with 95% confidence intervals applied to each set of normalized temperature vs. test fuel energy fraction (left) and difference between experimental and simulated *PI*s with uncertainty (right) for all operating conditions of *PI* fuel substitution testing with isooctane.

10.4.10 Isooctane

Figure 10.29 shows the slope of normalized temperature vs. test fuel energy fraction (left) and the difference between experimental and simulated *PI*s with uncertainty (right) for all operating conditions of the *PI* fuel substitution testing with isooctane, using the LLNL mechanism. The reactivity of isooctane relative to methane/propane was under-predicted at all conditions, with lower magnitudes of under-prediction at the medium and low pressure, high temperature conditions (4 and 6).

Figure 10.30 shows the slope of normalized temperature vs. test fuel energy fraction (left) and the difference between experimental and simulated *HI*s with uncertainty (right) for all operating conditions of the *HI* fuel substitution testing with isooctane, using the LLNL mechanism. The reactivity of isooctane relative to methane/hydrogen was under-predicted at all conditions, with the magnitude of under-prediction lowest at the low pressure conditions (5 and 6).

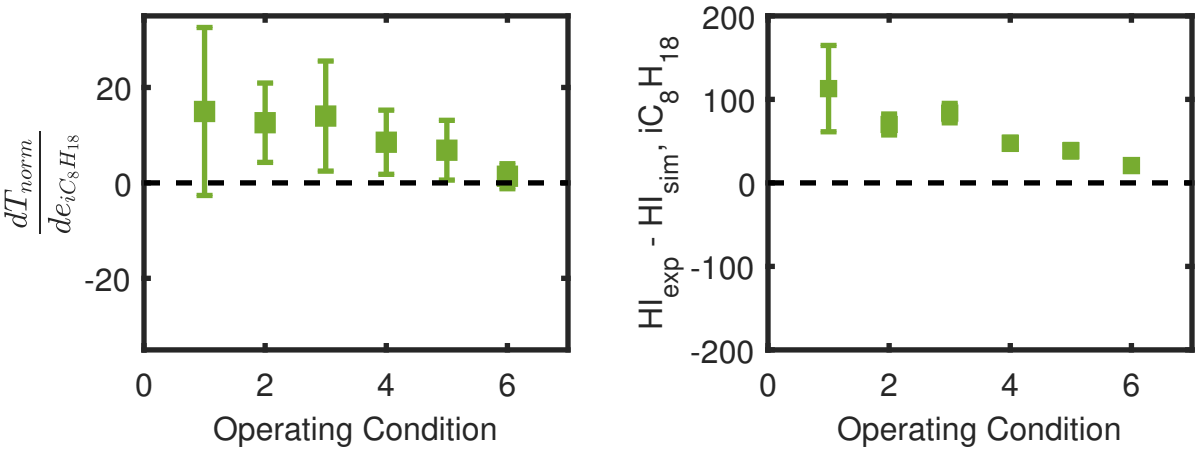

(a) (b)

Figure 10.30: Slope of linear curve-fit with 95% confidence intervals applied to each set of normalized temperature vs. test fuel energy fraction (left) and difference between experimental and simulated *HI*s with uncertainty for all operating conditions of *HI* fuel substitution testing with isooctane.

10.4.11 Summary and Discussion of Results

A summary of the relative fuel reactivities for each mechanism compared to the experimental data is shown in Tables 10.1 and 10.2 and Figure 10.31. Tables 10.1 and 10.2 show the amount of over- or under-prediction for each fuel relative to the methane/propane and methane/hydrogen reference fuels. Table 10.3 shows the comparison of ignition delays for the Aramco and C5-49 mechanisms relative to the LLNL mechanism for conditions 1 and 6. Figure 10.31 shows a direct comparison of the experimental *PI/HI*s and the simulated *PI/HI*s, where points lying above (below) the 45 degree line indicate under-(over)-prediction.

When comparing the test fuel reactivities relative to methane/propane seen in Table 10.1, the Aramco and C5-49 mechanisms produced fairly similar results, but substantial differences were seen between the Aramco/C5-49 mechanisms and the LLNL mechanism. Ethane, ethylene, and hydrogen data points are all shifted towards the under-predicted direction with the LLNL mechanism. The propane chemistry for these mechanisms was most likely a large contributor to these differences. Figure 10.12 showed that the LLNL

mechanism produced shorter ignition delays for propane compared to the Aramco and C5-49 mechanisms; this difference in the absolute reactivity of the reference fuels will affect the relative reactivity results for each test fuel.

A clear example of this is seen with the *n*-butane. Figure 10.19 shows nearly identical amount of under-prediction for *n*-butane relative to methane/hydrogen, while Figure 10.18 shows a larger magnitude of under-prediction for *n*-butane relative to methane/propane. Looking at ignition delays for methane (Figure 10.8), hydrogen (Figure 10.10), propane (Figure 10.12), and *n*-butane (Figure 10.20, the only substantial difference between the two mechanisms is the lower ignition delays for propane with the LLNL mechanism. Because methane, hydrogen, and *n*-butane have consistent ignition delays with both mechanisms, it follows that the reactivity of *n*-butane relative to methane/hydrogen is consistent with both mechanisms. Because the ignition delay of propane is inconsistent between the two mechanisms, it follows that propane is the cause of the inconsistent *n*-butane reactivity differences relative to methane/propane. The reactivity of propane is larger with the LLNL mechanism, evidenced by the shorter ignition delays, so it would follow that the reactivity of *n*-butane relative to methane/propane would have a larger amount of under-prediction with the LLNL mechanism compared to the C5-49 mechanism, which is consistent with the results seen in 10.18. It is important to keep in mind that results showing an under-prediction or over-prediction of the relative reactivity of a test fuel does not necessarily mean that the mechanism is predicting that test fuel incorrectly on an absolute reactivity basis; the relative reactivity errors can be caused by the absolute reactivity of the reference fuels being incorrect.

The relative fuel reactivity analysis was simplified for the methane/hydrogen studies, seen in Table 10.2, because all three mechanisms produced similar ignition delays for methane and hydrogen. All three mechanisms under-predicted the relative reactivity of ethane, with the LLNL mechanism having the largest magnitude of under-prediction and the C5-49 mechanism having the smallest magnitude of under-prediction. All three

mechanisms over-predicted the relative reactivity of ethylene, with the Aramco mechanism having the largest magnitude of over-prediction and the LLNL mechanism having the smallest magnitude of over-prediction. The relative reactivity of propane was under-predicted with both the Aramco and C5-49 mechanisms, while the LLNL mechanism well-predicted the relative reactivity at all conditions other than condition 1. All three mechanisms showed the largest amount of over-prediction at high-pressure conditions (1 and 2). The relative reactivity of n-butane was over-predicted by nearly identical magnitudes with both the C5-49 and LLNL mechanisms. The relative reactivity of the MN65 and MN80 gas mixtures was reasonably well matched for all conditions other than being under-predicted at high pressure conditions (1 and 2) for MN80. The relative reactivities of both n-heptane and isooctane were under-predicted with the LLNL mechanism.

While the methane/hydrogen relative fuel reactivity analysis is more straightforward due to similarities in the chemistry of methane and hydrogen with all three mechanisms, the methane/propane relative fuel reactivity analysis provides a useful consistency check on the methane/hydrogen results. Similar to the consistency check applied to the experimental data in Section 4.2.3, a predicted HI can be calculated from the simulated PIs by

$$HI_{pred} = 100 \times \frac{PI_{TF}}{PI_{H2}}. \tag{10.2}$$

Figure 10.32 shows the predicted HIs, calculated from the simulated PIs, vs. the simulated HIs; good correlation is seen for all three mechanisms, although a few outliers exist. Interestingly, the largest outlier, isooctane at operating condition 1 with the LLNL mechanism, was also an outlier when comparing the predicted vs. actual PIs for the experimental data in Section 4.2.3. It is unclear why this point is an outlier, but a deeper investigation between the predicted and actual PIs and HIs could be a useful area for future work. Overall, the good correlation between the predicted and actual results for both the experimental datasets and simulated datasets suggests that the relative fuel reactivity testing can be performed with different baseline fuels and yield consistent

results.

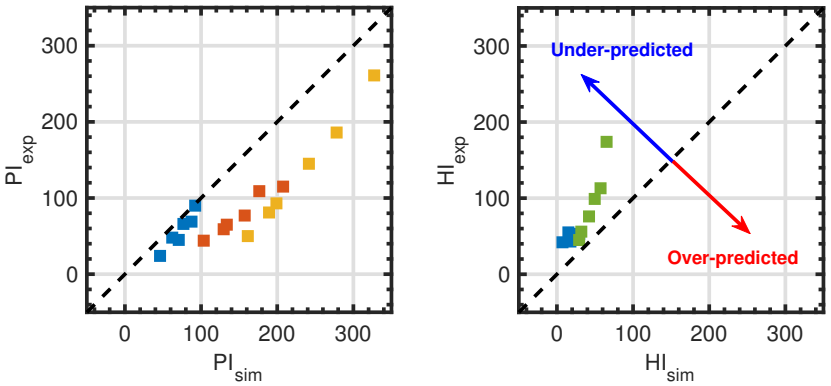

(a) Aramco, PI

(b) Aramco, HI

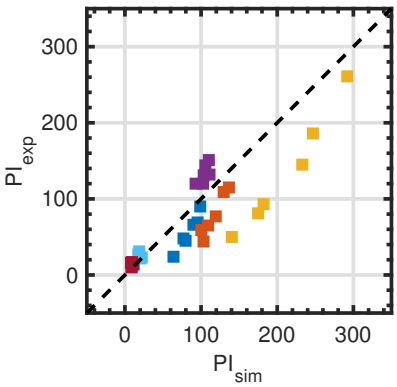

(c) C5-49, PI

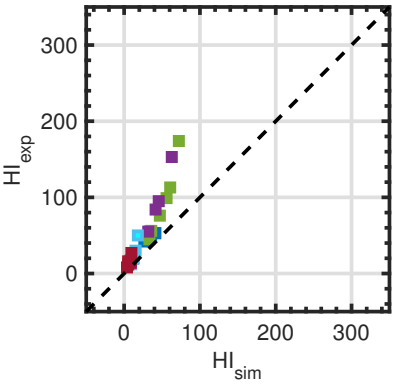

(d) C5-49, HI

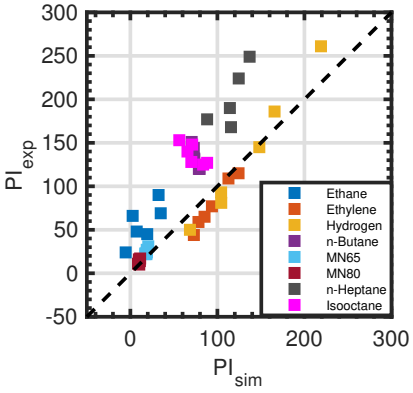

(e) LLNL, PI

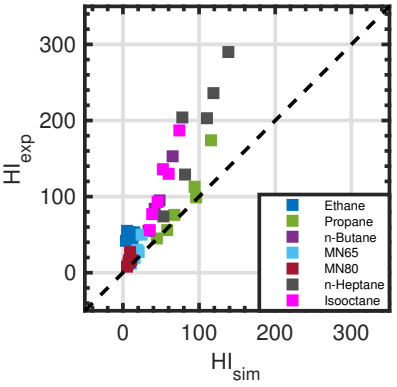

(f) LLNL, HI

Figure 10.31: Experimental *PI/HI* vs. simulated *PI/HI* with the Aramco, C5-49, and LLNL mechanisms.

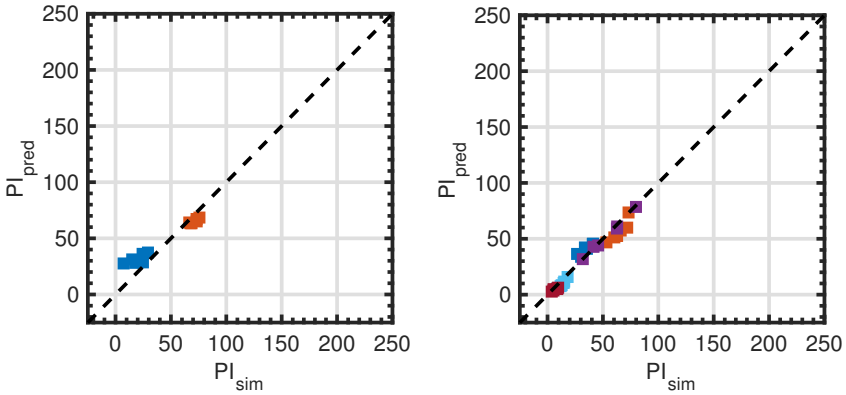

(a) Aramco

(b) C5-49

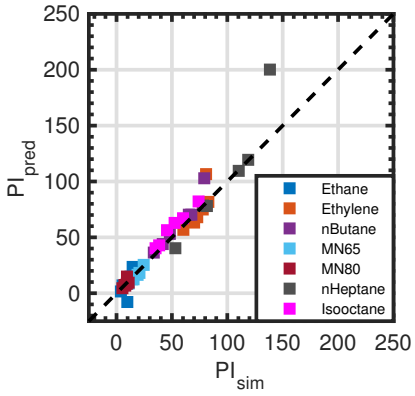

(c) LLNL

Figure 10.32: Predicted *PI*s generated using simulated *HI*s vs. directly simulated *PI*s with the Aramco, C5-49, and LLNL mechanisms.

Table 10.1: General comparison of simulated *PI*s vs. experimental data, where ⇑(⇓) indicates the reactivity was over(under)-predicted, ⇑⇑(⇓⇓) indicates the reactivity was substantially over(under)-predicted, and = indicates the reactivity was reasonably well predicted. In general, *PI* errors >30 were classified as substantially over- or under-predicted.

Fuel	Aramco	C5-49	LLNL
Ethane	⇑	⇑	⇓⇓
Ethylene	⇑⇑	⇑⇑	⇑
Hydrogen	⇑⇑	⇑⇑	=
MN65	N/A	=	=
MN80	N/A	=	=
n-Butane	N/A	⇓	⇓⇓
n-Heptane	N/A	N/A	⇓⇓
Isooctane	N/A	N/A	⇓⇓

Table 10.2: General comparison of simulated *HI*s vs. experimental data, where ⇑(⇓) indicates the reactivity was over(under)-predicted, ⇑⇑(⇓⇓) indicates the reactivity was substantially over(under)-predicted, and = indicates the reactivity was reasonably well predicted. In general, *HI* errors >30 were classified as substantially over- or under-predicted.

Fuel	Aramco	C5-49	LLNL
Ethane	⇓⇓	⇓	⇓⇓
Propane	⇓	⇓	=
MN65	N/A	⇓	⇓
MN80	N/A	⇓	⇓
n-Butane	N/A	⇓⇓	⇓⇓
n-Heptane	N/A	N/A	⇓⇓
Isooctane	N/A	N/A	⇓⇓

Table 10.3: General comparison of ignition delays calculated using the Aramco and C5-49 mechanisms relative to the LLNL mechanism, where ⇑(⇓) indicates the ignition delays were shorter(longer), ⇑⇑(⇓⇓) indicates the ignition delays were substantially shorter(longer), and = indicates the reactivity was reasonably well predicted. Ignition delays were compared at the high pressure, low temperature condition 1 and low pressure, high temperature condition 6

	Aramco		C5-49	
	Mode 1	Mode 6	Mode 1	Mode 6
Hydrogen	=	=	=	=
Methane	=	⇓	=	=
Ethane	⇑	=	⇑⇑	⇑⇑
Ethylene	⇓⇓	⇓⇓	⇓⇓	⇓⇓
Propane	⇓⇓	⇓⇓	⇓⇓	⇓⇓
MN65	N/A	N/A	⇓⇓	⇓⇓
MN80	N/A	N/A	⇓	⇓
n-Butane	N/A	N/A	=	=

10.5 Using Ignition Delays to Describe Relative Fuel Reactivity

10.5.1 Original Ignition Delay Method

In order to expand these results beyond the six conditions tested, a method to calculate the propane index from constant pressure ignition delays was developed. The original procedure went as follows: for each pressure and temperature, the test fuel's ignition delay is compared to propane's ignition delay. If the test fuel had a shorter ignition delay than propane, methane was added to the test fuel in increasing amounts until the test fuel/methane mixture's ignition delay was equal to propane's. If the test fuel had a longer ignition delay than propane, methane was added to propane in increasing amounts until the propane/methane mixture's ignition delay was equal to the test fuel's. Representative results for ethane (left) and ethylene (right) can be seen in Figure 10.33, where ethane had a longer ignition delay compared to propane, and ethylene had a shorter ignition delay compared to propane. At this condition (90 bar, 1050 K), ethane had the same ignition delay as a 59/41 mixture of propane/methane and propane had the same ignition delay as a 88/11 mixture of ethylene/methane. The PI for each test fuel is calculated by

$$PI = \frac{e_{C3H8}}{e_{C3H8} + e_{CH4}} 100, \tag{10.3}$$

$$PI = \frac{e_{CH4} + e_{tf}}{e_{tf}} 100, \tag{10.4}$$

where Equation 10.3 is used when the test fuel has a longer ignition delay than propane, and Equation 10.4 is used when the test fuel has a shorter ignition delay than propane. The boundary value for the result of Equation 10.3 is equal to 0 when no propane is included in the propane/methane mixture and equal to 100 when no methane is included in the propane/methane mixture. The boundary value for the result of Equation 10.4

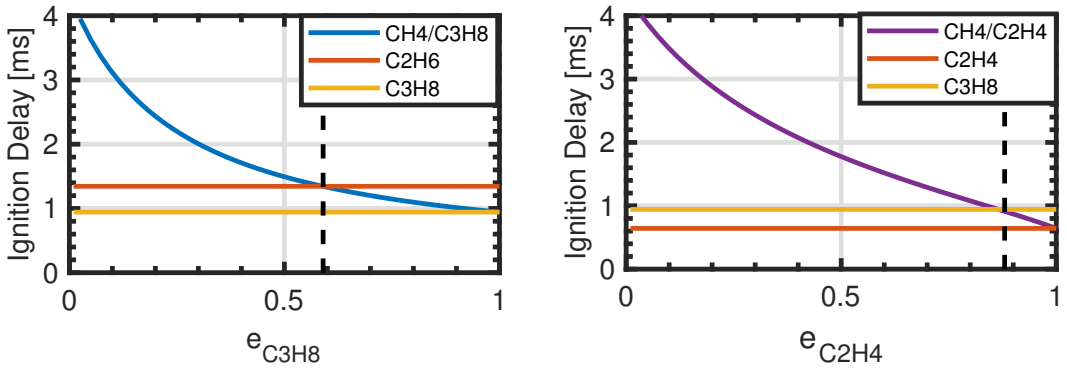

(a) (b)

Figure 10.33: Ignition delays of ethane, propane, and methane/propane mixture (left) and ethylene, propane, and methane/ethylene mixture (right) at 90 bar and 1050 K using the C5-49 mechanism. The vertical dashed lines indicate where the methane/propane mixture and ethane have identical ignition delays (left) and where the methane/ethylene mixture and propane have identical ignition delays (right).

is equal to 100 when no methane is included in the test fuel/methane mixture and approaches infinity as the test fuel amount approaches 0 in the test fuel/methane mixture. This matches the PI definition for the fuel substitution testing, where a PI of 0 indicates an equivalent reactivity to methane, a PI of 100 indicates an equivalent reactivity to propane, and a PI >100 indicates a greater reactivity than propane.

Propane index results using this ignition delay method were calculated and compared to the PI results from the engine fuel substitution simulations. It was assumed that the ignition delay method, which is performed at static TDC conditions, captured the relevant temperature/pressure thermodynamic history from the engine simulation. It is noted that for improved accuracy, other strategies for calculating a potentially more accurate representative temperature and pressure were discussed in Section 2.3.5. Figure 10.34 shows the results of the PIs calculated using the ignition delay method vs. the PIs calculated using the engine fuel substitution simulation method. In both cases, the C5-49 mechanism was used, so relatively good agreement was expected if the static TDC conditions were an adequate representation of the thermodynamic history of the engine simulation. Reasonable agreement between the PIs calculated using each method was

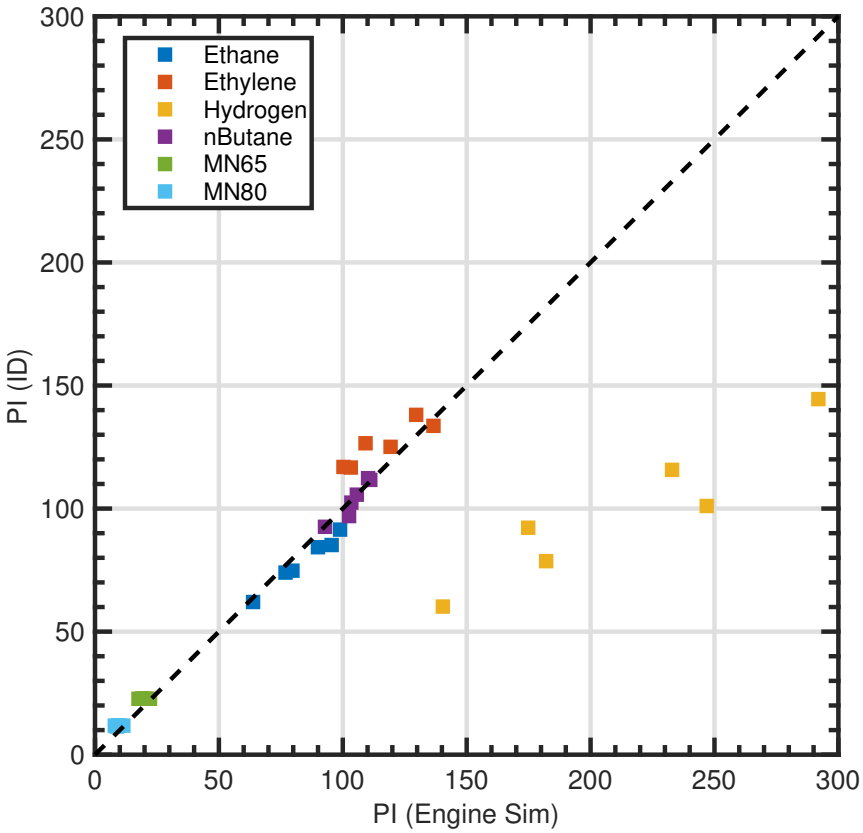

Figure 10.34: Calculated *PI*s using the ignition delay method vs. *PI*s using the engine simulation method with the C5-49 mechanism.

seen for all fuels except for hydrogen, which had substantially lower *PI*s from the ignition delay method.

10.6 Modified Ignition Delay Method

10.6.1 Thermodynamic Effects

The original ignition delay method calculated the ignition delays of both the test fuel and the methane/propane reference fuel mixtures at a fixed starting temperature and pressure. The engine simulation, because it simulates a physical engine cycle starting at IVC, is dependent on the different thermodynamic properties of the fuels. Figure

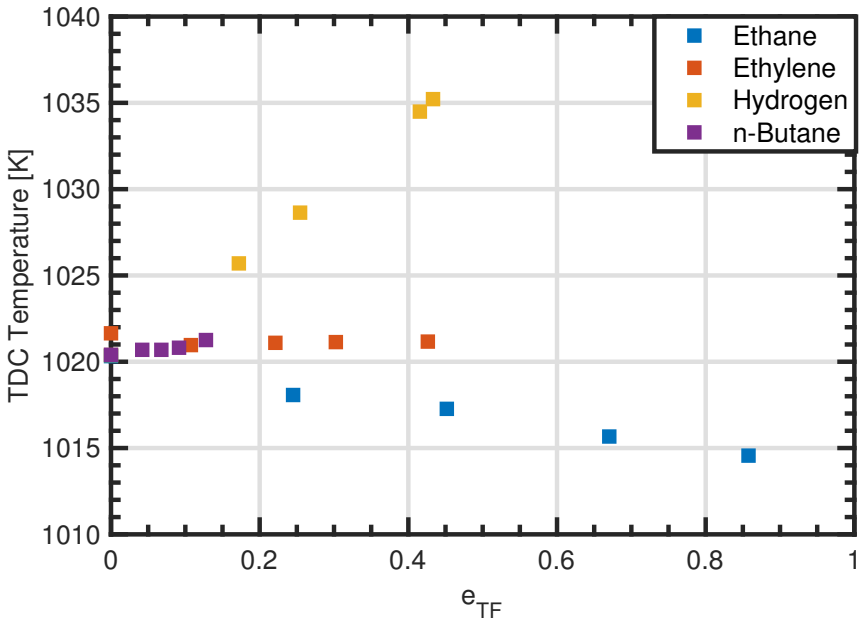

Figure 10.35: TDC temperature for engine simulations at operating condition 1 using the C5-49 mechanism with chemistry turned off.

10.35 shows the temperature at TDC for the engine simulations at operating condition 1 using the C5-49 mechanism. Chemistry was disabled to ensure that no fuel reactions were influencing the temperature. The TDC temperature showed a strong sensitivity to the hydrogen concentration, and a modest sensitivity to the ethane concentration and no sensitivity to the other fuels at this operating condition. These differences in compression temperatures were caused by the changing gas mixture specific heats.

The original iteration of the ignition delay method did not account for changing thermodynamic properties. In the case of hydrogen, the increased compression temperature will increase the calculated 'relative reactivity' compared to methane/propane mixtures that reach lower compression temperatures. This trend was seen in Figure 10.34, where the *PI* for hydrogen from the engine simulation method was substantially larger than the *PI* from the ignition delay method.

To capture the effect of the changing specific heats, the ignition delay method was modified to mimic a compression process. The gas is first initialized at the simulation

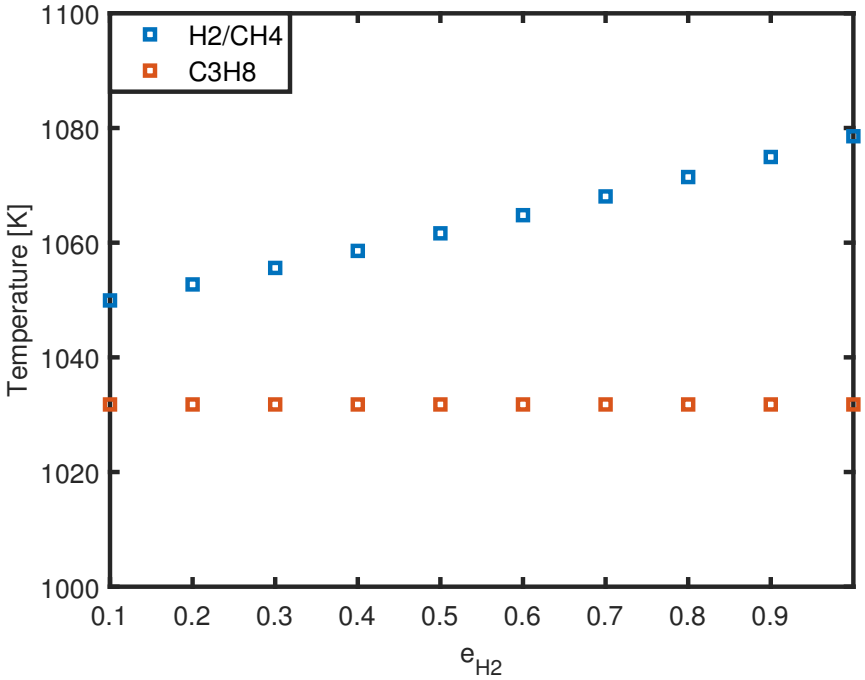

Figure 10.36: Isentropically compressed temperature of hydrogen/methane/air mixture as a function of hydrogen fraction and isentropically compressed temperature of propane/air at an equivlanece ratio of 0.35.

IVC temperature and pressure, and then isentropically compressed to TDC pressure before performing each ignition delay calculation. This causes mixtures with greater amounts of hydrogen to have their ignition delay calculated at higher temperatures. An example of the TDC temperatures using the revised ignition delay method is seen in Figure 10.36. The original method calculated the ignition delays for both propane and the hydrogen/methane mixtures at the same starting temperature; the new method compensates for the varying ratio of specific heats before computing ignition delays. Figure 10.37 shows the comparison of PIs calculated using the engine simulation and ignition delay methods for hydrogen with the C5-49 mechanism, with both the original and isentropically compensated ignition delay method shown. It can be seen that there was a large effect on the calculated PIs for hydrogen. The correlation between PIs for hydrogen using the revised ignition delay method is still not perfect, but it resulted in values much closer to PIs calculated from the engine simulations.

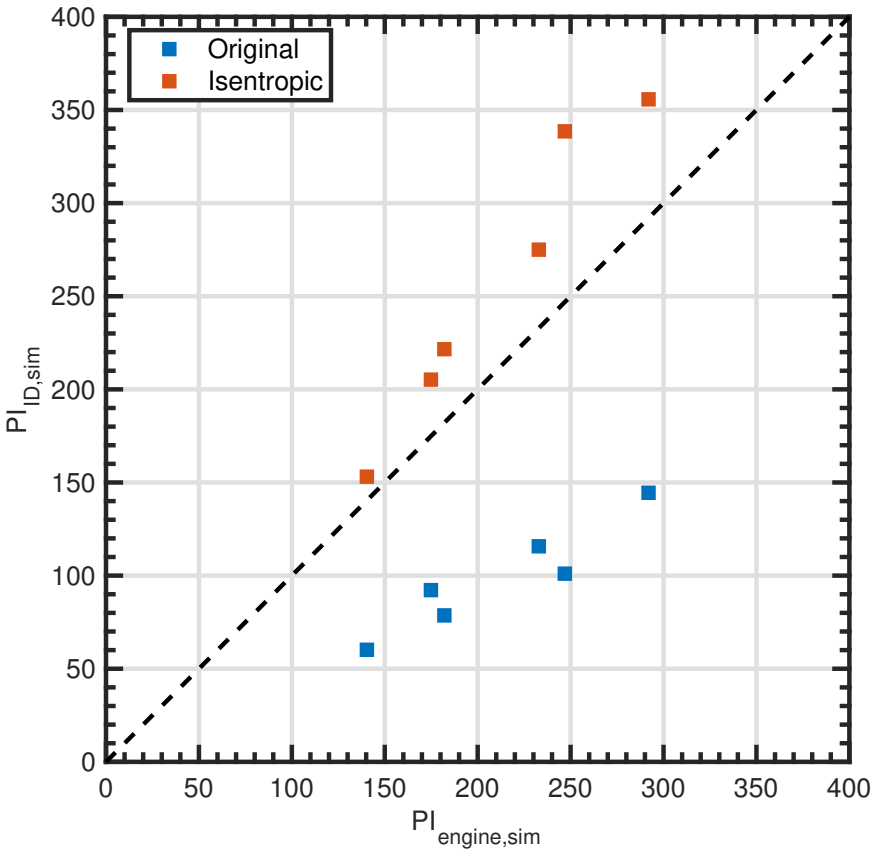

Figure 10.37: Calculated *PI*s using the ignition delay method, both original and revised with isentropic compensation, vs. *PI*s using the engine simulation method.

10.6.2 Non-linear Mixing Effects

Another potential source of disagreement between the ignition delay method and the engine simulation method is non-linear effects of the individual fuels' contributions to the overall mixture reactivity. The engine fuel substitution method started with a baseline fuel mixture of propane and methane, and added in the test fuel in increasing amounts until all of the propane was removed from the system. The ignition delay method compared a pure propane/air mixture to a mixture of the test fuel/methane/air when the test fuel/air was more reactive than propane, and the method compared the pure test fuel/air to a mixture of propane/methane/air when the test fuel was less reactive than propane.

The ignition delay method was modified to use a test fuel mixture that consisted of the test fuel/methane, rather than the pure test fuel. The PI of the test fuel/methane mixture, PI_{mix}, is calculated in the same manner as the original method, with Equations 10.3 and 10.4. The PI_{tf} is calculated by dividing PI_{mix} by the test fuel fraction in the test fuel/methane mixture, e_{tf},

$$PI_{tf} = \frac{PI_{mix}}{e_{tf}}. \tag{10.5}$$

To illustrate this procedure, consider a test mixture of 25/75 ethane/methane that is found to have an identical ignition delay to a mixture of 10/90 propane/methane, giving a PI_{mix} for the ethane/methane mixture of 10. From Equation 10.5, this results in a PI_{tf} of 40 for pure ethane. If ethane/methane and propane/methane mixture reactivities could be perfectly described by a linear blending rule, a 50/50 ethane/methane mixture would have a PI_{mix} of 20 and a 75/25 ethane/methane mixture would have a PI_{mix} of 30, both of which would result in a calculated PI_{tf} of 40 for pure ethane. If the mixture reactivities perfectly follow the linear blending rule, the PI_{mix} of each ethane/methane mixture will be proportional to the ethane fraction, and the calculated PI_{tf} for pure ethane will be independent of e_{tf}.

Figure 10.38 shows an example of the modified ignition delay method for test fuels of hydrogen and ethane for operating condition 6 using the C5-49 mechanism, where the x axis refers to the test fuel fraction in a test fuel/methane mixture. Figures 10.38a shows the calculated PI_{mix} as a function of hydrogen energy fraction for mixtures of hydrogen/methane. Because hydrogen is more reactive than methane, as the hydrogen energy fraction increases, PI_{mix} increases. If the mixture reactivity perfectly followed a linear energy-based blending rule, the blue curve would be a straight line. Some curvature is seen, with the maximum deviation occurring at a hydrogen fraction of about 0.6. Comparing the hydrogen/methane PI_{mix} to the ethane/methane PI_{mix}, seen in Figure 10.38c, the ethane/methane mixtures show a more linear relationship between PI_{mix} and test fuel fraction than the hydrogen/methane mixtures. Figure 10.38b shows the calculated PI_{tf}, using Equation 10.5, for pure hydrogen as a function of hydrogen fraction used in the test mixture, while Figure 10.38d shows the same results for ethane. If the mixture reactivities perfectly followed a linear blending rule, the calculated PI_{tf} would be independent of test fuel fraction. For both hydrogen and ethane, the PI_{tf} calculated for the pure test fuel varied based on the starting test fuel fraction used for the ignition delay method; it can also be seen that the calculated PI_{tf} values for pure hydrogen had greater variability compared to the values for pure ethane, which agrees with the more non-linear behavior seen for hydrogen in Figure 10.38a compared to ethane in Figure 10.38c.

It is clear that using different test fuel/methane mixtures for the ignition delay method may result in very different results for PI_{tf}. Because an accurate comparison to the engine fuel substitution tests was desired, the criteria of a PI_{mix} equal to the baseline propane/methane ratio, PI_{ref}, from the fuel substitution tests was used. For the fuel substitution tests, the underlying assumption is that the overall mixture reactivity stays constant and equal to the baseline propane/methane mixture reactivity. The PI_{ref} was approximately 23 for conditions 1-4, 37 for condition 5, and 51 for condition 6. For a

discussion on why these baseline fuel mixtures were used for the experimental PI testing, the reader is referred to Chapter 4.

The modified method compares the ignition delays of the test fuel mixed with increasing amounts of methane until the mixture ignition delay, PI_{mix}, is equal to the ignition delay of a propane/methane mixture defined by the PI_{ref} baseline condition, which for condition 6, for example, was 51/49 propane/methane. Referring to Figure 10.38a, for hydrogen this occurs at a 19/81 hydrogen/methane mixture. Referring to Figure 10.38b, using the modified ignition delay method results in a PI_{tf} for pure hydrogen of 280, whereas the original ignition delay method resulted in a PI_{tf} for pure hydrogen of 330. In a similar manner, Figure 10.38c shows that a mixture of 50/50 ethane/methane has the same ignition delay as the 51/49 propane/methane mixture. From Figure 10.38d, this results in a PI_{tf} for pure ethane of 102, compared to a PI_{tf} of 93 when using the original method. An alternative method to picking a single PI_{ref} for the calculations would be to perform a sweep for multiple value of PI_{ref} and apply a linear fit to the results to calculate the final PI_{tf}; this method was briefly investigated, but the PI_{tf} calculated from the linear fit were very similar to the PI_{tf} calculated for the largest PI_{ref} value used in the sweep, so in the interest of limiting computational time the single point method was used.

Figure 10.39 shows the comparison of PIs calculated using the engine simulation and ignition delay methods, with the original, the isentropically compensated, and the isentropically compensated and mixture-compensated ignition delay methods for hydrogen shown. The modified ignition delay with isentropic and mixture compensation shows good agreement with the engine simulations. Figure 10.40 shows the results for all fuels with both the original and revised ignition delay methods with the C5-49 mechanism. The main differences between the original and revised methods are seen with hydrogen, and the revised method shows reasonably good agreement with the engine simulations for all test fuels.

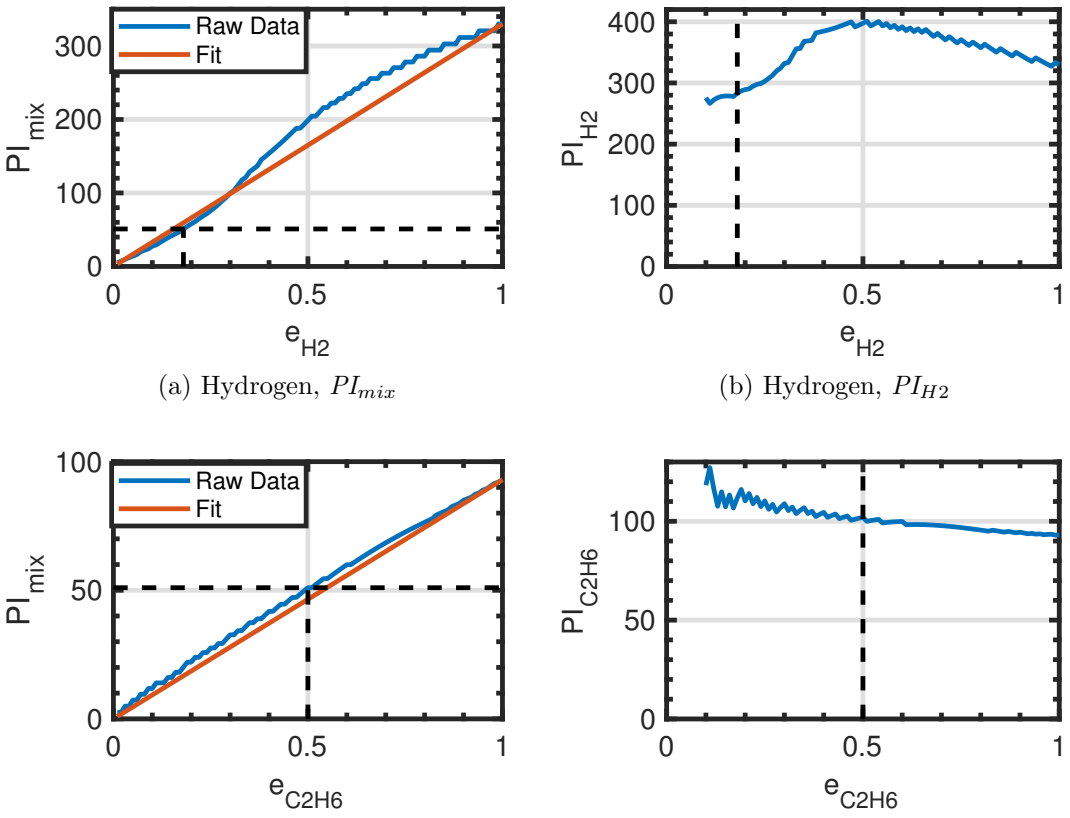

(a) Hydrogen, PI_{mix}

(b) Hydrogen, PI_{H2}

(c) Ethane, PI_{mix}

(d) Ethane, PI_{C2H6}

Figure 10.38: $PI_{TF,mix}$ vs. hydrogen energy fraction (a) and PI_{H2} vs. hydrogen energy fraction (b) for operating condition 6 using the C5-49 mechanism, and the equivalent plots with ethane instead of hydrogen (c and d).

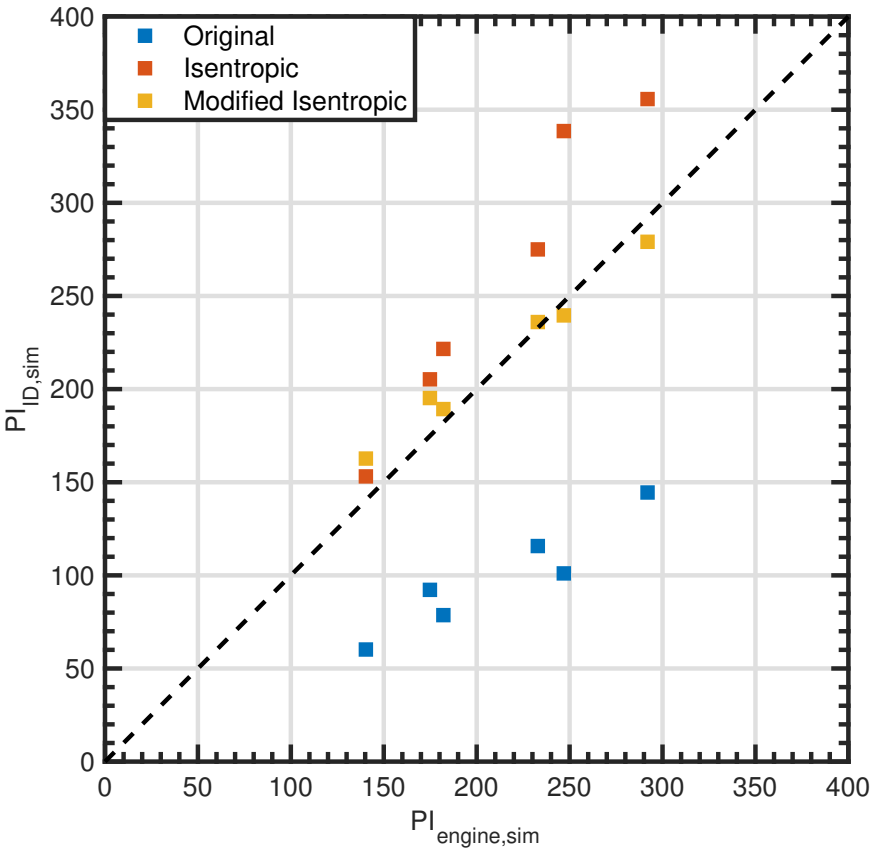

Figure 10.39: Calculated *PI*s for hydrogen using the ignition delay method, both original and revised with isentropic and mixture compensation, vs. *PI*s using the engine simulation method.

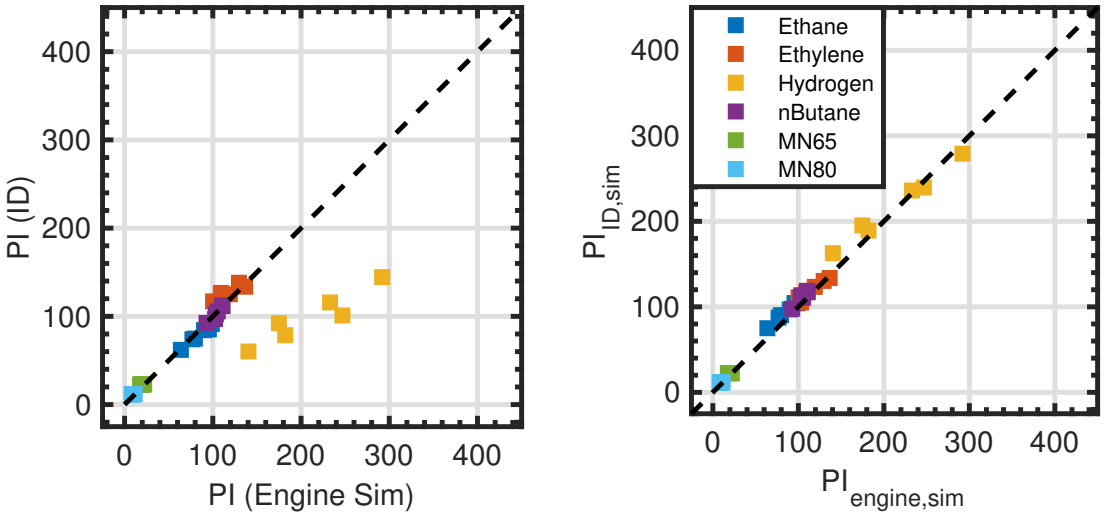

Figure 10.40: Calculated *PI*s using the ignition delay method, both original (a) and revised with isentropic and mixture compensation (b), vs. *PI*s using the engine simulation method with the C5-49 mechanism

As seen in the previous discussions, combustion performance in an engine application can be strongly affected by both the individual fuel kinetics and the fuel thermodynamic properties, such as the ratio of specific heats. Typical natural gas composition does not contain large amounts of hydrogen, which is the fuel that will have the biggest impact on physical properties, but this will be an important factor for applications using syngas. Using the ignition delay method with isentropic compensation improved the comparison between *PI*s calculated from ignition delays and *PI*s calculated with the engine simulations. However, the isentropic compensation is dependent on the compression ratio of the specific engine being modeled, and thus is not as useful for a general discussion of relative fuel reactivity. For the remaining sections, the *PI*s shown were calculated using the revised method with a mixture compensation criteria, *i.e.*, initial propane index of 20/80 propane/methane and no isentropic compensation. The mixture compensation value was chosen to be representative of the baseline fuel mixtures used in the experimental fuel substitution testing and corresponds to a MN of approximately 70. Referring

to Figure 10.38, the *PI* results are potentially sensitive to the initial propane index. A more in-depth analysis of how dependent the *PI* results are on the initial propane index could be a useful area of future work. Omitting the isentropic compression will show a comparison purely of fuel relatively reactivity and how it changes as a function of pressure and temperature, but it should be noted that in an engine application thermodynamic properties can also play an important role. Additionally, fuels that exhibit non-negligible amounts of low-temperature heat release also may show quite different performance in an engine application compared to this ignition delay comparison.

In the interest of brevity, the ignition delay method *PI*s will not be compared to the experimental *PI*s. It is noted that similar over-/under-prediction trends would be expected to those seen with the engine fuel substitution simulations. The purpose of comparing the simulation and experimental results was to evaluate the accuracy of the kinetics mechanisms; the engine simulations are a more accurate model of the engine experiments. The main objective of this ignition delay method is to provide insight to general fuel reactivity trends seen over a wide range of temperatures and pressures that may not have been achievable in the engine experiments.

10.6.3 Using Ignition Delays to Describe Relative Fuel Reactivity

The *PI* was generated for a wide range of pressure and temperature values, and the results provide insight as to how the reactivity of the test fuel relative to methane/propane and methane/hydrogen changes with thermodynamic conditions. Figure 10.41 shows the *PI* for ethane as a function of pressure and temperature using the ignition delay method with mixture compensation along with the simulated engine pressure/temperature compression curves; the TDC conditions from the engine simulation are marked with a star for each of the six operating conditions and *PI*s from the engine simulations are listed in next to each TDC location. Reasonable agreement is seen between *PI*s calculated us-

ing each simulation method, with the ignition delay method producing *PI*s 5-10 higher compared to the *PI*s from the engine simulations. More importantly, the trends in *PI* as a function of temperature and pressure are similar between the two methods, suggesting that the ignition delay method can be used to predict relative fuel reactivity trends at conditions not tested in the engine simulations. Figure 10.42 shows the *HI* for ethane as a function of pressure and temperature using the ignition delay method with mixture compensation along with the simulated engine pressure/temperature compression curves. The ignition delay method produced *HI*s 10-25 higher compared to the *HI*s from the engine simulations. The *HI*s from the ignition delay method are expected to be higher than the engine simulations because the ignition delay method is not compensating for the increased compression temperatures that occur for hydrogen due to the increased specific heat ratio, as discussed in the previous section. However, the ignition delay generated *HI*s are still useful to gain insight on how each test fuel's reactivity relative to methane/hydrogen changes with thermodynamic conditions.

Hydrogen

The calculated *PI*s as a function of temperature and pressure for hydrogen using the Aramco, C5-49, and LLNL mechanisms are seen in Figure 10.43. Similar trends are seen with all three mechanisms. The reactivity of hydrogen relative to methane/propane is strongly dependent on both temperature and pressure, with the relative reactivity of hydrogen increasing with increasing temperatures and decreasing pressures.

Propane

The calculated *HI*s as a function of temperature and pressure for propane using the Aramco, C5-49, and LLNL mechanisms are seen in Figure 10.44. Similar trends are seen with all three mechanisms, although the LLNL mechanism produced larger *HI*s than the Aramco and C5-49 mechanisms, which is consistent with previously shown results with

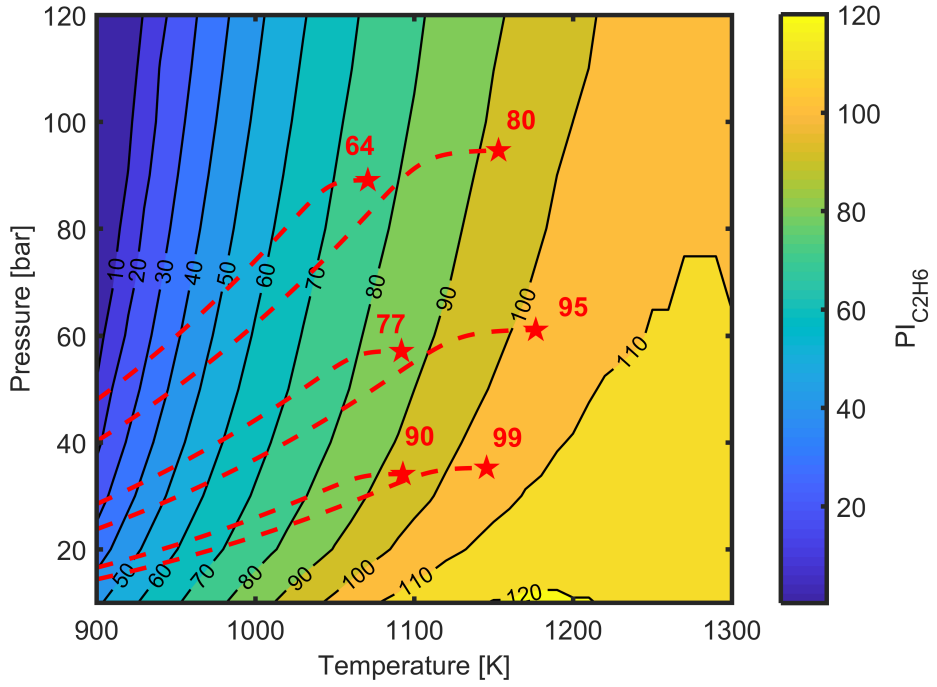

Figure 10.41: Calculated PIs for ethane using the ignition delay method with mixture compensation as a function of pressure and temperature with the C5-49 mechanism, along with engine simulation pressure/temperature curves with stars marking TDC locations. Red numbers indicate PI_{sim} from the engine simulations.

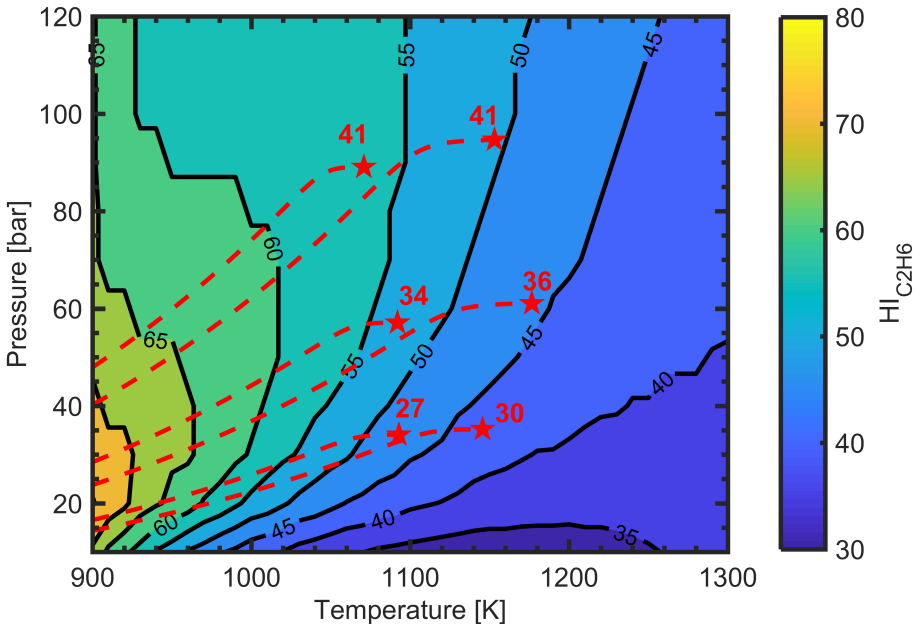

Figure 10.42: Calculated *HI*s for ethane using the ignition delay method with mixture compensation as a function of pressure and temperature with the C5-49 mechanism, along with engine simulation pressure/temperature curves with stars marking TDC locations. Red numbers indicate HI_{sim} from the engine simulations.

propane. The reactivity of propane relative to methane/hydrogen is strongly dependent on both temperature and pressure, with the relative reactivity of propane increasing with decreasing temperatures and increasing pressures.

Ethane

The calculated *PI*s as a function of temperature and pressure for ethane using the Aramco, C5-49, and LLNL mechanisms are seen in Figure 10.45. Similar trends were seen for all three mechanisms. The reactivity of ethane relative to methane/propane increases substantially as temperature increases. The relative reactivity also increases as pressure decreases, especially at higher temperatures. At elevated temperatures, the Aramco and C5-49 mechanisms results suggest that ethane is more reactive than propane, while the LLNL mechanism results suggest that ethane is less reactive than propane for all conditions except the highest temperature and lowest pressure shown.

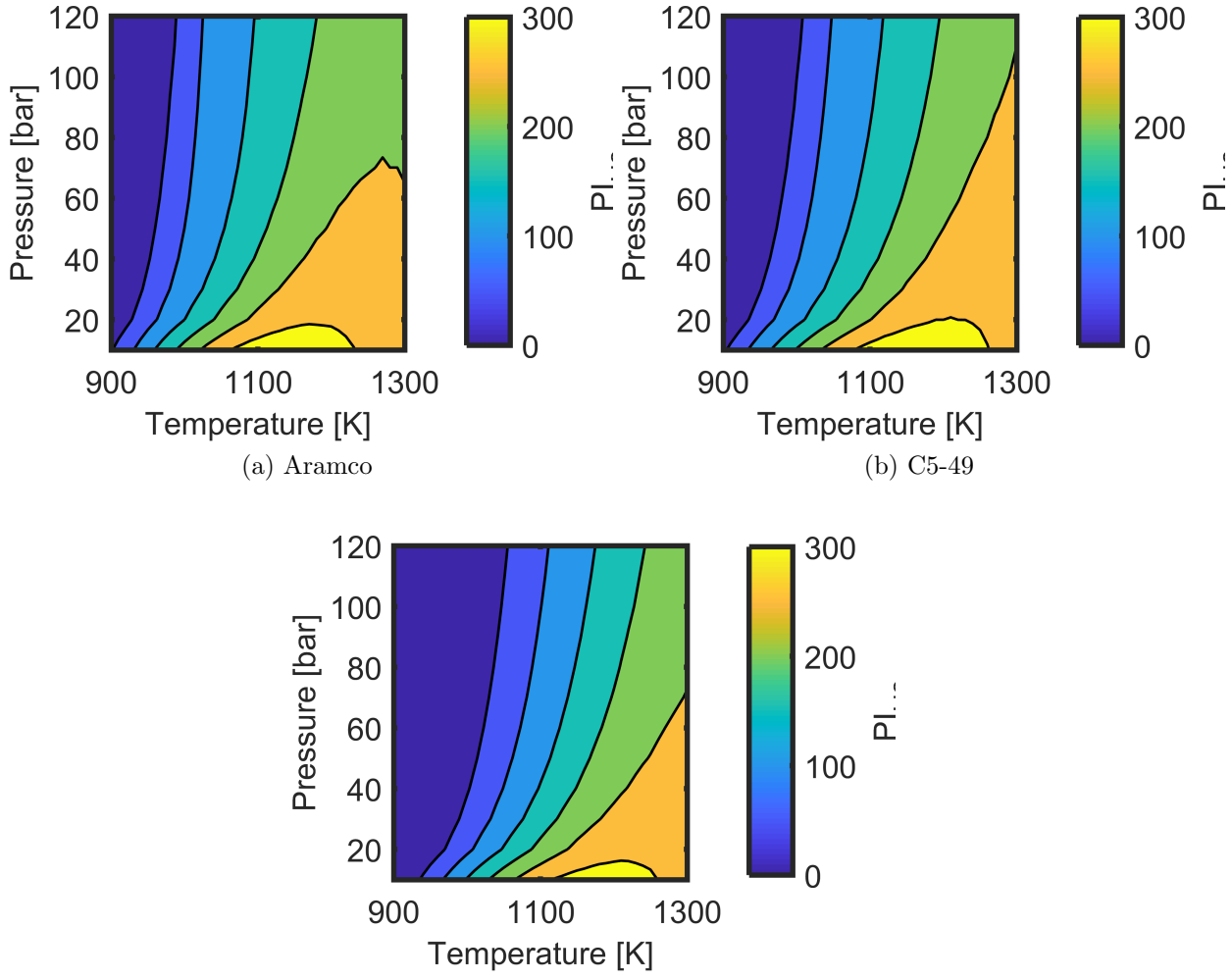

(a) Aramco

(b) C5-49

(c) LLNL

Figure 10.43: Calculated PIs for hydrogen using the ignition delay method.

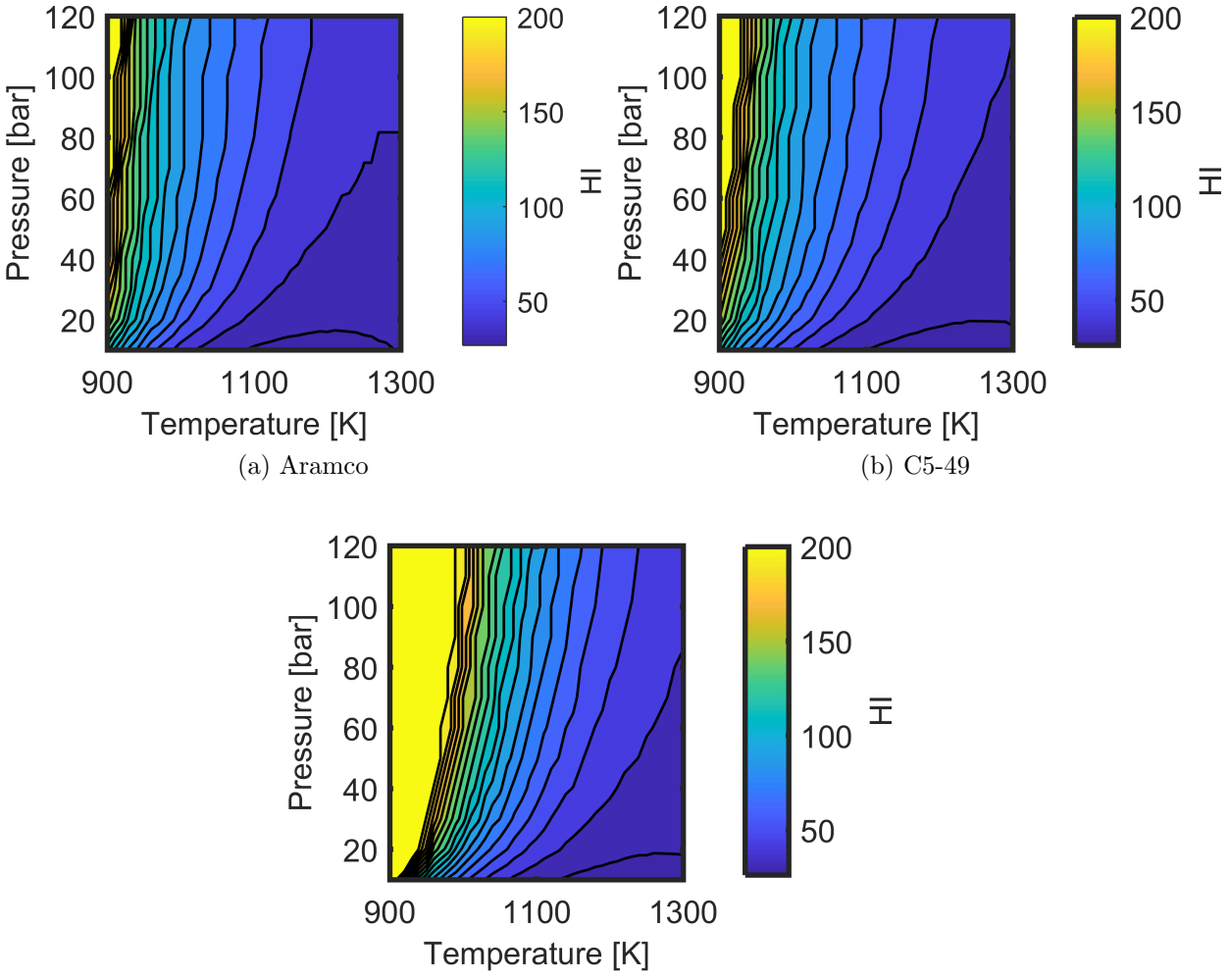

(a) Aramco

(b) C5-49

(c) LLNL

Figure 10.44: Calculated *HI*s for propane using the ignition delay method.

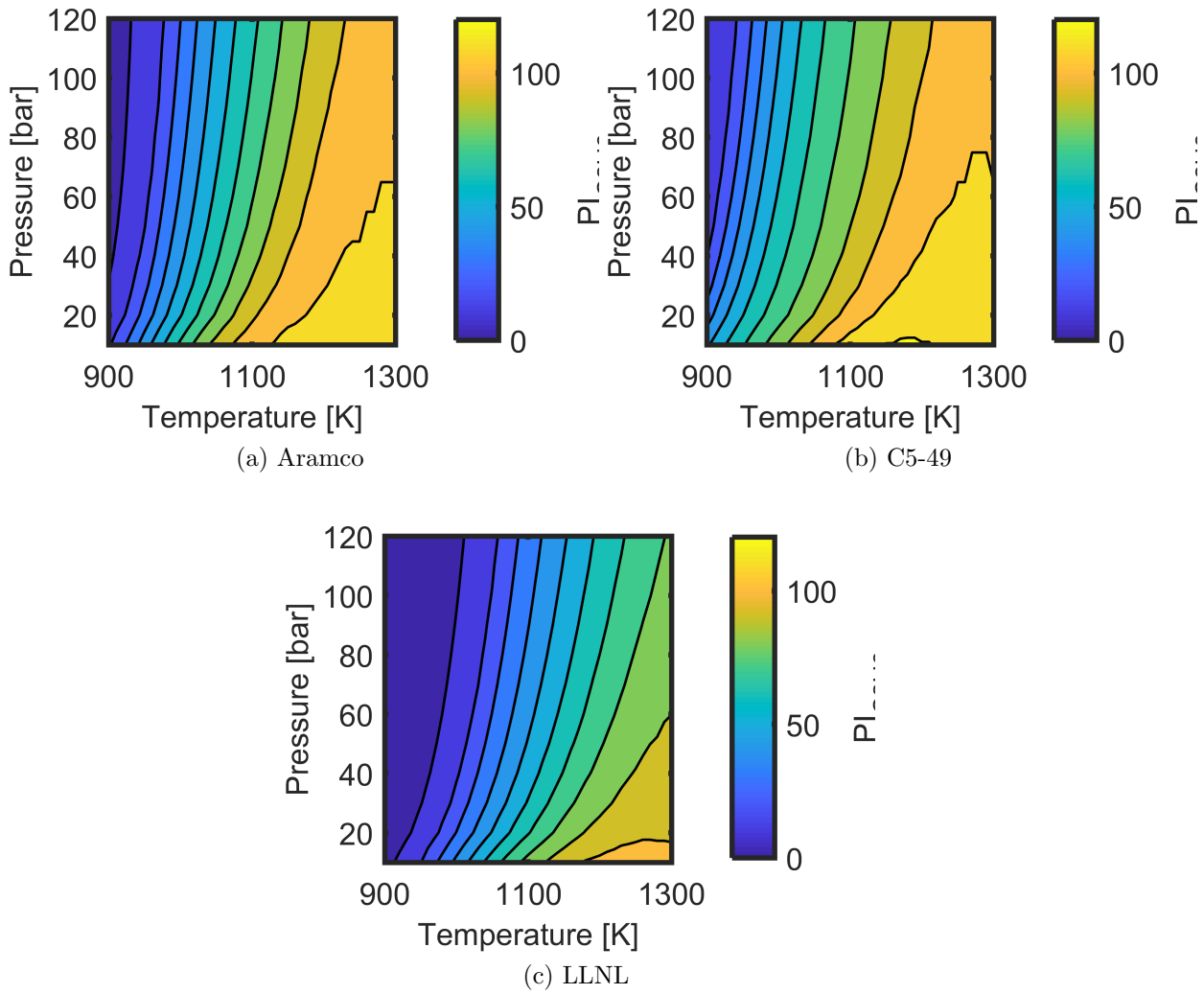

Figure 10.45: Calculated *PI*s for ethane using the ignition delay method.

The calculated *HI*s as a function of temperature and pressure for ethane using the Aramco, C5-49, and LLNL mechanisms are seen in Figure 10.46. The Aramco and LLNL mechanisms produced *HI*s that were nearly independent of temperature and pressure, decreasing at temperatures below 950-1000 K. The C5-49 mechanism showed more temperature and pressure sensitivity, with *HI*s increasing with decreased temperature and increased pressure.

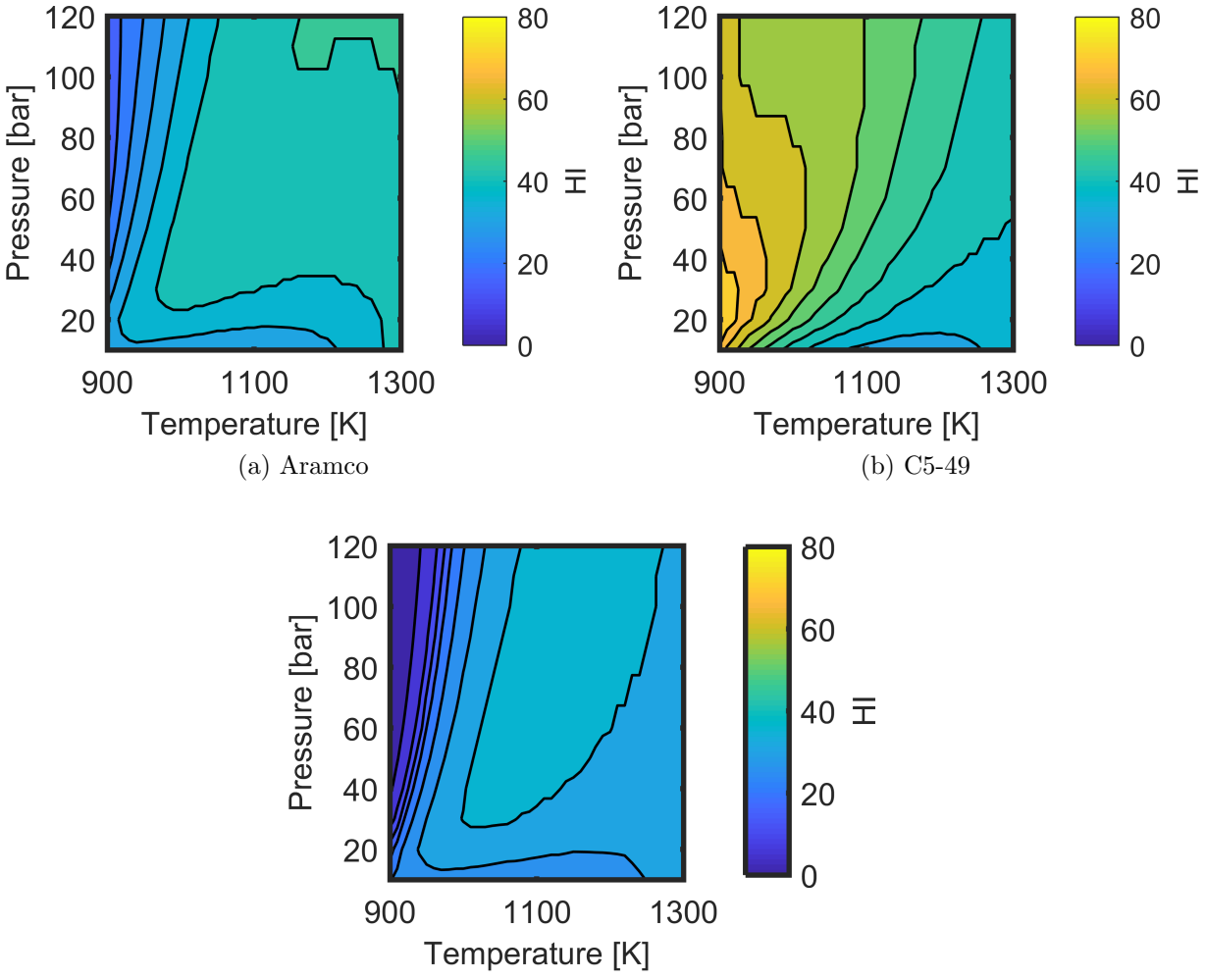

(a) Aramco

(b) C5-49

(c) LLNL

Figure 10.46: Calculated *HI*s for ethane using the ignition delay method.

Ethylene

The calculated *PI*s as a function of temperature and pressure for ethylene using the Aramco, C5-49, and LLNL mechanisms are seen in Figure 10.47. The C5-49 and LLNL mechanisms show similar trends, where the reactivity of ethylene relative to methane/propane is relatively constant over the range of pressures and temperatures tested. The Aramco mechanism shows a strong sensitivity to temperature, especially at temperatures below 1100 K, where the relative reactivity of ethylene increases with increasing temperature.

The calculated *HI*s as a function of temperature and pressure for ethylene using the Aramco, C5-49, and LLNL mechanisms are seen in Figure 10.48. The C5-49 and LLNL mechanisms produced similar *HI*s, with the *HI*s increasing with decreased temperature and increased pressure. The Aramco mechanism produced *HI*s that were relatively independent of temperature and pressure.

n-Butane

The calculated *PI*s as a function of temperature and pressure for *n*-butane using the C5-49 and LLNL mechanisms are seen in Figure 10.49. Both mechanisms show consistent trends, with the reactivity of *n*-butane relative to methane/propane fairly insensitive to temperature and pressure; however, the LLNL produced consistently lower *PI*s. Interestingly, the LLNL mechanism indicates that propane is more reactive than *n*-butane over nearly the entire operating map.

The calculated *HI*s as a function of temperature and pressure for *n*-butane using the C5-49 and LLNL mechanisms are seen in Figure 10.50. The C5-49 and LLNL mechanisms produced nearly identical *HI*s, with the *HI*s increasing with decreased temperature and increased pressure.

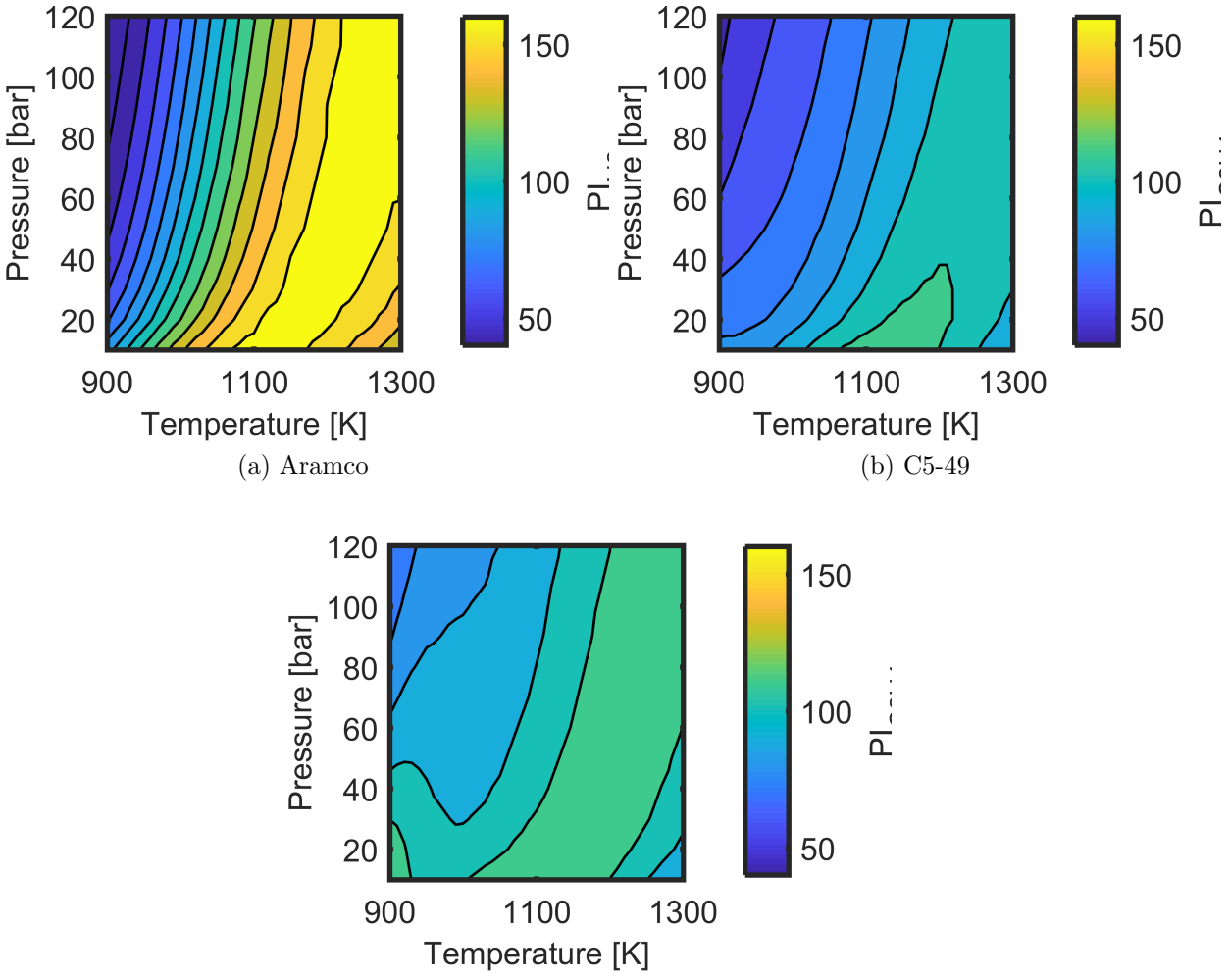

(a) Aramco

(b) C5-49

(c) LLNL

Figure 10.47: Calculated PIs for ethylene using the ignition delay method.

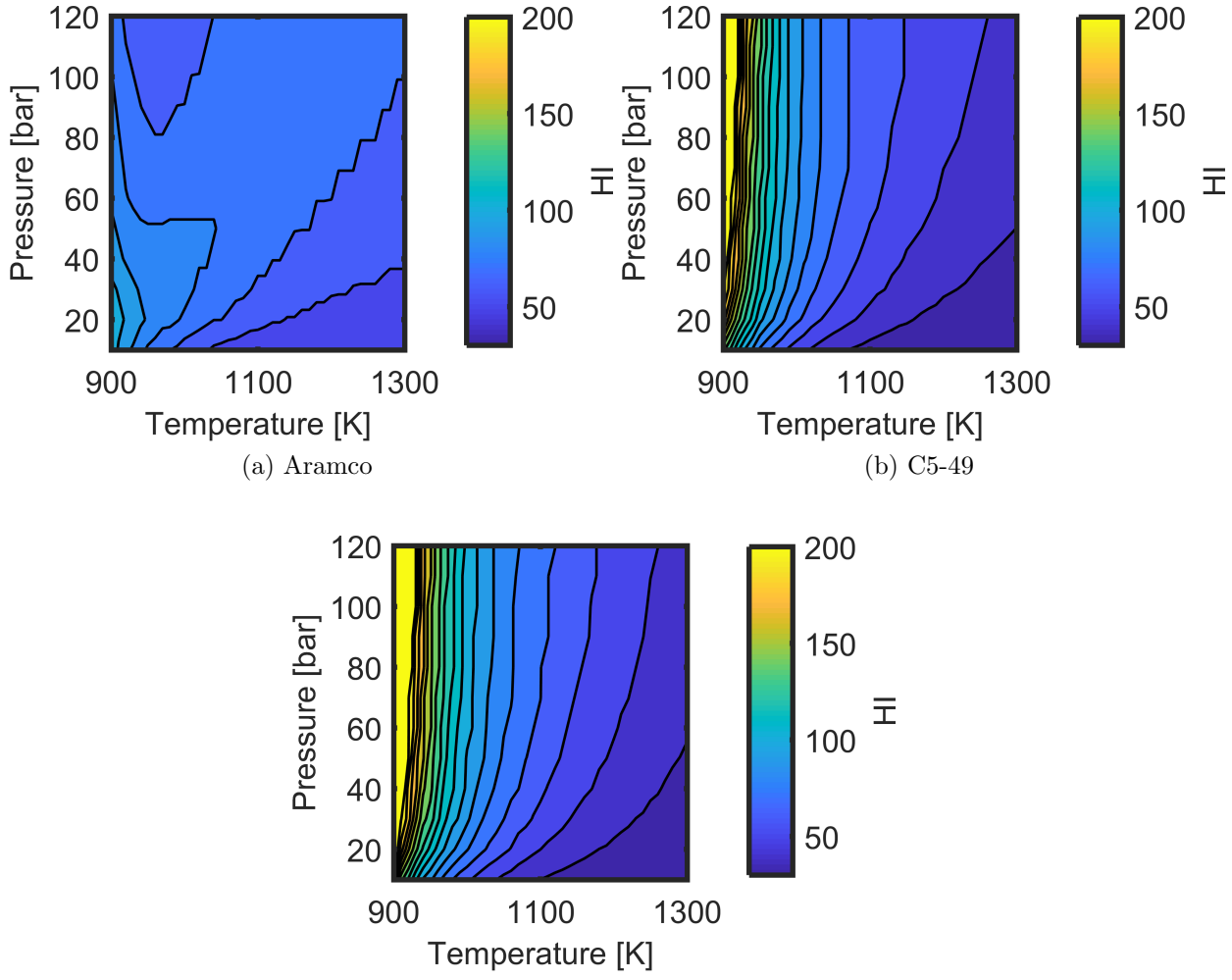

(a) Aramco

(b) C5-49

(c) LLNL

Figure 10.48: Calculated *HI*s for ethylene using the ignition delay method.

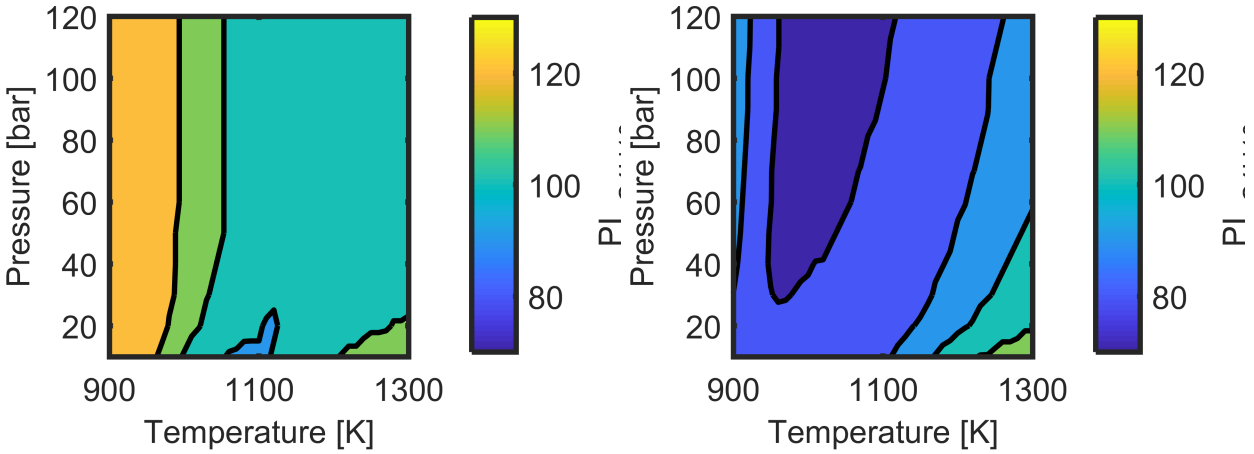

(a) C5-49 (b) LLNL

Figure 10.49: Calculated PIs for n-butane using the ignition delay method.

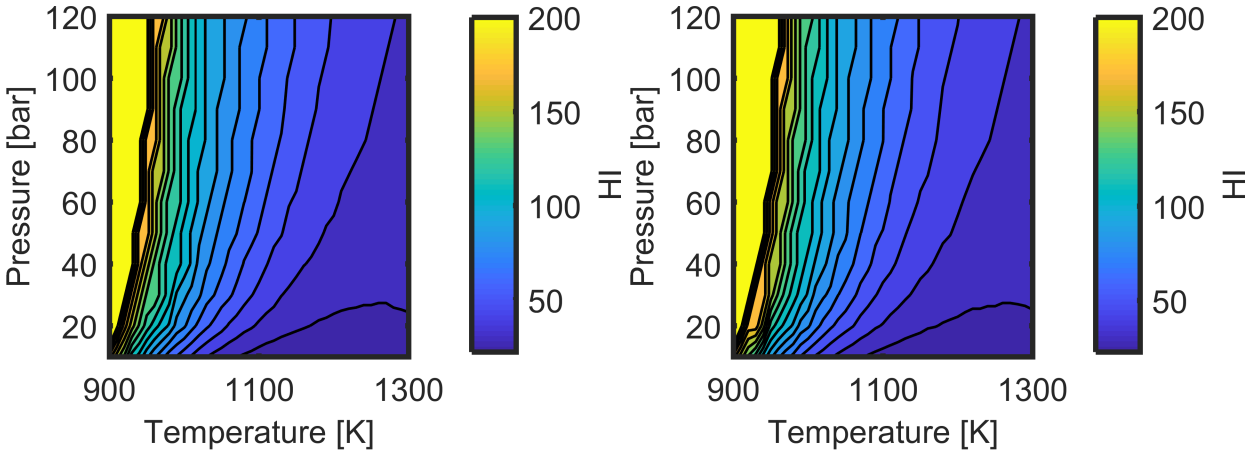

(a) C5-49 (b) LLNL

Figure 10.50: Calculated HIs for n-butane using the ignition delay method.

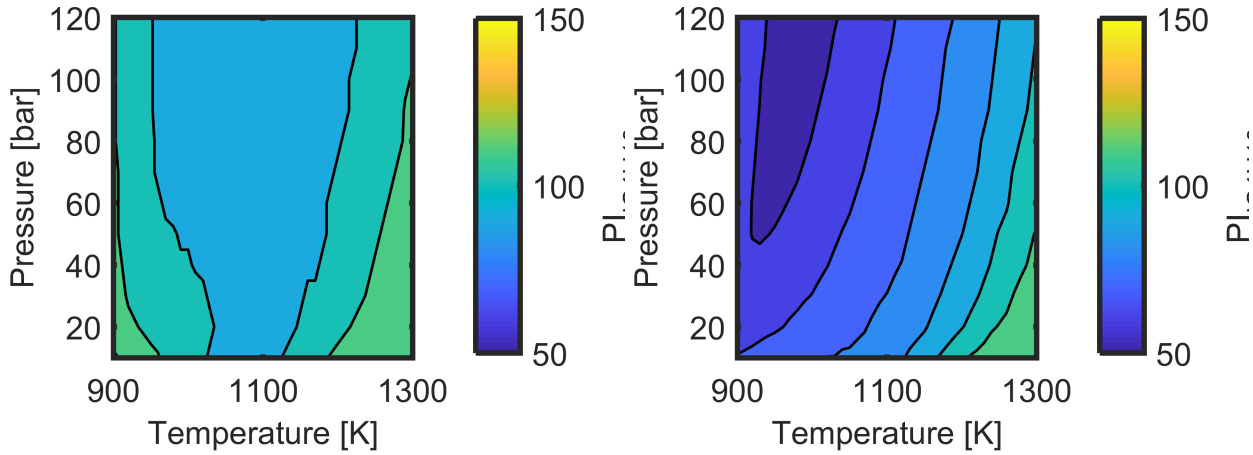

(a) C5-49 (b) LLNL

Figure 10.51: Calculated *PI*s for isobutane using the ignition delay method.

Isobutane

The calculated *PI*s as a function of temperature and pressure for isobutane using the C5-49 and LLNL mechanisms are seen in Figure 10.51. The C5-49 mechanism produced *PI*s that were fairly insensitive to operating condition, while the LLNL mechanism produced *PI*s that increased with increasing temperature and decreasing pressure.

The calculated *HI*s as a function of temperature and pressure for isobutane using the C5-49 and LLNL mechanisms are seen in Figure 10.52. The C5-49 and LLNL mechanisms produced nearly identical *HI*s, with the *HI*s increasing with decreased temperature and increased pressure.

MN65

The calculated *PI*s as a function of temperature and pressure for MN65 using the C5-49 and LLNL mechanisms are seen in Figure 10.53. Both mechanisms produced similar *PI*s that were fairly independent of pressure and temperature.

The calculated *HI*s as a function of temperature and pressure for MN65 using the C5-49 and LLNL mechanisms are seen in Figure 10.54. The C5-49 and LLNL mechanisms produced similar *HI*s, with the *HI*s increasing with decreased temperature and increased

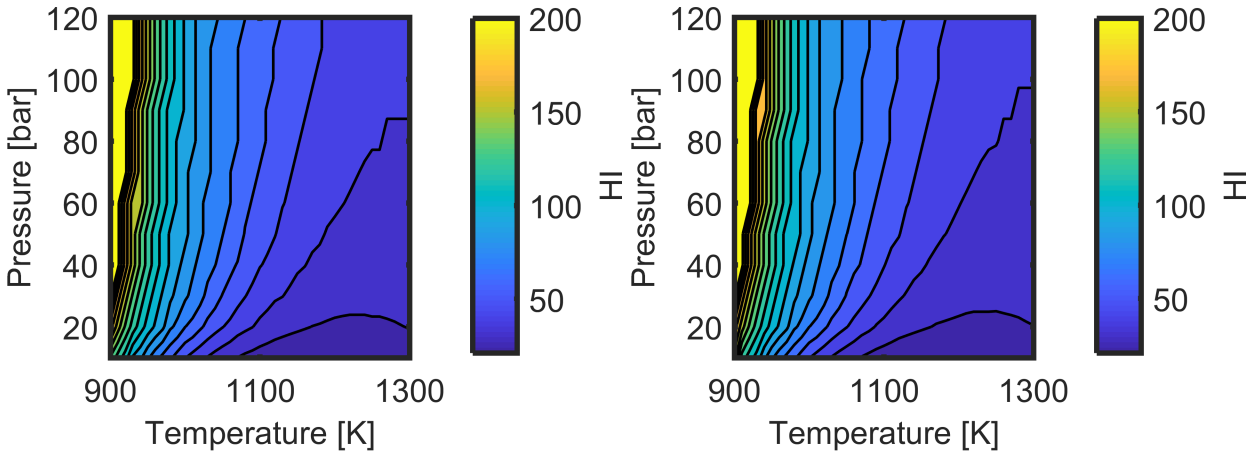

(a) C5-49 (b) LLNL

Figure 10.52: Calculated *HI*s for isobutane using the ignition delay method.

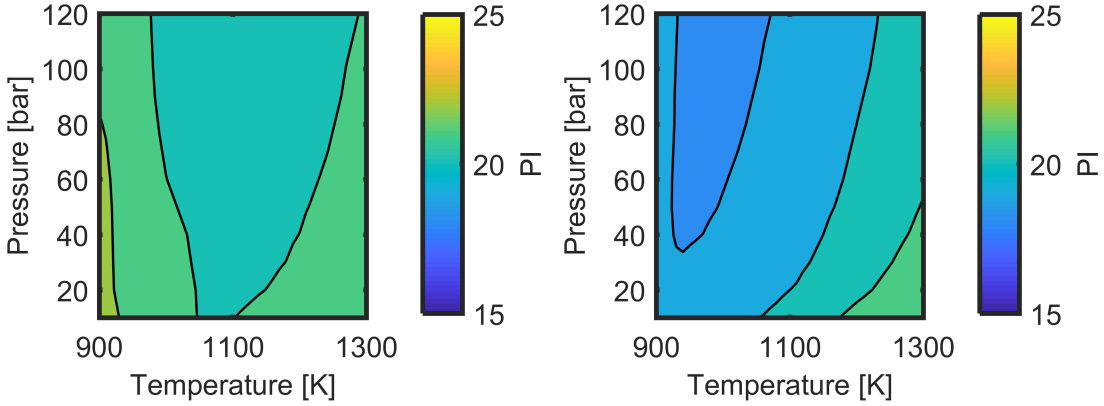

(a) C5-49 (b) LLNL

Figure 10.53: Calculated *PI*s for MN65 using the ignition delay method.

pressure. The LLNL mechanism produced slightly higher *HI*s compared to the C5-49 mechanism, which is consistent with previous results shown for propane, the main high reactivity component in MN65.

MN80

The calculated *PI*s as a function of temperature and pressure for MN80 using the C5-49 and LLNL mechanisms are seen in Figure 10.55. Both mechanisms produced similar *PI*s that were fairly independent of pressure and temperature.

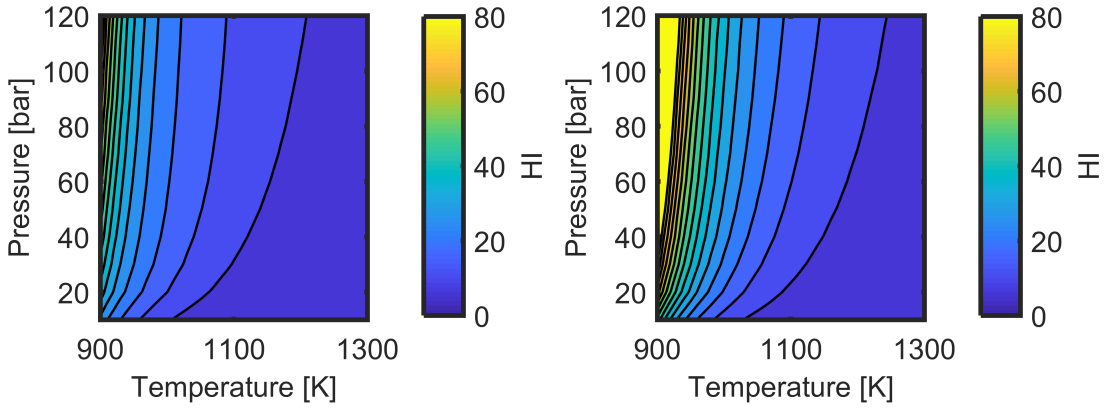

(a) C5-49 (b) LLNL

Figure 10.54: Calculated *HI*s for MN65 using the ignition delay method.

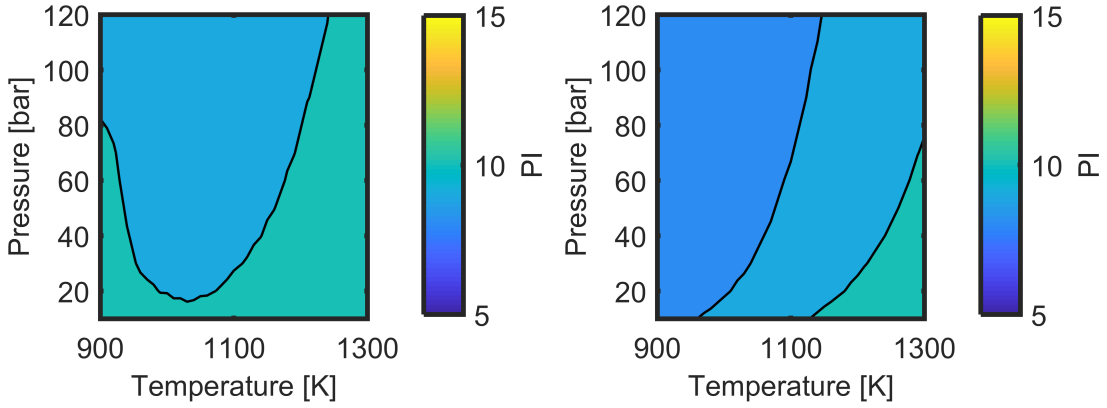

(a) C5-49 (b) LLNL

Figure 10.55: Calculated *PI*s for MN80 using the ignition delay method.

The calculated *HI*s as a function of temperature and pressure for MN80 using the C5-49 and LLNL mechanisms are seen in Figure 10.56. The C5-49 and LLNL mechanisms produced similar *HI*s, with the *HI*s increasing with decreased temperature and increased pressure. The LLNL mechanism produced slightly higher *HI*s compared to the C5-49 mechanism, which is consistent with previous results shown for propane, the main high reactivity component in MN80.

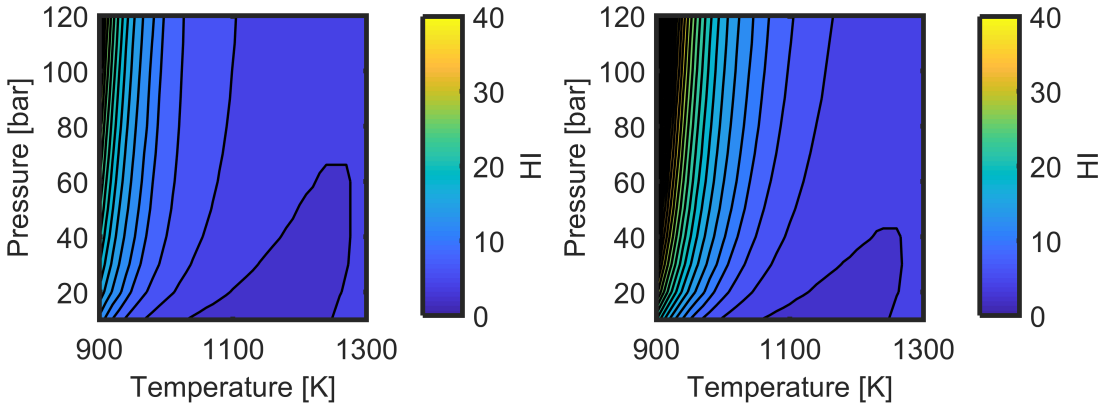

(a) C5-49 (b) LLNL

Figure 10.56: Calculated *HI*s for MN80 using the ignition delay method.

n-Heptane and Isooctane

The calculated *PI*s (a) and *HI*s (b) as a function of temperature and pressure for *n*-heptane using the LLNL mechanism are seen in Figure 10.57. The reactivity of *n*-heptane relative to methane/propane ranges from 120-160, with the minimum value occuring near 1050 K. The reactivity of *n*-heptane relative to methane/hydrogen increases with decreased temperature and increased pressure.

The calculated *PI*s (a) and *HI*s (b) as a function of temperature and pressure for isooctane using the LLNL mechanism are seen in Figure 10.58; different color scales are used for each plot. The reactivity of isooctane relative to methane/propane is a strong function of temperature, increasing with increasing temperatures and decreasing pressures. The reactivity of isooctane relative to methane/hydrogen increases with decreased temperatures and increased pressures.

Summary of Fuels

Figure 10.59 shows the calculated *PI*s and *HI*s using the ignition delay method with the LLNL mechanism as a function of temperature at a constant pressure of 60 bar. For the *PI* data, the trend of hydrogen relative reactivity vs. temperature is quite different from

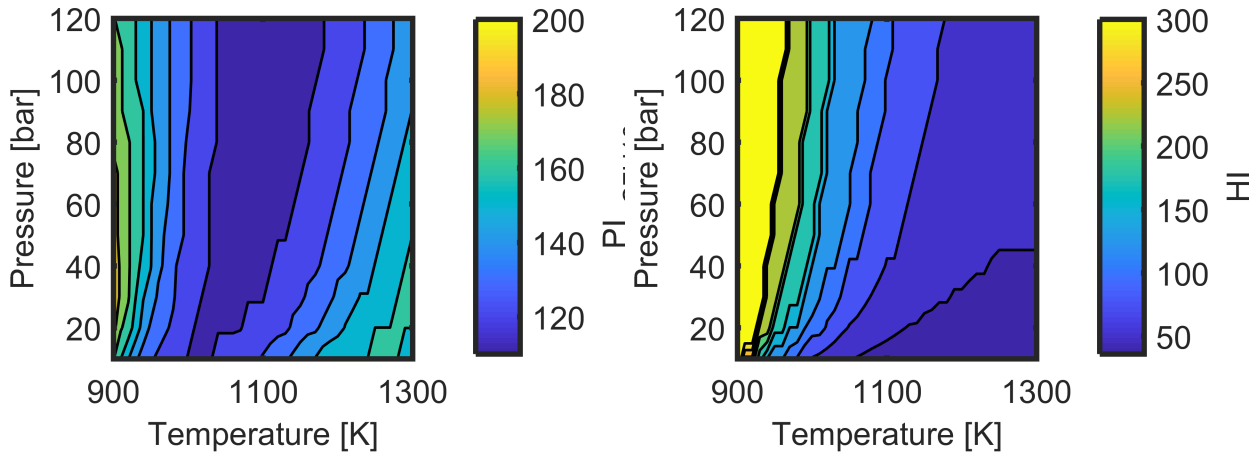

(a) PI (b) HI

Figure 10.57: Calculated *PI*s (a) and *HI*s (b) for *n*-heptane using the ignition delay method. Different color scales are used for each plot

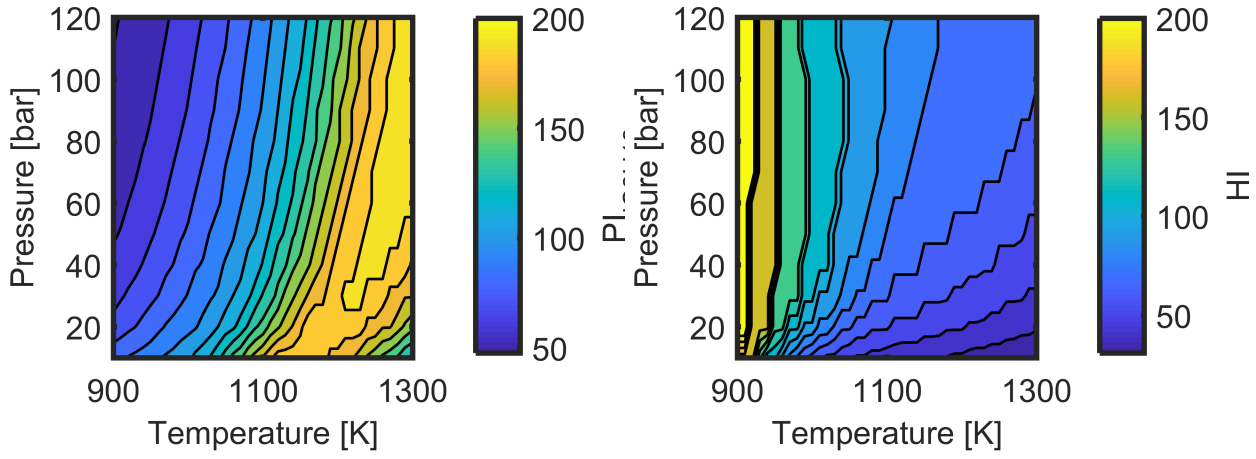

(a) PI (b) HI

Figure 10.58: Calculated *PI*s (a) and *HI*s (b) for isooctane using the ignition delay method. Different color scales are used for each plot

the hydrocarbon fuels; hydrogen has a PI near 0 at low temperatures (<1000 K) and a PI >200 at high temperatures (>1200 K). The hydrocarbon fuels have a wide spread of PIs at low temperatures, ranging from a PI of near 0 for ethane to a PI of over 175 for n-heptane. However, at high temperatures, all of the hydrocarbon fuels have more similar PIs, with values ranging from 90 to 160. Excluding n-heptane and isooctane, all hydrocarbon fuels have PIs from 90 to 120 at high temperatures.

For the HI data, all of the hydrocarbon test fuels other than ethane show very similar trends, where the HIs decrease rapidly as temperature increases. All of the test fuels other than ethane have HIs >100 at low temperatures, but their HIs fall below 100 between 1000 and 1100 K. The HI of ethane is nearly constant at temperatures greater than 1000 K. All test fuels have similar HIs at higher temperatures, with values ranging from 30-50. Excluding n-heptane and isooctane, the remaining hydrocarbon fuels have nearly identical HIs.

These trends with increasing temperature are an important result; they indicate that at high temperature conditions, natural gas mixtures containing negligible amounts of hydrogen would be expected to exhibit similar reactivities, independent of mixture composition. However, at low temperature conditions, the mixture reactivities can be highly dependent on composition. Table 10.4 shows the mole and energy fractions for a number of binary fuel mixtures consisting of a test fuel and methane, all of which have a MN of 80, calculated using the Cummins Westport fuel quality calculator [81]. According to their MN characterization, each mixture should have an identical reactivity.

Figure 10.60 shows the calculated PIs using the energy blending rule as a function of temperature for the binary fuel mixtures containing ethane, propane, and n-butane mixed with methane at several different pressures, simulating a boosted engine application, with both the C5-49 and LLNL mechanisms. Isooctane and n-heptane were omitted due to their lack of relevance to natural gas combustion, and isobutane was omitted due to its similarity to n-butane. By definition, a binary mixture of propane and methane has

a constant PI that is independent of temperature and pressure. Calculated PI trends were similar between both mechanisms, with the ethane mixture PIs having a strong sensitivity to temperature, and the n-butane mixture PIs having a modest sensitivity to temperature. The C5-49 mechanism produced larger PIs for both the ethane and butane mixtures compared to the LLNL mechanism, especially at lower temperatures, which is consistent with previously discussed relative reactivity engine simulations. The only non-negligible pressure dependence seen was an increasing PI of the ethane mixture as pressure decreases. Figure 10.61 shows the same fuel mixtures at 60 bar and equivalence ratios of 0.35 and 0.7. Increasing the equivalence ratio had almost no effect on the PIs of the n-butane mixture, while at higher equivalence ratios the ethane mixture had slightly larger PIs at higher temperatures. According to their MN characterization, these fuel mixtures are all expected to have identical reactivities. However, the n-butane mixture was consistently less reactive than the propane mixture, and the ethane mixture's relative reactivity changed substantially with temperature, becoming much less reactive than the propane mixture at low temperatures and more reactive than the propane mixture at high temperatures.

Figures 10.62 and 10.63 show the calculated HIs using the energy blending rule as a function of temperature for binary fuel mixtures containing ethane, propane, n-butane, and hydrogen mixed with methane at different pressures and equivalence ratios, with both the C5-49 and LLNL mechanisms. By definition, a binary mixture of hydrogen and methane has a constant HI that is independent of temperature and pressure. The HIs of the n-butane mixture were nearly identical between the two mechanisms, but the HIs of the propane and ethane mixtures were substantially different. As discussed previously, compared to the LLNL mechanism, the C5-49 mechanism under-predicts the relative reactivity of propane; this trend is seen at temperatures below 1100 K, where the LLNL mechanism produced greater HIs for the propane mixture. The HIs for the ethane mixture were different between the mechanisms over the entire range of temperatures,

Table 10.4: Summary of binary fuel mixtures, balanced by methane, that resulted in a mixture Methane Number of 80, calculated using Cummins Westport online calculator [81]. The hydrogen mole and energy fractions are fixed from the definition of the Methane Number. Experimental TDC temperature range indicated with vertical lines.

	Mole Fraction	Energy Fraction
Hydrogen	20	7.03
Ethane	9.3	15.4
Propane	4.5	10.7
n-Butane	2.1	6.6
Isobutane	2.1	6.6
n-Heptane	1.6	8.2
Isooctane	1.6	9.3

and the differences became larger with decreasing temperature. Pressure had a modest effect, with the *HI*s increasing with increased pressure. Equivalence ratio had a negligible effect on the calculated *HI*s. According to their MN characterization, each of these fuel mixtures are expected to have identical reactivities. In the temperature range of 1000 to 1100 K the reactivities are reasonably similar, but the values are quite different outside of this range, especially at lower temperatures.

10.7 Conclusions

The fuel substitution engine experiments described in Chapter 4 were simulated using two independent methods. The first simulation method used the experimental fuel concentrations and solved for the $T_{IVC,sim,core}$ required to match the experimental combustion phasing. The second method simulated a fuel substitution sweep with a fixed $T_{IVC,sim,core}$; the amounts of methane/propane or methane/hydrogen reference fuels were adjusted to match the experimental combustion phasing and a *PI* or *HI* was calculated for each fuel at the six operating conditions.

By analyzing the $T_{IVC,sim,core}$ vs. test fuel fraction trends, each mechanism was evaluated on its ability to match the experimental results of each test fuel's reactivity relative to the reference fuels. The simulated *PI*s and *HI*s were compared to the experimental values and used to evaluate the relative fuel reactivity accuracy of each mechanism.

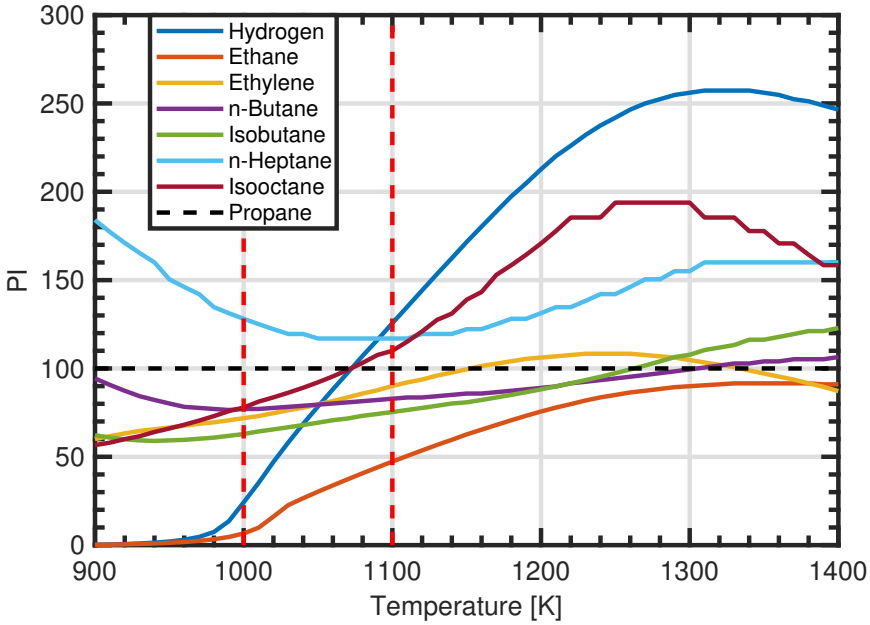

(a) PI

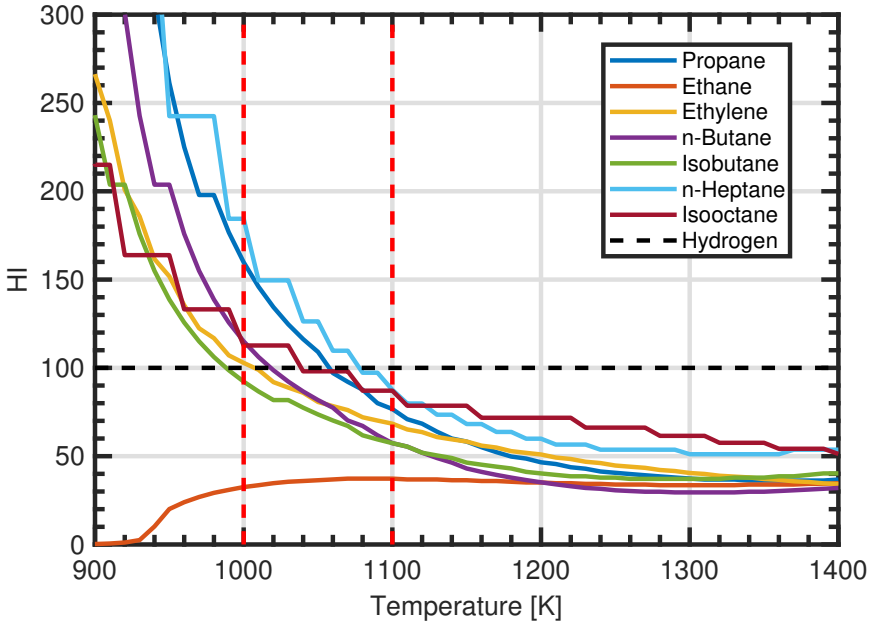

(b) HI

Figure 10.59: Calculated *PI*s (a) and *HI*s (b) as a function of temperature using the ignition delay method using the LLNL mechanism at a constant pressure of 60 bar. Experimental TDC temperature range indicated with vertical lines.

Results were similar between the two simulation methods, and the relative reactivities were seen to follow consistent trends with both the *HI* and *PI* fuel substitution testing.

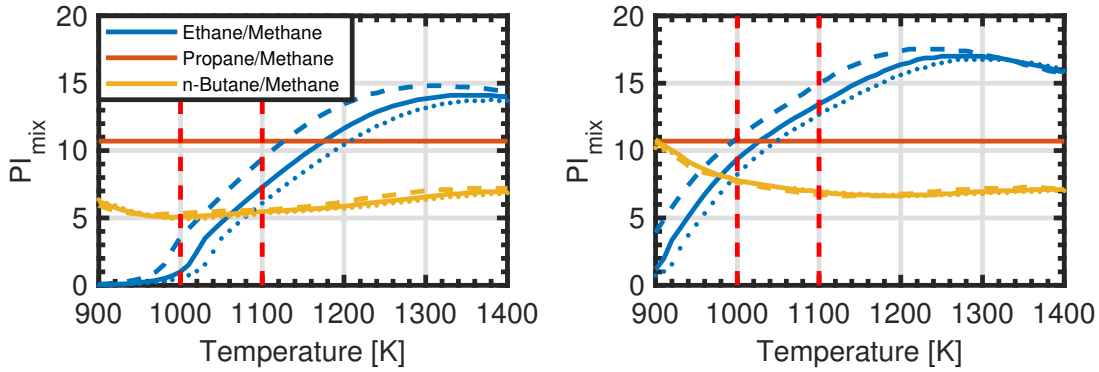

(a) LLNL (b) C5-49

Figure 10.60: Calculated *PI*s for binary fuel mixtures listed in Table 10.4 as a function of temperature using the ignition delay method using the LLNL and C5-49 mechanism at constant pressures of 30 (dash), 60 bar (solid), and 90 (dots) bar. Experimental TDC temperature range indicated with vertical lines.

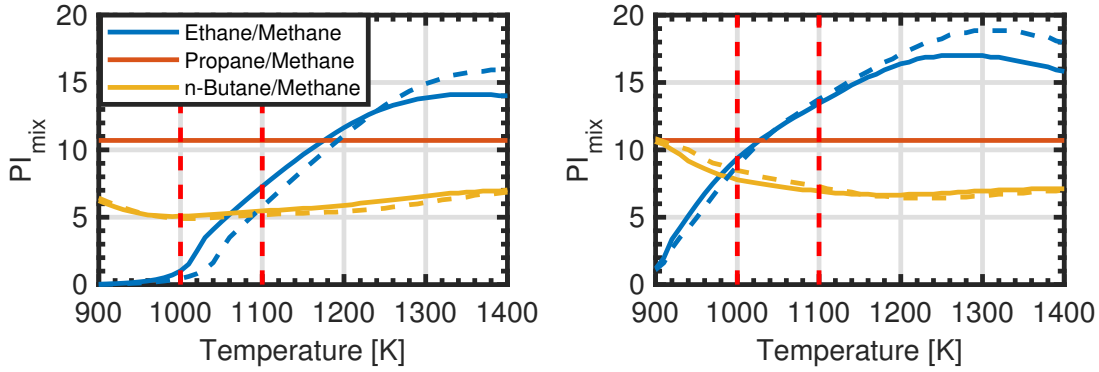

(a) LLNL (b) C5-49

Figure 10.61: Calculated *PI*s for binary fuel mixtures listed in Table 10.4 as a function of temperature using the ignition delay method using the LLNL and C5-49 mechanism at constant pressures of 60 bar and an equivalence ratio of 0.35 (solid) and 0.7 (dashed). Experimental TDC temperature range indicated with vertical lines.

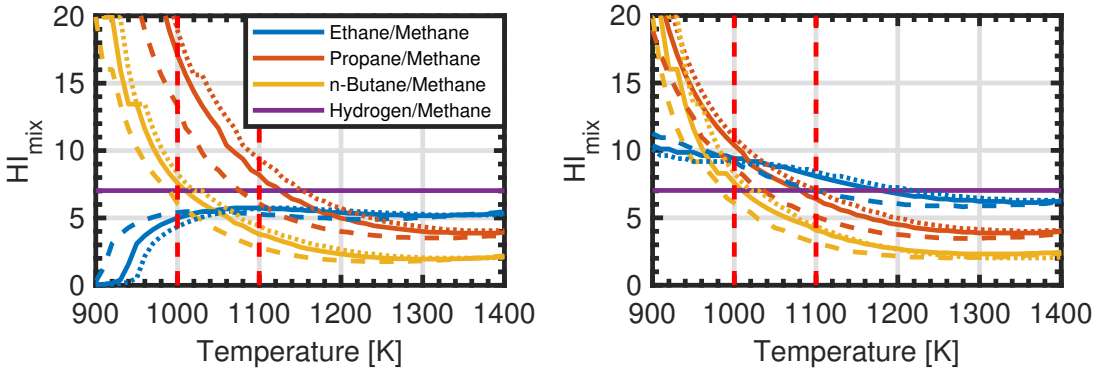

(a) LLNL (b) C5-49

Figure 10.62: Calculated *HI*s for binary fuel mixtures listed in Table 10.4 as a function of temperature using the ignition delay method using the LLNL and C5-49 mechanism at constant pressures of 30 (dash), 60 bar (solid), and 90 (dots) bar. Experimental TDC temperature range indicated with vertical lines.

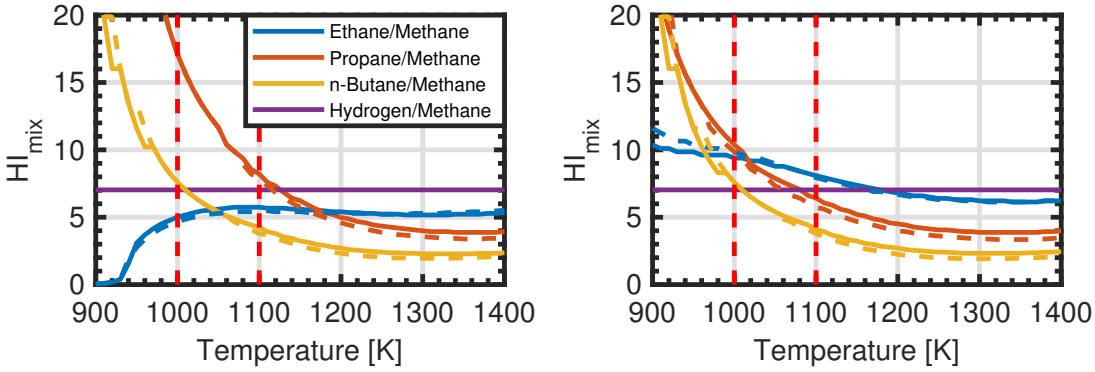

(a) LLNL (b) C5-49

Figure 10.63: Calculated *PI*s for binary fuel mixtures listed in Table 10.4 as a function of temperature using the ignition delay method using the LLNL and C5-49 mechanism at constant pressures of 60 bar and an equivalence ratio of 0.35 (solid) and 0.7 (dashed). Experimental TDC temperature range indicated with vertical lines.

A general summary of the relative reactivity comparisons was given in Tables 10.1 and 10.2. Ignition delays were computed along the simulation thermodynamic history, and the relative reactivity differences seen between the mechanisms were consistent with the ignition delays generated with each mechanism.

Because all three mechanisms produced similar ignition delays for hydrogen and methane, but the LLNL mechanism produced substantially different ignition delays for propane compared to the Aramco and C5-49 mechanisms, the methane/hydrogen fuel substitution results were simpler to directly compare mechanism performance for each test fuel. The methane/propane fuel substitution results were also used to compare mechanism performance, but the propane chemistry differences inherently affect each test fuel's relative reactivity results. This is an important characteristic of fuel substitution testing and indicates the importance of the reference fuels selection.

A method to calculate a *PI* from ignition delays at TDC thermodynamic conditions was developed and compared to the engine simulation results. Initially, reasonable agreement was seen between the ignition delay method and the engine fuel substitution simulations for hydrocarbon fuels; the hydrogen results showed a substantial difference. When the ignition delay method was revised to include isentropic compression and mixture compensation, the revised method and engine simulation results showed good agreement for all test fuels.

The ignition delay *PI*s and *HI*s were used to investigate the relative reactivity trends over a wide range of pressures and temperatures. At high temperatures, all test fuels other than hydrogen showed a reasonably close reactivity to pure propane. However, at low temperatures a large difference in the relative fuel reactivities was seen, highlighted by ethane having a similar reactivity to pure methane and *n*-heptane having a much greater reactivity than pure propane. These trends, which were relatively independent of pressure and equivalence ratio, show that the natural gas composition can have a large effect on overall mixture reactivity, especially at lower temperatures. Additionally,

the strong temperature sensitivity of the fuels' relative reactivities suggests that a single value, such as MN, is not adequate to describe a fuel's relative reactivity over a range of operating conditions.

Chapter 11

Conclusions and Future Work

The objective of this work was to use well-controlled engine experiments to evaluate chemical kinetics mechanisms, on both an absolute and relative basis. Five kinetic mechanisms were investigated, all of which were discussed in detail in Section 2.4.

11.1 Conclusions

11.1.1 Fuel Substitution Experimental Testing

Fuel substitution tests were performed at six operating conditions with varying engine speeds and intake temperatures and pressures using HCCI combustion in a manner that fixed combustion load and phasing for the entirety of the sweep. Each test fuel was combined with methane/propane or methane/hydrogen reference fuels, and the amount and ratio of the reference fuels was adjusted to maintain combustion load and phasing as the amount of test fuel was varied. By analyzing the ratio of reference fuels required to maintain combustion phasing as a function of test fuel energy fraction, an effective *PI/HI* was calculated for each fuel. The *PI/HI* is an indication of the test fuel's reactivity relative to the methane/propane or methane/hydrogen reference fuels. The *PI/HI*s of several test fuels were seen to have a strong dependence on the in-cylinder thermodynamic

conditions.

Important results from the experimental fuel substitution testing are:

- Quantitative data relating the reactivities of nine test fuels to methane/hydrogen and methane/propane reference fuels were acquired for six operating conditions, spanning a range of pressures from 30-90 bar and temperatures from 1000 to 1100 K.

- Relative to methane/hydrogen, the hydrocarbon fuels tested, other than ethane, had consistent trends of increased reactivity at the high pressure, low temperature condition and decreased reactivity at the low pressure, high temperature condition. Ethane had a reactivity relative to methane/hydrogen that was fairly insensitive to operating condition.

- Relative to methane/propane, hydrogen, ethane, and ethylene all showed consistent trends of decreased reactivity at the high pressure, low temperature condition 1 and increased reactivity at the high pressure, low temperature condition 6. The larger hydrocarbon fuels, *n*-butane, *n*-heptane, and isooctane, had reactivities relative to methane/propane that were fairly insensitive to operating condition.

- Calculated *HI*s and *PI*s for each test fuel could be directly related to each other in a simple manner, suggesting consistent results.

11.1.2 In-Cylinder Temperature Measurement

Three methods of in-cylinder temperature estimation were investigated with a focus on temperature estimation at IVC: a trapped-mass calculation, water-absorption spectroscopy, and fast-response thermocouples. The trapped-mass temperature is the most commonly used method, as all of the values needed are often readily available in single-cylinder engine laboratories. A rigorous uncertainty analysis resulted in 95% confidence

uncertainty bounds of ±8 K at IVC, or about 2% of the IVC temperature. The downside to this method is that there is a dependence on upwards of 10 measured values, and each value can have a large effect on the calculated temperature. Early testing involved in the current work had artificially low trapped mass temperatures due to errors from the in-cylinder pressure measurement. Any leak in the intake system after the airflow is measured will also cause errors in the measured trapped mass. Assuming all sensors are properly functioning, the residual mass fraction must still be estimated using a simple model. Due to the stack-up of uncertainties and conceptual bias, it would be difficult to achieve 95% confidence uncertainty bounds below ±2%.

Water-absorption spectroscopy was used to obtain crank-angle resolved in-cylinder temperature data. This involved a complex optical setup and a custom polished piston. Additionally, the method cannot work with dry air; a water-seeder was used to increase the intake air water mole fractions to 2-4%. The processing to calculate a temperature from the raw water absorption data is a complex, non-linear process that involves a number of processing parameters, which can each be adjusted, and is also dependent on the simulation database accuracy. A rigorous analysis of each individual processing parameter, the combined processing parameter interactions, and simulation database comparison resulted in estimated 95% confidence uncertainty bounds of ±10 K at IVC, or about 2.5% of the IVC temperature. It is believed that mirroring the experimental setup in a controlled temperature environment, such as a furnace, could be used to further reduce this uncertainty. While the cost and complexity of this method is a drawback, it shows promise as a non-invasive technique to accurately measure temperature.

Two type K fast-response thermocouples of different sizes were installed in the engine and used to measure temperatures under motoring conditions. Measurements were also attempted under firing conditions, but no usable data was collected due to the thermocouples physically failing. The effect of the thermocouple's time constants was non-negligible, and had to be corrected for. This correction added a source of uncer-

tainty, as the thermocouple's time constant was not known, and varied with changing thermodynamic and flow conditions. Even with the additional time constant uncertainty, the thermocouples had the lowest estimated 95% uncertainty bounds of ±4 K at IVC, or about 1% of the IVC temperature. While there are durability concerns, the thermocouples are a relatively inexpensive method that involve a fairly simple experimental setup. The main drawback is that the thermocouples could not be used under firing conditions; other thermocouple materials may be able to survive firing conditions. Since temperature estimation of firing conditions was the the value of interest, the main use of the thermocouple data was to validate the other temperature measurement methods under motoring conditions.

Each of the temperature determination methods measures a slightly different temperature due to the measurement methods, all of which are slightly different than the desired temperature. The magnitudes of the conceptual biases associated with each temperature measurement method were investigated using CFD simulations. The simulation results predicted small biases at IVC when the engine wall and gas temperatures were similar. The measured temperatures from each method were compared to each other, and consistent trends were seen for both motored and fired conditions.

Important results from the in-cylinder temperature measurement testing are:

- Temperatures measured using the trapped-mass method, water-absorption spectroscopy, and fast-response thermocouples under motoring conditions had reasonable agreement, with most measured values lying within the uncertainty bounds. Compared to the trapped-mass temperatures for motored conditions, the thermocouples temperatures were 5-10 K higher, and the spectroscopic temperatures were about 15 K higher.

- For fired conditions, similar trends were seen between the trapped-mass and spectroscopic temperatures, with the spectroscopic temperatures consistently 5-10 K higher than the trapped mass temperatures.

- The final temperature values used for comparison to simulations were calculated using a weighted average based on the trapped-mass and spectroscopy temperatures and their respective uncertainties, and resulted in 95% confidence uncertainty bounds of ±5-10 K.

11.1.3 Absolute Fuel Reactivity

A Cantera two-zone model was created to simulate the engine experiments. The baseline methane/propane and methane/hydrogen experimental cases were simulated with the five kinetics mechanisms. The IVC temperature required in the simulation to match experimental combustion phasing was compared to the experimental IVC temperatures. For the methane/propane cases, the LLNL mechanism showed the best agreement with the experimental temperatures, a higher temperature, up to 3× the experimental 95% confidence uncertainty bounds, was required for the Aramco and C5-49 mechanisms, a much higher temperature, up to 6× the experimental 95% confidence uncertainty bounds, was required for the GRI mechanism, and a much lower temperature, up to 5× the experimental 95% confidence uncertainty bounds, was required for the UBC mechanism. For the methane/hydrogen cases, all mechanisms showed reasonable agreement with the experimental IVC temperatures, with the UBC requiring a lower temperature, up to 2× the experimental 95% confidence uncertainty bounds.

Ignition delays for methane, propane, and hydrogen provided insight into why the required simulation IVC temperatures required varied between the different mechanisms. All mechanisms had very similar ignition delays for hydrogen. The GRI mechanism produced substantially longer propane ignition delays relative to the other mechanisms, which was likely the reason it required higher IVC temperatures for the baseline methane/propane cases. The LLNL mechanism produced shorter ignition delays for propane compared to the Aramco and C5-49 mechanisms, which was likely the reason it required lower temperatures compared to the Aramco and C5-49 mechanisms for the methane/propane

cases. The UBC mechanism produced substantially shorter methane ignition delays relative to the other mechanisms, hence the lower required IVC temperatures for both the methane/propane and methane/hydrogen cases. The LLNL mechanism was the only mechanism that was well-matched to experimental baseline conditions for both the methane/propane and methane/hydrogens cases, which suggests that the Aramco and C5-49 mechanisms under-predict the reactivity of propane.

Important results for the absolute fuel reactivity simulations are:

- The LLNL mechanism required T_{IVC} in the simulation fell within the experimental 95% confidence uncertainty bounds for both the methane/propane and methane/hydrogen baseline cases.

- The Aramco and C5-49 mechanisms showed good agreement with experimental T_{IVC} values for the methane/hydrogen cases, but required higher temperatures for the methane/propane cases. Relative to the LLNL mechanism, both mechanisms had similar ignition delays for methane and hydrogen, but longer propane ignition delays.

- The GRI mechanism performed well for the methane/hydrogen cases, but the simulation required much higher T_{IVC} for the methane/propane cases. Relative to the LLNL mechanism, the GRI mechanism had slightly longer ignition delays for hydrogen, substantially longer ignition delays for propane, and ignition delays for methane that were sometimes longer and sometimes shorter than the LLNL mechanism depending on operating condition.

- The UBC mechanism showed poor agreement with the experimental results for both methane/propane and methane/hydrogen cases, requiring lower temperatures for all cases. Relative to the LLNL mechanism, the UBC mechanism had similar ignition delays for hydrogen and propane, but substantially shorter ignition delays for methane.

11.1.4 Relative Fuel Reactivity

The experimental fuel substitution sweeps for all test fuels and operating conditions were simulated in Cantera. Two simulation methods were used, one that fixed fuel concentrations at the experimental values and varied the T_{IVC} to match experimental combustion phasing, and one that fixed T_{IVC} and varied the fuel concentrations, akin to the engine experiments. Both methods were used to evaluate the kinetics mechanisms' accuracy at predicting the test fuel reactivity relative to the methane/propane or methane/hydrogen reference fuels. Based on the absolute reactivity results, only the Aramco, C5-49, and LLNL mechanisms were investigated. Consistent results were seen between the two simulation methods. A summary of the results for each mechanism and test fuel was shown in Tables 10.1 and 10.2.

The relative reactivity results for each test fuel with the LLNL mechanism were consistent between the *PI* and *HI* testing; the LLNL mechanism generally under-predicted test fuel relative reactivities. The relative reactivity results were not consistent between the *PI* and *HI* testing for the Aramco and C5-49 mechanisms, with test fuel reactivities tending to be over-predicted with the *PI* simulations and under-predicted with the *HI* simulations. The cause for this observed behavior was the longer ignition delays for propane with the C5-49 and Aramco mechanisms compared to the LLNL mechanism. In addition to propane, substantial differences were seen between the calculated ignition delays for ethane and ethylene with the three mechanisms, and the differences in ignition delays were consistent with the differences in relative reactivities calculated from the engine fuel substitution simulations.

A method to calculate relative fuel reactivity from constant pressure ignition delay calculations instead of full engine simulations was developed. The *PI*s calculated from the engine simulations were compared to the *PI*s calculated using the ignition delay method at the static TDC thermodynamic conditions from each corresponding engine simulation. When isentropic compression and mixture-compensation effects were included in

the ignition delay method, good agreement was seen between the revised ignition delay method and the engine simulations.

The ignition delay method was used to generate *PI* maps over a wide range of temperatures and pressures beyond the six engine operating conditions. The relative fuel reactivities had a strong dependence on temperature, with all hydrocarbon test fuels having a wide spread of relative reactivity at low temperatures, but converging to a similar relative reactivity at high temperatures. The effect of pressure and equivalence ratio on relative fuel reactivities was small compared to the temperature sensitivity. For natural gas applications, the most important results are that ethane has a similar reactivity to methane at low temperatures, and transitions to a similar reactivity to propane at high temperatures; this trend was seen both in engine experiments and simulations. This temperature dependence cannot be captured with a single classification, such as the Methane Number.

Important results for the relative fuel reactivity simulations are:

- The LLNL mechanism reasonably matched the reactivity of propane relative to methane/hydrogen and the reactivities of ethylene and hydrogen relative to methane/propane. The reactivities of ethane, *n*-butane, and isooctane were all under-predicted relative to both methane/hydrogen and methane/propane.

- The C5-49 mechanism under-predicted the reactivities of ethane, propane, and *n*-butane relative to methane/hydrogen. Relative to methane/propane, the reactivities of ethane, ethylene, and hydrogen were all over-predicted, while the reactivity of *n*-butane was under-predicted. The inconsistent results for ethane when comparing to methane/hydrogen and methane/propane are most likely caused by the under-prediction of the reactivity of propane relative to hydrogen.

- The Aramco mechanism under-predicted the reactivities of ethane and propane relative to methane/hydrogen. Relative to methane/propane, the reactivities of

ethane, ethylene, and hydrogen were all over-predicted. The inconsistent results for ethane when comparing to methane/hydrogen and methane/propane are most likely caused by the under-prediction of the reactivity of propane relative to hydrogen.

- The reactivity of hydrocarbon fuels relative to methane/propane is strongly dependent on temperature, with a wide range of relative reactivities at low temperatures and a small range of relative reactivities at high temperatures. These trends were consistent with the experimental results. The relative reactivity trends were mostly insensitive to changing pressures and equivalence ratios.

- The reactivity of hydrocarbon fuels relative to methane/hydrogen is also strongly dependent on temperature, with all hydrocarbon test fuels other than ethane having a much higher reactivity than hydrogen at low temperatures, and all fuels including ethane having similar relative reactivities to a 40/60 hydrogen/methane mixture at high temperatures. This trend was consistent with the experimental results.

- The dependence of fuel relative reactivities on thermodynamic conditions indicates that a single parameter, such as Methane Number, is not adequate to describe a fuel's reactivity over a range of engine operating conditions.

11.2 Future Work

11.2.1 Fuel Substitution Testing

It would be useful to expand the thermodynamic envelope of TDC conditions. A wide range of pressures was covered in the engine experiments, but the temperature range was fairly narrow, <100 K at each pressure. There are challenges involved with achieving stable combustion at different temperatures, but higher engine speed and/or a less reactive baseline fuel mixture would allow for higher temperatures, while a lower engine speed and/or a more reactive baseline fuel mixture would allow for lower temperatures.

Performing similar fuel substitution tests on a much different engine platform would also be a useful validation of the fuel substitution procedure and results. The proposed method would be to use the same engine speed, baseline fuel mixture, and equivalence ratio, adjust intake pressure until TDC pressure matches, and adjust intake temperature until combustion phasing matches. With the intake conditions fixed, the fuel substitution sweep is then performed and results can be directly compared to the original experiments. The ability to reproduce similar reactivity results on an independent engine platform would be a useful way to validate the conclusions from the current work.

An SI knock or diesel pilot ignition application would also be an interesting area for future work. Due to possible complications involving the thermodynamic properties of hydrogen, using methane/propane as baseline fuels is recommended. Similar to the fuel substitution testing, a baseline operating condition would be set with a methane/propane mixture. With all inlet conditions fixed, fuel substitution sweeps would be performed while keeping knock or combustion metrics constant. The relative reactivity of test fuels would then be derived from the substitution results for each operating condition in a similar manner to the current work.

Another interesting application of the current work would be to generate a response surface model that takes fuel composition, temperature, and pressure as inputs and outputs a mixture reactivity that could be classified as a *HI*, *PI*, or an alternative scale. This model could then be tested with a combustion strategy such as SI or diesel pilot ignition. For example, consider a spark timing modifier that retards spark as a function of the mixture reactivity. An open-loop controller could react to changing fuel compositions using the response surface model outputs to avoid knock without having to rely on feedback from knock sensors.

11.2.2 In-Cylinder Temperature Estimation

With regards to in-cylinder temperature estimation, there are several areas where improvements could be made. For the trapped mass calculations, the largest source of uncertainty is the residual mass fraction estimation. Investigating the residual mass fraction more thoroughly with full CFD simulations or via experimental in-cylinder sampling could reduce the experimental uncertainty.

The water absorption spectroscopy estimation uncertainty could be reduced by mimicking the experimental setup in a controlled pressure/temperature environment. With the true temperature known, both processing parameter biases and database uncertainty biases could be reduced. It is the author's opinion that this method provides the potential for the most accurate temperature measurements throughout the compression cycle.

Different thermocouple materials could be investigated to find one that would survive firing conditions while still having a relatively small time constant. The thermocouple temperature measurements had the lowest uncertainty near IVC, but the main drawback was that data were only available for motored conditions. It would also be useful to have surface mounted thermocouples in the cylinder liner, engine head, and piston to obtain a more accurate estimate of the boundary conditions for bias estimation.

11.2.3 Absolute Fuel Reactivity

Expanding the range of operating conditions would be useful for the absolute fuel reactivity simulations. While a broad range of pressures was examined, the temperature range was relatively small. While simulations using the LLNL mechanism showed good agreement with the experimental data, some disagreement was seen for the low temperature, high pressure condition 1 with methane/propane. It would be useful to expand the temperature range on the low end to investigate whether this point was an outlier, or the mechanism becomes less accurate at lower temperatures. Additionally, reaching higher equivalence ratio would be useful to see if the mechanisms produce similar results.

As new kinetics mechanisms are released, it would also be useful to compare their performance against these experimental datasets. The AramcoMech2.0, a revised version of the AramcoMech1.3 used in the current work, would be a good candidate for future work.

11.2.4 Relative Fuel Reactivity

Similar to the previous section, expanding the range of operating conditions, especially with regards to temperature and equivalence ratio would be useful for evaluating mechanism performance. Adding carbon monoxide to the test fuel matrix would be useful for syngas applications. A more thorough investigation into the kinetics mechanisms to find which specific reactions are causing the differences seen in ignition delays and relative fuel reactivities would be a useful area of future work.

Appendix A

Medtherm Thermocouple Data Sheet

MEDTHERM CORPORATION

FINE WIRE THERMOCOUPLE PROBES

for Measuring Transient Gas Temperatures

FEATURING

- **WIRE SIZES AS SMALL AS 0.0005 INCH**
- **MILLISECOND RESPONSE TO GAS TEMPERATURE**
- **RUGGED MOUNTING**
- **EXTENDED LIFE**
- **RADIATION SHIELD AND DIFFUSER ACCESSORIES**
- **CUSTOM DESIGNS AVAILABLE**

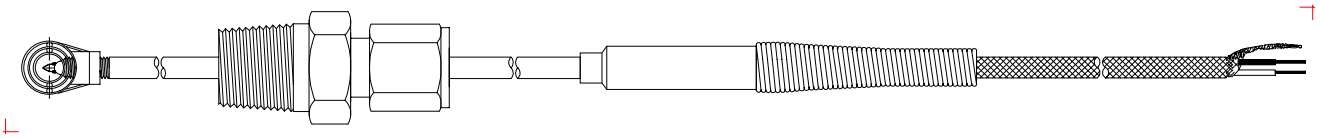

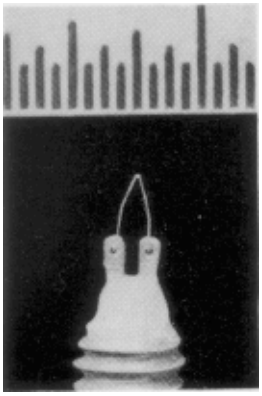

MEDTHERM fine wire thermocouple probes provide a rugged mounting method for inserting ultra-fine wire thermocouple junctions for precise rapid response gas temperature measurements. These probes are designed for applications such as air compressors, internal combustion engines, and wind tunnels where vibration, shock, or bending conditions in the environment preclude use of ordinary fine wire thermocouples.

Thermocouple wires as small as 0.0005 inch are made capable of extended life by use of a unique fine wire mounting technique. Large (.010 - .013 inch diameter) thermocouple wires are swaged with magnesium oxide insulation within a corrosion resistant metal sheath. The ends of the wires are flattened and 0.005 inch dia. holes are drilled through the flattened ends. Each fine wire is then welded to the appropriate large wire, coiled around it, passed through the drilled hole and fusion welded at the hot junction. The welds to the large wire are then encapsulated in high temperature ceramic cement. With this construction, the fine wires can be bent or vibrated without weakening the welded connection of the fine wire at its weld to the large wire. *This feature assures a longer life for the fine wire thermocouple than would a conventional welded connection.*

PERFORMANCE

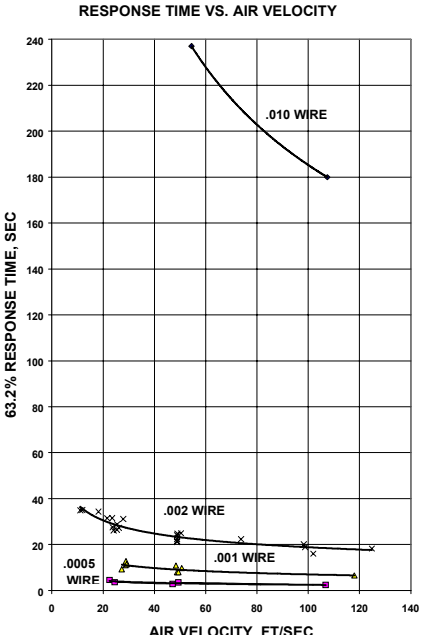

TIME CONSTANT, 63.2 % of STEP CHANGE IN GAS TEMPERATURE.

TYPICAL RECORD FROM GASOLINE ENGINE, 0.001” DIA FINE WIRE

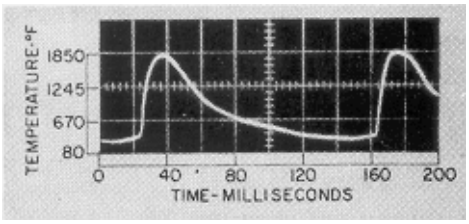

TYPICAL RECORD FROM AIR COMPRESSOR, 0.001” DIA FINE WIRE

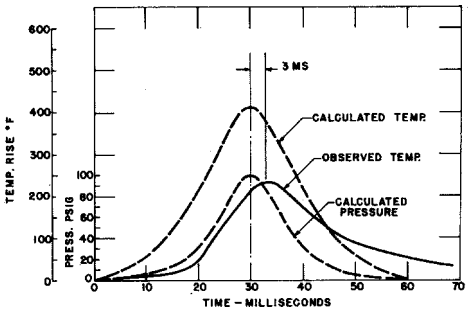

WIRE SIZE	LOW GAS FLOW	HIGH GAS FLOW
.0005" dia.	5 milliseconds	4 milliseconds
.001" dia.	10 milliseconds	7 milliseconds
.002" dia.	20 milliseconds	15 milliseconds
.003" dia.	50 milliseconds	35 milliseconds

MODELS

MEDTHERM fine wire probes are available in either 1/16" sheath diameter for minimum cross section or in 1/8" sheath diameter for sturdier mount or support of a radiation shield. The 1/16" sheath diameter probes can be ordered with 1/4" of #1-72 thread on the sheath end and the 1/8" sheath diameter probes may be ordered with 1/4" of #5-56 thread on the sheath end for mounting in close quarters or for attachment of radiation shields or diffusers. The probes may be bent to within 3/4" of the hot end.

The standard probes are supplied 5" long with 3 feet of fiberglass insulated lead wire. Other lengths may be specified. Probes may also be ordered with other terminations, such as a quick disconnect thermocouple plug attached directly to the sheath or a miniature thermocouple head with cover. Custom designs are available, including makeup of thermocouple rakes to customer specification.

Probe sheath diameter is 0.062" or 0.125". Standard probe length is 5".

Standard transition piece is stainless steel, 1/4" diameter 1-1/4" long, epoxy filled, with strain relief spring.

Standard cable is 24 AWG solid conductor duplex, three feet long with fiberglass insulation and metallic overbraid.
Other terminations are available, such as standard size or miniature thermocouple connectors, smaller transitions, etc.

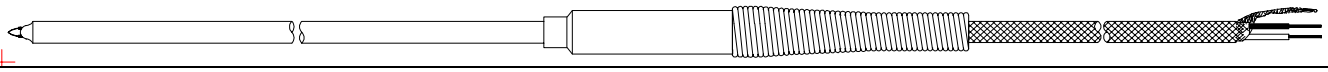

ASSEMBLY CATALOG NUMBERS

	TYPE S (INCONEL SHEATH)		TYPE K (INCONEL SHEATH)		TYPE E (304 SS SHEATH)		TYPE J (304 SS SHEATH)	
FINE WIRE DIAMETER	SHEATH DIAMETER		SHEATH DIAMETER		SHEATH DIAMETER		SHEATH DIAMETER	
	1/16"	1/8"	1/16"	1/8"	1/16"	1/8"	1/16"	1/8"
0.0005"	203-05S05	202-05S05	203-05K05	202-05K05	203-05E05	202-05E05	203-05J05	202-05J05
0.001"	203-05S10	202-05S10	203-05K10	202-05K10	203-05E10	202-05E10	203-05J10	202-05J10
0.002"	203-05S20	202-05S20	203-05K20	202-05K20	203-05E20	202-05E20	203-05J20	202-05J20
0.003"	203-05S30	202-05S30	203-05K30	202-05K30	203-05E30	202-05E30	203-05J30	202-05J30

1. Specify catalog number.
2. Specify probe length if other than 5".
3. Specify lead wire length if other than 3 feet.
4. Add suffix "C" if ceramic filled 540°C transition is desired.
5. Specify special termination if required.
6. Add suffix "T" if 1/4" of #1-72 thread is desired on 1/16" sheath diameter probe or if 1/4" of #5-56 thread is desired on 1/8" sheath diameter probe.
7. Specify fine wire size if other than standard P/N callout.
8. Copper/Constantan, Type T, can be supplied on request. (0.0005" dia. fine wire not available in Type T)

ACCESSORIES

RADIATION SHIELDS FIT "T" THREADS ON THE PROBE

	RADIATION SHIELD 3 - LAYER			RADIATION SHIELD HALF - CYLINDER DIFFUSER			RADIATION SHIELD OPEN END DIFFUSER			RADIATION SHIELD CLOSED TIP		
PROBE DIA	P/N	DIA	LENGTH	P/N	DIA	LENGTH	P/N	DIA	LENGTH	P/N	DIA	LENGTH
1/16"	10211	.25	.25	10210	.10	.50	10201	.10	.50	11109	.10	.50
1/8"	10630	.31	.25	10190	.16	.75	10191	.16	.75	11010	.16	.75

	NPT COMPRESSION FITTINGS, ADJUSTABLE, 304 SST		NPT COMPRESSION FITTINGS, NOT ADJUSTABLE, 304 SST	
	(AN FITTINGS ALSO AVAILABLE)		(AN FITTINGS ALSO AVAILABLE)	
MALE NPT	P/N, 1/16 DIA	P/N, 1/8 DIA	P/N, 1/16 DIA	P/N, 1/8 DIA
1/16"	50370	50371	50380	50381
1/8"	50372	50373	50382	50383
1/4"	50368	50369	50384	50385

NPT FIXED MOUNTING , 304 SST, BRAZED (500°C MAX)

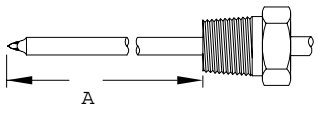

(AN FITTINGS ALSO AVAILABLE)

FITTING MALE NPT	P/N
1/16"	50390
1/8"	50391
1/4"	50392

BULLETIN 112.1
7/95

MEDTHERM CORPORATION

POST OFFICE BOX 412
HUNTSVILLE, ALABAMA 35804

TELEPHONE (256) 837-2000
FAX (256) 837-2001

Bibliography

[1] William Liss and W H. Thrasher. Variability of natural gas composition in select major metropolitan areas of the united states. 1992.

[2] Daniel Janecek, David Rothamer, and Jaal Ghandhi. Fuel-substitution method for investigating the kinetics of low-volatility fuels under enginelike operating conditions. *Energy and Fuels*, 30(2):1400–1406, 2016. doi: 10.1021/acs.energyfuels.5b02542. URL https://doi.org/10.1021/acs.energyfuels.5b02542.

[3] David G. Goodwin, Harry K. Moffat, and Raymond L. Speth. Cantera: An object-oriented software toolkit for chemical kinetics, thermodynamics, and transport processes. http://www.cantera.org, 2017. Version 2.3.0.

[4] Standard test method for motor octane number of spark-ignition engine fuel, 2014. ASTM MON.

[5] Gautam Kalghatgi. Fuel anti-knock quality - part i, engine studies. *SAE Technical Papers*, sep 2001. ISSN 0148-7191. doi: 10.4271/2001-01-3584. URL https://doi.org/10.4271/2001-01-3584.

[6] Andy D. B. Yates, André Swarts, and Carl L. Viljoen. Correlating auto-ignition delays and knock-limited spark-advance data for different types of fuel. *SAE Technical Papers*, may 2005. ISSN 0148-7191. doi: 10.4271/2005-01-2083. URL https://doi.org/10.4271/2005-01-2083.

[7] M. Leiker, Rankl M. Christoph, K., W. Cartellion, and U Pfiefer. Evaluation of anti-knock property of gaseous fuels by means of the methane number and its practical application to gas engines. *Diesel and Gas Engine Power*, pages 1–15, 1973. ISSN 72-DGP-4.

[8] John Kubesh, Steven R. King, and William E. Liss. Effect of gas composition on octane number of natural gas fuels. *SAE Technical Papers*, oct 1992. ISSN 0148-7191. doi: 10.4271/922359. URL https://doi.org/10.4271/922359.

[9] F.S. Schaub and R.L. Hubbard. A procedure for calculating fuel gas blend knock rating for large bore gas engines and predicting engine operation. *Diesel and Gas Engine Power*, 85-DGP-5, feb 1985.

[10] T.W. Ryan, T.J. Callahan, and S.R. King. Engine knock rating of natural gases - methane number. *Gas Turbines Power*, 115(4):769–776, oct 1993. doi: 10.1115/1.2906773. URL https://doi.org/10.1115/1.2906773.

[11] Gautam Kalghatgi. Auto-ignition quality of practical fuels and implications for fuel requirements of future si and hcci engines. *SAE Technical Papers*, apr 2005. ISSN 0148-7191. doi: 10.4271/2005-01-0239. URL https://doi.org/10.4271/2005-01-0239.

[12] Sander Gersen, Martijn van Essen, Howard Levinsky, and Gerco van Dijk. Characterizing gaseous fuels for their knock resistance based on the chemical and physical properties of the fuel. *SAE Technical Papers*, 9(1), mar 2016. ISSN 1946-3960. doi: doi.org/10.4271/2015-01-9077. URL https://doi.org/10.4271/2015-01-9077.

[13] Hagar Alm El-Din, Medhat Elkelawy, and Zhang Yu-Sheng. Hcci engines combustion of cng fuel with dme and h2 additives. *SAE Technical Papers*, may 2010. ISSN 0148-7191. doi: doi.org/10.4271/2010-01-1473. URL https://doi.org/10.4271/2010-01-1473.

[14] Daesu Jun, Kazuaki Ishii, and Norimasa Iida. Combustion analysis of natural gas in a four stroke hcci engine using experiment and elementary reactions calculation. *SAE Technical Papers*, mar 2003. ISSN 0148-7191. doi: 10.4271/2003-01-1089. URL https://doi.org/10.4271/2003-01-1089.

[15] D. Yap, A. Megaritis, S. Peucheret, M.L. Wyszynski, and Hongming Xu. Effect of hydrogen addition on natural gas hcci combustion. *SAE Technical Papers*, jun 2004. ISSN 0148-7191. doi: doi.org/10.4271/2004-01-1972. URL https://doi.org/10.4271/2004-01-1972.

[16] Scott B. Fiveland, Rey Agama, Magnus Christensen, Bengt Johansson, Joel Hiltner, Fabian Maus, and Dennis N. Assanis. Experimental and simulated results detailing the sensitivity of natural gas hcci engines to fuel composition. *SAE Technical Papers*, sep 2001. ISSN 0148-7191. doi: 10.4271/2001-01-3609. URL https://doi.org/10.4271/2001-01-3609.

[17] R.K. Hanson and D.F. Davidson. Recent advances in laser absorption and shock tube methods for studies of combustion chemistry. *Progress in Energy and Combustion Science*, 44:103–114, 2014. doi: 10.1016/j.pecs.2014.05.001. URL https://doi.org/10.1016/j.pecs.2014.05.001.

[18] G.A. Pang, D.F. Davidson, and R.K. Hanson. Experimental study and modeling of shock tube ignition delay times for hydrogen-oxygen-argon mixtures at low temperatures. *Proceedings of the Combustion Institute*, 32:181–188, 2009. ISSN 1540-7489. doi: 10.1016/j.proci.2008.06.014. URL http://www.sciencedirect.com/science/article/pii/S1540748908000230.

[19] Chih-Jen Sung and Henry J. Curran. using rapid compression machines for chemical kinetics studies. *Progress in Energy and Combustion Science*, 44:1–18, 2014. ISSN

0360-1285. doi: 10.1016/j.pecs.2014.04.001. URL https://doi.org/10.1016/j.pecs.2014.04.001.

[20] Gilles Bourque, Darren Healy, Henry Curran, Christopher Zinner, Danielle Kalitan, Jaap de Vries, Christopher Aul, and Eric Petersen. Ignition and flame speed kinetics of two natural gas blends with high levels of heavier hydrocarbons. *Gas Turbines Power*, 132(2), oct 2009. doi: 10.1115/1.3124665. URL https://doi.org/10.1115/1.3124665.

[21] Gaurav Mittal and Chih-Jen Sung. Aerodynamics inside a rapid compression machine. *Combustion and Flame*, 145(1):160–180, 2006. ISSN 0010-2180. doi: 10.1016/j.combustflame.2005.10.019. URL https://doi.org/10.1016/j.combustflame.2005.10.019.

[22] Nicolas Dronniou and John E. Dec. Investigating the development of thermal stratification from the near-wall regions to the bulk-gas in an hcci engine with planar imaging thermometry. *SAE Technical Papers*, apr 2012. ISSN 1946-3944. doi: 10.4271/2012-01-1111. URL https://doi.org/10.4271/2012-01-1111.

[23] Magnus Sjoberg and John E. Dec. An investigation of the relationship between measured intake temperature, bdc temperature, and combustion phasing for premixed and di hcci engines. *SAE Technical Papers*, jun 2004. ISSN 0148-7191. doi: 10.4271/2004-01-1900. URL https://doi.org/10.4271/2004-01-1900.

[24] H. J. Yun and W. Mirsky. Schlieren-streak measurements of instantaneous exhaust gas velocities from a spark-ignition engine. *SAE Technical Papers*, feb 1974. ISSN 0148-7191. doi: 10.4271/741015. URL https://doi.org/10.4271/741015.

[25] Jonathan W. Fox, Wai K. Cheng, and John B. Heywood. A model for predicting residual gas fraction in spark-ignition engines. *SAE Technical Papers*, mar 1993. ISSN 0148-7191. doi: 10.4271/931025. URL https://doi.org/10.4271/931025.

[26] B. P. Albert and J. B. Ghandhi. Residual gas measurements in a utility engine. *SAE Technical Papers*, sep 2004. ISSN 0148-7191. doi: 10.4271/2004-32-0029. URL https://doi.org/10.4271/2004-32-0029.

[27] M.A. Bolshov, Yu.A. Kuritsyn, and Yu.V. Romanovskii. Tunable diode laser spectroscopy as a technique for combustion diagnostics. *Spectrochimica Acta Part B: Atomic Spectroscopy*, 106:45–66, 2015. ISSN 0584-8547. doi: doi.org/10.1016/j.sab.2015.01.010. URL https://doi.org/10.1016/j.sab.2015.01.010.

[28] Scott. T. Melin and Scott T. Sanders. H2o absorption thermometry accuracy in the 7321-7598 cm-1 range studied in a heated static cell at temperatures up to 1723 k. *Journal of Quantitative Spectroscopy and Radiative Transfer*, apr 2018. ISSN 0022-4073. doi: doi.org/10.1016/j.jqsrt.2018.04.012. URL https://doi.org/10.1016/j.jqsrt.2018.04.012.

[29] R J. Barber, Jonathan Tennyson, G.J. Harris, and Roman Tolchenov. A high accuracy computed water line list. *Monthly Notices of the Royal Astronomical Society*, jan 2006. doi: 10.1111/j.1365-2966.2006.10184.x. URL https://doi.org/10.1111/j.1365-2966.2006.10184.x.

[30] L.S. Rothman, I.E. Gordon, R.J. Barber, H. Dothe, R.R. Gamache, A. Goldman, V.I. Perevalov, S.A. Tashkun, and J. Tennyson. Hitemp, the high-temperature molecular spectroscopic database. *Journal of Quantitative Spectroscopy and Radiative Transfer*, 111(15):2139–2150, jan 2010. ISSN 0022-4073. doi: 10.1016/j.jqsrt.2010.05.001. URL https://doi.org/10.1016/j.jqsrt.2010.05.001.

[31] L.S. Rothman, I.E. Gordon, A. Barbe, D.Chris Benner, P.F. Bernath, M. Birk, V. Boudon, L.R. Brown, A. Campargue, J.-P. Champion, K. Chance, L.H. Coudert, V. Dana, V.M. Devi, S. Fally, J.-M. Flaud, R.R. Gamache, A. Goldman, D. Jacquemart, I. Kleiner, N. Lacome, W.J. Lafferty, J.-Y. Mandin, S.T. Massie,

S.N. Mikhailenko, C.E. Miller, N. Moazzen-Ahmadi, O.V. Naumenko, A.V. Nikitin, J. Orphal, V.I. Perevalov, A. Perrin, A. Predoi-Cross, C.P. Rinsland, M. Rotger, M. Šimečková, M.A.H. Smith, K. Sung, S.A. Tashkun, J. Tennyson, R.A. Toth, A.C. Vandaele, and J. Vander Auwera. The hitran 2008 molecular spectroscopic database. *Journal of Quantitative Spectroscopy and Radiative Transfer*, 110(9):533–572, jan 2009. ISSN 0022-4073. doi: 10.1016/j.jqsrt.2009.02.013. URL https://doi.org/10.1016/j.jqsrt.2009.02.013.

[32] D.W. Mattison, J.B. Jeffries, R.K. Hanson, R.R. Steeper, S. De Zilwa, J.E. Dec, M. Sjoberg, and W. Hwang. In-cylinder gas temperature and water concentration measurements in hcci engines using a multiplexed-wavelength diode-laser system: Sensor development and initial demonstration. *Proceedings of the Combustion Institute*, 31(1):791–798, 2007. ISSN 1540-7489. doi: 10.1016/j.proci.2006.07.048. URL https://doi.org/10.1016/j.proci.2006.07.048.

[33] G.B. Rieker, H. Li, X. Liu, J.T.C Liu, J.B. Jeffries, R.K. Hanson, M.G. Allen, S.D. Wehe, P.A. Mulhall, H.S. Kindle, A. Kakuho, K.R. Sholes, T. Matsuura, and S. Takatani. Rapid measurements of temperature and h2o concentration in ic engines with a spark plug-mounted diode laser sensor. *Proceedings of the Combustion Institute*, 31(2):3041–3049, 2007. ISSN 1540-7489. doi: 10.1016/j.proci.2006.07.158. URL https://doi.org/10.1016/j.proci.2006.07.158.

[34] Apurba Kumar Das, Mruthunjaya Uddi, and Chih-Jen Sung. Two-line thermometry and h2o measurement for reactive mixtures in rapid compression machine near 7.6μm. *Combustion and Flame*, 159(12):3493–3501, nov 2012. ISSN 0010-2180. doi: 10.1016/j.combustflame.2012.06.020. URL https://doi.org/10.1016/j.combustflame.2012.06.020.

[35] Mruthunjaya Uddi, Apurba Kumar Das, and Chih-Jen Sung. Temperature measurements in a rapid compression machine using mid-infrared h2o absorption spec-

troscopy near 7.6μm. *Appl. Opt.*, 51:5464–5476, aug 2012. doi: 10.1364/AO.51.005464. URL https://doi.org/10.1364/AO.51.005464.

[36] Laura A. Kranendonk, Xinliang An, Andrew W. Caswell, Randy E. Herold, Scott T. Sanders, Robert Huber, James G. Fujimoto, Yasuhiro Okura, and Yasuhiro Urata. High speed engine gas thermometry by fourier-domain mode-locked laser absorption spectroscopy. *Opt. Express*, 15:15115–15128, nov 2007. doi: 10.1364/OE.15.015115. URL https://doi.org/10.1364/OE.15.015115.

[37] Laura A. Kranendonk, Andrew W. Caswell, and Scott T. Sanders. Robust method for calculating temperature, pressure, and absorber mole fraction from broadband spectra. *Appl. Opt.*, 46:4117–4124, nov 2007. doi: 10.1364/AO.46.004117. URL https://doi.org/10.1364/AO.46.004117.

[38] Eric Gingrich, Jaal Ghandhi, and Rolf D. Reitz. Experimental investigation of piston heat transfer in a light duty engine under conventional diesel, homogeneous charge compression ignition, and reactivity controlled compression ignition combustion regimes. *SAE Technical Papers*, apr 2014. ISSN 1946-3944. doi: 10.4271/2014-01-1182. URL https://doi.org/10.4271/2014-01-1182.

[39] Terry Hendricks, Jaal Ghandhi, and John Brossman. Instantaneous local heat flux measurements in a small utility engine. *Internal Combustion Engine Division Spring Technical Conference*, 2009. doi: 10.1115/ICES2009-76035. URL https://doi.org/10.1115/ICES2009-76035.

[40] Junseok Chang, Orgun Güralp, Zoran Filipi, Dennis N. Assanis, Tang-Wei Kuo, Paul Najt, and Rod Rask. New heat transfer correlation for an hcci engine derived from measurements of instantaneous surface heat flux. *SAE Technical Papers*, oct 2004. ISSN 0148-7191. doi: 10.4271/2004-01-2996. URL https://doi.org/10.4271/2004-01-2996.

[41] Peter Schaal, Byron Mason, Sotiris Filippou, Ioannis Souflas, and Mark Cary. Robust methodology for fast crank angle based temperature measurement. *SAE Technical Papers*, apr 2016. ISSN 0148-7191. doi: 10.4271/2016-01-1072. URL https://doi.org/10.4271/2016-01-1072.

[42] Robert J. Kee, Peter Hung, Bryan Fleck, George Irwin, Robert Kenny, John Gaynor, and Sean McLoone. Fast response exhaust gas temperature measurement in ic engines. *SAE Technical Papers*, apr 2006. ISSN 0148-7191. doi: 10.4271/2006-01-1319. URL https://doi.org/10.4271/2006-01-1319.

[43] T.M. Shapland, R.L. Snyder, K.T. Paw U, and A.J. McElrone. Thermocouple frequency response compensation leads to convergence of the surface renewal alpha calibration. *Agricultural and Forest Meteorology*, 189-190:36–47, 2014. ISSN 0168-1923. doi: 10.1016/j.agrformet.2014.01.008. URL https://doi.org/10.1016/j.agrformet.2014.01.008.

[44] Marvin D. Scadron and Warshasky Isidor. Experimental determination of time constants and nusselt numbers for bare-wire thermocouples in high-velocity air streams and analytic approximation of conduction and radiation errors. 1952.

[45] M. Tagawa, T. Shimoji, and Y. Ohta. A two-thermocouple probe technique for estimating thermocouple time constants in flows with combustion: In situ parameter identification of a first-order lag system. *Review of Scientific Instruments*, 69(9): 3370–3378, 1998. doi: 10.1063/1.1149103. URL https://10.1063/1.1149103.

[46] T. Asmus Zhao, D. Assanis, J. Dec, J. Eng, and P. Najt. *Homogeneous Charge Compression Ignition (HCCI) Engines: Key Research and Development Issues*. SAE International, 2003.

[47] Hongming Xu, Michael Liu, Shadi Gharahbaghi, Steve Richardson, Miroslaw Wyszynski, and Thanos Megaritis. Modelling of hcci engines: Comparison of single-

zone, multi-zone and test data. *SAE Technical Papers*, may 2005. ISSN 0148-7191. doi: 10.4271/2005-01-2123. URL https://doi.org/10.4271/2005-01-2123.

[48] Mattia Bissoli, Alessio Frassoldati, Alberto Cuoci, Eliseo Ranzi, M Mehl, and T Faravelli. A new predictive multi-zone model for hcci engine combustion. *Applied Energy*, 178:826–843, jul 2016.

[49] Toru Noda and David E. Foster. A numerical study to control combustion duration of hydrogen-fueled hcci by using multi-zone chemical kinetics simulation. *SAE Technical Papers*, mar 2001. ISSN 0148-7191. doi: 10.4271/2001-01-0250. URL https://doi.org/10.4271/2001-01-0250.

[50] William L. Easley, Apoorva Agarwal, and George A. Lavoie. Modeling of hcci combustion and emissions using detailed chemistry. *SAE Technical Papers*, mar 2001. ISSN 0148-7191. doi: 10.4271/2001-01-1029. URL https://doi.org/10.4271/2001-01-1029.

[51] Marco Mehl, Tiziano Faravelli, Eliseo Ranzi, David Miller, and Nicholas Cernansky. Experimental and kinetic modeling study of the effect of fuel composition in hcci engines. *Proceedings of the Combustion Institute*, 32(2):2843–2850, 2009. ISSN 1540-7489. doi: 10.1016/j.proci.2008.08.001. URL https://doi.org/10.1016/j.proci.2008.08.001.

[52] Darko Kozarac, Zoran Lulic, and Goran Sagi. A six-zone simulation model for hcci engines with a non-segregated solver of zone state. *Combustion Theory and Modelling*, 14:425–451, jun 2010. doi: 10.1080/13647830.2010.489959. URL https://doi.org/10.1080/13647830.2010.489959.

[53] Salvador M. Aceves, Daniel L. Flowers, Joel Martinez-Frias, Francisco Espinosa-Loza, Magnus Christensen, Bengt Johansson, and Randy P. Hessel. Analysis of the effect of geometry generated turbulence on hcci combustion by multi-zone modeling.

SAE Technical Papers, may 2005. ISSN 0148-7191. doi: 10.4271/2005-01-2134. URL https://doi.org/10.4271/2005-01-2134.

[54] Benjamin Lawler, Mark Hoffman, Zoran Filipi, Orgun Guralp, and Paul Najt. Development of a postprocessing methodology for studying thermal stratification in an hcci engine. *Gas Turbines and Power*, 134(10), aug 2012. doi: 10.1115/1.4007010. URL http://dx.doi.org/10.1115/1.4007010.

[55] Benjamin Lawler, Joshua Lacey, Nicolas Dronniou, Jeremie Dernotte, John E. Dec, Orgun Guralp, Paul Najt, and Zoran Filipi. Refinement and validation of the thermal stratification analysis: A post-processing methodology for determining temperature distributions in an experimental hcci engine. *SAE Technical Papers*, apr 2014. ISSN 0148-7191. doi: 10.4271/2014-01-1276. URL https://doi.org/10.4271/2014-01-1276.

[56] Fabian Hoppe, Ultan Burke, Matthias Thewes, Alexander Heufer, Florian Kremer, and Stefan Pischinger. Tailor-made fuels from biomass: Potentials of 2-butanone and 2-methylfuran in direct injection spark ignition engines. *Fuel*, 167:106–117, mar 2016. ISSN 0016-2361. doi: 10.1016/j.fuel.2015.11.039. URL http://dx.doi.org/10.1016/j.fuel.2015.11.039.

[57] J.C. Livengood and P.C. Wu. Correlation of autoignition phenomena in internal combustion engines and rapid comession machines. *Proceedings of the Combustion Institute*, 5(1):347–356, 1955. ISSN 0082-0784. doi: 10.1016/S0082-0784(55)80047-1. URL https://doi.org/10.1016/S0082-0784(55)80047-1.

[58] A. M. Douaud and P. Eyzat. Four-octane-number method for predicting the anti-knock behavior of fuels and engines. *SAE Technical Papers*, feb 1978. ISSN 0148-7191. doi: 10.4271/780080. URL https://doi.org/10.4271/780080.

[59] Gregory P. Smith, David M. Golden, Michael Frenklach, Nigel W. Moriarty, Boris

Eiteneer, Mikhail Goldenberg, C. Thomas Bowman, Ronald K. Hanson, Soonho Song, William C Jr Gardiner, Vitali V. Lissianski, and Zhiwei Qin. URL http://www.me.berkeley.edu/gri_mech/. GRI-Mech 3.0.

[60] Daniel J Seery and Craig T. Bowman. An experimental and analytical study of methane oxidation behind shock waves. *Combustion and Flame*, 14(1):37–47, 1970. ISSN 0010-2180. doi: 10.1016/S0010-2180(70)80008-6. URL https://10.1016/S0010-2180(70)80008-6.

[61] Y. Hidaka, Jr. Gardiner W.C., and C.S. Eubank. Shock tube and modeling study of the ignition chemistry of small hydrocarbons. *J. Mol. Sci.*, 2(4):141–153, 1982.

[62] Michael Frenklach and David E. Bornside. Shock-initiated ignition in methane-propane mixtures. *Combustion and Flame*, 56(1):1–27, 1984. ISSN 0010-2180. doi: 10.1016/0010-2180(84)90002-6. URL https://doi.org/10.1016/0010-2180(84)90002-6.

[63] L.J. Spadaccini and M.B. Colket. Ignition delay characteristics of methane fuels. *Progress in Energy and Combustion Science*, 20(5):431–460, 1994. ISSN 0360-1285. doi: 10.1016/0360-1285(94)90011-6. URL https://doi.org/10.1016/0360-1285(94)90011-6.

[64] E.L. Petersen, D.F. Davidson, and R.K. Hanson. Ignition delay times of ram accelerator ch_4/o_2/diluent mixtures. *Journal of Propulsion and Power*, 15(1):82–91, 1999. doi: 10.2514/2.5394. URL https://doi.org/10.2514/2.5394.

[65] J. Huang and W.K. Bushe. Experimental and kinetic study of autoignition in methane/ethane/air and methane/propane/air mixtures under engine-relevant conditions. *Combustion and Flame*, 144(1):74–88, 2006. ISSN 0010-2180. doi: doi.org/10.1016/j.combustflame.2005.06.013. URL https://doi.org/10.1016/j.combustflame.2005.06.013.

[66] Marco Mehl, William J. Pitz, Charles K. Westbrook, and Henry J. Curran. Kinetic modeling of gasoline surrogate components and mixtures under engine conditions. *Proceedings of the Combustion Institute*, 33(1):193–200, 2011. ISSN 1540-7489. doi: doi.org/10.1016/j.proci.2010.05.027. URL `https://doi.org/10.1016/j.proci.2010.05.027`.

[67] Wayne Metcalfe, Sinéad Burke, Syed Ahmed, and H.J. Curran. A hierarchical and comparative kinetic modeling study of c1 c2 hydrocarbon and oxygenated fuels. *International Journal of Chemical Kinetics*, 45), oct 2013.

[68] D. Healy, D.M. Kalitan, C.J. Aul, E.L. Petersen, G. Bourque, and H.J. Curran. Oxidation of c1-c5 alkane quinternary natural gas mixtures at high pressures. *Energy and Fuels*, 24(3):1521–1528, mar 2010. ISSN 0887-0624. doi: 10.1021/ef9011005. URL `https://doi.org/10.1021/ef9011005`.

[69] D. Healy, M. M. Kopp, N. L. Polley, E. L. Petersen, G. Bourque, and H.J. Curran. Methane/n-butane ignition delay measurements at high pressure and detailed chemical kinetic simulations. *Energy and Fuels*, 24(3):1617–1627, 2010.

[70] D. Healy, N. S. Donato, C. J. Aul, E. L. Petersen, C. M. Zinner, G. Bourque, and H. J. Curran. Isobutane ignition delay time measurements at high pressure and detailed chemical kinetic modeling. *Combustion and Flame*, 157(8):1540–1551, 2010.

[71] D. Healy, N. S. Donato, C. J. Aul, E. L. Petersen, C. M. Zinner, G. Bourque, and H. J. Curran. n-butane ignition delay time measurements at high pressure and detailed chemical kinetic modeling. *Combustion and Flame*, 157(8):1526–1539, 2010.

[72] N. Donato, C. Aul, E. Petersen, C. Zinner, H. Curran, and G. Bourque. Ignition and oxidation of 50/50 butane isomer blends. *Gas Turbines and Power*, 132, may 2010.

[73] E. L. Petersen, D. M. Kalitan, S. Simmons, G. Bourque, H. J. Curran, and J. M. Simmie. Methane/propane oxidation at high pressures: Experimental and detailed chemical kinetic modelling. *Proceedings of the Combustion Institute*, 31:447–454, 2007.

[74] Adam Dempsey. *Dual-Fuel Reactivity Controlled Compression Ignition (RCCI) with Alternative Fuels*. University of Wisconsin-Madison, 2013.

[75] Emiliano Pipitone, Alberto Beccari, and Stefano Beccari. Reliable tdc position determination: a comparison of different thermodynamic methods through experimental data and simulations. *SAE Technical Papers*, oct 2008. doi: 10.4271/2008-36-0059. URL `https://doi.org/10.4271/2008-36-0059`.

[76] H. J. Yun and W. Mirsky. Schlieren-streak measurements of instantaneous exhaust gas velocities from a spark-ignition engine. *SAE Technical Papers*, feb 1974. ISSN 0148-7191. doi: 10.4271/741015. URL `https://doi.org/10.4271/741015`.

[77] D. F. Swinehart. The beer-lambert law. *Journal of Chemical Education*, 39(7), 1962. ISSN 0021-9584. doi: 10.1021/ed039p333. URL `https://doi.org/10.1021/ed039p333`.

[78] Scott Melin. *Development of a Gas Cell for Quantitative Spectroscopic Studies at Combustion Relevant Temperatures with Absorption Spectroscopy Applications*. University of Wisconsin-Madison, 2017.

[79] K. J. Richards, P. K. Senecal, and E. Pomraning. Converge. Convergent Science, 2017. Version 2.4.

[80] W.J.D. Annand. Heat transfer in the cylinders of reciprocating internal combustion engines. *Proceedings of the Institution of Mechanical Engineers*, 177:973–996, oct 1963. doi: 10.1243/PIME_PROC_1963_177_069_02. URL `https://doi.org/10.1243/PIME_PROC_1963_177_069_02`.

[81] Cummins westport fuel quality calculator. http://www.cumminswestport.com/fuel-quality-calculator. Accessed: 2018-06-10.